JUL 15

Journal of Research

of the National Bureau of Standards

UNIVERSITY OF MICHIGAN
JUL 11 1958
PHYSICS LIBRARY

MAY 1958

VOLUME 60 NUMBER 5

DEPARTMENT OF COMMERCE
Sinclair Weeks, Secretary
BUREAU OF STANDARDS
A. V. Astin, Director

MAY • 1958
VOLUME • 60
NUMBER • 5

JOURNAL OF RESEARCH
of the
NATIONAL BUREAU OF STANDARDS

The National Bureau of Standards

Functions and Activities

The functions of the National Bureau of Standards are set forth in the Act of Congress, March 3, 1901, as amended by Congress in Public Law 619, 1950. These include the development and maintenance of the national standards of measurement and the provision of means and methods for making measurements consistent with these standards; the determination of physical constants and properties of materials; the development of methods and instruments for testing materials, devices, and structures; advisory services to Government Agencies on scientific and technical problems; invention and development of devices to serve special needs of the Government; and the coordination of standards, codes, and specifications. The work includes basic and applied research, development, engineering, instrumentation, testing, evaluation, calibration services, and various consultation and information services. Research projects are also performed for other Government agencies when the work relates to and supplements the basic program of the Bureau or when special competence is required. The scope of activities is suggested by the listing of divisions and sections on the inside of the back cover.

Publications

The results of the Bureau's work take the form of either actual equipment and devices or published papers. Papers appear either in the Bureau's own series of publications or in the journals of professional and scientific societies. The Bureau itself publishes three monthly periodicals available from the Government Printing Office: The Journal of Research, which presents complete papers reporting technical investigations; the Technical News Bulletin, which presents summary and preliminary reports on work in progress; and Basic Radio Propagation Predictions, which gives data for determining the best frequencies to use for radio communications throughout the world. There are also five series of nonperiodical publications: The Applied Mathematics Series, Circulars, Handbooks, Building Materials and Structures Reports, and Miscellaneous Publications.

Information on the Bureau's publications can be found in NBS Circular 460, Publications of the National Bureau of Standards ($1.25) and its Supplement ($1.50), available from the Superintendent of Documents, Government Printing Office, Washington 25, D. C.

Order all publications from the Superintendent of Documents
U. S. Government Printing Office, Washington 25, D. C.

Publication approved by the Director of the Bureau of the Budget (May 14, 1956)

Journal of Research of the National Bureau of Standards Vol. 60, No. 5, May 1958 Research Paper 2857

Forces on Cylinders and Plates in an Oscillating Fluid [1]

Garbis H. Keulegan and Lloyd H. Carpenter

The inertia and drag coefficients of cylinders and plates in simple sinusoidal currents are investigated. The midsection of a rectangular basin with standing waves surging in it is selected as the locale of currents. The cylinders and plates are fixed horizontally and below the water surface. The average values of the inertia and drag coefficients over a wave cycle show variations when the intensity of the current and the size of the cylinders or plates are changed. These variations, however, can be correlated with the period parameter $U_m T/D$, where U_m is the maximum intensity of the sinusoidal current, T is the period of the wave and D is the diameter of the cylinder or the width of the plate. For the cylinders $U_m T/D$ equaling 15 is a critical condition yielding the lowest value of the inertia coefficient and the largest value of the drag coefficient. For the plates the higher values of the drag coefficient are associated with the smaller values of $U_m T/D$ and the higher values of the mass coefficient with the larger values of $U_m T/D$. The variation of the coefficients with the phase of the wave is examined and the bearing of this on the formula for the forces is discussed. The flow patterns around the cylinders and plates are examined photographically, and a suggestion is advanced as to the physical meaning of the parameter $U_m T/D$.

1. Introduction

In a remarkable paper on the motion of pendulums Stokes showed that the expression for the force on a sphere oscillating in an unlimited viscous fluid consists of two terms, one involving the acceleration of the sphere and the other the velocity [1].[2] Furthermore, the inertia coefficient involved in the acceleration term is modified because of viscosity and, indeed, is augmented over the theoretical value valid for irrotational flow. The drag coefficient associated with the velocity term is modified because of the acceleration, and its value is greater than it would be if the sphere were moving with a constant velocity. Subsequent to Stokes' studies, the forces on a sphere moving in a viscous fluid in an arbitrary manner were investigated by Boussinesq and also by Basset [2, 3]. They found that the force experienced by a sphere at a given time depends, in general, on the entire history of its acceleration as well as the instantaneous velocity and acceleration. As an example, if a sphere is accelerated, say with a constant acceleration, from a position of rest to a finite velocity and is then kept at this velocity, the force during the initial instants of uniform velocity differs from the force occurring at a later time. Rayleigh has given the formula for the force for this case [4]. The force expression of Boussinesq-Basset contains three terms, one of which is in the form of an integral involving the history of acceleration. If the integral is evaluated when the acceleration is represented by a sinusoidal function it then yields the modifications of the inertia and drag coefficients in Stokes' formula.

One expects quantitatively different results when the oscillating velocities are large and the flow turbulent. As yet a theoretical analysis of the problem is difficult and much of the desired information must be obtained experimentally. In this respect the experimental studies have been dealt with variously. One method is due to McNown and Wolf [5], who considered the force on a two-dimensional object immersed in a flow as made up of three parts:

$$F = A_0 \rho \frac{d(kU)}{dt} + \oint p_x dS + \frac{1}{2} C_d D \rho U |U|, \qquad (1)$$

where F is the force per unit length in the direction of flow, x; U the velocity at points far removed from the object; p_x, the x-component of the ambient pressure in the absence of the body; dS, an element of the surface area; C_d, the coefficient of drag; and k, the virtual mass coefficient. The dimension of the body normal to the flow is D, and A_0 is a circular area, $A_0 = \pi D^2/4$, to which the added mass is referred. If A is the cross-sectional area of the body, $A = rA_0$, r being a ratio, then

$$\oint p_x dS = \rho r A_0 \frac{dU}{dt},$$

and finally

$$F = A_0 \rho \left[\frac{d(kU)}{dt} + r \frac{dU}{dt} \right] + \frac{1}{2} C_d D \rho U |U|.$$

In this approach the variability of the mass coefficient, k, is implied. Thus, introducing a new coefficient k' such that

$$k' \frac{dU}{dt} = \frac{d}{dt}(kU)$$

and putting

$$C_m = (k' + r), \qquad (3)$$

there is obtained from eq (1), the expression

$$F = C_m \rho A_0 \frac{dU}{dt} + \frac{1}{2} C_d D \rho U |U|, \qquad (4)$$

which in fact constitutes a second approach utilized first by Morison and coinvestigators [6, 7]. The form of the expression is in agreement with the Stokes formula for force on a sphere oscillating in a viscous medium. In a general sense one may still regard C_m as a kind of mass or inertia coefficient.

[1] Investigation sponsored by the Office of Naval Research.
[2] Figures in brackets indicate the literature references at the end of this paper.

A third approach was proposed by Iversen and Balent, who considered the force on an accelerated disk moving in one direction [8]. Briefly,

$$F=C\rho DU^2, \tag{5}$$

where

$$C=C\left(\frac{DU}{\nu},\frac{D}{U^2}\frac{dU}{dt}\right).$$

Keim has considered the case of accelerated cylinders [9] and Bugliarello that of accelerated spheres [10], all motions being in one direction. Here the resort is to a single coefficient C and attempts to separate the effects of acceleration and viscosity have not been shown to be successful. Accordingly, the adoption of this method can have a meaning only for monotonic motions subject to definite limitations as to initial and final conditions.

For oscillatory motions, although the forces are more accurately described either using eq (2) or eq (4), the latter might be preferred provided the coefficients C_m and C_d could be predicted with some precision. The application of the expression to vertical piling and large submerged objects by Reid and Bretschneider stresses the necessity of having these coefficients better determined [11].

On the basis of irrotational flow around the cylinder, C_m should equal 2, and one may suppose that the value of C_d should be identical with that applicable to a constant velocity. Morison and coinvestigators have obtained the values of C_d and C_m in particular cases by considering the observed forces in the phases of the wave cycle where U or dU/dt vanishes. Such determinations show considerable variations of C_m from the theoretical value and of C_d from the steady state value at the corresponding Reynolds number. Dealing with field studies at Caplen, Texas, R. O. Reid found similar variations in C_m and C_d [12]. The variations in the coefficients, however, have not yet been correlated with any appropriate parameter.

The present investigation was undertaken with the following two objectives in mind. The first was in regard to a supplementary function ΔR that could be introduced in eq (4) for a truer representation of force when considering the coefficients C_m and C_d as being constant throughout a given wave cycle. The necessity for the term ΔR is associated with the eventuality that the point values of C_m and C_d deviate from their average values. The second objective was to examine the possibility of correlating the average values of C_m and C_d with a parameter U_mT/D, where U_m is the amplitude of the harmonically varying velocity, T is the period of the oscillations, and D is the diameter of a cylinder or the breadth of a rectangular plate. The mid-cross section of a large rectangular vessel with standing waves surging in it was chosen as the field of harmonically varying current. The cylinders and plates were held fixed horizontally, totally submerged in water and extending from one side of the vessel to the other to approximate as closely as possible the condition of infinite length.

2. Fluid Forces on an Immersed Body at Rest in a Moving Liquid

It would be instructive to consider the momentum equations discussed by Murnaghan for the evaluation of force on objects immersed in a perfect liquid [13]. The method, however, is now generalized to apply to imperfect liquids.

Consider the case of two-dimensional flow with x horizontal and z vertical. The equation of motion in the x-direction is

$$\rho\left(\frac{\partial u}{\partial t}+u\frac{\partial u}{\partial x}+w\frac{\partial u}{\partial z}\right)=\frac{\partial p_{xx}}{\partial x}+\frac{\partial p_{zx}}{\partial z}, \tag{6}$$

where u and w are the velocity components along the axes x and z, ρ the density of the liquid, p_{xx} the normal stress on an elementary surface perpendicular to x, and p_{zx} the tangential stress on an elementary surface normal to z, the stress being in the direction of x. Because of the incompressibility of the liquid,

$$\frac{\partial u}{\partial x}+\frac{\partial w}{\partial z}=0 \tag{7}$$

and eq (2) becomes

$$\rho\frac{\partial u}{\partial t}+\rho\left(\frac{\partial}{\partial x}u^2+\frac{\partial}{\partial z}uw\right)=\frac{\partial p_{xx}}{\partial x}+\frac{\partial p_{zx}}{\partial x}. \tag{8}$$

Take the immersed cylindrical body of surface S, as in figure 1, and draw a surface S' of arbitrary shape which encloses the cylinder. Let ω be the region bounded by S and S' and l and n the direction cosines of the normal drawn inward into the region. Integrating eq (8) throughout ω, and in this making use of Green's Theorem, one finds

$$\rho\int\frac{\partial u}{\partial t}d\omega-\rho\int u(lu+nw)dS-\rho\int u(lu+nw)dS'=$$
$$-\int(lp_{xx}+np_{zx})dS-\int(lp_{xx}+np_{zx})dS'. \tag{9}$$

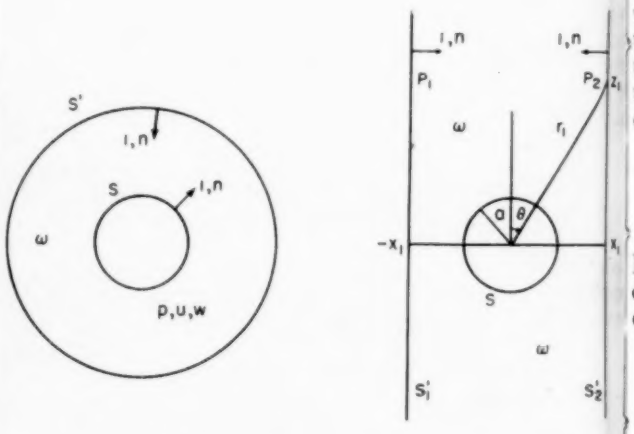

FIGURE 1. *Notation diagram for force analysis.*

Over the surface S of the immersed body $lu+nw$ vanishes because the body is at rest. Also $\int(lp_{xx}+np_{xz})dS=F$, that is, the x-component of the force exerted on the solid by the moving liquid. It may be assumed that if S' is removed sufficiently from the body the tangential stress p_{xz} on S' vanishes and the normal stress p_{xx} reduces to the hydrostatic pressure $-p$. Solving for F,

$$F=-\rho\int\frac{\partial u}{\partial t}d\omega+\rho\int u(lu+nw)dS'+\int lpdS'. \quad (10)$$

The later relation may be given in another form, suitable for the present purpose. Select the bounding surface S' as the rectangular strip shown in figure 1. The plane S_1' to the left of the cylinder passes through the point $x=-x_1$ and the plane S_2' to the right passes through $x=x_1$. Denoting the horizontal velocity components at the points P_1 and P_2 with the common elevation z_1 by u_1 and u_2, and the pressures by p_1 and p_2, eq (10) now reduces to

$$F=-\rho\int_\omega\frac{\partial u}{\partial t}d\omega+\rho\int_{-\infty}^{+\infty}(u_1^2-u_2^2)dz_1+\int_{-\infty}^{+\infty}(p_1-p_2)dz_1, \quad (11)$$

which is the momentum equation of familiar form.

This may be specialized to evaluate the force on a circular cylinder when the motion is irrotational. Letting U be the undisturbed velocity and referring to Lamb [14],

$$\left.\begin{aligned} u&=U\left[1+\frac{a^2}{r^2}\cos 2\theta\right]\\ w&=-U\frac{a^2}{r^2}\sin 2\theta\\ \frac{p}{\rho}&=\frac{dU}{dt}\left(r+\frac{a^2}{r}\right)\sin\theta-\frac{1}{2}(u^2+w^2)\end{aligned}\right\}, \quad (12)$$

where a is the radius of the cylinder, r is radial distance, and θ is the angle between a radius vector and the vertical line $x=0$ passing through the center of the cylinder. Clearly, $u_1=u_2$ and the momentum equation, eq (11), reduces to

$$F_1=-\rho\int_\omega\frac{\partial u}{\partial t}d\omega+\int_{-\infty}^{\infty}(p_1-p_2)dz_1. \quad (13)$$

Introducing the values of u and p from eq (12), and omitting the straightforward but somewhat lengthy evaluations, the result is

$$F_1=2\pi\frac{dU}{dt}a^2\rho,$$

or in terms of the diameter D of the cylinder

$$F_1=C_m\frac{\rho\pi D^2}{4}\frac{dU}{dt}, \quad (14)$$

where $C_m=2$.

Next, suppose that the undisturbed velocity is constant and that the body experiences a drag. With the liquid extending to infinity and ignoring the variation of pressures from the shedding eddies, or, more properly, assuming that the surfaces S_1' and S_2' are far removed from the cylinder, $p_1=p_2$, and eq (11) reduces to

$$F_2=\rho\int_{-\infty}^{+\infty}(u_1^2-u_2^2)dz_1. \quad (15)$$

The velocity $u_1=U$, and $u_2=mU$, where m is dependent on z_1/D and on Reynolds number UD/ν. Thus,

$$F_2=C_d\rho D\frac{U^2}{2} \quad (16)$$

where

$$C_d=2\int_{-\infty}^{+\infty}(1-m^2)d\frac{z_1}{D}.$$

It appears that in ordinary cases where the flow departs from irrotationality and becomes unsteady and eddying, eq (11) is still the basis for evaluating the force, since the first and third integrals may be associated with acceleration and the second with drag. That is, the coefficients C_m and C_d are derived from eq (13) and (15) provided the velocities and pressures can be given. The force of the statement is only academic, since in the flows involving separation and intermittent eddy formation the pressures and velocities are not known and the integrations in eq (11), at present, cannot be carried out. Nevertheless, experience suggests that eq (4) remains useful at least for sinusoidal motions, if allowance can be made for the variations in C_m and C_d.

Had one carried out the integrations in eq (11) for an extended plate using the known velocity expressions derived from the Kirchoff solution for the impact on a lamina, definite values for C_m and C_d would have resulted. This would have shown in principle the existence of a relation between C_m and C_d in the absence of eddy formation. In the Kirchoff solution the wake is of infinite length and this is cause for concern. McNown overcomes this difficulty by considering the case of a closed wake as between two plates and finds a relation between k and C_d or between C_m and C_d [15]. This result is very significant as it points to the path to be followed in analytical approaches taking into account also the effect of the eddy processes. With cylinders the changing separation seats are a cause of added difficulty.

Meanwhile, the tasks of the experimental investigations become more necessary. Not only are the needs of the applied arts to be fulfilled, but also there must be clarification as regards the flow processes during unsteady flows.

3. Cylinder in a Field of Sinusoidal Motion

Forces on a cylinder admit an easier representation when the undisturbed portion of the flow, infinite in extent, is varying harmonically. Let the velocity be given by

$$U=-U_m \cos \sigma t, \tag{17}$$

where U_m is the semiamplitude of the current, T the period of the alternations, and $\sigma=2\pi/T$. The force on the cylinder per unit length F is in general

$$F=f(t,T,U_m,D,\rho,\nu). \tag{18}$$

Grouping the variables on the basis of dimensional reasoning

$$\frac{F}{\rho U_m^2 D}=f\left(\frac{t}{T},\frac{U_m T}{D},\frac{U_m D}{\nu}\right),$$

or introducing

$$\theta=2\pi t/T, \tag{19}$$

$$\frac{F}{\rho U_m^2 D}=f\left(\theta,\frac{U_m T}{D},\frac{U_m D}{\nu}\right), \tag{20}$$

where $U_m D/\nu$ is a Reynolds number and $U_m T/D$ will be termed the "period parameter." Bearing in mind that F is periodic, and that because of flow symmetry

$$F(\theta)=-F(\theta+\pi),$$

we have

$$\frac{F}{\rho U_m^2 D}=A_1 \sin\theta+A_3 \sin 3\theta+A_5 \sin 5\theta+\ldots$$
$$+B_1 \cos\theta+B_3 \cos 3\theta+B_5 \cos 5\theta+\ldots. \tag{21}$$

Here the coefficients $A_1, A_3 \ldots$, and $B_1, B_3 \ldots$ are independent of θ, and are at most functions of $U_m T/D$ and $U_m D/\nu$. A sure method of approach in the analysis of the observed force curve is to resort to a Fourier analysis to determine the coefficients $A_1 \ldots B_1 \ldots$.

$$A_n=\frac{1}{\pi}\int_0^{2\pi}\frac{F \sin n\theta}{\rho U_m^2 D}\,d\theta \tag{22}$$

and

$$B_n=\frac{1}{\pi}\int_0^{2\pi}\frac{F \cos n\theta}{\rho U_m^2 D}\,d\theta. \tag{23}$$

Once the coefficients are obtained, their dependence on $U_m T/D$ and $U_m D/\nu$ may be established, provided the observational data are of sufficient number and of large extent.

The above general and fundamental relation, eq (21), may be reconciled with eq (4), which is the form which Morison and coinvestigators Reid, Bretschneider and others, have adopted in their numerous studies. Introducing U from eq (17) into eq (4)

$$\frac{F}{\rho U_m^2 D}=\frac{\pi}{4}C_m\cdot\frac{D\sigma}{U_m}\sin\theta-\frac{C_d}{2}|\cos\theta|\cos\theta. \tag{24}$$

By the rule of Fourier

$$|\cos\theta|\cos\theta=\sum_{n=0}^{\infty}\frac{\int_0^{2\pi}|\cos\theta|\cos\theta\cos n\theta\,d\theta}{\int_0^{2\pi}\cos^2 n\theta\,d\theta}$$
$$=a_0+a_1\cos\theta+a_2\cos 2\theta+a_3\cos 3\theta+\ldots$$

where

$$a_n=0 \text{ for } n \text{ even},$$

$$a_n=(-1)^{\frac{n+1}{2}}\frac{8}{n(n^2-4)\pi} \text{ for } n \text{ odd},$$

$$a_1=\frac{8}{3\pi},\ a_3=\frac{8}{15\pi},\ a_5=-\frac{8}{105\pi},\ \ldots. \tag{25}$$

Introducing this in eq (21), and writing

$$\left.\begin{aligned} B_1'&=\frac{B_1}{a_1}\\ B_3'&=B_3-\frac{a_3}{a_1}B_1\\ B_5'&=B_5-\frac{a_5}{a_1}B_1 \end{aligned}\right\} \tag{26}$$

one has

$$\frac{F}{\rho U_m^2 D}=A_1\sin\theta+A_3\sin 3\theta+A_5\sin 5\theta+\ldots$$
$$+B_1'|\cos\theta|\cos\theta+B_3'\cos 3\theta+B_5'\cos 5\theta+\ldots. \tag{27}$$

Now eq (24) and (27) may be compared. One can write

$$\frac{\pi}{4}C_m\cdot\frac{D\sigma}{U_m}=A_1+A_3\frac{\sin 3\theta}{\sin\theta}+A_5\frac{\sin 5\theta}{\sin\theta}\ldots$$

and

$$\frac{C_d}{2}=-B_1'-B_3'\frac{\cos 3\theta}{|\cos\theta|\cos\theta}-\frac{B_5'\cos 5\theta}{|\cos\theta|\cos\theta}+\ldots,$$

or

$$C_m(\theta)=\frac{2}{\pi^2}\frac{U_m T}{D}[A_1+A_3+A_5+2(A_3+A_5)\cos 2\theta+2A_5\cos 4\theta+\ldots] \tag{28}$$

and

$$C_d(\theta)=-2B_1'+\frac{2}{|\cos\theta|}[2(B_3'-B_5')+4(B_5'-B_3')\cos 2\theta-4B_5'\cos 4\theta+\ldots]. \tag{29}$$

Thus if A_3, A_5, and B_3', B_5' vanish, the coefficient of mass and drag remain constant for all the phase

in the wave cycle and

$$C_m=\frac{2}{\pi^2}\frac{U_mT}{D}A_1=\frac{2}{\pi^3}\frac{U_mT}{D}\int_0^{2\pi}\frac{F\sin\theta d\theta}{\rho U_m^2D} \tag{30}$$

and

$$C_d=-2B_1'=-\frac{3}{4}\int_0^{2\pi}\frac{F\cos\theta d\theta}{\rho U_m^2D}. \tag{31}$$

In the event that these coefficients vary with the phase θ of the wave cycle, the values given by eq (30) and (31) are in a sense the weighted averages

$$C_m=\frac{1}{\pi}\int_0^{2\pi}C_m(\theta)\sin^2\theta d\theta \tag{32}$$

and

$$C_d=+\frac{3}{4}\int_0^{2\pi}C_d(\theta)\,|\cos\theta|\cos^2\theta d\theta. \tag{33}$$

With the above possibilities in mind, it is preferable to adopt the expressions

$$\frac{F}{\rho U_m^2D}=A_1\sin\theta+B_1'\cos\theta\,|\cos\theta|+\Delta R \tag{34}$$

or

$$\frac{F}{\rho U_m^2D}=\frac{\pi}{4}C_m\frac{D\sigma}{U_m}\sin\theta-\frac{C_d}{2}|\cos\theta|\cos\theta+\Delta R, \tag{34a}$$

where A_1, B_1', C_m, and C_d are constant, and ΔR has the value

$$\Delta R=A_3\sin 3\theta+A_5\sin 5\theta+B_3'\cos 3\theta+B_5'\cos 5\theta. \tag{35}$$

The function ΔR will be referred to as the remainder function, and then this remainder function is obtained by subtracting the computed values of $A_1\sin\theta$ and $B_1'|\cos\theta|\cos\theta$ from the observed $F/\rho U_m^2D$. The remainder thus obtained may be examined in regard to its Fourier structure and also as to its magnitude.

4. Characteristics of the Experimental Waves

The region under the nodal area of a standing wave that may be realized in a rectangular vessel furnishes a velocity field of simple harmonic motion in the velocity component U. This circumstance is not seriously modified even when the surges are moderately high.

Taking the x-axis in the plane surface of the undisturbed water, the z-axis vertical and upwards and the origin at one end of the basin, (see fig. 2), the surface elevation as reckoned from the undisturbed level, according to the second-approximation theory, from Miche [16], is

$$h=a\cos kx\sin\sigma t+a\frac{ak}{4}N_1\cos 2kx-a\frac{ak}{4}N_2\cos 2kx\cos 2\sigma t, \tag{36}$$

where

$$N_1=\frac{\cosh 2kH}{\sinh 2kH}$$

and

$$N_2=\frac{\cosh^2 kH\,(\cosh 2kH+2)}{\sinh^2 kH\sinh kH}.$$

Here $k=\pi/L$, L being the length of the basin; $\sigma=2\pi/T$, T being the period of oscillation; H the depth of water; and a the semiwave height, that is, the mean value of the extreme end deflections in a cycle. The expression for the period is the same as in the first-approximation theory, that is,

$$\sigma^2=gk\tanh kH. \tag{37}$$

Focusing attention on the basin end $x=0$, the surface displacement is

$$h=a\sin\sigma t+a\frac{ak}{4}N_1-a\frac{ak}{4}N_2\cos 2\sigma t;\qquad x=0. \tag{38}$$

Thus, the maximum elevation, occurring at $t=\pi/2\sigma$, is

$$h_1=a+a\frac{ak}{4}[N_1+N_2], \tag{39}$$

and the maximum depression, at $t=3\pi/2\sigma$, is

$$h_2=-a+a\frac{ak}{4}[N_1+N_2].$$

The ratio of the elevation to the depression is

$$\frac{h_1}{h_2}=-\left(1+\frac{Hk}{4}[N_1+N_2]\frac{a}{h}\right)\Big/\left(1-\frac{Hk}{4}[N_1+N_2]\frac{a}{H}\right), \tag{40}$$

and accordingly its value increases with wave height.

The surface configuration for $t=0$ is

$$h=a\frac{ak}{4}[N_1-N_2\cos 2kx],\qquad t=0. \tag{41}$$

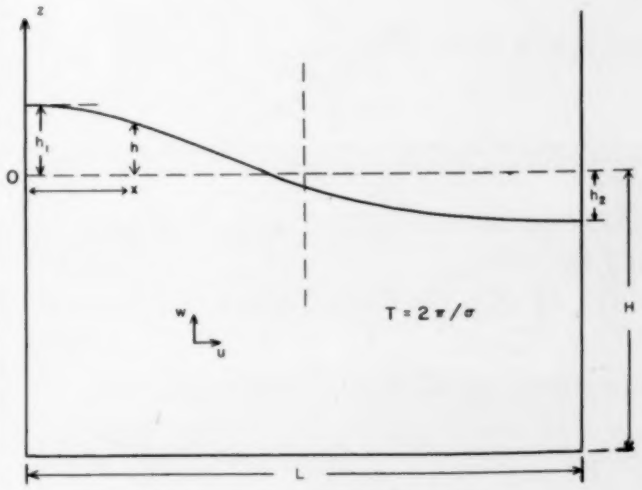

FIGURE 2. *Notation diagram for wave profile.*

This represents a positive hump at the center of the basin and depressions at the ends. As a result, the duration of time that the surface of the water at one end of the basin is found to be above the undisturbed level is shorter than the duration that it is below. This matter has a bearing on the manner of fixing the reference time of the force cycles studied, and requires further discussion.

At a small positive time $t=\tau_0$, the elevation h is nil, and this is the time when the wave in its upward surge reaches the undisturbed level.

Since $\sigma\tau_0$ is a small angle, $\sin \sigma\tau_0=\sigma\tau_0$, and from eq (38)

$$\sigma\tau_0=(N_2-N_1)\frac{ak}{4}-\frac{1}{2}(N_2-N_1)^2\frac{a^3k^3}{16}N_2. \tag{42}$$

At a later time, $t=T/2+\tau_1$, once more $h=0$. This is the time when the wave in its downward surge reaches the undisturbed level. Since $\sigma\tau_1$ is also a small angle, $\sin \sigma\tau_1=\sigma\tau_1$, and from eq (38)

$$\sigma\tau_1=(N_1-N_2)\frac{ak}{4}+\frac{1}{2}(N_1-N_2)^2\frac{a^3k^3}{16}N_2,$$

and, thus,

$$\tau_1=-\tau_0 \tag{43}$$

Let T_t denote the duration of time that the surface of the water at the end of the basin, $x=0$, is above the undisturbed level, and T_0 the duration below the same level. Accordingly,

$$T_t+T_0=T,$$

and

$$\frac{2(T_0-T_t)}{T}=2\left(1-\frac{2T_t}{T}\right).$$

By definition

$$T_t=\frac{T}{2}+\tau_1-\tau_0,$$

and in view of eq (43)

$$T_t=\frac{T}{2}-2\tau_0$$

or

$$\frac{2T_t}{T}=1-\frac{2\sigma\tau_0}{\pi}$$

and, thus

$$\frac{2(T_0-T_t)}{T}=\frac{4\sigma\tau_0}{\pi}.$$

Introducing the value of $\sigma\tau_0$ from eq (42)

$$\frac{2(T_0-T_t)}{T}=(N_2-N_1)\frac{kH}{\pi}\frac{a}{H}-(N_2-N_1)^2N_2\frac{H^3k^3}{8\pi}\left(\frac{a}{H}\right)^3. \tag{44}$$

If the instant when the upsurging wave at the end $x=0$, reaches the level of the undisturbed water is observed, this then determines the instant $t=\tau_0$. Since $4\tau_0=T_0-T_t$, the value of τ_0 may be obtained from the time durations that the water surface is below or above the still level. If on the other hand these observations have not been made, then τ_0 must be obtained from eq (42), introducing in it the wave height a of the observed surge deflections.

The expressions for the particle velocities within the order of the approximations considered are from Miche [16],

$$u=\frac{gak}{\sigma}\frac{\cosh k(z+H)}{\cosh kH}\sin kx\cos\sigma t$$

$$-\frac{3}{4}\frac{ga^2k^2}{\sigma}\frac{\cosh 2k(z+H)}{\sinh^2 kH\sinh 2kH}\sin 2kx\sin 2\sigma t \tag{45}$$

and

$$w=\frac{gak}{\sigma}\frac{\sinh k(z+H)}{\cosh kH}\cos kx\cos\sigma t$$

$$+\frac{3}{4}\frac{g}{\sigma}a^2k^2\frac{\sinh 2k(z+H)}{\sinh^2 kH\sinh 2kH}\cos 2kx\sin 2\sigma t. \tag{46}$$

At the vertical plane through the midsection of the basin, that is, at the plane $x=L/2$ or $kx=\pi/2$, the velocities are

$$u=\frac{gak}{\sigma}\frac{\cosh k(z+H)}{\cosh kH}\cos\sigma t \tag{47}$$

and

$$w=-\frac{3}{4}\frac{g}{\sigma}a^2k^2\frac{\sinh 2k(z+H)}{\sinh^2 kH\sinh 2kH}\sin 2\sigma t. \tag{48}$$

Thus at the channel midsection, the horizontal component of the particle velocities is simple harmonic. The vertical component is also simple harmonic except that the frequency is twice as large. The effect of vertical velocity decreases with wave height. It is further reduced by lowering the object in the basin. Denoting the position of the object in the basin by z_1 and putting

$$U_m=\frac{gak}{\sigma}\frac{\cosh k(z_1+H)}{\cosh kH}, \tag{49}$$

the velocity components are

$$u=-U_m\cos\sigma t \tag{50}$$

and

$$w=-\frac{3}{4}kH\frac{\sinh k(z_1+H)}{\sinh^3 kH}\cdot\frac{a}{H}U_m\sin 2\sigma t. \tag{51}$$

It is inferred that w becomes less significant when kH is larger than 0.9. This limits the length of the basin for a given depth of water. For studies of wave forces in basins of greater length or with water of less depth the present theory proves inadequate.

All the experiments discussed subsequently were made in a basin of length $L=242$ cm and water

depth $H=70$ cm. The objects, cylinders or plates, were placed 25 cm below the water surface, that is $z_1=-25$ cm in the midsection plane $x_1=121$ cm.

For this condition, $Hk=0.908$, $N_1=1.054$, and $N_2=3.322$. From eq (40), the ratio of end deflections reduces to

$$\frac{h_1}{h_2}=-\frac{1+0.993\,a/H}{1-0.993\,a/H}. \tag{52}$$

The graph of this equation is shown in figure 3, and values from observation are given by circles. The agreement between theory and observation is satisfactory for a/H less than 0.3. With this restriction in mind, the value of the semiwave height a may be inferred from (39), that is,

$$\frac{h_1}{a}=1+0.993\,a/H. \tag{53}$$

During the tests the elevation h_1 was most easily observed.

From eq (49) the relation between the current semiamplitude and the wave height, in cgs units, is

$$U_m=3.43\,a. \tag{54}$$

At z_1 the horizontal velocity is not uniform in the vertical direction. In the absence of a cylinder, with z measured in centimeters,

$$\frac{1}{U_m}\frac{dU_m}{dz}=0.00685.$$

Thus, if ΔU_m be the difference in the maximum velocities at two points differing in elevation by D, then

$$\frac{\Delta U_m}{U_m}=0.48\,D/H.$$

For the largest cylinder used in the experiments, $D=7.62$ cm, the value of the ratio $\Delta U_m/U_m$ is 0.052.

The maximum value, during the cycle, of the vertical velocity component is given by

$$w_m/U_m=0.38\,a/H.$$

The majority of the experiments were made with a less than 10 cm. For these cases, w_m/U_m is less than 0.055.

From eq (44) the proportion of time that the surface of the water at one end of the channel is above or below the undisturbed level is given by

$$\frac{T_0-T_i}{T}=0.328\,\frac{a}{H}-0.254\left(\frac{a}{H}\right)^3. \tag{55}$$

The graph of this expression is shown in figure 4 and values from observation are given by circles. For the observations, there was introduced into the basin at each end a parallel-wire resistance electrode, the bare parts of the wires being about 5 cm long and placed in a horizontal position just touching the surface of water at rest. The time that the electric current was traversing the electrodes gave the time that the water surface was above the undisturbed level, as in figure 5.

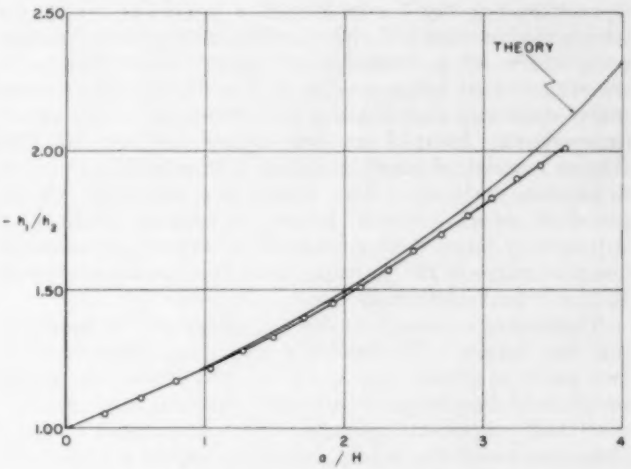

FIGURE 3. *Variation of end deflections with wave height.*

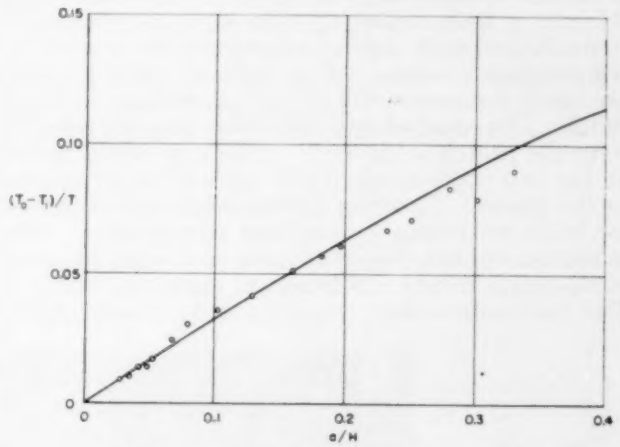

FIGURE 4. *Difference in the durations of the end elevations and depressions.*

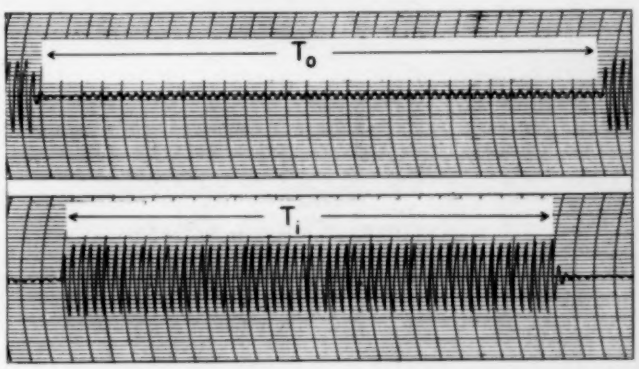

FIGURE 5. *Time record of the durations of the end deflections.*

5. Dynamometer and Calibration

The sketch of the dynamometer assembly is shown in figure 6. The rigid and massive base A for supporting purposes is firmly attached to the steel frame of the rocking basin directly above the water. The dynamometer itself consists of a pendular frame to which is attached the object to be immersed in water, a cylinder or a rectangular plate. The frame is constructed of brass angles and is strong enough to resist torsional and flexural deformation. The pivot depressions, located at the upper corners of the frame, consist of small bores of 1 mm in diameter in a bronze bedding. The bores are centered about polished steel conical points emerging from the supporting base. At a lower level two duraluminum annular rings of rectangular cross section are clamped to the frame and to the base.

These rings constitute elastic elements for measuring the forces. To indicate the ring deformations two pairs of strain gages, SR–4, 120 ohms, are glued to each of the rings, inside and outside, and at diametrically opposite points. The four strain gage elements form the bridge which is led to a universal analyser. The latter is relayed to one of the channels of a two-channel magnetic oscillograph. The second channel is reserved for timing observations. A similar connection is adopted for the other ring. By having four strain gages on each ring the sensitivity is increased and no corrections are needed for temperature changes. Two different sets of rings are used for measuring forces of different magnitudes. The method of calibration may be inferred from the sketch in figure 7. The sum of the forces on the two rings equals 0.625 times the load applied to the frame. The ring deformations are examined for loads producing tension and compression. The indications of the ring deformations as read from the oscillograph record are linear as shown in figure 7. The calibrations were repeated before each run to guard against accidental changes in the strain-gage behavior.

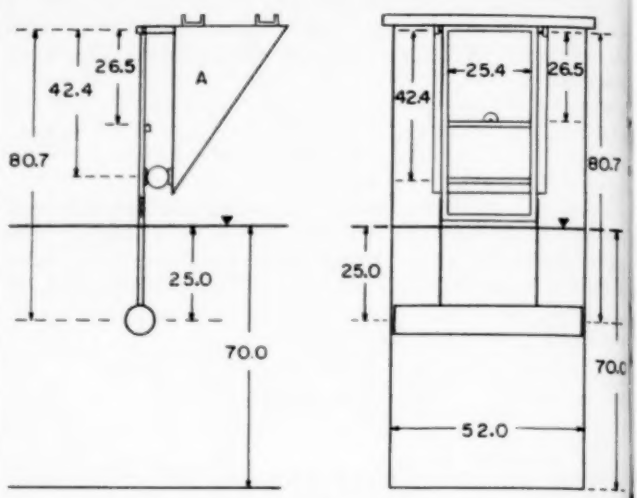

FIGURE 6. *Dynamometer assembly (dimensions in centimeters).*

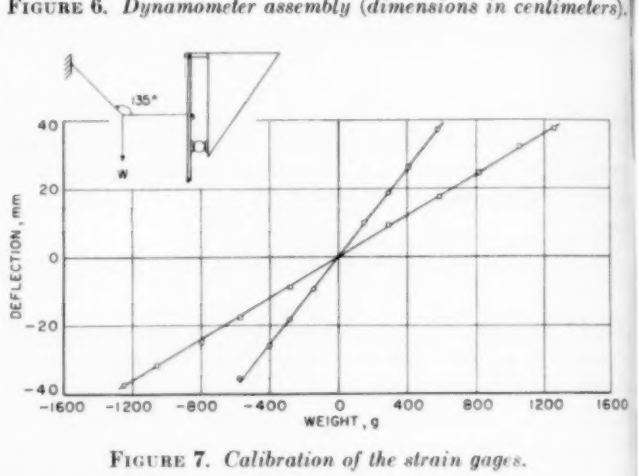

FIGURE 7. *Calibration of the strain gages.*

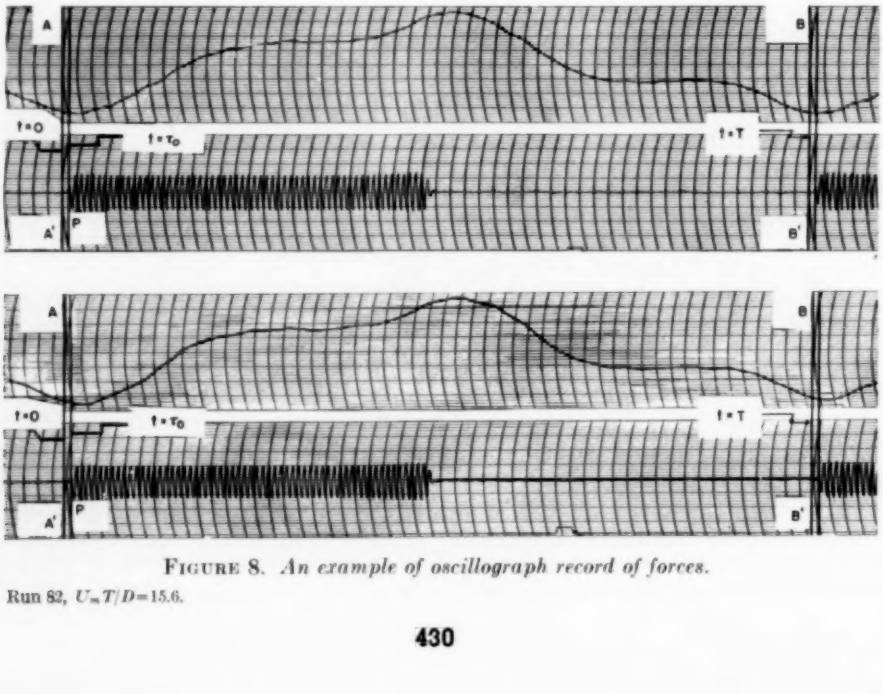

FIGURE 8. *An example of oscillograph record of forces.*

Run 82, $U_\infty T/D = 15.6$.

6. Record of Forces and the Reduction

An example of two oscillograph records of the forces, one from each ring, and of the timing is shown in figure 8. The nearly sinusoidal traces relate to the forces acting on the rings; the others, in steps, give the time sequence. The incidence of the larger deflections indicates the time that the parallel wire electrode at the basin end $x=0$ was immersed; and the incidence of no deflection indicates the time that the electrode was out of the water. The point P where the greater deflections appear to commence gives the instant that the upsurging water reached the undisturbed level. Thus the point P gives the time $t=\tau_0$, the value of which was computed from eq (55), $4\tau_0=T_0-T_t$, after introducing the semiwave height of the wave. This value was transferred to the record to mark the origin of time, $t=0$, shown by the line AA'. The line BB' indicates the end of the wave cycle and corresponds to $t=T$. To establish the correspondence of the records from the two rings, the timing marks appearing at the lower edges of the records were used.

At the time the record of the forces was being taken the wave elevation h_1 was read visually against a paper scale attached to the end wall of the basin. The water surface was readily discernable through the lucite walls of the basin. The magnitude of the semiwave height a was deduced from eq (53), using the observed value h_1. Maximum current U_m was deduced from eq (54).

The sum of the corresponding readings of the sinusoidal tracings in figure 8 gives the magnitude of the forces acting on the two rings when the calibration is applied. Taking moments about the dynamometer pivot point, the total force X on the cylinder is obtained. This is divided by the length of the cylinder to give F. The time history of the reduced force, $F/\rho U_m^2 D$, is shown in figure 9.

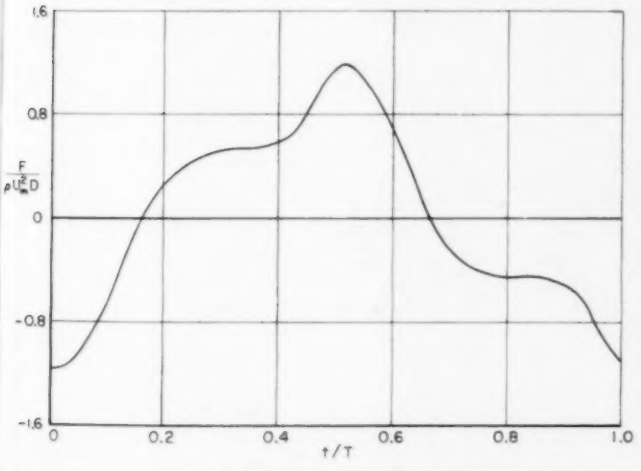

FIGURE 9. *An example of a curve of reduced forces on a cylinder.*
Run 82, $U_m T/D=15.6$.

7. Inertia and the Drag Coefficients of Cylinders and Plates

Considering the force data in dimensionless form, such as shown in figure 9, the coefficients A_1 and B_1' of eq (34) were determined by the method implied in eq (30) and (31). The desired integrations were carried out in the form of summations by giving to the differential multiplier $d\theta$ the incremental value $\Delta\theta=0.05\pi$. The values of A_1 and B_1' thus found are entered in table 5 for the cylinders and in table 6 for the plates. Tables 1 and 2 contain the diameters of the cylinders, or the width of the plates, the values of the maximum currents and the water temperatures. Next the values of the inertia coefficient, C_m, were determined on the basis of eq (30), and the values of the drag coefficient, C_d, on the basis of eq (31). These results are entered in table 3 for the cylinders and in table 4 for the plates. These tables also contain the Reynolds number $U_m D/\nu$ and the period parameter $U_m T/D$.

The inertia coefficient C_m varies from the theoretical value 2 as the diameter of the cylinder is changed, or with a given cylinder as the maximum current is varied. Similar variations occur in the drag coefficient C_d, the changes being in the form of additions to the value experienced in steady flow. A correlation between the coefficients and Reynolds number $U_m D/\nu$ does not appear to exist. On the other hand, when these coefficients are related to the period parameter $U_m T/D$, definite and regular dependencies are found. This is illustrated in figures 10 and 11 for the cylinders, and in figures 12 and 13 for the plates.

TABLE 1. *Cylinders*

[T=2.075 sec]

Run	D	U_m	θ	Run	D	U_m	θ
	in.	*cm/sec*	*° C*		*in.*	*cm/sec*	*° C*
1	3	36.2	23.0	30	1	71.7	30.0
2	3	30.2	22.0	31	1	58.7	30.0
3	3	27.7	23.0	32	1	45.3	30.0
4	3	24.5	22.5	33	1	36.0	30.0
5	3	21.1	22.5	34	0.75	70.7	30.0
6	3	19.2	22.0	35	.75	63.8	30.0
7	3	15.8	22.0	36	.75	53.5	30.0
8	3	13.1	23.0	37	.75	45.3	30.0
9	3	10.0	23.0	38	.75	38.1	30.0
10	2.5	33.1	24.0	39	.5	73.4	30.0
11	2.5	27.4	24.0	40	.5	58.7	30.0
12	2.5	20.7	24.0	41	.5	48.0	30.0
13	2.5	13.0	24.0	78	1.75	27.6	22.0
14	2.5	10.3	24.0	79	1.75	24.0	22.0
15	2	41.5	24.0	80	1.75	17.7	22.0
16	2	35.4	24.0	81	1.75	14.4	22.0
17	2	27.5	24.0	82	1.5	28.7	20.5
18	2	19.1	24.8	83	1.5	25.2	20.5
19	2	23.5	24.8	84	1.5	20.2	20.5
20	1.5	53.2	26.0	85	1.5	14.6	20.5
21	1.5	43.4	26.0	86	0.5	66.4	21.0
22	1.5	33.4	26.0	87	.5	54.8	21.0
23	1.5	25.7	26.0	88	.5	44.6	21.0
24	1.5	19.4	26.0	89	.5	32.6	21.0
25	1.25	62.9	24.0	90	.75	54.0	12.0
26	1.25	54.5	28.0	91	.75	49.6	12.0
27	1.25	43.8	24.0	92	.75	46.0	12.0
28	1.25	35.7	29.2	93	.75	41.0	12.0
29	1.25	27.1	29.2				

TABLE 2. *Plates*

[T=2.075 sec]

Run	D	U_m	θ	Run	D	U_m	θ
	in.	*cm/sec*	° *C*		*in.*	*cm/sec*	° *C*
42	3	14.1	23.0	60	1.5	13.7	24.8
43	3	12.7	23.0	61	1.25	37.0	28.5
44	3	9.8	23.0	62	1.25	29.5	28.5
45	3	8.0	23.0	63	1.25	22.0	28.5
46	3	6.4	23.0	64	1.25	16.1	28.5
47	2.5	18.5	24.0	65	1	41.2	30.4
48	2.5	15.8	24.0	66	1	34.5	30.4
49	2.5	13.0	24.0	67	1	27.4	30.4
50	2.5	10.3	24.0	68	1	18.9	30.4
51	2.5	6.5	24.0	69	0.75	57.1	30.8
52	2	21.6	27.0	70	.75	47.0	30.8
53	2	18.9	27.0	71	.75	37.7	30.8
54	2	16.1	27.0	72	.75	27.4	30.8
55	2	13.0	27.0	73	.5	72.4	30.0
56	2	9.9	27.0	74	.5	63.6	30.0
57	1.5	30.0	24.8	75	.5	54.0	30.0
58	1.5	25.0	24.8	76	.5	45.3	30.0
59	1.5	18.9	24.8	77	.5	35.8	30.0

For the cylinders, as one passes from the small values of the period parameter to the larger values, the inertia coefficient commences to fall from the initial value 2 to a minimum value of 1.00 at $U_mT/D=15$ and then gradually increases to a value of 2.5 at $U_mT/D=120$. In regard to the coefficient of drag, there is an increase from the initial value 0.9 to a maximum value 2.5 at $U_mT/D=15$ and then there is a gradual decrease to the value obtained in steady flow. It appears that for the cylinders the narrow region around $U_mT/D=15$ is a critical one.

As regards the plates, the course of the variations of C_m and C_d with the period parameter is of a very different kind. It will be noticed that C_m first increases, then decreases and finally rises again to a value of nearly 4.5. The most remarkable behavior, however, is in regard to C_d. The coefficient of drag, starting with an unusually large value, 10, decreases rapidly at first and then gradually for

TABLE 3. *Cylinders*

Run	C_m	C_d	U_mT/D	U_mD/ν	Run	C_m	C_d	U_mT/D	U_mD/ν
1	1.11	1.24	9.9	293×10²	30	1.66	1.09	58.6	227×10²
2	1.44	1.14	8.2	239	31	1.70	1.29	47.9	185
3	1.49	1.32	7.6	225	32	1.68	1.40	37.0	143
4	1.70	1.13	6.7	196	33	1.64	1.49	29.4	114
5	1.88	1.00	5.7	169	43	1.82	1.10	77.0	167
6	1.95	0.91	5.2	152	35	1.61	1.19	69.5	151
7	2.05	1.23	4.3	125	36	1.63	1.42	58.3	127
8	2.10	1.01	3.6	106	37	1.64	1.45	49.3	107
9	2.14	0.70	2.7	81	38	1.84	1.50	41.5	90
10	0.74	1.69	10.8	229	39	2.54	1.07	119.9	116
11	1.14	1.61	8.9	189	40	2.35	1.29	95.8	93
12	1.71	1.36	6.8	143	41	2.15	1.42	78.5	76
13	2.02	1.15	4.3	90	78	0.82	1.99	12.9	127
14	2.06	1.12	3.4	71	79	.84	2.08	11.2	111
15	0.72	1.73	17.0	230	80	1.41	2.06	8.3	82
16	.70	1.98	14.5	196	81	1.78	1.75	6.7	67
17	.83	2.18	11.2	152	82	0.80	2.05	15.6	109
18	1.50	1.89	7.8	108	83	.78	2.28	13.7	96
19	1.10	1.97	9.6	132	84	.87	2.36	11.0	77
20	1.02	1.30	29.0	231	85	1.46	2.18	7.9	56
21	1.02	1.49	23.6	188	86	2.52	1.18	108.4	85
22	0.85	1.73	18.2	145	87	2.60	1.31	89.5	71
23	.74	2.15	14.0	112	88	2.32	1.43	72.9	57
24	.87	2.21	10.6	84	89	2.26	1.54	53.2	42
25	1.24	1.15	41.1	218	90	1.82	1.28	58.8	83
26	1.27	1.23	35.6	206	91	1.81	1.38	54.0	76
27	1.40	1.46	28.6	152	92	1.81	1.42	50.1	71
28	1.26	1.52	23.3	138	93	1.76	1.54	44.7	63
29	0.87	1.75	17.7	105					

TABLE 4. *Plates*

Run	C_m	C_d	U_mT/D	U_mD/ν	Run	C_m	C_d	U_mT/D	U_mD/ν
42	1.94	8.75	3.8	114×10²	60	2.51	5.15	7.5	58×10²
43	1.74	8.81	3.5	103	61	2.14	3.25	24.2	142
44	1.56	9.76	2.7	80	62	1.07	3.94	19.3	113
45	1.51	10.21	2.2	65	63	1.43	4.09	14.3	84
46	1.35	11.55	1.7	52	64	2.25	4.43	10.5	62
47	2.28	5.50	6.1	128	65	2.45	3.13	33.6	131
48	2.12	7.06	5.2	109	66	2.10	3.55	28.2	110
49	2.00	8.01	4.2	90	67	2.01	3.68	22.4	87
50	1.91	8.64	3.4	71	68	1.56	4.38	15.4	60
51	1.57	11.44	2.1	45	69	3.17	2.43	62.2	138
52	2.22	5.21	8.8	128	70	2.88	2.86	51.2	113
53	2.44	5.48	7.7	112	71	2.89	3.06	41.1	91
54	2.42	6.31	6.6	95	72	2.71	3.36	29.9	66
55	2.17	7.25	5.3	77	73	4.96	1.81	118.2	114
56	2.16	8.04	4.1	59	74	4.09	2.03	104.0	101
57	0.95	4.11	16.3	127	75	4.00	2.32	88.3	85
58	1.07	4.28	13.6	106	76	3.58	2.45	74.0	72
59	2.08	4.61	10.3	80	77	3.70	2.59	58.6	57

TABLE 5. *Cylinders*

Run	A_1	B_1'	A_3	B_3'	A_5	B_5'	U_mT/D
1	0.56	−0.62	−0.11	−0.04	−0.03	−0.08	9.9
2	.87	−.57	−.06	−.03	−.02	−.06	8.2
3	.97	−.66	−.08	.00	−.02	−.04	7.6
4	1.26	−.56	−.03	+.05	−.01	−.03	6.7
5	1.62	−.51	−.02	.05	.00	−.03	5.7
6	1.84	−.46	+.02	.06	.00	−.01	5.2
7	2.35	−.62	.01	.12	−.01	−.02	4.3
8	2.91	−.51	.03	.14	+.01	.00	3.6
9	3.87	−.35	.01	.08	−.02	+.02	2.7
10	0.34	−.84	−.19	−.02	−.04	−.08	10.8
11	.63	−.80	−.14	−.05	−.04	−.09	8.9
12	1.25	−.68	−.07	−.02	.00	−.06	6.8
13	2.34	−.58	+.10	+.13	+.01	−.01	4.3
14	3.03	−.56	.01	.14	.00	+.01	3.4
15	0.21	−.96	−.18	.00	−.04	−.05	17.0
16	.24	−.99	−.22	−.01	−.02	−.07	14.5
17	.36	−1.09	−.19	−.05	−.02	−.12	11.2
18	.95	−0.95	−.14	−.04	−.02	−.11	7.8
19	.57	−.99	−.15	−.06	−.01	−.11	9.6
20	.17	−.65	−.05	.00	−.01	−.03	29.0
21	.21	−.74	−.07	.00	.00	−.04	23.6
22	.23	−.87	−.15	−.05	−.04	−.07	18.2
23	.26	−1.08	−.22	−.04	.00	−.08	14.0
24	.41	−1.10	−.20	−.07	.00	−.11	10.6
25	.15	−0.58	.00	+.01	.00	−.01	41.1
26	.18	−.62	−.01	.01	.00	−.02	35.6
27	.24	−.73	−.01	.02	.00	−.02	28.6
28	.27	−.76	−.04	.00	.00	−.05	23.3
29	.24	−.87	−.13	−.04	−.04	−.07	17.7
30	.14	−.55	+.02	+.01	.00	−.01	58.6
31	.17	−.64	.02	.01	−.01	−.01	47.9
32	.22	−.70	.01	.03	.00	−.02	37.0
33	.27	−.74	.01	.02	.00	−.02	29.4
34	.12	−.55	.03	.01	−.01	−.01	77.0
35	.11	−.60	.01	.01	−.01	−.01	69.5
36	.14	−.71	.01	.02	.00	−.02	58.3
37	.16	−.72	.01	.02	−.01	−.01	49.3
38	.22	−.75	.02	.02	.00	−.01	41.5
39	.10	−.54	.03	.00	.00	−.01	119.9
40	.12	−.65	.02	.01	.00	−.01	95.8
41	.14	−.71	.01	.02	.00	−.01	78.5
78	.31	−.99	−.18	−.05	−.01	−.10	12.9
79	.37	−1.04	−.19	−.02	−.03	−.12	11.2
80	.84	−1.03	−.15	−.10	−.01	−.13	8.3
81	1.30	−0.88	−.07	−.10	.00	−.10	6.7
82	0.25	−1.02	−.22	−.03	−.04	−.06	15.6
83	.28	−1.14	−.24	−.01	−.01	−.10	13.7
84	.39	−1.18	−.23	−.05	−.02	−.14	11.0
85	.91	−1.09	−.15	−.04	.00	−.12	7.9
86	.11	−0.59	+.03	+.01	.00	−.01	108.4
87	.14	−.65	.02	.01	−.01	−.01	89.5
88	.16	−.72	.01	.02	−.01	−.01	72.9
89	.21	−.77	.01	.04	+.01	−.01	53.2
90	.15	−.64	.02	.01	.00	−.01	58.5
91	.17	−.69	.02	.01	.00	−.01	54.0
92	.18	−.71	.02	.02	.00	.00	50.1
93	.19	−.77	.02	.02	.00	−.01	44.7

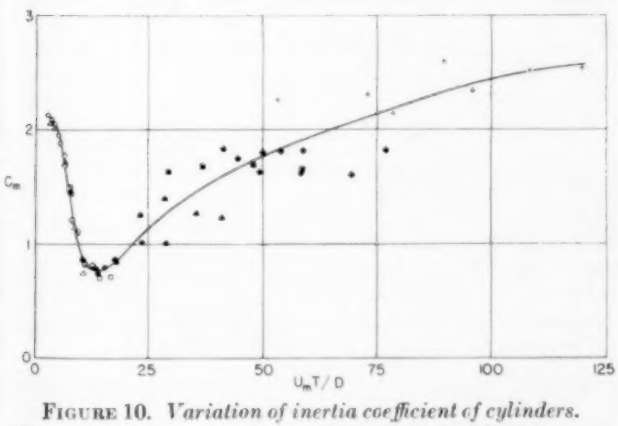

FIGURE 10. *Variation of inertia coefficient of cylinders.*

Diameter (inches): 3 2.5 2 1.75 1.5 1.25 1 0.75 0.5
Corresponding symbol: ○ △ □ ◇ ● ▲ ■ ◆ +

TABLE 6. *Plates*

Run	A_1	B_1'	A_3	B_3'	A_5	B_5'	U_mT/D
42	2.50	−4.38	0.58	0.56	0.01	−0.05	3.8
43	2.49	−4.41	.58	.47	.04	−.11	3.5
44	2.86	−4.88	.47	.40	−.02	−.18	2.7
45	3.42	−5.11	.53	.45	−.01	−.17	2.2
46	3.83	−5.77	.43	.48	−.02	−.16	1.7
47	1.86	−2.75	.37	.58	−.08	−.03	6.1
48	2.03	−3.53	.45	.59	−.04	−.02	5.2
49	2.32	−4.01	.53	.64	−.02	−.02	4.2
50	2.81	−4.32	.68	.52	+.07	−.06	3.4
51	3.63	−5.72	.61	.55	.01	−.14	2.1
52	1.24	−2.61	.35	.42	−.05	+.02	8.8
53	1.56	−2.74	.31	.49	−.06	−.03	7.7
54	1.81	−3.16	.38	.56	−.05	−.02	6.6
55	2.01	−3.63	.45	.54	−.01	−.03	5.3
56	2.63	−4.02	.66	.60	.00	−.01	4.1
57	0.29	−2.05	.29	.33	+.02	+.07	16.3
58	.39	−2.14	.30	.31	.00	.03	13.6
59	1.00	−2.31	.29	.43	−.08	.00	10.3
60	1.66	−2.58	.30	.54	−.07	−.04	7.5
61	0.44	−1.62	.11	.18	−.05	−.02	24.2
62	.27	−1.97	.18	.19	+.02	+.07	19.3
63	.49	−2.04	.31	.36	−.02	.04	14.3
64	1.05	−2.22	.30	.45	−.06	−.01	10.5
65	0.36	−1.56	.08	.13	−.05	−.01	33.6
66	.37	−1.77	.09	.16	−.04	−.01	28.2
67	.44	−1.84	.16	.19	−.02	+.03	22.4
68	.50	−2.19	.32	.38	−.01	.06	15.4
69	.25	−1.21	.05	.05	−.02	−.04	62.2
70	.28	−1.43	.06	.08	−.03	−.04	51.2
71	.35	−1.53	.08	.11	−.04	−.04	41.1
72	.45	−1.68	.11	.13	−.03	−.01	29.9
73	.21	−0.91	.06	.03	−.01	−.03	118.2
74	.19	−1.01	.06	.03	−.01	−.03	104.0
75	.22	−1.16	.05	.05	−.02	−.03	88.3
76	.24	−1.22	.05	.05	−.02	−.02	74.0
77	.31	−1.29	.07	.06	−.03	−.03	58.6

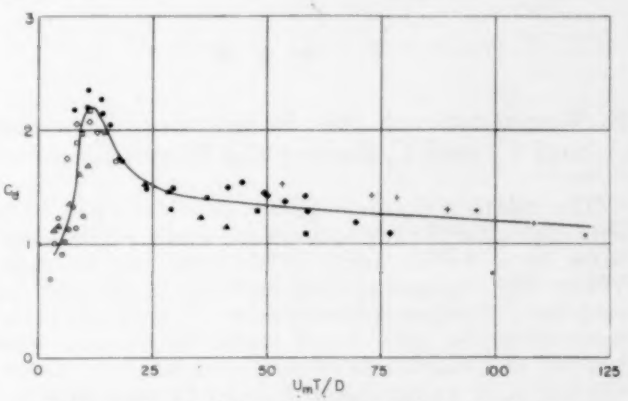

FIGURE 11. *Variation of drag coefficient of cylinders.*

Diameter (inches): 3 2.5 2 1.75 1.5 1.25 1 0.75 0.5
Corresponding symbol: ○ △ □ ◇ ● ▲ ■ ◆ +

increasing period parameter. The final value is almost identical with that found for steady flow. It is perhaps important to mention that O'Brien and Morison [17] noted equally large values of drag coefficients for spheres subjected to the action of progressive waves. It will be noted that the larger values of C_d are associated with the smaller values of C_m, and the larger values of C_m with the smaller values of C_d. Because the drag coefficient is large when U_mT/D is small and the variation of C_m is relatively moderate, the wave forces on plates are essentially due to drag, and the inertia effects play a small role almost independent of the period parameter.

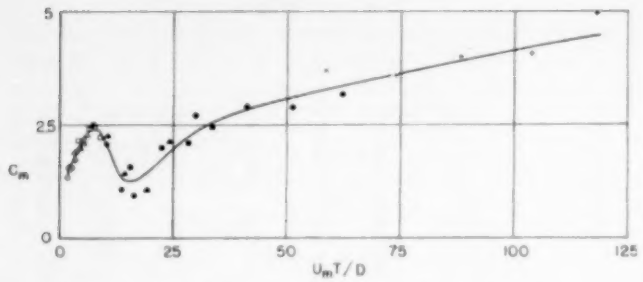

FIGURE 12. *Variation of inertia coefficient of plates.*

Diameter (inches): 3 2.5 2 1.5 1.25 1 0.75 0.5
Corresponding symbol: ○ △ □ ● ▲ ■ ♦ +

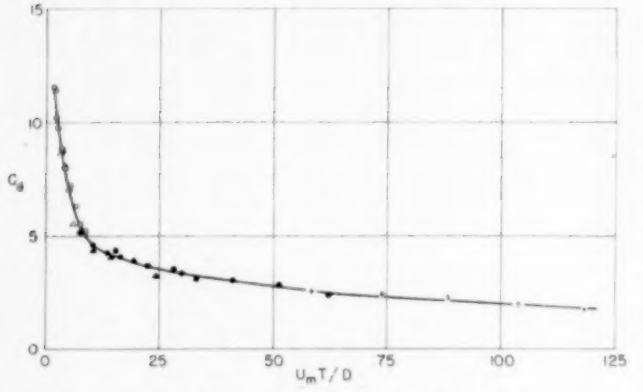

FIGURE 13. *Variation of drag coefficient of plates.*

Diameter (inches): 3 2.5 2 1.5 1.25 1 0.75 0.5
Corresponding symbol: ○ △ □ ● ▲ ■ ♦ +

8. Variations of the Remainder Function and C_m and C_d During the Wave Cycle

The values of C_m and C_d given in tables 3 and 4 are average values for the entire wave cycle, and in some cases local values may differ from the average. Where the inertia and drag coefficients, C_m and C_d, each have the same constant value at all phases of the wave cycle, eq (24) should suffice to describe adequately the magnitude of the forces at every phase. On the other hand, should C_m and C_d vary with the different phases, the forces are better represented by eq (34a). The variations in C_m and C_d should lead to the remainder force function ΔR. The examples of the remainder function ΔR are given in figures 14 and 15 where ΔR is the difference between $F/\rho U_m^2 D - A_1 \sin\theta$ and $B_1' \cos\theta \,|\cos\theta|$ in conformity with eq (34). Once a curve of ΔR as a function of θ is obtained, its structure in Fourier components may be considered and the coefficients A_3, A_5 . . ., and B_3', B_5' may be obtained. These determinations are given in tables 5 and 6 and in figures 16, 17, 18, and 19.

Now for the determinations of the local values of C_m and C_d, two methods are available. The first gives the point values of the coefficients in a wave cycle as determined from the observed values of $F/\rho U_m^2 D$, using eq (24). Two sets of evaluations

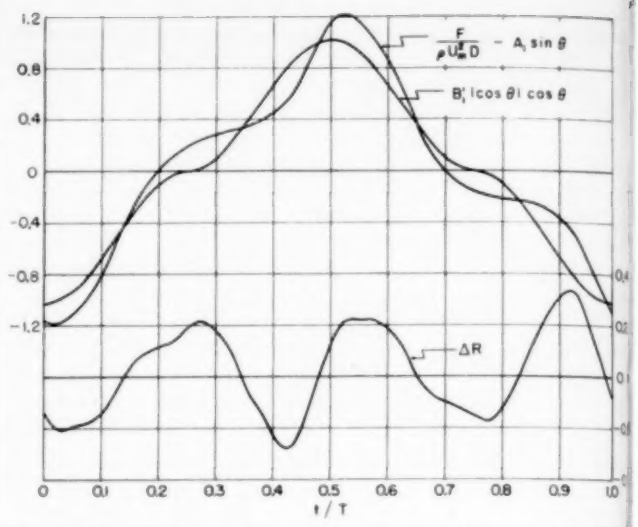

FIGURE 14. *Evaluation of remainder force ΔR for a cylinder.*
Run 82, $U_mT/D = 15.6$.

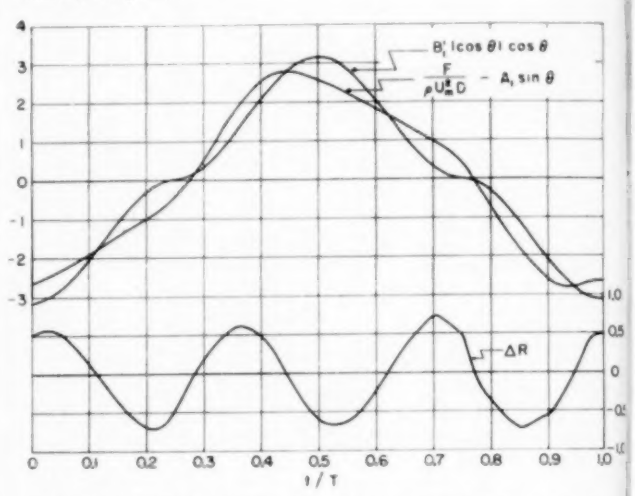

FIGURE 15. *Evaluation of remainder force ΔR for a plate.*
Run 54, $U_mT/D = 6.6$.

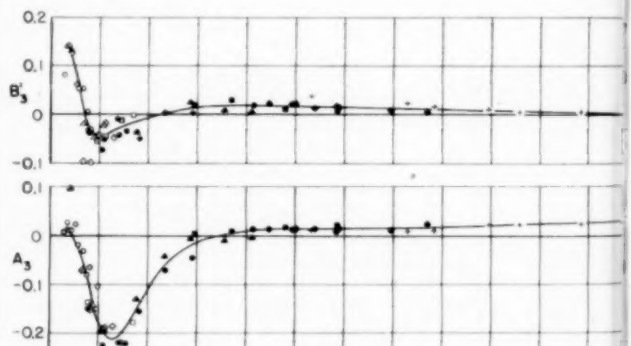

FIGURE 16. *Variation of coefficients of the remainder force for cylinders.*

Diameter (inches): 3 2.5 2 1.75 1.5 1.25 1 0.75 0.5
Corresponding symbol: ○ △ □ ◇ ● ▲ ■ ♦ +

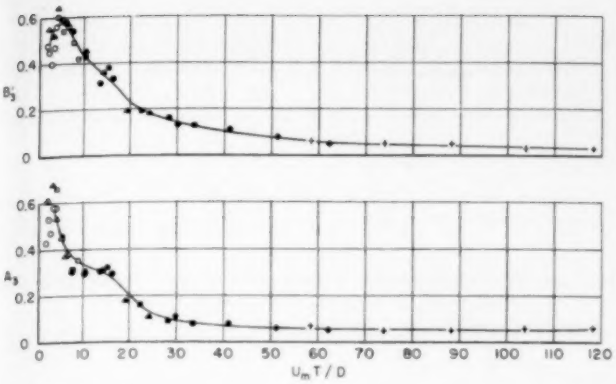

FIGURE 17. *Variation of coefficients of the remainder force of plates.*

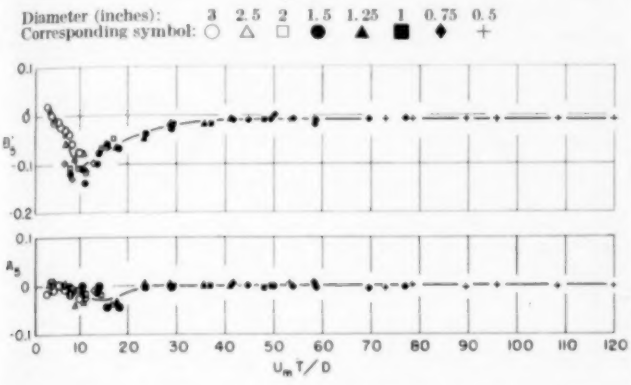

FIGURE 18. *Variation of coefficients of the remainder force of cylinders.*

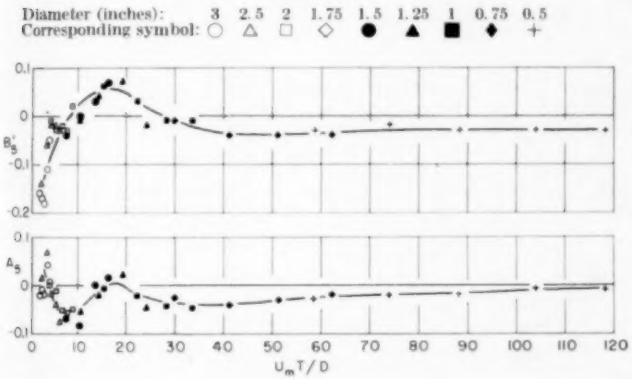

FIGURE 19. *Variation of coefficients of the remainder force of plates.*

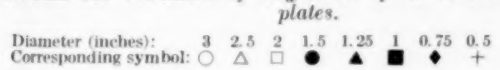

were made, the basic suppositions being as follows: It was assumed in the first evaluation that for $\theta_1=\pi/2+\alpha$ and $\theta_2=\pi/2-\alpha$, where α is an angle less than $\pi/2$, the coefficients C_m and C_d each have equal values, since these are the phases where the accelerations, du/dt, are equal, and the currents u, are equal in absolute value although of opposing signs. This is true also for $\theta_1=3\pi/2+\alpha$ and $\theta_2=3\pi/2-\alpha$. In the second evaluation, it was assumed that for $\theta=\pi+\beta$ and $\theta=\pi-\beta$, where β is an angle less than π, the coefficients C_m and C_d each have equal values, since these are the phases where the currents, u, are equal and the accelerations, du/dt, are equal in absolute value, although of opposing signs. Also since we know the values of the coefficients A_1, A_3, A_5 and B_1', B_3', B_5', the curves of C_m and C_d as function of θ may be obtained by using eq (28) and (29). The latter is the second method and is mathematically equivalent to the assumptions made above.

In the cylinder data the agreement between the observed and computed force is satisfactory when $U_m T/D$ is small. The computation was based on eq (24), introducing the values of C_m and C_d from the tables. Figure 20 illustrates this agreement. The local values of $C_m(\theta)$ and $C_d(\theta)$ for this case are shown in figure 21. The first determinations discussed above are shown by circles and squares, whereas the curves are determined by the second method. It is seen that $C_m(\theta)$ is independent of the phase t/T and that the coefficient $C_d(\theta)$ is constant except in short ranges of the phases $t/T=0.25$ and 0.75. This is expected, for at these phases the current u vanishes. The values of C_m and C_d determined by eq (30) and (31) are given in the caption.

The agreement between the observed and computed forces is also satisfactory when the period parameter is large. This is illustrated in figure 22. The local values of the coefficients for this case are shown in figure 23. Here again, allowing small deviations, $C_m(\theta)$ is practically independent of the phase t/T and differs very little from the value given in table 3. On the other hand, considerable variations are obtained between the observed and computed values of the forces in those cases where the period parameter is near $U_m T/D=15$, as shown in figure 24. The local values of the coefficients for this case are shown in figure 25. Now $C_m(\theta)$ varies considerably with the phase t/T, the smaller values occurring at $t/T=0.0$, 0.50, and 1, and the larger values at $t/T=0.25$ and 0.75. Also, $C_d(\theta)$ appears to be considerably augmented at the phases where the velocity u vanishes, that is, at $t/T=0.25$ and 0.75. The example shown is typical for all the cases where $U_m T/D$ is in the neighborhood of $U_m T/D=15$. In the example shown in figure 25, $C_m(\theta)$ shows large negative values at the points $t/T=0$, 0.5, and 1.0. The significance of this is not clear. It is believed, however, that the presence of negative values is not related altogether to the observational methods that were used.

For the plates deviations were always found between the observed values of the forces and the values computed on the basis of eq (24). An example is given in figure 26. The local values of $C_m(\theta)$ and $C_d(\theta)$ for this case are shown in figure 27. An additional example is given in figure 28. What is shown in these figures is typical for all the runs made with the plates. The coefficient $C_m(\theta)$ undergoes considerable variation in value for varying t/T, the greater values occurring at $t/T=0$, 0.5, and 1.0 and the lesser values at $t/T=0.25$ and 0.75. Furthermore, the increase in $C_d(\theta)$ at the points $t/T=0.25$ and 0.75 is very decided.

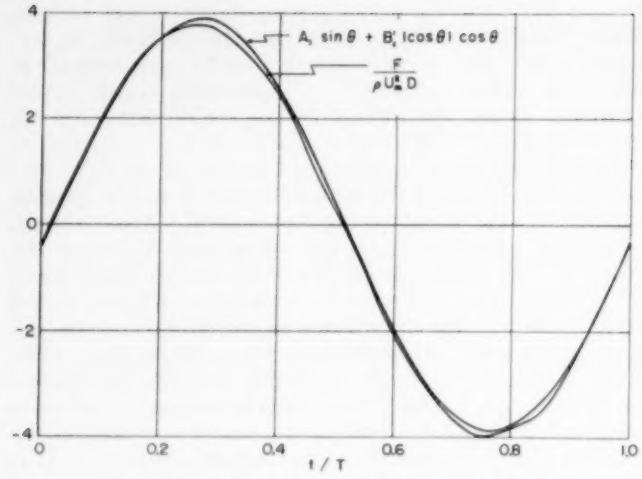

FIGURE 20. *Comparison of measured and computed forces on a cylinder.*

Run 9, $U_mT/D=3.0$.

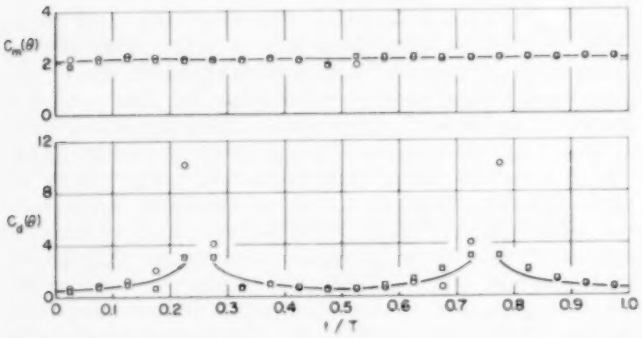

FIGURE 21. *An example of variation of the inertia and drag coefficients of a cylinder during a wave cycle.*

Run 9, $U_mT/D=3.0$, $C_m=2.14$, $C_d=0.70$.

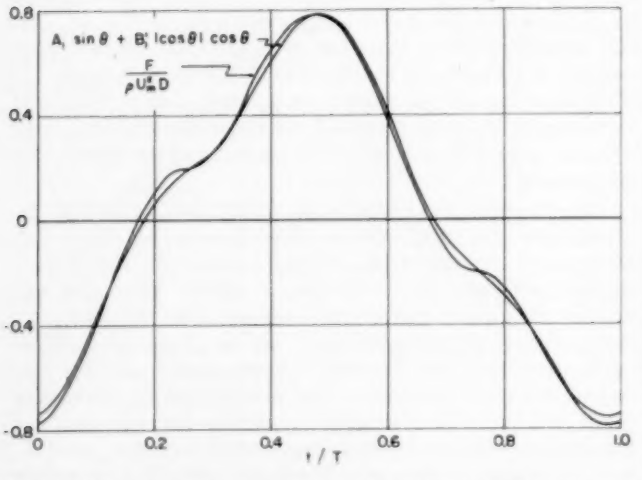

FIGURE 22. *Comparison of measured and computed forces on a cylinder.*

Run 93, $U_mT/D=44.7$.

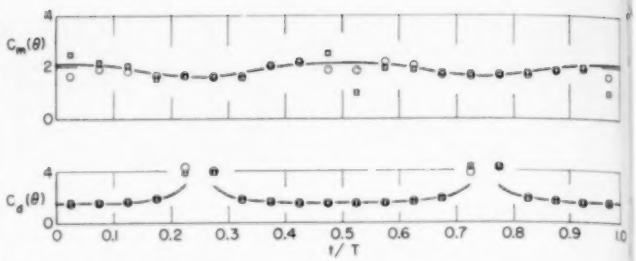

FIGURE 23. *An example of variation of the inertia and drag coefficients of a cylinder during a wave cycle.*

Run 93, $U_mT/D=44.7$, $C_m=1.76$, $C_d=1.54$.

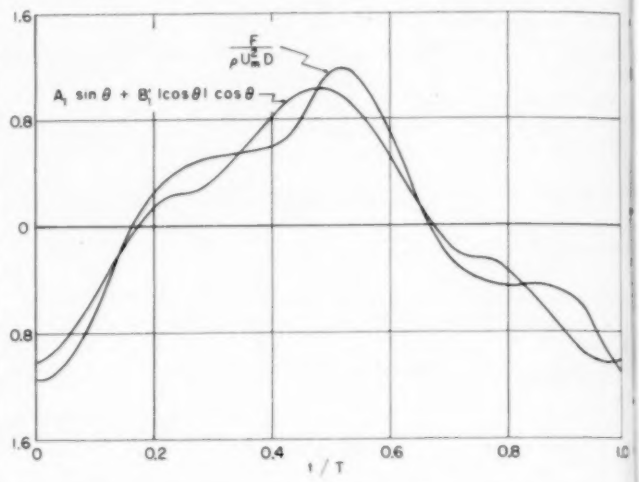

FIGURE 24. *Comparison of measured and computed forces on a cylinder.*

Run 82, $U_mT/D=15.6$.

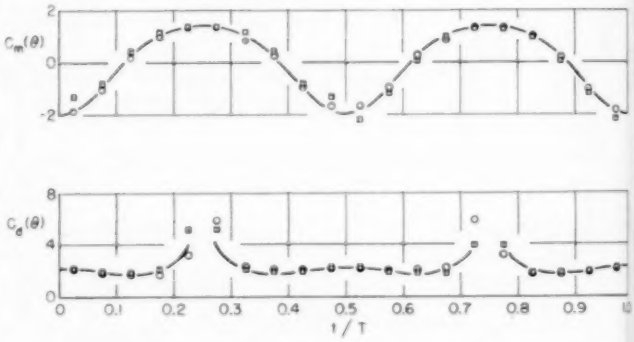

FIGURE 25. *An example of variation of the inertia and drag coefficients of a cylinder during a wave cycle.*

Run 82, $U_mT/D=15.6$, $C_m=0.80$, $C_d=2.05$.

For the cylinder data, as long as the period parameter is sufficiently small, or sufficiently large, the forces may be computed on the basis of eq (24); the remainder function, ΔR, is small. For period parameters in the neighborhood of the critical value, $U_mT/D=15$, the representation of forces is more exact using eq (34a); the remainder function is of significance. For the plate data the remainder may not be disregarded, in particular when the period parameter is small.

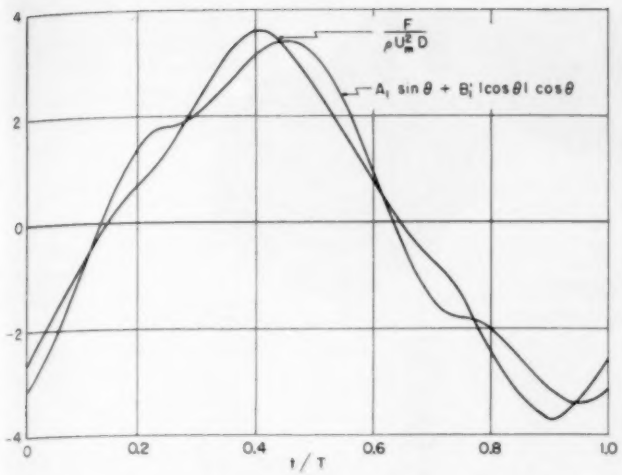

FIGURE 26. *Comparison of measured and computed forces on a plate.*

Run 54, $U_mT/D=6.6$.

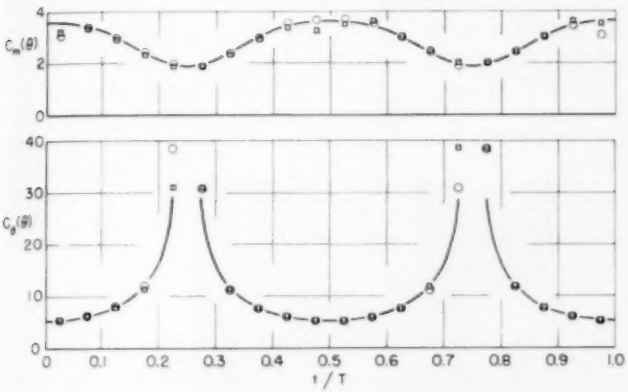

FIGURE 27. *An example of variation of the inertia and drag coefficients of a plate during a wave cycle.*

Run 54, $U_mT/D=6.6$, $C_m=2.42$, $C_d=6.31$.

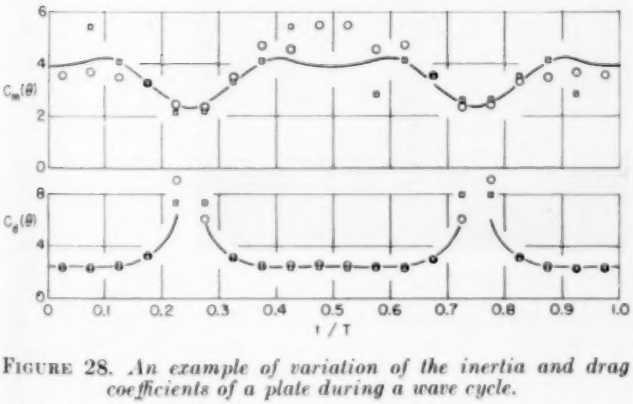

FIGURE 28. *An example of variation of the inertia and drag coefficients of a plate during a wave cycle.*

Run 69, $U_mT/D=62.2$, $C_m=3.17$, $Cd=2.43$.

9. Flow Pattern Around Cylinders and Plates

The flow patterns around the cylinders and plates for varying values of U_mT/D were examined, because they may have had a bearing on the fact that the nature of forces during a cycle is significantly affected by the period parameter. The flow pattern was visually examined by introducing a jet of colored liquid on one side of the immersed object. The disposition of the liquid close to the object during the cyclic motion was recorded by a still camera and also by a motion-picture camera. Some of these pictures are shown in figures 29 and 30.

Figure 29, a and b, were taken with the 3-inch cylinder, the first corresponding to $U_mT/D=4$, the second to a larger value $U_mT/D=10$. When the period parameter is small there is no separation of flow; the liquid near the cylinder clings to the cylinder, and the partitioning of flow from above and below is symmetrical. It will be remembered that at low period parameter the inertia coefficient is about equal to the theoretical value 2, and drag is negligible. As U_mT/D is increased there is separation of flow at the top surface of the cylinder during the relatively longer time that the flow continues in one direction. Although not visible in the picture, somewhat later, but prior to the reversal of current, liquid coming around the cylinder from below moves upward and, although transforming into an eddy, remains close to the cylinder.

Figure 29, c, illustrates the flow pattern for $U_mT/D=17$ with the 2-inch cylinder. Note the complete separation at the upper surface of the cylinder with the following flow around the lower surface directed upward with the subsequent eddy formation.

A completely different picture is obtained for large period parameter, as shown in figure 29, d, taken with the ½-inch cylinder, $U_mT/D=110$. Here one is confronted with the regular Karman vortices. The eddies are separated alternately from above and below.

With plates the flow patterns are decidedly different, especially for small period parameter. Figure 30, a and b, show the 3-inch plate, the first corresponding to $U_mT/D=1$, the second to a larger value, $U_mT/D=4$. Eddies are formed almost simultaneously at the upper and lower edges of the plates. For the smaller value of U_mT/D the eddies are apparently concentrated nearer the edges of the plate. Perhaps the large values of the drag coefficient for small period parameter are associated with the behavior of the eddies in this case, but the question is left open for another occasion.

Figure 30, c, illustrates the flow pattern for $U_mT/D=15$ with the 1½-inch plate. Here the eddy formation is no longer symmetrical, the separation occurring first at the upper edge of the plate followed by an eddy formed at the lower edge, remaining close to the plate.

Again the Karman vortices are obtained for large period parameter as shown in figure 30d taken with the ½-inch plate, $U_mT/D=110$.

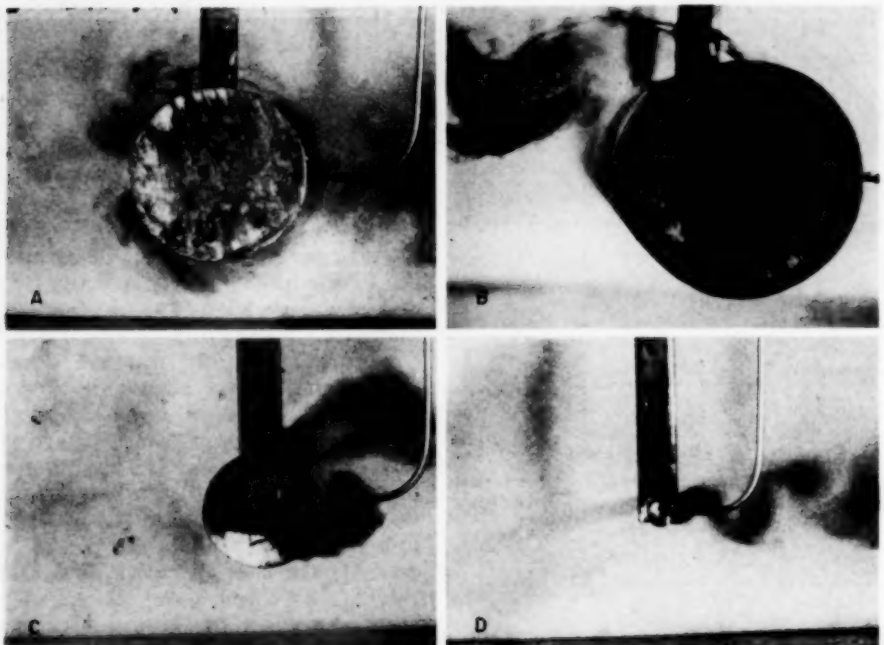

FIGURE 29. *Flow patterns around cylinders.*

(A) D=3 in., $U_\infty T/D$=4; (B) D=3 in., $U_\infty T/D$=10;
(C) D=2 in., $U_\infty T/D$=17; (D) D=0.5 in., $U_\infty T/D$=110.

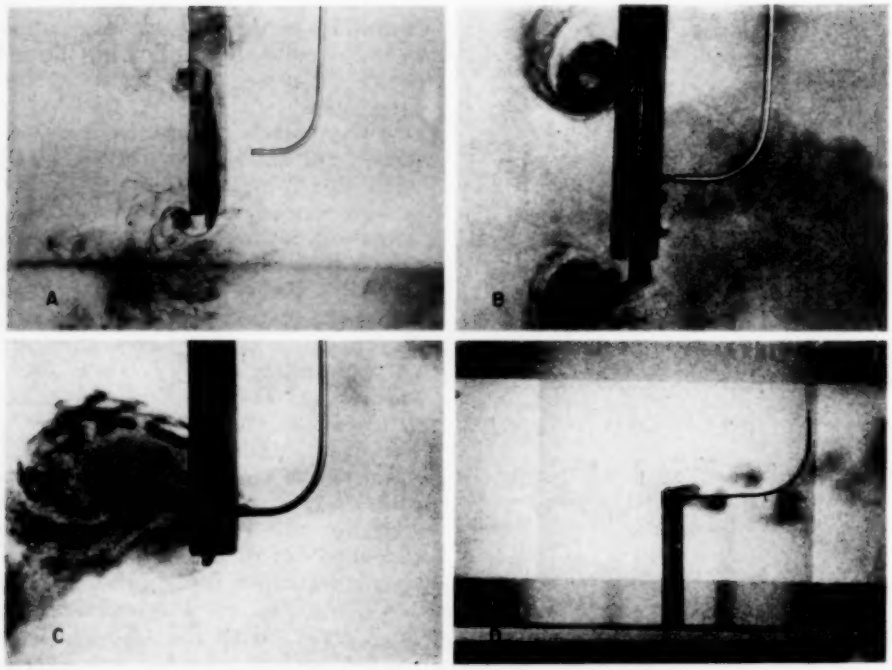

FIGURE 30. *Flow patterns around plates.*

(A) D=3 in., $U_\infty T/D$=1; (B) D=3 in., $U_\infty T/D$=4;
(C) D=1.5 in., $U_\infty T/D$=15; (D) D=0.5 in., $U_\infty T/D$=110.

The eddy appearances discussed above suggest the following interpretation as to the physical meaning of U_mT/D. If one defines a length, l, as the distance that a fluid particle would move in one direction in the absence of the cylinder, $l=U_mT/\pi$. Thus,

$$\frac{U_mT}{D}=\frac{\pi l}{D},$$

and accordingly the period parameter is proportional to the ratio of the distance traversed by a particle during a half cycle to the diameter of the cylinder. When the period parameter equals 15, l/D is 4.8. Perhaps when U_mT/D is smaller than 15, the distance traveled by a particle is not large enough to form complete eddies. When it equals 15, the distance suffices to form a single eddy, and when much larger than 15 the greater distances allow the formation of numerous vortices of the Karman vortex street. One can hardly refrain from pointing to the similarity between the period parameter and the Strouhal number, and as suggested by McNown and Keulegan [18], the product of Strouhal and period parameter numbers furnishes an alternate parameter as serviceable as the period parameter number. If T_s be the duration for the shedding of a single eddy, then the Strouhal number $fD/U=S$ may be written as $D/(2T_sU)=S$, since the number of alternative eddies shed during a second is $2f$ and $2fT_s$ equals 1 second. One may suppose that the relation is satisfied approximately also for sinusoidal motions, provided U is replaced by $U_m/2$. Hence, the Strouhal number for sinusoidal motion is $D/(U_mT_s)=S$.

Multiply the two sides by the wave parameter number U_mT/D,

$$\frac{T}{T_s}=S\frac{U_mT}{D}.$$

For cylinders, ignoring the dependence of S on the Reynolds number,

$$T/T_s=0.2\frac{U_mT}{D}.$$

As noted previously for the cylinders, C_m attains its least value, slightly less than unity, at about $U_mT/D=12.5$. This corresponds to the condition that $T/T_s=2$, nearly, and suggests that during a half cycle, that is, during a complete motion of fluid particle in one direction, a single eddy is formed and is separated (see also the figure 29, b). Obviously, the process of eddy shedding has a very significant bearing on the variations of the so-called coefficients of mass and drag, and account needs to be taken of this in the theoretical formulation of the basic process.

10. Maximum Force During a Wave Cycle

In engineering applications the main interest is in the magnitude of the maximum force experienced during a wave cycle. If the remainder function is neglected, the expression

$$F/\rho U_m^2D=A_1\sin\theta+B_1'|\cos\theta|\cos\theta$$

instead of the eq (24), may be utilized to evaluate the maximum force F_m and also its phase. If the maximum force $F_m/\rho U_m^2D$ occurs at $\theta=\theta_m$, the phase may be defined as

$$\Phi=\pi-\theta_m.$$

The maximum value of the computed force is given by

$$\frac{F_m}{\rho U_m^2D}=A_1\sin\theta_m+B_1'|\cos\theta_m|\cos\theta_m,$$

where θ_m satisfies the relation

$$A_1+2B_1'\sin\theta_m=0,\text{ or }\sin\theta_m=-\frac{A_1}{2B_1'},\qquad\text{for }\frac{\pi}{2}<\theta_m<\frac{3\pi}{2}.$$

As the coefficients A_1 and B_1' are functions of U_mT/D only, then $F_m/\rho U_m^2D$ and Φ both are functions of U_mT/D. For greater accuracy, the remainder function ΔR must be considered, but then the evaluations become somewhat involved. If these evaluations are made, the maximum force and phase are again functions of the period parameter.

An alternative procedure is the direct establishment of the maximum force and phase by merely taking these quantities from the reduced force curves of this investigation. Such readings for the cylinders are given in figure 31 and for the plates in figure 32.

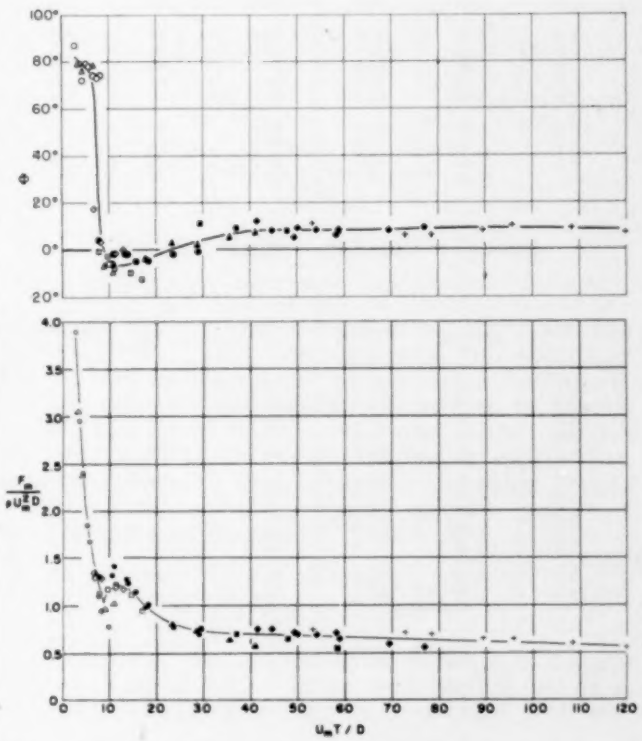

FIGURE 31. *Variations of the magnitude and phase of the maximum force on cylinders.*

Diameter (inches): 3 2.5 2 1.75 1.5 1.25 1 0.75 0.5
Corresponding symbol: ○ △ □ ◇ ● ▲ ■ ♦ +

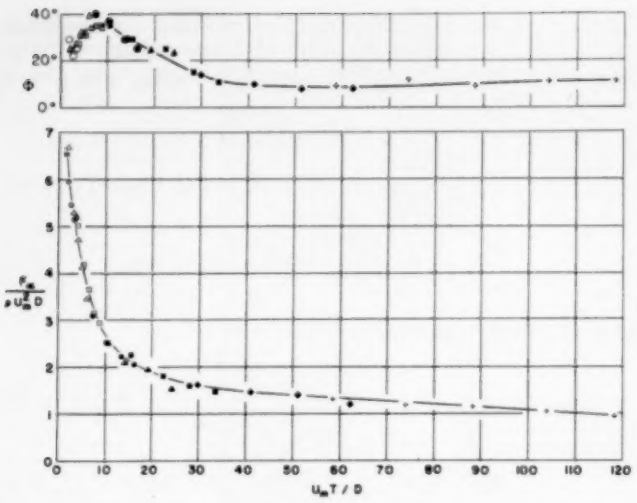

FIGURE 32. *Variations of the magnitude and phase of the maximum force on plates.*

Diameter (inches): 3 2.5 2 1.5 1.25 1 0.75 0.5
Corresponding symbol: ○ △ □ ● ▲ ■ ◆ +

TABLE 7. *Cylinders*

$U_m T/D$	$\frac{F_m}{\rho U_m^2 D}$	Φ (degrees)	$U_m T/D$	$\frac{F_m}{\rho U_m^2 D}$	Φ (degrees)
2.5	4.00	82.0	12.5	1.28	−6.8
3.0	3.45	81.2	15.0	1.15	−6.0
3.5	3.02	80.8	17.5	1.03	−5.0
4.0	2.65	80.0	20.0	0.93	−3.0
4.5	2.34	79.0	25.0	.80	1.0
5.0	2.10	78.0	30.0	.73	4.0
5.5	1.83	76.6	35.0	.70	6.5
6.0	1.60	75.0	40.0	.68	8.0
6.5	1.42	72.5	50.0	.66	8.0
7.0	1.30	65.0	60.0	.65	8.0
7.5	1.20	35.0	70.0	.63	8.3
8.0	1.20	5.0	80.0	.63	8.7
9.0	1.25	−3.0	90.0	.62	8.9
10.0	1.28	−6.0	100.0	.62	9.0

TABLE 8. *Plates*

$U_m T/D$	$\frac{F_m}{\rho U_m^2 D}$	Φ (degrees)	$U_m T/D$	$\frac{F_m}{\rho U_m^2 D}$	Φ (degrees)
2.0	6.50	24.0	10.0	2.71	34.9
2.5	6.00	25.6	12.5	2.44	32.0
3.0	5.55	27.0	15.0	2.25	28.5
3.5	5.20	28.2	17.5	2.10	26.0
4.0	4.85	29.5	20.0	1.96	23.5
4.5	4.55	30.8	25.0	1.76	18.3
5.0	4.30	32.0	30.0	1.63	13.6
5.5	4.05	33.0	35.0	1.53	11.1
6.0	3.82	33.6	40.0	1.45	9.7
7.0	3.43	34.9	50.0	1.33	8.9
8.0	3.10	35.5	60.0	1.25	8.7
9.0	2.86	35.5	70.0	1.18	9.0
.....	.....	.....	80.0	1.11	9.5
.....	.....	.....	90.0	1.06	10.1
.....	.....	.....	100.0	1.02	10.8

WASHINGTON, December 2, 1957.

For reference purposes, the data of the curves are given in tables 7 and 8, and can be used directly. In a future communication the forces on cylinders held in vertical positions will be computed on the basis of the data in these tables and will be compared with the laboratory observations already completed as a matter of concrete illustration.

The authors gratefully acknowledge the suggestions of G. B. Schubauer, the valuable and extensive endeavors of J. W. Lowry, a former colleague, in carefully examining the force records and preparing the corresponding charts and the diligence and resourcefulness of Victor Brame in carrying out the experiments.

11. References

[1] G. G. Stokes, On the effect of the internal friction of fluids on the motion of pendulums, Trans. Cambridge Phil. Soc. **9,** 8 (1851), (eq (51)).

[2] J. Boussinesq, Sur la résistance . . . d'une sphère solide . . . Compt. rend. **100,** 935 (1885).

[3] A. B. Basset, On the motion of a sphere in a viscous liquid Phil. Trans. Roy. Soc. London **179,** 43 (1888).

[4] Lord Rayleigh, On the motion of solid bodies through viscous liquid Phil. Mag. [6] **21,** 687 (1911).

[5] J. S. McNowan and L. W. Wolf, Resistance to unsteady flow: I. Analysis of tests with flat plate, Engineering Research Institute, The University of Michigan, 2446–I–P, June 1956. Internal report to Sandia Corporation.

[6] J. R. Morison, M. P. O'Brien, J. W. Johnson, and S. A. Schaaf, The forces exerted by surface waves on piles, J. Petrol. Technol. Am. Inst. Mining Engrs. **189,** 149 (1950).

[7] J. R. Morison, J. W. Johnson, and M. P. O'Brien, Experimental studies of forces on piles. Coastal Engineering, Proc. Fourth Conference (1953).

[8] H. W. Iverson and R. Balent, A correlating modulus for fluid resistance in accelerated motion, J. Appl. Phy. **22,** 324 (1951).

[9] S. R. Keim, Fluid resistance to cylinders in accelerated motion. J. of Hydraulics Div., Proc. Am. Soc. Civil Engrs. **82,** Paper 1113 (1956).

[10] G. Bugliarello, The resistance to accelerated motion of spheres in water, Ricerca Sci. **26,** 437 (1956).

[11] R. O. Reid and C. L. Bretschneider, The design wave in deep water or shallow water, storm tide, and forces on vertical piling and large submerged objects. A. and M. College of Texas, Dept. of Oceanography, Tech. Report on Contract NOy–27474, DA–49–005–eng–18 and N7onr–48704, 36 pp., Feb. 1954 (unpublished).

[12] R. O. Reid, Analysis of wave force experiments at Caplen, Texas (Sun Oil Company platform). A. and M. College of Texas, Dept. of Oceanography, Tech. Report on Contract NOy–27474, 49 pp., January 1956 (Unpublished).

[13] F. D. Mornaghan, Bul. Natl. Reséarch Council **84,** 4 (Washington, D. C., 1932).

[14] Sir Horace Lamb, Hydrodynamics, Sixth Ed., p. 7 Dover Publications.

[15] J. S. McNown, Drag in steady flow, The university of Michigan and Sandia Corporation, Proc. Intern. Congress Appl. Mech. Brussells (1957).

[16] R. Miche, Mouvements ondulatoires de la mer en profondeur constante ou décroissante, Ann. Ponts et Chaussées **114,** 25 (1944).

[17] M. P. O'Brien and J. R. Morison, The forces exerted by waves on objects. Trans. Am. Geophys. Union **33,** 3 (1952).

[18] J. S. McNown and G. H. Keulegan, Vortex formation and resistance in periodic motion (publication pending).

Journal of Research of the National Bureau of Standards Vol. 60, No. 5, May 1958 Research Paper 2858

Reaction of Portland Cement with Carbon Dioxide

Charles M. Hunt, Vernon Dantzler, Lewis A. Tomes,[1] and Raymond L. Blaine

The reaction of portland cement with carbon dioxide was found to be greatly influenced by the moisture environment of the cement. Reaction with carbon dioxide and water also affected the subsequent hydration of the cement.

1. Introduction

Portland cements stored for several months in an environment that permits gradual access to air sometimes appear to hydrate more slowly than when the cements were first tested. It is a well-known fact that cement can react with carbon dioxide when exposed to air or other atmospheres containing this gas [1].[2] The reaction is accompanied by a certain amount of hydration due to atmospheric moisture. A number of years ago Bonnell [2] studied the effect of carbonation of cement on setting time, heat of hydration, and tensile strength of the material after hydration. He found all of these properties to be influenced by carbonation of the original cement.

More recently, the determination of nonevaporable water in hardened cement pastes has been used rather extensively to estimate the degree of hydration of cement [3, 4, 5, 6]. The present paper considers the effect of carbonation of cement upon its subsequent hydration, using nonevaporable water as a measure of hydration.

Bonnell [2] and Lea [1] have mentioned that the reaction of cement with carbon dioxide is dependent upon relative humidity and that such reaction will not take place in a dry atmosphere. A brief reinvestigation of this matter is also described in this paper.

2. Methods and Materials

2.1. Carbon Dioxide Exposure

Cement was exposed to carbon dioxide in a tube similar to the one illustrated in figure 1. The carbon dioxide was brought to predesired relative humidity by passing it through gas-washing bottles containing sulfuric acid of appropriate concentration. Approximately 1 g of cement was taken for each exposure and the entire specimen analyzed. When larger amounts of cement were exposed, the cement was taken out and blended at intervals.

Cement was also carbonated in air by exposure in a large outdoor enclosure where it could have free access to air but be protected from wind and rain. The cement was spread in layers 2 mm thick or less for this type of exposure.

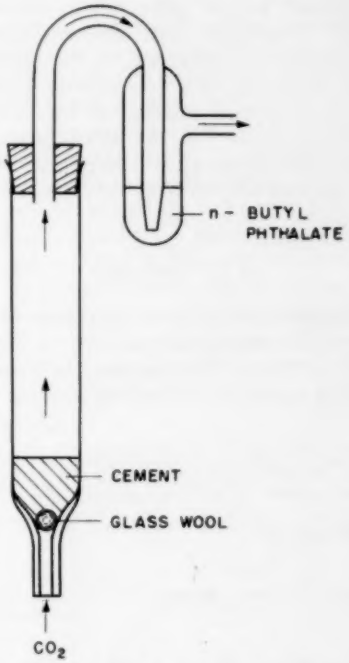

FIGURE 1. *Cell for exposing cement to carbon dioxide.*

2.2. Determination of Carbon Dioxide

The carbon dioxide content of the cement was determined by the evolution method, digesting the material with 4 *N* hydrochloric acid and absorbing the evolved carbon dioxide in Ascarite. Anhydrous calcium chloride was used in the system to absorb water, and silver sulfate in concentrated sulfuric acid was used to absorb any hydrogen sulfide that might be present. The apparatus and other details of the determination are similar to those described by Kolthoff and Sandell [7].

2.3. Hydration of Cement

The cement was mixed with water in a water-cement ratio of 0.5. Mixing was carried out in a soil-density balloon[3] to minimize contact with air.

[1] Research Associate at the National Bureau of Standards, representing the Calcium Chloride Institute.

[2] Figures in brackets indicate the literature references at the end of this paper.

[3] Soil-density ballons are supplied by the Rainhart Co., Austin, Tex. The type used in this work had a total volume of about 160 ml.

The paste was cast in the form of ½-in. cylinders by extrusion into paraffin-coated paper molds. The paste-filled molds were kept in stoppered glass tubes for 24 hr, after which the specimens were sawed into ½-in. sections. Hydration for periods greater than 24 hr was carried out in paraffin-sealed quart jars in the presence of a high concentration of water vapor.

2.4. Determination of Nonevaporable Water

The pastes were crushed and nonevaporable water was determined by a procedure similar to that described by Copeland and Hayes [5]. However, instead of applying a correction for ignition loss of the original cement, the specimens were analyzed for carbon dioxide and corrected for carbon dioxide content. Nonevaporable water computed in this way includes all nonevaporable water in the specimen, regardless of whether it was acquired before or after mixing.

2.5. Cements

Four cements were used in these experiments. All were type I cements according to Federal Specification SS–C–192a. The results of chemical analysis of the cements are given in table 1.

TABLE 1. *Chemical composition of cements*

Constituent	Cement			
	1	2	3	4
	Percentage by weight			
CaO	64.0	62.5	64.1	----
SiO_2	22.0	22.2	22.3	----
Al_2O_3	5.2	5.2	5.0	5.9
Fe_2O_3	4.6	2.6	3.0	2.3
MgO	1.6	3.8	1.9	1.9
SO_3	1.5	1.9	2.0	2.2
Ignition loss	0.2	0.5	1.0	0.7
Insoluble residue	.1	.3	0.3	.2

3. Results

3.1. Effect of Water on the Rate of Carbonation

Portland cement was exposed to carbon dioxide at different relative humidities for different periods of time and analyzed after exposure. In figure 2 the carbon dioxide content is plotted as a function of exposure time. At relative humidities of less than 25 percent, carbonation was found to be very slow. The slope of the bottom curve in figure 2 suggests that the cement would not have reacted with much more carbon dioxide even if it were exposed for a much longer period. At 50 to 55 percent, the rate of carbonation increased, and at 90- to 95-percent relative humidity the increase was most marked. The curves at these higher relative humidities showed no evidence of leveling off after a week of exposure.

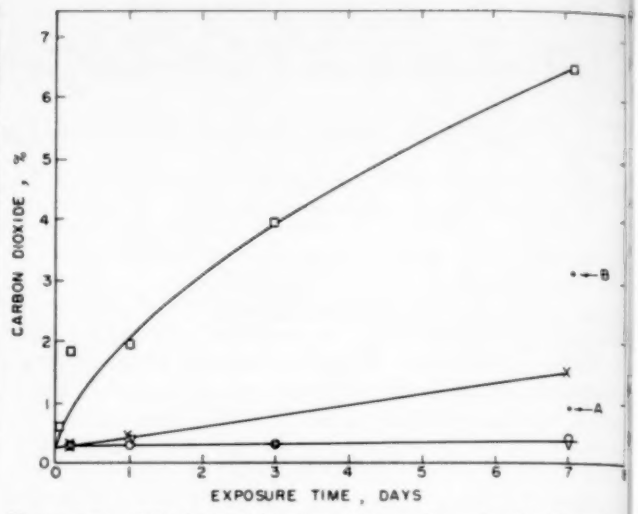

FIGURE 2. *Effect of relative humidity on the rate of carbonation of portland cement.*

▽, Cement exposed to dry carbon dioxide, ○, cement exposed to carbon dioxide at 20- to 25-percent relative humidity, ×, cement exposed to carbon dioxide at 50- to 55-percent relative humidity, □, cement exposed to carbon dioxide at 90- to 95-percent relative humidity, A, cement exposed to air for 1 week, B, fresh cement paste exposed to air for 1 week.

Because the rate of carbonation was so dependent on relative humidity, cement was also exposed by passing carbon dioxide into a freshly-mixed paste. The initial water-cement ratio of the paste was 0.5, but the mixture dried during exposure. In figure 3 the rate of carbonation of fresh paste is compared with that of cement at 90- to 95-percent relative humidity. It may be seen that during the first few hours the paste carbonated much faster than the cement, but thereafter the rate diminished sharply. The decrease in rate was probably due to drying of the paste. It is clear from the results in figure 2 and 3 that water is an important limiting factor in the rate of carbonation of cement.

Cement, and fresh cement paste, were also exposed to air. Figure 4 shows the amount of carbon dioxide gained upon exposure to air for periods up to 28 days. Again the fresh paste acquired much more carbon dioxide than the dry cement during the first day, but, after drying, the rate for paste was slightly less than that of the cement. From these results it is clear that even at the low carbon dioxide concentrations normally present in air, water can also be a rate-determining factor.

Point A, in figure 2, shows the amount of carbon dioxide in the cement after a week of exposure to air. It is included in the figure to point out that the cement contained more carbon dioxide after a week in air than in pure, dry carbon dioxide. Point B, in figure 2, shows that the cement paste contained more carbon dioxide after a week's exposure to air than was present in dry cement after a similar period in carbon dioxide at 50- to 55-percent relative humidity. From these observations it is concluded that the concentration of water can exert a greater effect on the rate of carbonation than the carbon dioxide concentration.

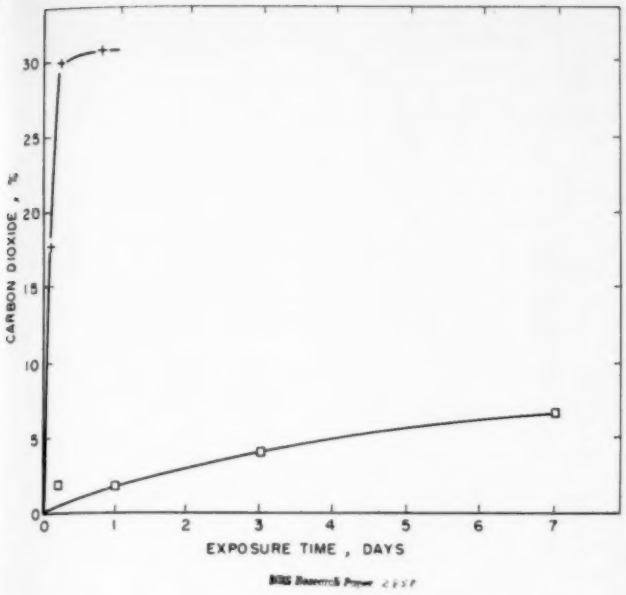

FIGURE 3. *Rate of carbonation of cement and fresh cement paste in carbon dioxide.*

□, Cement exposed to carbon dioxide at 90- 95-percent relative humidity; +, fresh cement paste exposed to dry carbon dioxide.

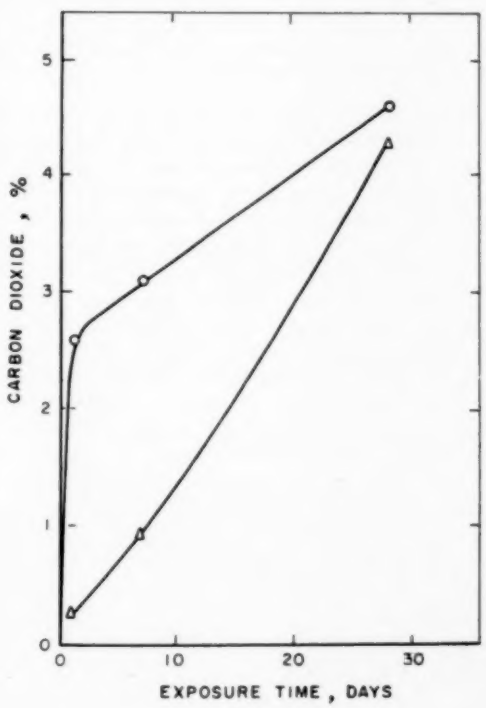

FIGURE 4. *Rate of carbonation of cement and fresh cement paste in air.*

△, Cement exposed to air, ○, fresh cement paste exposed to air.

The results shown in figures 2, 3, and 4 were all obtained with cement 1 in table 1.

3.2. Effect of Carbonization on the Hydration of Cement

Cements containing different amounts of carbon dioxide were mixed with water and allowed to hydrate. Nonevaporable water in the hardened paste was determined after 1 day, 7 days, and 28 days of hydration. The results are given in table 2. It may be seen that the more highly carbonated cements contained smaller amounts of nonevaporable water after hydration. In figures 5, 6, and 7, carbon dioxide content of the cement before mixing is plotted as a function of nonevaporable-water content of the hardened paste after hydration. Both quantities have been expressed in millimoles per 100 g of ignited cement. This comparison shows no simple stoichiometric relationship between the increase in carbon dioxide content of the cement and the decrease in nonevaporable water in the paste, but it shows that comparatively small differences in the number of millimoles of carbon dioxide in the cement are associated with rather large differences in the number of millimoles of nonevaporable water. The effect is just as evident after 28 days of hydration as after the first day.

Carbonation of cement is accompanied by a certain amount of hydration by water vapor in the carbonating atmosphere. For this reason, the effects shown in table 2 and in figures 5, 6, and 7 may

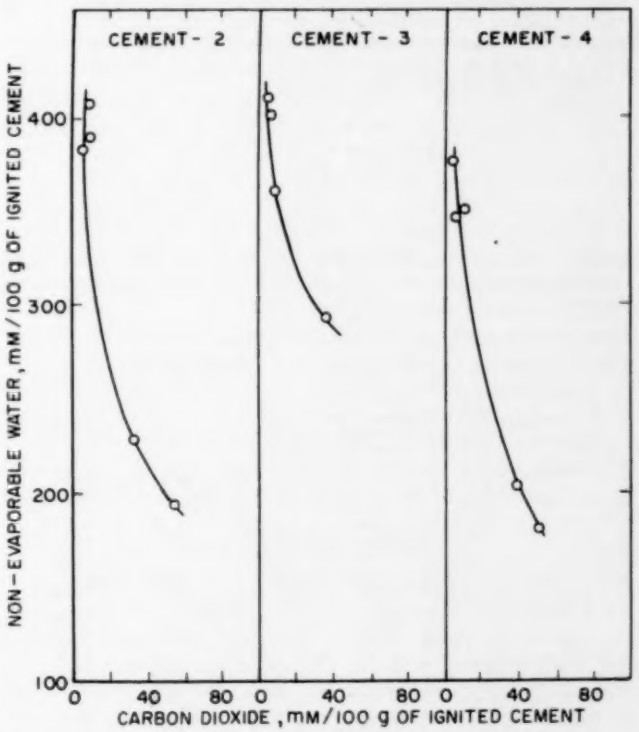

FIGURE 5. *Nonevaporable water content of cement pastes after 1 day of hydration as a function of carbon dioxide content of the cement before mixing.*

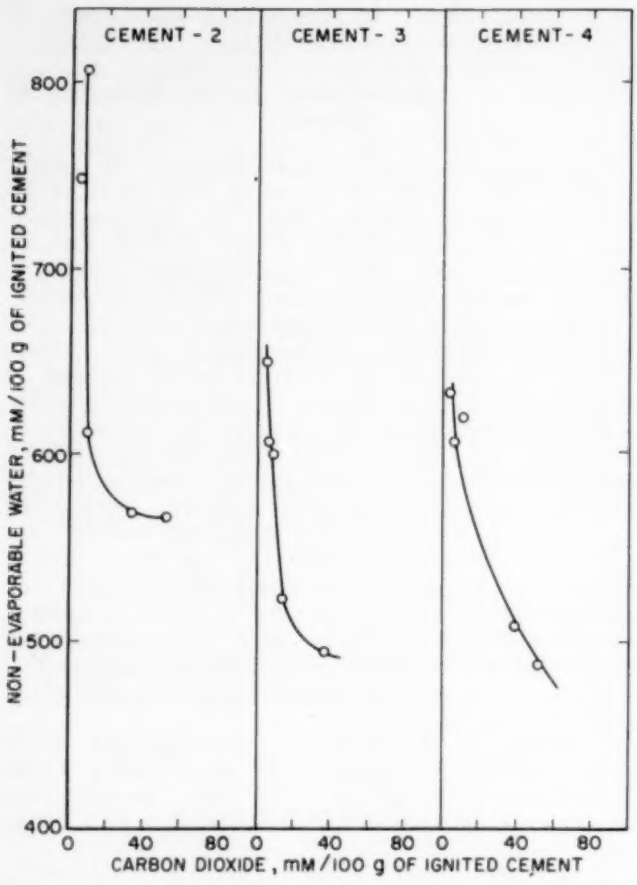

FIGURE 6. *Nonevaporable water content of cement pastes after 7 days of hydration as a function of carbon dioxide content of the cement before mixing.*

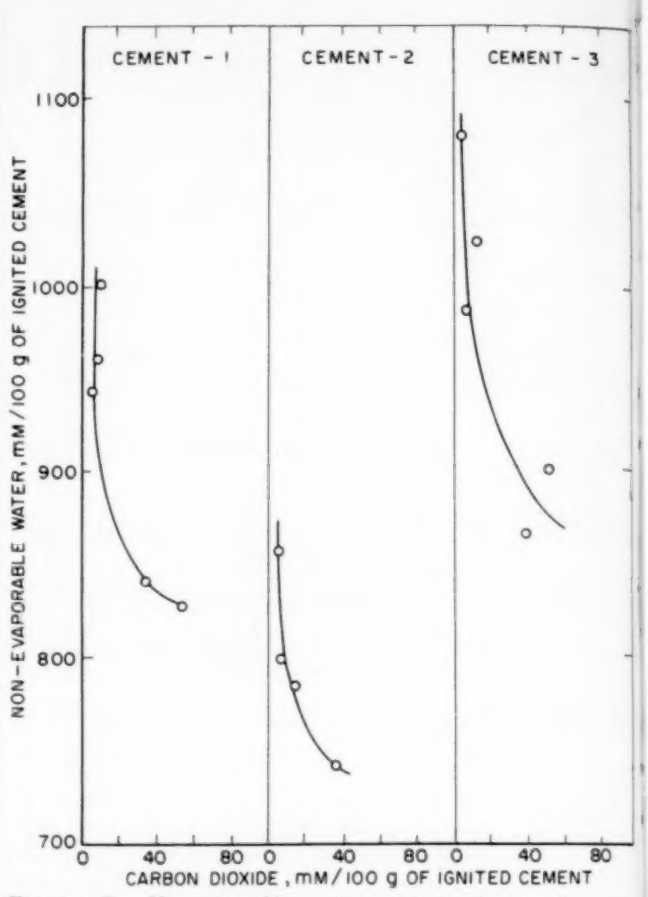

FIGURE 7. *Nonevaporable water content of cement pastes after 28 days of hydration as a function of carbon dioxide content of the cement before mixing.*

TABLE 2. *Nonevaporable water content of hardened pastes and carbon dioxide content of cement from which they were prepared*

Cement	Initial CO_2 (percentage of ignited cement)	Nonevaporable water		
		1-day hydration	1-week hydration	1-month hydration
		Percentage of ignited cement		
2	0.39	7.35	14.50	18.05
	.19	6.91	13.47	16.95
	.41	7.04	11.01	17.30
	1.48	4.11	10.22	15.15
	2.46	3.49	10.19	14.89
3	0.25	7.40	11.70	15.40
	.27	7.25	10.93	14.38
	.36	6.52	10.80	14.20
	.64	----	9.40	14.16
	1.68	5.28	8.91	13.34
4	0.23	6.78	11.46	19.47
	.28	6.22	10.91	17.75
	.52	6.38	10.98	18.42
	1.75	3.65	9.14	15.60
	2.31	3.27	8.79	16.22

not be exclusively due to carbon dioxide in the cement. Pastes were prepared from four specimens of cement in which the initial water content of the original cement varied from specimen to specimen, whereas the carbon dioxide content was nearly constant. These were compared with pastes from four specimens in which both carbon dioxide and water contents of the original cement varied from specimen to specimen. The nonevaporable water content of the eight pastes after 24 hr of hydration are given in table 3, along with the water and carbon dioxide contents of the original cement. It is evident that both the water and carbon dioxide in the original cement exerted an influence on subsequent hydration. The comparative effects of the water and carbon dioxide in the original cement can perhaps be best illustrated by considering nonevaporable water content of the hydrated paste as a function of the water content of the original cement, as has been done in figure 8. It may be seen from the figure that carbon dioxide produced an effect on hydration over and above that produced by water in the original cement. The decrease in millimoles of nonevaporable water in the paste was also somewhat greater than the total number of millimoles of carbon dioxide and water in the cement that were associated with the effect.

TABLE 3. *Nonevaporable water content of hardened cement pastes and carbon dioxide and water content of cement from which they were prepared*

Cement	Initial CO_2 (percentage of ignited cement)	Initial H_2O (percentage of ignited cement)	Nonevaporable water after 1 day (percentage of ignited cement)
2	0.44	0.97	6.79
	.65	1.00	5.52
	1.80	1.19	2.96
	2.76	1.55	2.25
2	0.43	0.74	7.08
	.48	.89	6.81
	.49	1.53	5.55
	.49	1.36	5.49

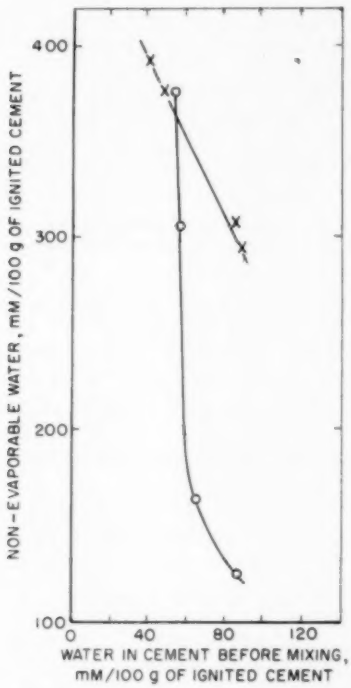

FIGURE 8. *Nonevaporable water content of cement pastes as a function of the water in the cement before mixing.*

×, 0.43- to 0.49-percent CO_2 in cement'
○, 0.44- to 2.76-percent of CO_2 in cement.

4. Discussion

The results in figure 2 are in essential agreement with the statements of Bonnell [2] and Lea [1] relating to the effect of relative humidity on the reaction of carbon dioxide with cement. A certain amount of water is necessary before carbonation can proceed, at least at any appreciable rate.

The results in figures 3 and 4 show that cement in a fresh paste is particularly susceptible to carbonation wherever the surface is exposed. This observation is of interest in connection with Kauer and Freeman's [8] investigation into the cause of softness of the surface of concrete floors where oil-burning heaters were used to keep the freshly placed concrete warm. They attributed this undesirable behavior to carbonation. The results in figures 2 and 3, although they give no direct evidence as to the quality of the cement after carbonation, show that the exposed surface of a freshly mixed cement will react with carbon dioxide many times as fast during the first few hours as will the same cement before mixing.

It is also evident from the results in figures 5, 6, and 7 that the amount of nonevaporable water in a hydrated cement after a given time of hydration is influenced to a measurable extent by the amount of carbon dioxide in the original cement before mixing. It is interesting to consider these results in the light of Bonnell's [2] observation that the tensile strength of mortars and pastes at early ages was adversely affected by small amounts of carbon dioxide in the original cement, whereas strength at 28 days was not adversely affected until carbon dioxide levels greater than those in the present experiments were encountered. If any comparison between the present observations and those of Bonnell is justified, it implies that cement containing different amounts of carbon dioxide can develop the same strength at 28 days, even though there may be measureable differences in the amount of hydration products present.

The mechanism by which carbonation and reaction with atmospheric moisture reduces subsequent hydration is not established. The similarity of the effect at all ages, as shown in figures 5, 6, and 7, suggests that changes produced during carbonation do not affect the rate of hydration, as such, unless possibly within the first few hours. However, as a result of carbonation, a fraction of the cement is made unavailable for hydration, and the amount of hydratable material so affected is not a linear function of carbon dioxide content.

From the standpoint of practical use it is doubtful if small amounts of carbon dioxide and water seriously impair the hydraulic properties of portland cement. All cement probably contains small amounts of these substances. In the experiments described here, cement was given maximum opportunity to come into contact with carbon dioxide and water, whereas in bulk storage the cement in the outer layers of the mass affords some protection to the cement on the interior. However, to obtain maximum reproducibility in carefully controlled hydration studies, it is desirable to avoid reaction with carbon dioxide and water during storage.

5. Summary

In confirmation of earlier observations reported by Bonnell [2] and Lea [1], cement was found to carbonate slowly or not at all when exposed to pure, dry carbon dioxide. In the presence of increasing concentrations of water vapor, however, the rate of carbonation increased rapidly. Cement was also found to carbonate faster when freshly mixed with water than in an atmosphere of high relative humidity.

The amount of nonevaporable water in a hardened cement after 1 day, 7 days, or 28 days of hydration was found to be smaller as the amount of carbon dioxide in the original cement increased. The reduction in the amount of hydration at any given age was greater than the amount of carbon dioxide associated with the effect, when both were compared on a molecular basis. Water in the original cement also appeared to curtail subsequent hydration of the cement, but the effect was less than the combined effect of water and carbon dioxide.

WASHINGTON, November 13, 1957.

6. References

[1] F. M. Lea, The chemistry of cement and concrete, p. 250 (St. Martins Press, New York, N. Y., 1956).

[2] D. G. R. Bonnell, Dept. Scientific and Industrial Research, Building Research Tech. Paper No. 19 (His Majesty's Stationery Office, 1936).

[3] T. C. Powers and T. L. Brownyard, Studies in the physical properties of portland cement paste, Part 2, studies of water fixation, Proc. Am. Concrete Inst. **43,** 249 (1946); Also included in Portland Cement Assoc. Bul. 22.

[4] T. C. Powers, Non-evaporable water content of hardened portland cement paste—its significance for concrete research and its methed of determination, ASTM Bul. No. 158 (May 1949); also published as Portland Cement Assoc. Bul. No. 29.

[5] L. E. Copeland and J. C. Hayes, Determination of non-evaporable water in hardened portland cement paste, ASTM Bul. No. 194, p. 70 (1953); also published as Portland Cement Assoc. Bul. No. 47.

[6] L. E. Copeland and R. H. Bragg, Self desiccation in portland cement pastes, ASTM Bul. No. 204, p. 34 (1955); also published as Portland Cement Assoc. Bul. No. 52.

[7] I. M. Kolthoff and E. B. Sandell, p. 373 (The MacMillan Co., New York, N. Y., 1952).

[8] J. A. Kauer and R. L. Freeman, Proc. Am. Concrete Inst. **52,** 447 (1955).

Journal of Research of the National Bureau of Standards Vol. 60, No. 5, May 1958 Research Paper 2859

Average Energy of Sulfur-35 Beta Decay

Howard H. Seliger, Wilfrid B. Mann, and Lucy M. Cavallo

The rate of energy emission in an approximately 400-millicurie source of sulfur-35 was measured by means of a "radiation-balance" microcalorimeter. This value and the disintegration rate of an accurate dilution of the sample measured by means of $4\pi\beta$-gas-proportional counting yield a mean energy for sulfur-35 beta decay of 50.4 $(^{+0.7}_{-1.2})$ kev. The half-life has been determined to be 87.16 ± 0.1 days.

1. Introduction

The rate of energy emission in approximately 400 mc of sulfur-35 was recently measured by means of the radiation balance [1, 2] [1] for the purpose of determining W_{air}, the average energy expended to produce one ion pair in air by the beta particles emitted by sulfur-35 [3, 4]. A part of this sample of sulfur-35, which was of high specific activity, was subsequently used to prepare radioactivity solution standards of the nuclide. From these standards a number of sources having extremely low solid content were subsequently prepared for $4\pi\beta$ counting [5, 6, 7]. These low-solids sources were prepared in the same manner as for the determination of W_{air} at the National Bureau of Standards [4].

The average energy of the sulfur-35 beta decay was derived from the results of disintegration rate measurements by $4\pi\beta$ counting and the rate of energy emission obtained from the radiation balance.

2. Radiation-Balance Measurements

The sample of sulfur-35 consisted of about 400 mc of sodium sulfate sealed in a soft-glass tube 3.3 mm in external diameter and 35 mm in length. A dummy source of the same dimensions containing inactive sodium sulfate was also prepared for use in the second cup of the radiation balance.

It so happened that there were available in the laboratory at the time two other radioactive preparations that were emitting energy at about the same rate as the sulfur-35 sample. One of these was a polonium-210 sample that had been used to measure the branching ratio in the decay of polonium-210 [8], and the other was a sample of about 4.8 curies of tritiated water sealed in a quartz tube under a partial pressure of about 2 cm Hg of hydrogen. This latter sample was subsequently used to prepare the National Bureau of Standards tritiated-water standards.

For the purpose of checking the internal consistency of the results obtained, it seemed that it would be advantageous to measure the tritium, sulfur-35, and polonium-210 samples together as a triad in the radiation balance in the manner described by Connor and Youden for the comparison of four national radium standards [9].

The results of a great many measurements on the polonium-210 preparation have already been reported [8] and were satisfactorily consistent.

[1] Figures in brackets indicate the literature references at the end of this paper.

The 4.8-curie tritium preparation was also measured over a period of about 4 months to insure that no error might arise from energy releases due to the chemical effects of radiation which might be expected to vary with time. Here again the consistency of the results was quite satisfactory. The National Bureau of Standards tritiated-water standards prepared from this sample were also subsequently compared by the method of liquid scintillation counting with the tritium standard samples distributed by Atomic Energy of Canada Limited and with the tritium standard of the University of California's Los Alamos Scientific Laboratory. Agreement was obtained to within 1.3 percent with the Canadian standard, and to within 0.7 percent with the Los Alamos standard.

The results of the microcalorimetric comparison of the tritium, sulfur-35, and polonium-210 preparations are shown in table 1. From these results "best estimates" for each of the three preparations, incorporating the difference measurements as well as measurements on the individual preparations, were obtained in the same way as has been described for the national radium standards [9]. These best estimates are 155.7 μw for the tritium as of May 10, 1955; 119.9 μw for the sulfur-35 as of 1430 EST on May 11, 1955; and 262.6 μw for the polonium-210 as of 1315 EST on May 11, 1955.

After measurement, the sulfur-35 preparation was put into solution by breaking the soft-glass container by the simple expedient of heating one end of it in an electrically heated coil and then plunging it, while hot, into cold distilled water.

TABLE 1. *Rate, and differences in the rate, of energy emission from preparations of tritium, sulfur-35, and polonium-210*

1955	Time (EST)	Source	Energy emission (μw)
May 10	1330	Po^{210}	264.6
May 10	1630	S^{35}-H^3	35.1
May 10	1730	H^3	154.8
May 11	1130	Po^{210}-H^3	106.5
May 11	1315	Po^{210}-S^{35}	142.8
May 11	1430	S^{35}	120.0

3. $4\pi\beta$-Gas-Proportional Counting

The low-energy beta-ray spectrum of sulfur-35 ($E_{\beta\ max}$=167 kev) would normally preclude the determination of the disintegration rate of this nuclide by the $4\pi\beta$-gas-proportional-counting technique. A self-absorption effect, which could be as

high as 5 to 10 percent, was observed even for cobalt-60 ($E_{\beta\ max}$=310 kev) [6]. However, the cobalt was in the chemical form of $CoCl_2$, which tends to form appreciably large crystals, whereas the sulfur was incorporated into an SO_4^{--} ion. With the active material as a part of a negative ion and in a different environment (H^+ and SO_4^{--} ions), it was felt that it might be possible to go to very low-solids concentrations where even agglomerization might be difficult, without the danger of adsorption on the glassware, which usually occurs with positive ions. Because of the high specific activity of the original source it was possible to obtain reasonably high activity $4\pi\beta$-counter sources even after dilution to low-solids concentration. The mass of sodium sulfate originally measured in the microcalorimeter was approximately 100 mg. The final dilution contained only 2.5 μg of solids per milliliter. Usually only 0.02 ml was delivered to a $4\pi\beta$-counter source-mount, so that the final source contained 0.05 μg. (The corresponding figure for the cobalt-60 sources prepared from $CoCl_2$ was 1.5 μg.) Stepwise dilutions were made of the original master solution, using conductivity water and 0.5-*N* redistilled hydrochloric acid with no additional sulfate carrier. If there were any adsorption at this very low concentration of sulfate ions, it was felt that the effect might be magnified in the absence of the strongly acid, 0.5-*N*, hydrochloric-acid solution. Therefore, parallel dilutions were made using only conductivity water. Over a period of several months, sources prepared from both solutions gave the same counting rates in the $4\pi\beta$ counter. This appeared to be strong evidence against the presence of appreciable adsorption effects.

Over extended periods of time, water will etch the surface of a Pyrex glass container. This etching process releases extremely minute silica flakes into the solution, and the additional solid material could increase the self-absorption in a $4\pi\beta$-counter source. Because the experiments on source preparation extended over a period of a year, it was considered advisable to look for this effect. In February 1956, some 9 months subsequent to the preparation of the original dilutions in glass flasks, a millicurie of high-specific-activity carrier-free sulfur-35 as H_2SO_4 in 0.1-*N* hydrochloric acid was obtained from the Oak Ridge National Laboratory. This material was diluted sufficiently with conductivity water and stored in a quartz flask in which there should be much less etching with time than in the regular Pyrex glass flasks. The ratio of disintegrations per second per milliliter of the new "quartz-flask" solution to the disintegrations per second per milliliter of the older "glass-flask" solutions was obtained to a high degree of precision by the technique of formamide counting [7, 10]. By use of this saturation-thickness method the solutions could be compared independently of any minute differences in solids content owing to the possible presence of silica in the glass-flask solutions. $4\pi\beta$-counter sources were then prepared under identical conditions from these solutions, and the counting rates observed were in the same ratio as the formamide counting rate within the precision of the measurements. This result provided substantial evidence that the effect of silica on the self-absorption was small, if present at all.

Aliquots of solution were delivered to collodion or Formvar-polystyrene laminated films ranging from 2.5 $\mu g/cm^2$ to 10 $\mu g/cm^2$. Six different methods of precipitating the source material were tried. These were, in order of their effectiveness in reducing source self absorption: (a) evaporation in air of the entire aliquot, (b) deposition of the aliquot in approximately 20 droplets covering almost the same area as (a) and evaporation in air, (c) evaporation in air of the aliquot, redissolving in water and re-evaporating in air, (d) evaporation in air, heating under an infrared lamp, redissolving in water plus the addition of a droplet of ammonium hydroxide, (e) evaporation in air, redissolving in water and re-evaporating in a saturated ammonia atmosphere, and finally, (f) evaporation in air without heat, heating under an infrared lamp, redissolving in water, and then drying in a saturated ammonia atmosphere. The tremendous differences in counting rates observed in the $4\pi\beta$ counter for sources prepared by these different methods are apparent in table 2, in which the averages of observed counting rates are given for the various methods. It should be emphasized that all sources contained identical amounts of activity.

TABLE 2. *Range of values obtained for various source-preparation methods*

Method	Number of sources	Average value (in counts per second)	Individual standard deviation (in counts per second)
(a)	11	11.50×10^2	±0.76
(b)	6	12.16	±1.10
(c)	23	12.62	±0.70
(d)	3	12.90	±0.25
(e)	58	13.08	±0.75
(f)	20	13.81	±0.47

Method (f), giving the optimum results, was also used to prepare sources for the measurement of W_{air} [4]. It was not possible to investigate the structure of method (f) sources as thoroughly as was done for iodine-131 sources, i. e., by shadow electron micrography, as described in reference [7]. Because of the high normality of the solutions, sources prepared for electron micrography were not too stable and usually corroded the stainless-steel supporting grids of the specimen holder. However, it was possible to examine briefly some portions of several sources. These showed one of two forms, either an extremely fine precipitate of particles of the order of 100 A in diameter or a structure similar to a flat "two-dimensional" crystal of thickness approximately 100 A. In any case it appeared that, by pure empiricism, a method that gave a minimum of self-absorption had been found for depositing the sulfur-35. It is not clear why this method is so much more effective than the others. There is perhaps some physical action on the substrate as

well as on the solution caused by the heating, redissolving, etc.

The small but significant spread of values obtained even when sources were prepared by method (f) is an indication that there still remains a small-self-absorption effect. Based on the observations in the electron microscope and on subsequent measurements of the absorption of sulfur-35 beta rays in thin films, a self-absorption correction of 1 percent was used in calculating the final result. Due to the uncertainty of particle size in the electron microscope this correction could vary over the range ($\pm^{2}_{0}$) percent.

Corrections for mounting-film absorption were made by means of the sandwich technique described in reference [6]. Owing to the low energy of the sulfur-35 the aluminum leaf normally used for the sandwich measurements introduced at least a 5-percent film-absorption correction factor. In order, therefore, to check the validity of the previous derivation over this larger range of mounting-film absorption, experiments were performed with much thinner conducting films as well. Observed counting rates as functions of film thickness were plotted for up to five layers of thin films of collodion made conducting by vacuum evaporation of extremely small quantities of aluminum. In these cases absorption amounted to only 1 percent per film. Straight-line extrapolation of this type of transmission curve to zero film thickness gave the same results as the original aluminum-leaf sandwich measurements.

Because the measurements of disintegration rate extended over a long interval, it was of considerable importance to obtain an accurate value for the half-life of sulfur-35. A least-squares analysis of disintegration-rate values obtained in the $4\pi\beta$ counter with the same sources over a period of 5 months gave a value of 87.16 $\pm$0.1 days. This value was used to correct all data.

As a final check on the accuracy of the $4\pi\beta$-gas-proportional-counter standardization, the solution that had been standardized was compared with a solution standard received from Atomic Energy of Canada Limited, Chalk River, Ontario, the latter having been sent to the National Bureau of Standards as part of a joint international program of intercomparison of radioactivity standards. The sample from Canada was too weak to be measured with high precision by means of the formamide-counting technique. A portion of the NBS standard solution was therefore diluted with sufficient carrier to be equivalent in solids concentration and in the same range of activity as the Canadian sample. Sources from each standard were prepared on palladium-faced silver disks, and activity ratios were obtained in (a) the top half of the $4\pi\beta$ counter and (b) the NBS $2\pi\beta$-ionization chamber. Both of these measurements gave the same ratio within 0.2 percent.

Table 3 summarizes the results obtained for similar samples distributed by AECL to other standardizing laboratories as well as the NBS results as deduced from the above precise comparison.

TABLE 3. *Intercomparison of AECL S^{35} solution standards* [a]

United States	Canada			England	
NBS $4\pi\beta$-prop. counter	AECL $4\pi\beta$-prop. counter	AECL internal gas counter	McGill U. $4\pi\beta$-prop. counter	RCH [b] 4π-GM counter	AERE [c] 4π-GM counter
1.37[d]	1.26	1.36	[d] 1.49	1.36	1.32

[a] Results are given in microcuries per milliliter as of April 6, 1955.
[b] Royal Cancer Hospital.
[c] Atomic Energy Research Establishment, Harwell.
[d] The apparent disagreement shown here is probably due to solution differences rather than differences in counting techniques, based on previous agreement with other nuclides.

4. Results and Discussion

A rate of energy emission of 119.9 μw corresponds to 748.4×10^{12} ev/sec. The total disintegration rate of the original sodium sulfate was 401.5 mc. The mean energy per disintegration is therefore 50.4 kev. Table 4 gives a summary of the corrections and uncertainties associated with the measurements. The uncertainty of the experimentally determined mean energy is ($^{+0.7}_{-1.2}$) kev.

This experimentally determined value agrees quite well with the value of 49.4 kev calculated by Shimanskaia [12] from the Fermi distribution. Shimanskaia also reported an experimental value of 52 $\pm$3 kev, using a defined solid-angle Geiger counter for the absolute-activity measurements.

Recently, Loevinger [13] has calculated a value of 48.8 kev for the mean energy of sulfur-35 beta decay, with an uncertainty of $\pm$0.75 percent. Jesse and Sadaukis [14] have quoted a value, determined by calculation, of 48.7 $\pm$0.25 kev.

TABLE 4. *Sources of error in measurement of* $\overline{E}$

Source of error	Uncertainty
	%
Source preparation and 4π counting	$\pm$0.51
Source self-absorption correction	($^{+0}_{-2}$)
Half-life correction	$\pm$0.33
Film-absorption correction	$\pm$1
Radiation-balance measurement	$\pm$0.3
Dilution of 400-mc sample	$\pm$.3
Total uncertainty	($^{+1.3}_{-2.4}$)

5. References

[1] W. B. Mann, J. Research NBS **52,** 177 (1954) RP2486.
[2] W. B. Mann, J. Research NBS **53,** 277 (1954) RP2545.
[3] W. Gross, C. Wingate, and G. Failla, Radiology **66,** 101 (1956).
[4] Z. Bay, W. B. Mann, H. H. Seliger, and H. O. Wyckoff, Radiation Research **7,** 558 (1957).
[5] H. H. Seliger and L. Cavallo, J. Research NBS **47,** 41 (1951) RP2226.
[6] W. B. Mann and H. H. Seliger, J. Research NBS **50,** 197 (1953) RP2409.
[7] H. H. Seliger and A. Schwebel, Nucleonics **12:7,** 54 (1954).

[8] R. W. Hayward, D. D. Hoppes, and W. B. Mann, J. Research NBS **54,** 47 (1955) RP2564.
[9] W. S. Connor and W. J. Youden, J. Research NBS **53,** 273 (1954) RP2544.
[10] A. Schwebel, H. S. Isbell, and J. D. Moyer, J. Research NBS **53,** 221 (1954) RP2537.
[11] Excerpted from minutes of National Research Council Subcommittee On Beta and Gamma Ray Measurements and Standards, Feb. 10, 1956.
[12] N. S. Shimanskaia, Soviet Phys. JETP **4:3,** 355 (1957).
[13] R. Loevinger, Phys. in Med. Biol. **1,** 330 (1957).
[14] W. P. Jesse and J. Sadaukis, Phys. Rev., **107,** 766 (1957).

WASHINGTON, November 13, 1957.

(1957) Journal of Research of the National Bureau of Standards Vol. 60, No. 5, May 1958 Research Paper 2860
(1957),

Effect of Structure on the Thermal Decomposition of Polymers[1]

Leo A. Wall and Roland E. Florin

During recent years a considerable number of theoretical and experimental studies have been published on the kinetics and mechanism of the thermal decomposition of polymers. The treatment of depolymerization as a free-radical chain reaction involving the four basic steps of initiation, propagation, transfer, and termination seems adequate for a fairly complete understanding of the process in a large number of cases. Rate data now available are discussed from this point of view. It is shown that most of the characteristics of the thermal decomposition rate curves are a result of their basic structure and not of trace impurities. The magnitude of the rates and activation energies are, however, sensitive to trace structures or impurities. It is shown that intermolecular transfer will account for the rate behavior in a large number of polymers. In a relatively few other cases intramolecular transfer is indicated to be of more importance.

1. Introduction

The hydrolytic degradation of polymers that are bonded by functional groups has been studied for a long time. For example, the mechanism of degradation of cellulose by dilute acid appears to be an attack of the reagent upon functional groups located at random. The kinetics of this type of random or near-random degradation are now well known [1].[2] Incidental to this mechanism are a very sharp initial drop in molecular weight of the polymers and the appearance of very little monomer until very late in the reaction.

In contrast, the degradation of vinyl polymers by heat shows a much wider variety of phenomena. The initial drop in molecular weight may be sharp or negligible, and the yield of monomer may be very small or nearly 100 percent. If monomer is formed, it usually is found even at the start of the reaction. In some cases, e. g., vinyl chloride, the main reaction observed is a stripping of side groups (here H and Cl atoms), leaving the carbon skeleton nearly intact. This stripping reaction [2,3] will not be considered further here.

There is fairly general agreement that the phenomena of most pyrolytic degradations of vinyl polymers require a free-radical chain mechanism. Several authors have developed special theories along this line [4,5]. A comprehensive theory was developed in several papers by Simha, Wall, and Blatz [6,7,8].

The necessary reaction steps, according to this scheme, are

(1) *Initiation.*

$$\sim\!\!\sim CHX{-}CHY{-}CHX{-}CHY\sim\!\!\sim \xrightarrow{k_1} \sim\!\!\sim CHX{-}CHY\cdot + \cdot CHX{-}CHY\sim\!\!\sim.$$

Modifications may involve end-groups, peroxidic fragments, etc.

(2) *Propagation.*

$$\sim\!\!\sim CHX{-}CHY{-}CHX{-}CHY\cdot \xrightarrow{k_2} \sim\!\!\sim CHX{-}CHY\cdot + CHX{=}CHY.$$

This is the reverse of the propagation step in free-radical polymerizations.

(3) *Transfer.*

$$\sim\!\!\sim CHX{-}CHY\cdot + \sim CHX{-}CHY{-}CHX{-}CHY\sim\!\!\sim \xrightarrow{k_3} \sim\!\!\sim CHX{-}CHYH + \sim\!\!\sim CHX{-}CHY\cdot + CHX{=}CY\sim\!\!\sim$$

The relative importance of transfer is a principal distinction from the mechanism of polymerization and also from some other theories of degradation. An internal transfer is also possible:

$$\sim\!\!\sim CHX{-}CHY{-}CHX{-}(CHY{-}CHX)_n{-}CHY\cdot \xrightarrow{k_3'} \sim\!\!\sim CHX\cdot + CHY{=}CX{-}(CHY{-}CHX)_n{-}CHYH.$$

Internal transfer can be treated formally as a special variety of propagation.

(4) *Termination.*

$$\sim\!\!\sim CHX{-}CHY\cdot + \cdot CHY{-}CHX\sim\!\!\sim \xrightarrow{k_4} \sim\!\!\sim CX{=}CHY + CHYH{-}CHX\sim\!\!\sim$$

With the usual steady-state assumption, the rate equations can be solved in general, and solutions have been published for some extreme cases [6, 7, 8]. For intermediate cases, the labor of computation appears formidable.

It was necessary to consider the effects of the usual experimental procedure of conducting the pyrolysis in an open system, with continual volatilization of all products lying below some minimum molecular weight. The corresponding minimum degree of polymerization (DP) is denoted as L. The principal results are the appearance in some cases of an initial rate of volatilization and a maximum in the curve of rate against percent volatilized, both of which are greater the higher the limiting molecular weight for volatilization [7].

[1] This paper was presented in part before the 126th meeting of the American Chemical Society, September 1954.
[2] Figures in brackets indicate the literature references at the end of this paper.

The present results of theory can be surveyed in terms of several kinetic parameters:

$$\text{Reduced time, } \tau = k_1 t,$$

$$\text{Initial degree of polymerization} = N/2,$$

Transfer constant, σ, =

$$\frac{\text{probability of transfer}}{\text{probability of initiation}} = k_3 R/_1,$$

where R has its usual meaning of radical concentration.

Approximate "zip" length, Z, $(1/\epsilon - 1)$,

$$= \frac{\text{probability of propagation}}{\text{probability of termination} + \text{transfer}},$$

$$= k_2/k_4 R(1+\sigma/2) \text{ for random initiation,}$$

$$= k_2/k_4 R\,[1+\sigma/2(N-1)] \text{ for end initiation.}$$

The zip represents that part of the kinetic chain length confined to the depropagation within a single molecule. It is analogous to the degree of polymerization in addition polymerization. Both become the actual kinetic chain length when transfer is absent.

The salient features of the theory are shown in figure 1, in which results for the extreme cases are compared. For all curves, σ is taken as zero. Nevertheless, the probable effect of transfer can be pointed out. In the figure the theoretical values for the rate of volatilization and for the relative degree of polymerization, both plotted as a function of conversion, are given for certain extreme cases. The values of the zip lengths are shown on the curves. From this figure one can compare the monomer yield, the rate of conversion, and the DP behavior for any combination of random- and end-initiation reactions with large or small zip. Regardless of method of initiation, large zip goes with a linearly decreasing rate curve, while the molecular weight curves are initially horizontal and above the diagonal. With random initiation and zero zip the rate and DP curves are those for simple random decomposition, the rate showing a maximum and the DP coinciding almost exactly with the axes of the ordinates and the abscissas. With end initiation zero zip produces a horizontal rate curve and a diagonal DP curve. Unless transfer occurs, end initiation cannot produce DP curves that drop below the diagonal. Introduction of transfer would tend to push the curves toward the random curves, i. e., those for the case of random initiation and zero zip. In this paper it will be seen, qualitatively at least, that molecular structures favorable for transfer reactions to occur on thermal decomposition give low monomer yields [9] and generally exhibit maximum-type rate curves.

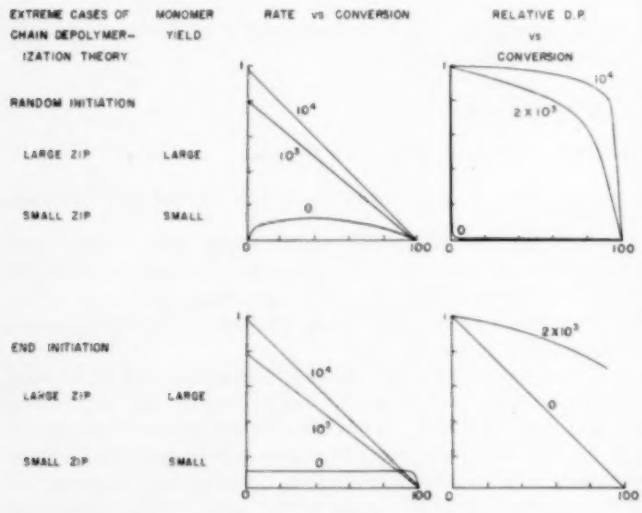

FIGURE 1. *Theoretical results for extreme cases of the depolymerization theory.*

Zip length values, $(1/\epsilon - 1)$, are shown on curves. N=1,000, σ=0, and L=4, for all curves. For curves, zip=0, rate is multiplied by factor of 100 for random initiation and by 50 for end initiation. The conversion is represented by the abscissa for all curves shown.

2. Discussion of Experimental Results

Over several years a large number of polymers have been pyrolyzed, and it is now interesting to apply the theory as far as possible in interpreting the experimental results. The experimental details and data referred to are those of Madorsky and coworkers [10]. Because changes in molecular weight were followed in only a few instances, they will not be discussed here. The basic data consist of volatilization as a function of time and also the composition of volatile products. From these data are derived curves of rates of volatilization versus percent conversion, and also activation energies and monomer yields. During the first few percent of reaction there is an uncertainty in the experimental data due to the time necessary for the sample to reach constant temperature. For this reason, the initial region of a curve should probably be given less weight when either the temperature, the rate of decomposition, or both are very high.

The volatilization curves of Madorsky et al were used unaltered when the experimental points were numerous and closely spaced. From plots of conversion to volatiles, c, against time, t, Madorsky takes $\Delta c/\Delta t$ for adjacent points as the rate dc/dt, and the average conversion, $C+\Delta C/2$, as the conversion. This has the advantage of exhibiting and even somewhat enlarging the scatter of experimental data. Where experimental points were less closely spaced, the data were plotted in a different manner, designed to secure the best empirical smooth curve. The plot of C versus t was roughly fitted to an arbitrary function, $C=a+bt$, or $C=ae^{-bt}$. For given values of t, the difference of ordinates, C (experimental) minus C (algebraic), was taken numerically to a sufficient number of decimal places. This relatively small difference C' was plotted against t, and the derivative dC'/dt taken graphically. For a given t the rate dC/dt was taken as dC/dt (algebraic) $+dC'/dt$, and the conversion C as C (algebraic) $+C'$. It is evident

that graphical errors and the exercise of judgment are concentrated in the relatively small and meaningless difference functions. No method gave satisfactory results in the initial part of the pyrolysis of one methyl methacrylate sample, where, because of the very rapid rate, few experimental points were secured until after a sudden change had taken place in the rate. The curves of rate versus conversion are shown in figures 2 to 6.

The polymers may be classed chemically as in table 1. For each polymer the monomer yield and activation energy for decomposition are also listed.

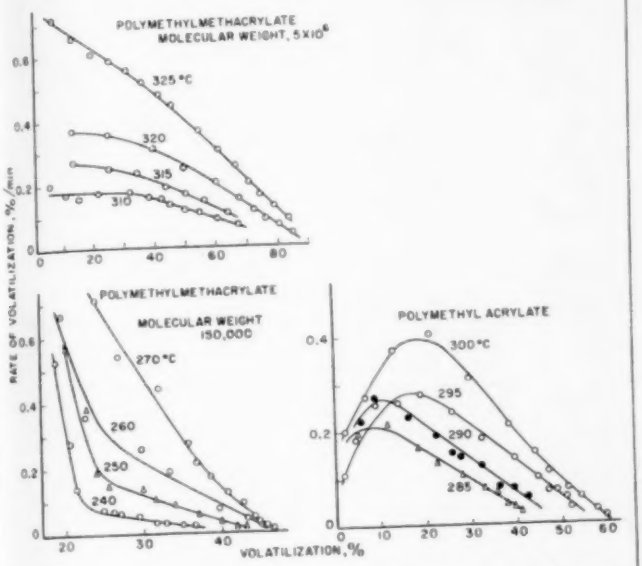

FIGURE 2. *Volatilization rates for polymers of methyl methacrylate and methyl acrylate* [10].

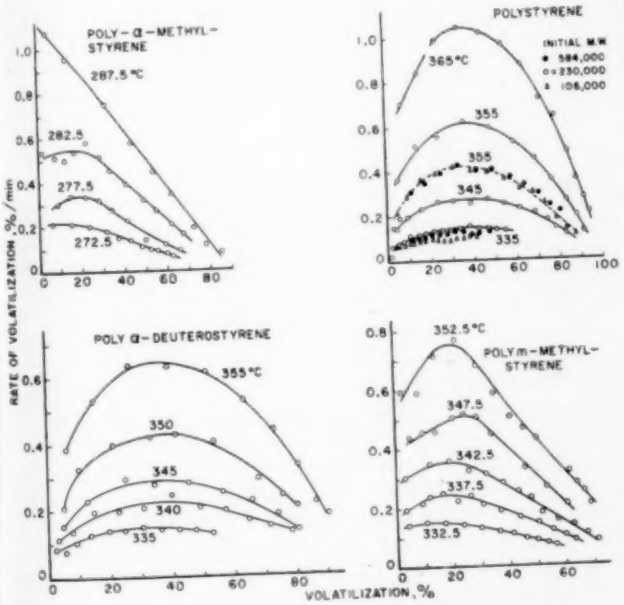

FIGURE 3. *Volatilization rates for the styrene family of polymers* [10].

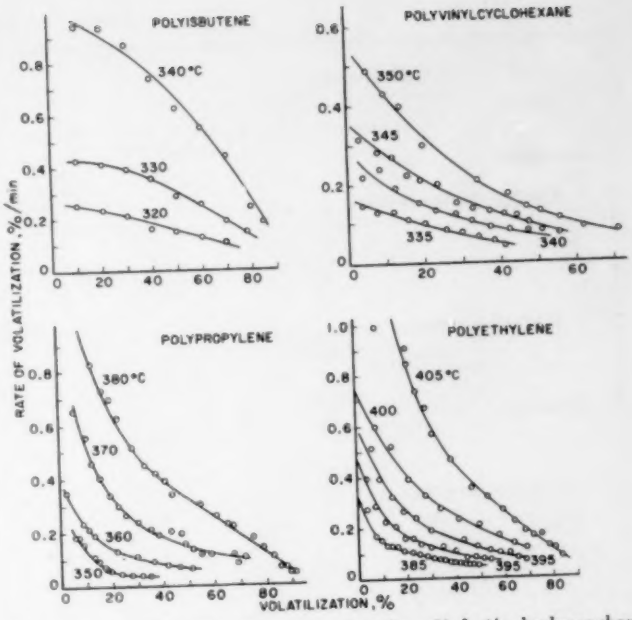

FIGURE 4. *Volatilization rates for the aliphatic hydrocarbon polymers* [10].

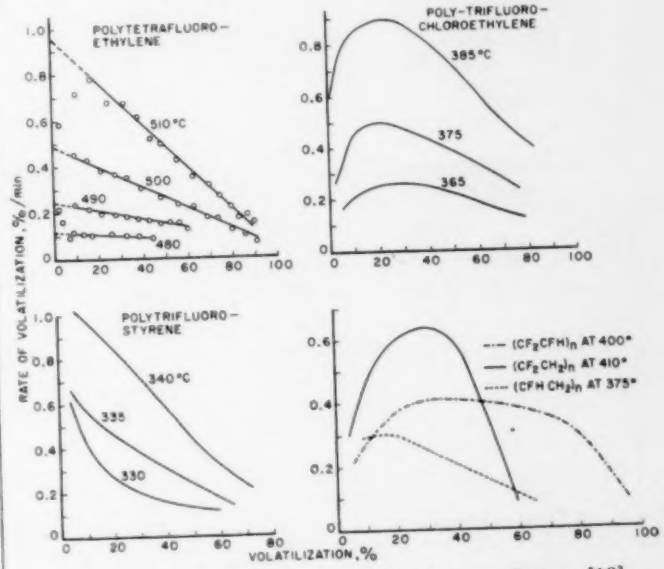

FIGURE 5. *Volatilization rates for fluoro polymers* [10].

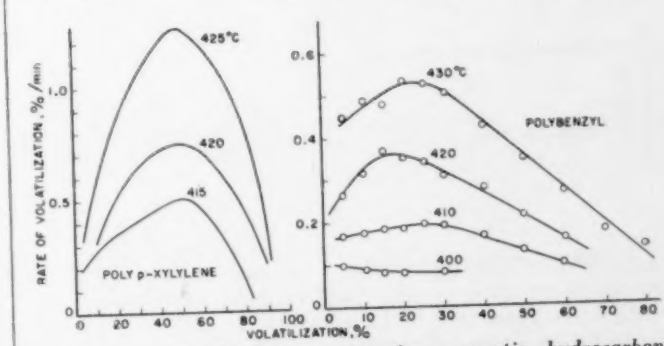

FIGURE 6. *Volatilization rates for aromatic hydrocarbon polymers* [10].

TABLE 1. *Pyrolysis of polymers*

Polymer	Structure	Monomer yield	Activation energy	Rate at 350° C
Acrylates:		*wt %*	*kcal*	*wt %/min*
Methyl methacrylate	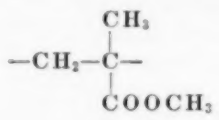	>95	55 to 32	5. 2 to 220
Methyl acrylate	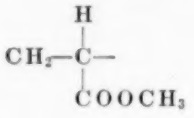	2	37	~10
Styrenes:				
α-Methylstyrene	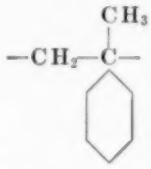	>95	58	228. 0
α-Deuterostyrene	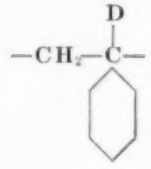	70	58	0. 268
m-Methylstyrene	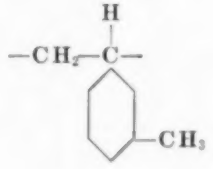	52	59	. 900
Styrene	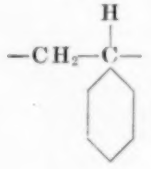	42	58	. 235
β-Deuterostyrene	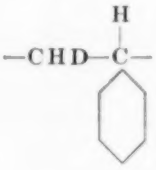	42	.....	.....
Aliphatic hydrocarbons:				
Isobutylene	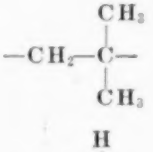	≈20	52	2. 4
Propylene	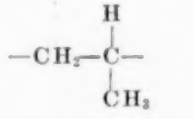	2	61	0. 069
Ethylene (linear) (polymethylene)	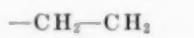	0. 1	70	. 004

TABLE 1. *Pyrolysis of polymers*—Continued

Polymer	Structure	Monomer yield	Activation energy	Rate at 350° C
		wt %	*kcal*	*wt %/min*
Aliphatic hydrocarbons—Continued				
Ethylene (branched)	$-CH_2-CH_2$	.025	70	.008
Vinyl cyclohexane	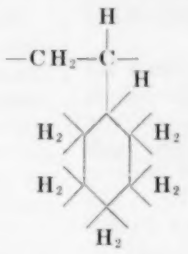	≈.1	52	.450
Fluorocarbons:				
Tetrafluoroethylene	$-CF_2CF_2-$	>95	80	2×10^{-6}
Trifluorostyrene	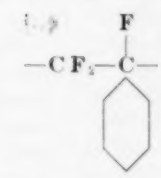	75	67	2.4
Trifluorochloroethylene	$-CF_2CFCl-$	28	66	0.044
Trifluoroethylene	$-CF_2CFH-$	<1	53	.046
Vinylidene fluoride	$-CF_2CH_2-$	<1	------	------
Vinyl fluoride	$-CH_2CHF$	<1	------	------
Aromatic chains:				
p-Xylylene		0 (?)	76	.002
Benzyl	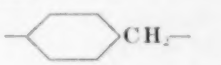	0	53	.006
Phenyl		0	------	------

2.1. Monomer Yields

The occurrence of transfer, either inter or intra, offers a chance of forming nonmonomeric material and should, therefore, reduce the monomer yield. It would seem plausible that if one type of transfer occurred in a given system, the other would also occur to some degree. It is also likely that a small amount of intermolecular transfer would be more noticeable on the DP changes than on the monomer yield. From experience with small molecules, tertiary hydrogen atoms are especially readily removed in a transfer reaction. Experience with chain transfer in polymerization suggests that chlorine atoms are also vulnerable. Transfer will be favored by active radicals, and less likely with resonance-stabilized or sterically hindered radicals. The higher monomer yields in the various chemical classes are experienced with the structures

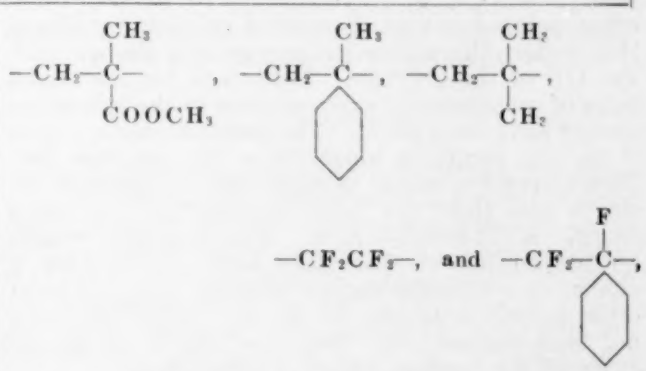

which are all devoid of tertiary hydrogen. The importance of location in the tertiary position is shown further by the comparison of α-deuterostyrene with β-deuterostyrene [12]. Substitution of tertiary H by D reduces transfer and raises monomer yield

from 42 to 70 percent, whereas substitution of a methylenic β-hydrogen has no marked effect. The lower monomer yield of polytrifluorochloroethylene is considered to be related to the vulnerability of the Cl atom to transfer.

The class of styrenes all show relatively high monomer yields. Although transfer is favored by the tertiary hydrogens present in most members, it is presumably lessened because of the relatively stable radicals involved.

Polymers of the aliphatic hydrocarbon class all show relatively low monomer yields even when tertiary hydrogen is absent. The activity of the alkyl radicals appears to compensate for the lack of tertiary hydrogens. As some estimates give a reactivity ratio of tertiary/primary of only 10/1, the compensation required is not great. Vinyl cyclohexane has a multitude of secondary hydrogens on the cyclohexyl group, as well as the tertiary hydrogen. Nevertheless, the order of monomer yield increased with methyl substitution. Substituent groups act in at least two ways: (1) by blocking specific positions and (2) by activating specific positions and weakening the main chain, thus affecting the temperature of decomposition and indirectly the rate of transfer. In general, with the exception of polytetrafluoroethylene, higher temperature of decomposition is associated with low monomer yield, which is due to more transfer.

2.2. Activation Energies

The activation energy for initiation E_1 is the largest, but not always the only important, contribution to the over-all activation energy. The activation energy for propagation is not as low as in polymerization because it will be at least as large as the thermochemical heat of polymerization, usually 10 to 20 kcal per mole of monomer. For methyl methacrylate the over-all energy of activation varies from 32 to 55 kcal, depending on the molecular weight and history of the polymer. This is an indication that initiation sometimes occurs at particular labile groups, the nature of which depends upon the polymerization catalyst and similar details. However, an important effect pointed out on theoretical grounds by Simha [13] is that the activation energy will change with the DP of the polymer. Equations for the initial rates of volatilization and variation in the activation energy have been given. The essential point is that if the zip length is longer than the polymer DP, then activation energy is equal to E_1, whereas if the zip is less than the polymer DP, the activation energy is $E_1/2+E_2-E_4/2$. Experimental results on polymethyl methacrylate have shown such a change in activation energy with DP [14]. In most other polymers, studies of the rate versus DP have not been carried out. Therefore, the detail significance of the energies reported is not clear.

Except for the acrylate class the activation energies are often not very far below the usual carbon-carbon bond strength of 80 kcal, and may reflect initiation by a random break of a carbon-carbon bond. The highest activation energies are found for tetrafluoroethylene, 80 kcal, and ethylene, 70 kcal. Substitution in the chain lowers the activation energy. There is a regular sequence 70, 61, 52 for ethylene, propylene, and isobutylene, respectively; but among the styrenes the extra methyl of α-methylstyrene seems to have no effect.

2.3. Rates of Volatilization

The method of plotting experimental data has varied considerably in the literature. In order to illustrate the situation, especially with regard to random decomposition, figure 7 shows theoretical curves for over-all random decomposition (solid-line curves). They show random theory when plotted as rate in percentage of original material (lower curve) and rate in percentage of material remaining at the various stages (upper curve). Because experimental data often scatter to some degree, it is evident that when points at low conversion are given little weight, straight lines such as the dashed lines in the figure, may fit the experimental data very well.

With curves such as the theoretical ones, true initial points are practically impossible to measure. Final points are likewise impossible to measure both because of the shape of the curves and because in practice no reaction is 100 percent pure. Thus, curves of the upper type tend to drop, as indicated by the dotted curve in upper right of figure, because there is invariably a finite residue of carbon or ash. It is evident that the maximum-type plot and the use of the maximum rate should give the best esti-

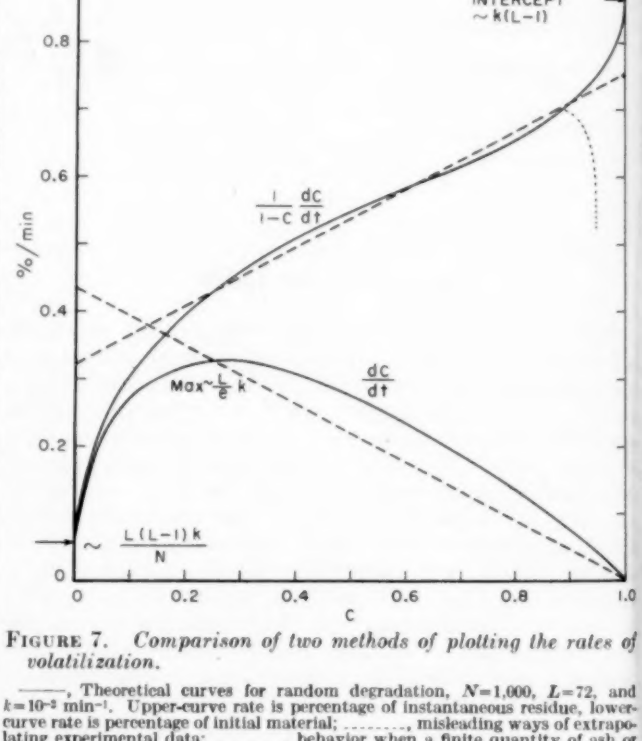

FIGURE 7. *Comparison of two methods of plotting the rates of volatilization.*

———, Theoretical curves for random degradation, $N=1{,}000$, $L=72$, and $k=10^{-2}$ min^{-1}. Upper-curve rate is percentage of instantaneous residue, lower-curve rate is percentage of initial material; ·····, misleading ways of extrapolating experimental data; . . . . ., behavior when a finite quantity of ash or residue is present.

mates of rate constant and the activation energy. A knowledge of L, which is the DP of the smallest molecule that decomposes in order to volatilize, is required for precise evaluation of the defined rate constant, k. The value of L is easily estimated from product analysis. Fortunately, activation energies taken by the use of the initial points of the dashed lines cannot be greatly in error. However, rates obtained in this manner have doubtful significance and obscure the elucidation of the actual mechanism. In this article all rates plotted are in units of weight percent of original sample per minute, dC/dt. Thus a significant comparison can be made.

Except for the hydrocarbon polymers in figure 4 the rate curves in figures 2, 3, 5, and 6 show that maximum-type rate curves appear when the structure allows transfer, and this effect coincides with low monomer yield. It is evident, qualitatively at least, that intermolecular transfer affords the most general mechanistic explanation of the results. There are, however, many unexplained features. At the lower temperatures the distinction between the various curves diminishes. This is believed to be a result of the larger importance of diffusion at these temperatures. Therefore, in this discussion, the greatest weight is placed on the curves obtained at the highest temperature in each case.

The rate curves for polyisobutylene, polypropylene, polyvinyl cyclohexane, and polyethylene all show no maxima, although none give very high monomer yields. All yields are lower than that of monomer from polystyrene. However, it has been previously shown experimentally that the absence of a maximum in the rate of pyrolysis of polyethylene is due to the presence of branching [15]. When linear samples of polymethylene made from diazomethane are pyrolyzed, maximum-type curves are produced [15]. Commercial linear polyethylene and polyamides also give rate curves with maxima very similar to that for random theory [11].

Theoretical treatment of the degradation of branched structures on a statistical basis and the use of various ratios for the rate constant for breaking bonds at and near the branched points versus those between branched points could not eliminate the maximum in the rate curves without going to unreasonable values for the ratios of constants for bond cleavage [16]. The situation is, then, that the low monomer yield indicates transfer, whereas the rate curves for these hydrocarbon polymers suggest long zip lengths, and the branch structure with a statistical type of treatment does not produce other than maximum-type curves. The only readily apparent alternative is that intramolecular transfer predominates. In polymers of isobutene, vinyl cyclohexane, propylene, and branched polyethylene the structure must favor an internal isomerization such as that used by Kossiakoff and Rice [17] in order to fit with theory the thermal decomposition results of relatively small aliphatic hydrocarbons. Their isomerization is essentially the same process as the first part of our intramolecular transfer. For polyisobutylene it is suggested that the following process of radical isomerization, followed by cleavage, i. e., intramolecular transfer, occurs to an appreciable extent;

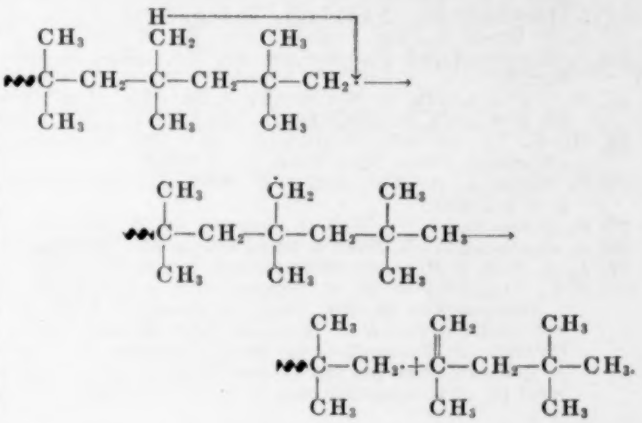

The formation of the neopentyl radical would occur if the isomerized radical cleaves by the alternate path available. Neopentane is found in the pyrolysis of polyisobutene in an amount of 2 weight percent of the polymer decomposed. Intramolecular transfer is not limited to only the process depicted, but is assumed to occur in such a manner as to produce trimer, tetramer, etc., and other products, as well as the dimer depicted. An interesting point in this mechanism is that usually the depropagating radical is assumed to be the one where the odd electron is located on the carbon with the substituents. Here the primary and more active radical appears to be the most likely intermediate. Consideration of models suggests that the tertiary radical would have little chance of reaction except by disproportionation and depropagation.

In the polyethylene studied, branches must also effectively lead to greater kinetic zip lengths by increasing the probability of intramolecular transfer at the expense of intermolecular transfer. The polypropylene that was used was prepared with $AlBr_3$-HBr as catalyst and is probably highly branched [18]. A study of linear polypropylene would be desirable to establish whether branches are responsible for the nonexistence of a maximum here.

3. Conclusions

On qualitative grounds it is evident that the pyrolytic behavior of polymers studied is a result of their basic structure and not of trace impurities or structures, at least within certain limits. Furthermore, the degree of intermolecular transfer is a deciding factor, and occurs to a significant extent in a large number of polymers. On the other hand, it is apparent that the ratio of inter- to intramolecular transfer is quite sensitive to detailed molecular structure. The exact evaluation of inter- versus intramolecular transfer will require extensive investigation of products, rate and DP versus conversion, and the dependence of the latter two quantities on the initial molecular weight.

4. References

[1] L. F. McBurney, Cellulose and cellulose derivatives, part I, p. 99, edited by Emil Ott et al., (Interscience Publishers, Inc., New York, N. Y., 1954).
[2] R. F. Boyer, J. Phys. Colloid Chem. **51**, 80 (1947).
[3] N. Grassie, Trans. Faraday Soc. **48**, 379 (1952); **49**, 835 (1953).
[4] N. Grassie and H. W. Melville, Proc. Roy. Soc. (London) [A] **199**, 1, 14, 24, 39 (1949).
[5] H. H. G. Jellinek, Degradation of vinyl polymers, (Academic Press, New York, N. Y. 1955).
[6] R. Simha, L. A. Wall, and P. J. Blatz, J. Polymer Sci. **5**, 615 (1950).
[7] R. Simha and L. A. Wall, J. Polymer Sci. **6**, 39 (1951).
[8] R. Simha and L. A. Wall, J. Phys. Chem. **56**, 707 (1952).
[9] L. A. Wall, J. Research NBS **41**, 315 (1948) RP1928.
[10] S. L. Madorsky et al., J. Polymer Sci. **9**, 133 (1952); J. Polymer Sci. **11**, 491 (1953); J. Research NBS **40**, 417 (1948) RP1886; J. Research NBS **42**, 499 (1949) RP1989; J. Research NBS **51**, 327 (1953) RP2461; J. Research NBS **53**, 361 (1954) RP2553; J. Research NBS **55**, 223 (1955) RP2624.
[11] S. Straus and L. A. Wall, J. Research NBS **60**, 39 (1958) RP2819.
[12] L. A. Wall, D. W. Brown, and V. E. Hart, J. Polym. Sci. **15**, 157 (1955).
[13] R. Simha, J. Polymer Sci. **9**, 465 (1952).
[14] S. Bywater, J. Phys. Chem. **57**, 879 (1953).
[15] L. A. Wall, S. L. Madorsky, D. W. Brown, S. Straus and R. Simha, J. Am. Chem. Soc. **76**, 3430 (1954).
[16] R. Simha, J. Chem. Phys. **24**, 796 (1956).
[17] A. Kossiakoff and F. O. Rice, J. Am. Chem. Soc. **65** 590 (1943).
[18] C. M. Fontana, Cationic polymerization and related complexes, p. 121, edited by P. H. Plesch, (W. Heffer and Sons Ltd., Cambridge, England, 1953).

Washington, October 15, 1957.

Journal of Research of the National Bureau of Standards Vol. 60, No. 5, May 1958 Research Paper 2861

Comparison of Theoretical and Empirical Relations Between the Shear Modulus and Torsional Resonance Frequencies for Bars of Rectangular Cross Section

Sam Spinner and Rudolph C. Valore,[1] Jr.

The relations between the modulus of elasticity in shear and the fundamental torsional resonance frequency, mass, and dimensions for bars of rectangular cross section have been evaluated experimentally. The empirical relation was found to be less than the theoretical approximation given by Pickett by an amount increasing to about 1 3/4 percent as the crosssectional width to depth ratio of the bars approached 10.

In addition to the fundamental torsional resonance frequency, the first overtone of the specimens was also determined. The overtone was found not to be an exact multiple of the fundamental; it increased more than 5 percent over double the value of the fundamental as the width to depth ratio increased to 10.

1. Introduction

The exact relation between the modulus of elasticity in shear and the torsional resonance frequency for bars of various cross-sectional shapes is of considerable practical as well as theoretical importance. For certain cross-sectional shapes, including circular and square, the relations for the shape factors involved in determining the shear modulus from the angular deformation have been rigorously developed.[2] Consequently, it is possible to derive an exact expression for the shear modulus as a function of the torsional resonance frequency for these shapes, as is done by Pickett.[3] For a rectangular cross section, however, the situation is not so satisfactory. For this cross section, Roark gives a simplified equation for the shape factor which, he states, involves an approximation resulting in an error not greater than 4 percent. Pickett's shear modulus-torsional frequency equation for this shape, based on Roark's equation, is therefore also approximate, as Pickett notes. Cady [4] also gives an approximate equation relating the shear modulus to the torsional frequency for rectangular bars. It will be shown later that Pickett's and Cady's equations, although different in appearance, lead to essentially the same numerical results.

This lack of a more exact expression for bars of rectangular cross section is unfortunate. This shape of bar can be easily fabricated for most materials and, in addition, lends itself to the experimental excitation of torsional vibration more easily than other simple shapes. Indeed, it is sometimes the only simple shape for which this can be accomplished.

Modern refinements in the sonic method permit the determination of resonance frequencies to a high degree of accuracy (see section 3.3). It would be desirable, then, to develop a relationship between the torsional resonance frequency and the shear modulus that would be comparable in accuracy with the determination of the resonance frequency itself. The main purpose of this paper is to establish such a relationship empirically and to compare this empirical relationship with the approximate theoretical ones given by Pickett and Cady. From here on, since only torsional resonance frequencies are discussed, the term "resonance frequency" always refers to the torsional resonance frequency.

2. Theory

The general form of the relationship between the shear modulus and the resonance frequency is given by Pickett as follows:

$$G=Bmf^2, \tag{1}$$

where m is the mass of the specimen in grams, f is the resonance frequency in cps, and G is the shear modulus in dynes/cm^2 (G is often given in kilobars, where 10^9 dynes/cm^2=1 kilobar). B, in cm^{-1}, is related to the shape in the following manner:

$$B=\frac{4lI_p}{n^2aK}, \tag{2}$$

where [5]

l=length (cm),
a=cross-sectional area,
n=the order of vibration (for the fundamental $n=1$, first overtone $n=2$, etc.),
I_p=polar moment of inertia of cross-sectional area,[6]
K=shape factor for same cross section (see footnote 2).

[1] Present address, Texas Industries, Inc., Dallas, Tex.
[2] See, for instance, Raymond J. Roark, Formulas for stress and strain, p. 166, 2d ed. (McGraw-Hill Publishing Co., Inc., New York, N. Y., 1943).
[3] Gerald Pickett, Equations for computing elastic constants from flexural and torsional resonant frequencies of vibration of prisms and cylinders, Am. Soc. Testing Materials, Proc., **45**, 846 (1945).
[4] Walter Guyton Cady, Piezoelectricity, p. 114, 1st ed. (McGraw-Hill Publishing Co., Inc., New York, N. Y., 1946).
[5] The cgs system used in this paper eliminates g, the acceleration of gravity from the denominator of the right-hand side of eq (2), making the values for B, and hence G, independent of this factor. Conversion from kilobars to psi's may be accomplished by means of the equation

Kilobars×14.5038×10^3=psi.

The conversion factor assumes a value of g=980.66 cm/sec^2.
[6] See pages 10 and 68 of reference in footnote 2.

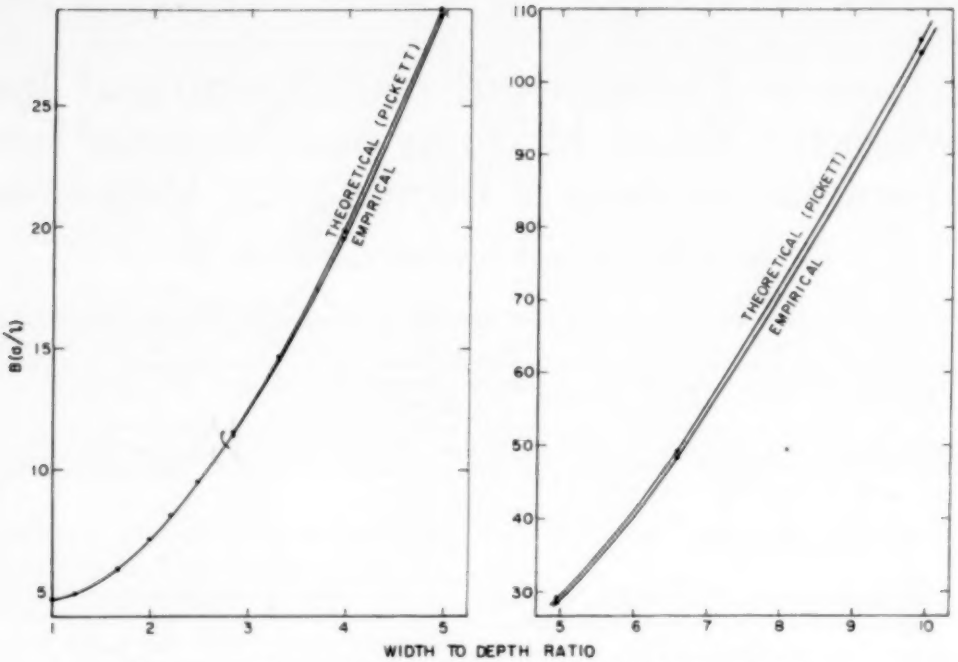

FIGURE 1. *Comparison of theoretical and empirical values of $B(a/l)$.*

The ratio I_p/K, designated as R, is exactly equal to 1.0 for a circular cross section. For a square cross section $R=1.185+$. The value of R for a square cross section is based on Roark's rigorous solution for the shape factor and is accurate to the number of places given. For a rectangular cross section, the following approximate expression for R is given:

$$R=\frac{\left(\frac{w}{d}\right)+\left(\frac{d}{w}\right)}{4\left(\frac{d}{w}\right)-2.52\left(\frac{d}{w}\right)^2+0.21\left(\frac{d}{w}\right)^6}. \tag{3}$$

It should be noted that the approximation given by Roark for K for a rectangular cross section does not reduce to the exact expression for a square cross section. For this reason, the value of $R=1.183$, given by Pickett for a square cross section and obtained by substituting $(w/d)=1$ in eq (3), is lower than the exact value of $R=1.185$ obtained by using Roark's exact expression for the shape factor for a square cross section.

The calculation of the factor, B, in eq (1), has been simplified by means of the following procedure:

If only the fundamental is considered $(n=1)$, eq (2) may be rewritten as

$$B\frac{a}{l}=4R. \tag{2a}$$

R has been calculated for about 30 values of w/d from 1 to 10, using eq (3). Substituting these values of R in eq (2a), corresponding values of $B(a/l)$ have been computed. These are plotted as the upper curve of each section of figure 1. From this graph, it is possible to determine $B(a/l)$ and, consequently, B as a function of w/d, thus eliminating the cumbersome computation of R by eq (3).

The equation given by Cady for the relation between resonance frequency and G has the form

$$f=\frac{Adn}{l\sqrt{w^2+d^2}}\sqrt{\frac{G}{\rho}}, \tag{4}$$

where ρ=density in g/cm^3, A is a shape factor different from K, and other symbols have the same significance and units as in previous equations. Then

$$G=\frac{l(w^2+d^2)}{A^2d^3wn^2}mf^2. \tag{4a}$$

Let

$$B=\frac{l(w^2+d^2)}{A^2d^3w}$$

and

$$n=1,$$

then

$$B\frac{a}{l}=\frac{1}{A^2}\left[\left(\frac{w}{d}\right)^2+1\right], \tag{5}$$

where $A^2=3K_1$. Values for K_1 are given by Timo-

shenko and Goodier.[7] Table 1 gives the values of $B(a/l)$ from Pickett's and Cady's equations for comparison.

TABLE 1. *Values of B (a/l) from Pickett's and Cady's equations*

w/d	$B(a/l)$	
	Pickett	Cady
1.0	4.734	4.742
1.2	4.92	4.90
1.5	5.55	5.53
2.0	7.27	7.28
2.5	9.66	9.71
3.0	12.66	12.67
4.0	20.17	20.17
5.0	29.71	29.78
10.0	107.8	107.9

The values of $B(a/l)$ are seen to be in good agreement. Cady states that his equation loses accuracy for $(w/d)<3$.[8] However, for $w/d=1$, Cady's value of $B(a/l)=4.742$ is identical with the one based on Roark's rigorous expression for the shape factor. This value is believed to be more accurate than the corresponding one from Pickett in table 1.

3. Experimental Approach

3.1. Specimens

Specimens consisted of 12 steel bars of rectangular cross section, all cut from the same stock. All of the specimens were ground to the same length (15.202 cm) and, with one exception, to the same width (3.143 cm), while the depths were varied so that the ratio of width to depth, w/d, ranged from about 10 to 1. The one exception was the specimen of square cross section, which was 3.150 by 3.150 cm. The dimensions of all specimens were uniform to 0.001 cm. Width over depth ratios for all specimens are to be found in column 2 of table 3.

Inasmuch as the evaluation of G required that the mass as well as the dimensions of the specimens be known, the necessary data to calculate the density was available. This served as an internal check on the homogeneity of the specimens and the consistency of the data. The average value of the density of the 12 specimens was found to be 7.814 g/cm³ with an extreme variation of ± 0.003 and standard deviation of about 0.002.

3.2. Procedure

The fundamental and first overtones of the resonance frequencies of the specimens were determined by a sonic method, taking advantage of certain refinements previously described.[9] These refinements are briefly summarized as follows:

1. Reading the resonance frequency on a frequency counter.

2. Probing with the pickup by hand to establish clearly the mode of vibration at resonance.

3. Supporting the specimens on foam rubber at the nodal points and driving them with a tweeter-type speaker coupled through the air. This method of support and driving provides virtually zero coupling to the driving system, with specimens of the size and mass used here, and results in the truest natural resonance frequencies of the specimens.

An alternate method of driving the seven lighter specimens was also used. In this method, the specimens were suspended from cotton threads, one thread being hung from the pickup and the other thread was hung from a magnetic record-cutting head, which replaced the speaker as the driving unit. The torsional frequencies were obtained by tying the string at opposite edges of the specimen, as shown in the sketch in figure 2. Table 2 lists the fundamental, $f_{n=1}$, and first overtones, $f_{n=2}$, of the resonance frequencies of all the specimens.

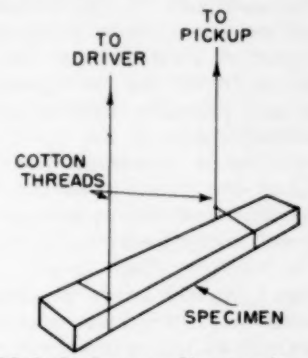

FIGURE 2. *Method of suspending specimen for torsional vibrations.*

TABLE 2. *Fundamental and first overtones of the resonance frequencies of all specimens*

Specimen	Fundamental, $f_{n=1}$ (cps)	First overtone, $f_{n=2}$ (cps)	$\left[\frac{f_{n=2}}{f_{n=1}}-2\right]\times 100$
			%
1	9797	19585	−0.0927
2	9584	19160	−.084
3	8725	17465	+.17
4	7958	15966	.63
5	7477	15025	.95
6	6920	13939	1.43
7	6294	12709	1.92
8	5589.1	11333	2.77
9	4822.2	9789	3.19
10	3981.4	8115	3.84
11	3069.3	6268	4.23
12	2091.3	4289.1	5.12

3.3. Accuracy

The over-all damping of the entire system, consisting of specimen, driver, pickup, and coupling mechanism, was so small that the accuracy of the resonance frequency measurements approached the accuracy of the frequency counter. This is 1 cycle for the 1-sec gate of the counter, and 0.1 cycle, using

[7] S. Timoshenko and J. N. Goodier, Theory of elasticity, p. 277, 2d ed. (McGraw-Hill Publishing Co., Inc., New York, N. Y., 1951).

[8] Both Roark's and Cady's equations appear to be approximations based on a power-series expansion given by Timoshenko and Goodier, p. 278, eq (160).

[9] Sam Spinner, Elastic moduli of glasses by a dynamic method. J. Am. Ceram. Soc. **37**, 229 (1954).

the 10-sec gate. Generally, the 1-sec gate was sufficient for the specimens of low value of w/d, i. e., those having a high resonance frequency, whereas the 10-sec gate was used for specimens having high values of w/d (low resonance frequency). An additional small source of error is introduced by the coupling mechanism. For those specimens vibrated by the suspension method, it was found that although the resonance frequencies were reproducible up to the maximum accuracy of the counter for any particular given position of the threads on the specimen, nevertheless, the fundamental resonance frequencies were found to vary by about 2 cycles, depending on whether the threads were placed near or far from the nodes; the highest values resulted when the threads were nearest the nodes.[10] The frequencies obtained by driving through air (given in table 2) were usually intermediate between the highest and lowest values for the suspended specimens. In general, the bulkier the specimens, the less the measured resonance frequencies were affected by the mode of coupling or the position of the supports. The accuracy of the fundamental resonance frequencies, then, was estimated to range from about 1 part in 2,000 for the flattest specimen to about 1 part in 10,000 for the square specimen.

To evaluate any possible effect of air damping on the resonance frequencies of the specimens, some of the flatter bars were vibrated, both in air and, without changing the position of the fibers, also in vacuum, using the suspension method. The resonance frequencies were found to be about 1 part in 6,000 higher in vacuum than in air. Because this variation is less than the error in measurement for the flatter specimens, it was not considered sufficient to justify vibrating all the specimens in this manner.

[10] The entire problem of these small variations in measured resonance frequencies with differences in suspension position requires further study. For lighter and smaller specimens than those used in this investigation, the suspension method yields even more reliable results than does the method of air coupling. Also, for the most accurate results, specimens should be vibrated in vacuum (see next paragraph of text). The suspension method is easily adapted to this. For flexural vibrations, in contrast with torsional, the highest frequencies are obtained when the supports are placed furthest from the nodes. In all cases it is believed that the truest resonance frequencies are obtained when the driving and pickup fibers are nearest the nodes.

3.4. Calculations

Comparison of the experimental results will first be made with the curve based on Pickett's equation.[4] The empirical (lower) curve shown in figure 2 was obtained in the following manner: For some particular value of w/d say $(w/d)=1$,

$$G=B_1'\frac{l_1}{a_1}m_1f_1^2,$$

where $B'=B(a/l)$ and the subscripts indicate particular values for $w/d=1$. For any other value of w/d, the specimen will have the same value of G, and all the terms on the right-hand side have the subscript 2 thus,

$$G=B_2'\frac{l_2}{a_2}m_2f_2^2.$$

Therefore,

$$\frac{B_2'}{B_1'}=\frac{m_1}{m_2}\cdot\frac{l_1}{l_2}\cdot\frac{a_2}{a_1}\left(\frac{f_1}{f_2}\right)^2. \tag{6}$$

All the members on the right-hand side are known and B_2'/B_1' may be evaluated. Values of this ratio are given in column 3 of table 3.

In order to obtain $B(a/l)$ (experimental) directly as a function of w/d, it is first necessary to select a reliable base value of $B(a/l)$ for some particular value of w/d. It has already been shown that the value of $B(a/l)=4.742$ for $w/d=1$ is believed most accurate. This number then, is selected as the base value for $w/d=1$. Values of $B(a/l)$ (experimental) for higher w/d ratios are then obtained by multiplying this base value by the B_2'/B_2', ratio for the corresponding value of w/d. These are given in column 5 of table 3.

It should be noted that the choice of a base value for $B(a/l)$ (experimental) is somewhat arbitrary. Should it develop that some other value of $B(a/l)$ either at $w/d=1$, or at some other w/d ratio, is more

TABLE 3. *Theoretical and empirical data for rectangular bars of varying w/d ratios*

[Data rounded off to final figure. Calculations are on basis of more significant figures]

Specimen	$\frac{w}{d}$	$\frac{B_2'}{B_1'}$	$B(a/l)$		$\left[\frac{B\frac{a}{l}\text{ (theor.)}}{B\frac{a}{l}\text{ (exp.)}}-1\right]\times 100$	A^2
			Theoretical	Experimental		
1	1	1	4.734	4.742	−0.17	0.4218
2	1.237	1.045	4.973	4.955	+.36	.51065
3	1.650	1.261	5.979	5.981	−.03	.6222
4	1.980	1.516	7.198	7.186	+.17	.6847
5	2.198	1.7175	8.162	8.144	.23	.7160
6	2.473	2.005	9.544	9.505	.40	.7489
7	2.827	2.424	11.563	11.495	.59	.7822
8	3.298	3.074	14.681	14.577	.71	.8148
9	3.957	4.130	19.815	19.583	1.18	.8509
10	4.938	6.060	29.096	28.734	1.26	.8834
11	6.586	10.198	49.068	48.352	1.48	.9177
12	9.908	21.959	105.90	104.12	1.71	.9524

accurate, then a readjustment could easily be made in column 5, using the more basic data from column 3.

The data in column 5 was obtained without assuming any particular value for G for the specimens, but merely that all the specimens had the same value of G. An alternative method for calculating the data in column 5 may be used if, in addition to assuming that the value of G of all the specimens is the same, a definite value of G is derived for some particular value of w/d. Thus, using $B(a/l)=4.742$ for $w/d=1$, and substituting in eq (1) and (2), leads to a value of 822.1 kilobars for G. Then, resubstituting this value in the same two equations, one obtains the following expression, from which $B(a/l)$ (experimental) for the corresponding w/d values may be calculated,

$$B\frac{a}{l}\text{ (experimental)}=\frac{822.1a}{lmf^2}. \tag{7}$$

Comparison between theoretical and experimental curves can now also be made in terms of A^2, used in Cady's equations. A^2 is evaluated empirically by substituting $B(a/l)$ (experimental) and the corresponding value of w/d in eq (5). The resulting values of A^2 are given in column 7 of table 3 and are plotted as a function of w/d in the upper curve of figure 3. The lower curve in figure 3 is a plot of the factor $3K_2(=A^2$ "theoretical") against the selected values of w/d from Timoshenko and Goodier (given in table 1).

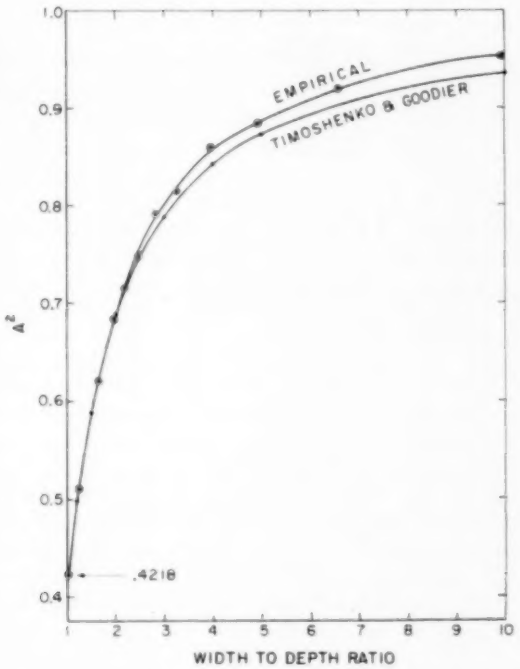

FIGURE 3. *Comparison of empirically determined shape factor, A^2, with that obtained by using Timoshenko and Goodier's values of K_1, where $A^2=3K_1$.*

4. Results and Discussion

The empirical curves of figures 1 and 3, along with their appropriate equations, should yield the same values for the shear modulus. Also, since the theoretical curves based on Pickett's and Cady's equations yield similar results, the percentage difference between the theoretical and empirical curves should be of the same magnitude in both cases. These observations are shown to hold in figures 1 and 3. It is also noted that in figure 1, at high values of w/d, a given change in abscissa is associated with a relatively large change in ordinate, whereas in figure 3 this occurs at low values of w/d. Therefore, for graphs of comparable size, the empirical curve in figure 1 would yield more precise results at low values of w/d, and conversely figure 3 would yield the more precise results at high w/d ratios.

Column 6 of table 3 gives the percentage by which $B(a/l)$ (theoretical) from Pickett is larger than $B(a/l)$ (experimental). The values of $B(a/l)$ (theoretical) are given to the same number of significant figures as $B(a/l)$ (experimental) for comparison. Figure 4 illustrates this variation between the theoretical and experimental curves. It is seen that, using the fundamental mode of vibration, Roark's estimate of an error "not greater than 4 percent" is quite justified—even conservative, the actual deviation being less than half Roark's figure up to $w/d=10$. Furthermore, the appearance of the curves in figures 1 and 3 suggests that at higher values of w/d the deviation will not increase significantly above that already observed.

The empirical curves of figures 1 and 2, and the data on which they are based, even though obtained by using steel specimens, do not lose generality and are applicable to any elastic solid. Some random checks comparing the theoretical and empirical curves of figures 1 and 3 were made by using glass specimens.

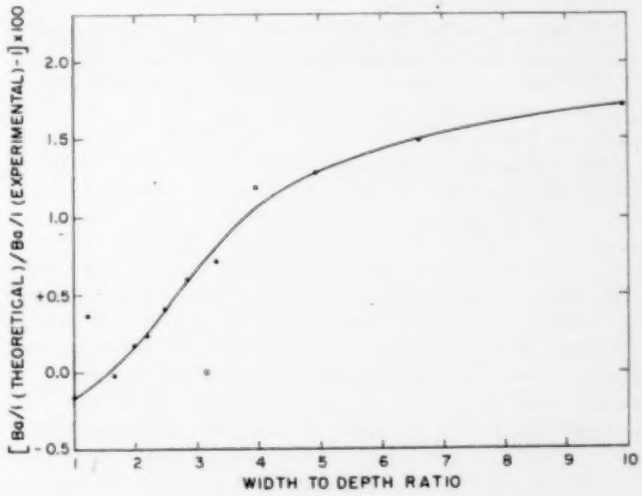

FIGURE 4. *Percentage difference between empirical and theoretical curves as a function of width to depth ratio.*

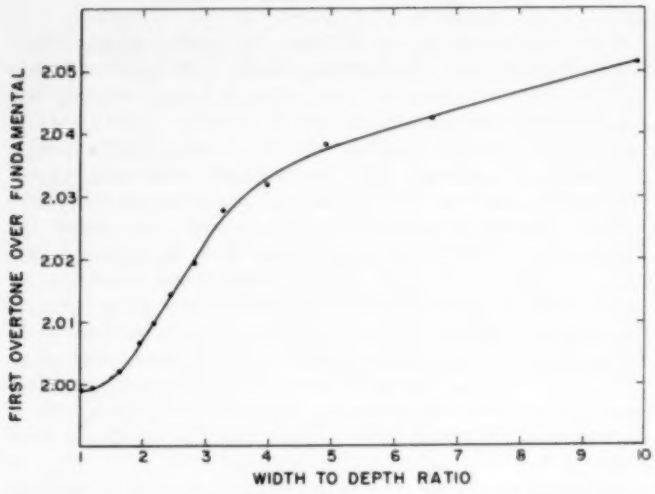

FIGURE 5. *Ratio of first overtone of torsional vibration over fundamental overtone as a function of width to depth ratio.*

Length 15.202 cm.

Results showed that for the same glass, a more nearly consistent value of the shear modulus was obtained for different values of w/d when the empirical curves were used.

It is recalled that, in addition to the fundamental, the first overtones of the resonance frequencies were also determined. Column 4, table 2, gives the percentage variation of the first overtone, $f_{n=2'}$ from the exact double of the fundamental, $f_{n=1'}$, and figure 5 shows the same data graphically as a function of w/d.

Giebe and Blechschmidt [11] resonated quartz bars at the fundamental and higher overtones of the torsional resonance frequency. They also found that the harmonic law did not hold. Their results for the first overtone are in general agreement with those obtained here in that the deviation from the exact double of the fundamental was usually positive and the amount of deviation tended to increase as the w/d ratio increased.

[11] E. Giebe and E. Blechschmidt, Uber Drillungsschwingungen von Quarzstäben und ihre Benutzung für Frequenznormale, Hochfrequentztechnik und Electroakustik—Jahrbuch der drahtlosen Telegraphie und Telephonie 56 (3) 65-87 (1940).

Equations (2) and (4a) show that the overtones of vibration are taken to be whole-number multiples of the fundamental. Use of the term n^2 in the denominator is merely a device for finding the fundamental frequency on the assumption that the overtones are whole-number multiples of the fundamental. The present investigation of the overtones is obviously far from complete, inasmuch as it was determined only for a single length and for one overtone. However, there is already sufficient evidence to show that the belief that the overtone is a whole-number multiple of the fundamental is unjustified. At a w/d ratio of 10, the first overtone is more than 5 percent higher than the exact double of the fundamental. If this were overlooked, it would lead to an error of about the same amount in the calculation of the shear modulus.

5. Summary

1. Two empirical curves have been presented which can be used to determine the shear modulus of bars of rectangular cross section from their resonance frequencies.

2. These empirical curves show a small but significant difference from their corresponding theoretical approximations. This difference increases to about 1¾ percent for a specimen having a cross-sectional width to depth ratio of 10.

3. The resonance frequencies of the first overtone of vibration of a rectangular bar is found to deviate from the harmonic law by more than 5 percent as the ratio of width to depth reaches 10.

The authors are indebted to W. Capps of the Bureau for his assistance in performing many of the calculations involved in preparing table 3.

WASHINGTON, October 28, 1957.

Journal of Research of the National Bureau of Standards Vol. 60, No. 5, May 1958 Research Paper 2862

Specific Volume and Degree of Crystallinity of Semicrystalline Poly(chlorotrifluoroethylene), and Estimated Specific Volumes of the Pure Amorphous and Crystalline Phases

John D. Hoffman and James J. Weeks

The specific volume of poly(chlorotrifluoroethylene) has been measured from −40° to +260° C. Both quenched and well-crystallized specimens prepared by reproducible procedures were studied. Well-defined glass transitions were found close to 52° C in both specimens. Hence the glass temperature of this polymer is essentially independent of the degree of crystallinity. The quasi-equilibrium melting point of the particular type of crystallized specimen used in the investigation was 216° C. The equilibrium melting temperature is undoubtedly somewhat higher, and probably lies between 220° and 225° C.

The degree of crystallinity of the crystallized and quenched specimens was calculated at T_g from specific-volume measurements alone, using a straightforward thermodynamic procedure. The method avoids a long "unguided" extrapolation of the liquid data to low temperatures, and does not involve the inexact approximation that the volume-temperature derivative of the glassy and crystalline states are the same. It has the further advantage of not requiring a pure crystal density from another source, such as a unit-cell determination from X-ray data. It was found that the quenched sample was 39 percent crystalline and the well-crystallized one 82 percent. A simple extension of the theory permits the degree of crystallinity to be computed as a function of temperature. The results are compared with those obtained in earlier investigations.

The specific volumes and volume-temperature derivatives of the pure supercooled liquid, glassy, and crystalline phases are estimated over a wide range of temperature. Certain quantities related to the free volume of the glassy state are discussed.

The methods outlined may be of utility in analyzing specific-volume–temperature data on other semicrystalline polymers where the rapid onset of crystallization interferes with a direct study of the supercooled liquid and glassy states, and where independent data on the properties of the pure crystalline phase are not available.

1. Introduction

Poly(chlorotrifluoroethylene) is a comparatively high-melting and semicrystalline polymer whose degree of crystallinity is strongly dependent on thermal history, samples rapidly quenched from the melt to room temperature being considerably less crystalline than those cooled slowly from the melt. Knowledge of the degree of crystallinity of this material is of interest in the analysis of its physical properties because these frequently depend on the extent of crystallization. For example, the mechanical [1] [1] and dielectric [2] properties of highly crystallized and strongly quenched specimens are decidedly different. One of the principal objectives of the present research was to determine the degree of crystallinity of both strongly quenched and highly crystallized specimens prepared by procedures that could easily be reproduced in any laboratory. A refined method of analysis based on specific-volume–temperature measurements is used to obtain the degree of crystallinity of the samples. Information obtained from this study has been used in the analysis of dielectric [2] and rate-of-crystallization [3] data on specimens of poly(chlorotrifluoroethylene) from the same source as that employed in the present research.

Previous estimates of the degree of crystallinity of poly(chlorotrifluoroethylene) as a function of temperature for both quenched and slow-cooled samples have been obtained by Hoffman [4], using specific-heat data, and by Matsuo [5, 6], using an infrared method. Also, Price [7] has determined the degree of crystallinity of a crystallized specimen of this polymer as a function temperature, using a simple but approximate method based on specific-volume–temperature measurements.

Although the results of the various investigators mentioned above are in fair agreement, there are good reasons for redetermining the degree of crystallinity of this polymer by the proposed method. First, the particular crystallization and quenching procedures used in the aforementioned investigations might well have led to sample variations that would account for at least part of the differences in the results, and it would undoubtedly be better to compare the results of various methods by using specimens prepared in a more definite and reproducible manner. Also, it is clear that it would be advantageous to deal with a more highly crystalline specimen than was formerly used in order to determine the properties of the completely crystalline material more precisely. Further, the proposed method of determining the degree of crystallinity is capable of yielding more accurate results than those obtained by previous methods based on specific-volume measurements because certain approximations inherent in these methods are removed. Another point is that most of the determinations of the degree of crystallinity mentioned above were made without knowledge of the glass-transition temperature of this polymer. The situation concerning the glass

[1] Figures in brackets indicate the literature references at the end of this paper.

transition in this polymer has been recently clarified by Mandelkern, Martin, and Quinn [8], who conclusively demonstrated the existence of such an effect about 20° C above room temperature. Lack of knowledge of the general whereabouts of the glass transition will lead to a rather large uncertainty in a determination of the degree of crystallinity based on specific-volume measurements [7]. Finally, it was considered to be of interest to determine whether or not specific-volume measurements at room temperature could be used to measure the degree of crystallinity of this material for the reason that such a method would be both simple and of general utility. It was found that this type of determination could be successfully carried out.

As implied above, it is necessary to know the glass-transition temperature, T_g, for a polymer in order to determine the degree of crystallinity by a method based on specific volume measurements. In the course of this investigation T_g was measured by a method based on a comparison of the specific-volume-temperature curves for highly crystallized and strongly quenched specimens. The quasi-equilibrium melting temperature of the crystallized sample was also measured and compared with values obtained in other investigations.

Entirely apart from the degree of crystallinity, other information concerning poly(chlorotrifluoroethylene) is obtained from the measurements. A direct experimental study of most of the pure supercooled liquid range is prevented by the rapid onset of crystallization as the material is cooled from the melt; furthermore, samples of ordinary thickness cannot be quenched rapidly enough to obtain the pure crystal-free glass. The purely crystalline state is also not obtained in isolated form owing at least partly to the extraordinary slowness of the crystallization process when the degree of crystallinity becomes fairly high. However, by a study of the present type on two samples of widely differing degrees of crystallinity, it is possible to obtain quantitative information concerning the specific volumes and volume-temperature derivatives of the pure supercooled liquid, glassy, and crystallines states. A fairly precise estimate of the decrease of fractional free volume in the pure glassy state as the temperature is lowered is obtained.

2. Experimental Procedure

2.1. Materials

The poly(chlorotrifluoroethylene) used in this investigation was Kel-F grade 300 polymer, which was kindly supplied in sheet form by H. S. Kaufman of the Minnesota Mining & Manufacturing Co. The sheets were approximately 1.5 to 3.0 mm thick. The number average molecular weight of the polymer was stated to be approximately 415,000.

2.2. Preparation of Crystalline Samples

A simple crystallization procedure of reasonably short duration that yields reproducible results is to first melt out all the crystals by heating to 250° C, and then to bring the specimen successively to temperatures of 200° and 190° C for 1 day each, and finally to 180° C for 3 days. The material is then allowed to cool to room temperature over a period of a few hours. The long residence time at high temperatures permits the slow second stage [3] of the crystallization to proceed to an appreciable degree. The samples were crystallized in an atmosphere of nitrogen. Polymer crystallized by this technique is referred to in the text as "5-day" material. Specimens crystallized in this particular manner have a cloudy-white appearance.[2] The specific volume is 0.4620 cm^3g^{-1} at 25° C. Samples from different batches of polymer crystallized by using the 5-day procedure rarely exhibited specific volumes that deviated more than 0.0003 cm^3g^{-1} from this value at 25° C.

A strictly isothermal run of even several weeks duration at either 180°, 190°, or 200° C is less effective in producing highly crystalline material than the above-mentioned procedure lasting 5 days, which involves three different temperatures.

2.3. Preparation of Quenched Samples

Quenched samples were prepared by heating portions of sheet polymer 1.5 mm thick, which were clamped between 1-mm gold-plated copper disks, to 250° C, and then dropping the entire assembly into ice water. It was found that the specific volume of such specimens was 0.4727 cm^3g^{-1} at 25° C, the variation between samples generally being less than 0.0004 cm^3g^{-1}. Mandelkern and co-workers found a value of 0.4739 cm^3g^{-1} at 25° C for a 3-mm sheet of polymer quenched by an efficient procedure [8].[3] The specific volume of the 3-mm sheet as supplied, which was simply removed from the hot mold and quenched in air, was generally only about 0.0005 to .0010 cm^3g^{-1} lower than that produced by quenching in ice water. Quenched samples are optically clear.

2.4. Specific-Volume Measurements

The specific volume of the polymer was measured at various temperatures between −40° and +260° C, using a buoyancy method similar in many respects to that employed by Price [1]. Each polymer specimen used weighed approximately 5 g in air. The samples were suspended from a 0.1-mm diameter Chromel A wire and weighed in Dow Corning silicone oil contained in a long heavy-walled aluminum cup, which was placed in a vertical position in a 1,000-ml Dewar flask. Weighings were made with a magnetically damped analytical balance. It was found that the specimens could be weighed in the immersion liquid to ±0.5 mg (this includes the effect of temperature variations). For runs made above room temperature, grade DC 710 oil was used. The oil was heated by insulated electrical resistance wire wound around the aluminum cylinder. A thermo-

[2] Optically clear material that is highly crystalline may be obtained by heating the polymer to 250° C, rapidly quenching to 0° C, and then carrying out the crystallization for several days at 160° to 190° C. Such polymer contains no spherulites.

[3] The authors are indebted to L. Mandelkern for making this precise value obtained from the original data available to them.

couple attached to the aluminum cup was used as the sensing element for the d-c amplifier, that controlled the bath temperature. The temperature of the sample was determined by using a thermocouple placed within 3 mm of the sample; this thermocouple was checked against an NBS-calibrated platinum resistance thermometer. It was estimated that the mean temperature of the samples was known to at least 0.2° C. This figure includes the effect of temperature variations due to fluctuations in the controller, and thermal gradients in the bath (see below). Runs below room temperature were made by surrounding the 1,000-ml Dewar flask with a dry ice-acetone mixture contained in a larger Dewar flask. The less viscous grade DC 200 silicone oil was generally used for the low-temperature studies.

The buoyancy of the silicone oil was calibrated at all temperatures employed in each run by weighing a 5.7038-g piece of transparent and bubble-free fused silica in the oil. The density of the fused silica, as obtained by weighing it in distilled water, was found to be 2.204 g cm^{-3}, which is in good agreement with the best values of 2.202 to 2.204 g cm^{-3} given by Sosman [9]. This precaution was taken to show that the material was fused silica, and not crystalline quartz, and also served as a convenient calibration. The specific volume of the samples in cm^3g^{-1} was calculated with the formula

$$\overline{V}_s = \frac{W_{SiO_2}(\text{air}) \times [W_s(\text{air}) - W_s(\text{bath})]}{W_s(\text{air}) \times \rho_{SiO_2} \times [W_{SiO_2}(\text{air}) - W_{SiO_2}(\text{bath})]},$$

where W_{SiO_2} is the mass of the fused silica in the indicated medium (air or oil bath), W_s the mass of the polymer sample in the indicated medium, and ρ_{SiO_2} the density of the fused silica. The quantities W_s (bath) and W_{SiO_2} (bath), refer to the mass as measured in the bath at the temperature of measurement. The coefficient of expansion data of Souder and Hidnert [10] show that the density of fused silica remains within about 4 parts in 10,000 of its room-temperature value over the temperature range of interest here. Therefore, the value ρ_{SiO_2} (air) = 2.204 g cm^{-3} was used at all temperatures. The results for the specific volume of the polymer were occasionally checked between 3° and 95° C by weighing the samples in distilled water.

All of the solid specimens were annealed for a short time at a temperature of 70° to 90° C prior to making a series of measurements in order to relieve any strains in them.

Attention was given to a number of possible sources of error. The silicone oil bath was examined for the presence of thermal gradients of sufficient magnitude to affect the results. By mapping the oil bath with a thermocouple, it was demonstrated that these were always negligibly small (less than ±0.2° C) in the vicinity of the sample. It was determined by weighing a thin metal strip suspended vertically in the bath, and then crimping the strip and repeating the operation, that convection currents, if present, did not affect the measurements by altering the buoyancy. Special attention was also given to the problem of sorption of silicone oil into the samples. At temperatures below 200° C, the uptake of silicone oil (as measured by weighing the 5-g samples in air) was always less than 0.2 mg even after prolonged immersion. This is obviously insufficient to cause appreciable error. Furthermore, it was found that by making measurements as soon as possible after temperature equilibrium was fully attained (7 to 10 min), it was feasible to measure the specific volume in the liquid state up to 260° C without undue sorption of the oil in the polymer. (The polymer is still viscous enough even at this temperature to remain on the suspension wire for the required time.) After a number of runs the liquid polymer tended to inbibe about 10 mg of silicone oil, but even in such cases, results indistinguishable from those on specimens free of silicone were obtained if the *original* weight of the polymer prior to any sorption was used in the calculations. It is safe to conclude that the results are free of errors due to sorption of silicone oil. Two other effects that warranted consideration were the small downward thrust (about 1 mg) on the suspension wire due to surface tension at the silicone-oil–air interface, and the buoyant effect of the oil on that part of the wire in the bath. It was found that these two effects compensated one another over a wide range of temperature if a 12.5-cm length of the Chromel suspension wire was allowed to remain in the oil. The results obtained by using this procedure closely checked those obtained by using the usual but more cumbersome methods. Care was taken to remove any small deposits of silicone oil that might form on the suspension wire. Finally, no effects attributable to degradation were found. Under the conditions described, i. e., prolonged crystallization in nitrogen followed by measurement in silicone oil, the samples never exhibited any significant loss of weight or discoloration on heating, no bubbles were ever observed to form in them, and samples repeatedly heated to high temperatures always gave substantially the same results as fresh material.

The reproducibility of specific-volume measurements on any particular sample measured in silicone oil in the range of 0° to 120° C was ±0.0001 cm^3g^{-1}. The reproducibility was somewhat poorer at the extremes of the temperature range covered, but never exceeded ±0.0004 cm^3g^{-1}, except perhaps in the range between 190° and 216° C, where rapid melting took place. A comparison of the results for the same sample measured in distilled water, and then in silicone oil at the same temperature, usually showed agreement to within 0.0003 cm^3g^{-1}. It is estimated from the latter figure, by taking the density of distilled water as the appropriate reference standard, that the specific volume values quoted for the polymer are accurate to at least 1 part in 1,000.

3. Results

The specific-volume values obtained for the quenched and crystallized samples are plotted in figure 1 as a function of temperature. The

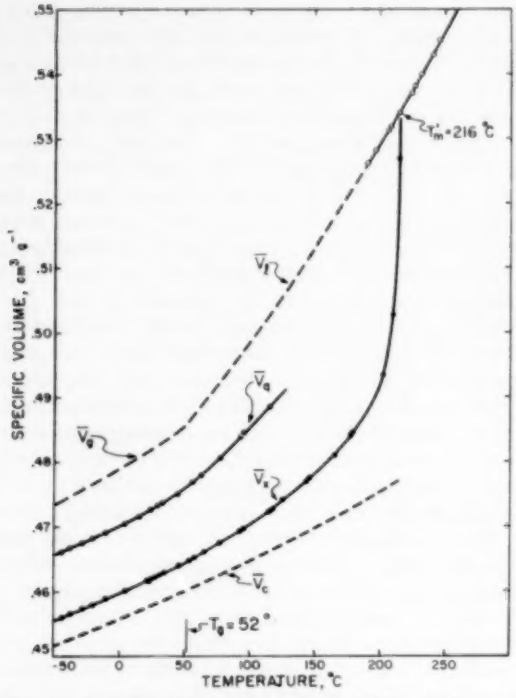

FIGURE 1. *Specific volume of poly(chlorotrifluoroethylene) as a function of temperature.*

●, experimental points for 5-day crystallized specimens (×~12); ◑, experimental points for quenched specimen (~12 ×); ○, experimental points for pure liquid and supercooled liquid (×~3). Dashed lines represent estimated specific volumes of pure glassy, crystalline, and highly supercooled phases (see text).

symbol $\overline{V}_x$ is used to denote the specific volume of the 5-day crystallized sample, and $\overline{V}_q$ is used to denote the corresponding quantity for the quenched sample. A number of the single points shown in figure 1 actually represent duplicate determinations that could not be plotted distinctly owing to the scale used in the diagram.

Values of $\overline{V}_x$ and $\overline{V}_q$ corresponding to the best line drawn through the data when plotted on a large scale are given in table 1 in boldfaced type (the numbers in ordinary type are derived quantities). This operation was carried out with special care in the range −40° to +115° C for both specimens, because it is in this region that volume-temperature derivatives must be known with good precision. In this temperature interval, the standard deviation of the experimental points from the best line was 0.0001 cm^3g^{-1}.

The 5-day sample is sufficiently stable to permit highly reproducible specific-volume-temperature data to be obtained. It was found that the $\overline{V}_x$ value at a given temperature anywhere in the range −40° to +205° C did not change in a period of 30 days; the specific-volume curve is essentially completely reversible if measured within this time interval. It will be shown subsequently that this specimen is about 82 percent crystalline. It is probable that it is in a quasi-equilibrium state with respect to the degree of crystallinity, though it may not be too far removed from the true equilibrium state. Thus, the apparent cessation of the crystallization process leading to the stability of the 5-day specimen may well be largely a result of the extreme slowness of the crystallization process characteristic of the highly crystalline material [3].

The melting point of the 5-day crystallized material is referred to as the *quasi-equilibrium melting point*, T'_m. This is defined experimentally as the temperature where the $\overline{V}_x$ and $\overline{V}_l$ curves intersect (fig. 1). For specimens crystallized in the manner described, T'_m=216°C. The *equilibrium melting temperature*, T_m, which is the one of thermodynamic significance [11], is certainly somewhat higher. Samples in which unstrained crystals melt at 218.0° C have already been prepared, and other lines of evidence [3,12] suggest that T_m lies in the range 220° to 225° C. For the time being, we have indicated the nominal value $T_m \cong 220°$ C in table 1.

TABLE 1. *Specific volume of poly-(chlorotrifluoroethylene) as a function of temperature* [a]

Temperature	Crystallized sample (5 day), $\overline{V}_x$	Quenched sample, $\overline{V}_q$	Pure crystal, $\overline{V}_c$	Pure liquid, supercooled liquid, or glass,[b] $\overline{V}_{l,g}$
°C				
−40	**0.45643**	**0.46595**	0.45254	0.47445
−20	**.45805**	**.46786**	.45404	.47659
0	**.45975**	**.46992**	.45563	.47884
+20	**.46156**	**.47213**	.45728	.48138
52(T_g)	**.46466**	**.47635**	.46007	.48560
65	**.46618**	**.47824**	.46125	.48890
80	**.46803**	**.48119**	.46265	.49284
100	**.47057**	**.48526**	.46458	.49830
115	**.47256**	**.48841**	.46608	.50255
130	**.4747**	.....	.46761	.50693
150	**.4780**	.....	.46972	.51297
180	**.4847**	.....	.47300	.52249
190	**.4881**	.....	.47414	**.52585**
200	**.4928**	.....	.47529	**.52915**
210	**.5027**	.....	.47645	**.53253**
215	**.5270**	.....	.47704	**.53425**
216(T'_m)	**.5346**	.....	.47716	**.53459**
220(T_m)[c]	.....	.....	.47763	**.53598**
225	.....	.....	.....	**.53774**
240	.....	.....	.....	**.54310**
260	.....	.....	.....	**.55050**

[a] Boldfaced numbers represent smoothed values of specific volume obtained from actual experimental data. Numbers in ordinary type are derived quantities. All specific volumes are in cm^3g^{-1}.

[b] The symbol $\overline{V}_l$ is used to denote the specific volume of both the liquid and supercooled liquid; $\overline{V}_g$ represents the specific volume of the glassy state.

[c] Approximate value.

The quenched sample is in a metastable state below about 115° C. Above this temperature, crystallization begins to take place at a perceptible rate, and the specific volume tends toward that found for the crystallized specimen. So long as the residence time in the temperature range 110° to 120° C is kept short, the $\overline{V}_q$ curve shown in figure 1 is reversible (*cf* [8]). It will be shown that the quenched specimen is about 39 percent crystalline.

Specific-volume data for the liquid and supercooled liquid polymer are also plotted in figure 1, the symbol $\overline{V}_l$ being used to denote both of these phases. Values were obtained in the supercooled region by cooling the samples from the melt to the indicated temperature, and making the measurements prior to the onset of any appreciable amount

of crystallization It was found that the crystallization became too rapid to permit reliable data to be obtained when the temperature fell below 190° C.[4] The specific-volume data for the liquid and supercooled region from 260° to 190° C, 20 experimental points in all, were fitted by using least-squares to an equation of the form $\overline{V}_l = \alpha + \beta T + \gamma T^2$, using an electronic computer.[5] Values of the specific voulme obtained from this analysis are given at selected temperatures in table 1 in boldfaced type. The standard deviation in this region proved to be 0.00037 $cm^3 g^{-1}$.

The method that will be used to calculate the degree of crystallinity makes use of the volume-temperature derivatives of the quenched and crystalline samples as they would exist at or near T_g. The volume-temperature derivatives,[6] $d\overline{V}/dT$, of the crystalline, quenched, liquid, and supercooled liquid polymer are plotted as a function of temperature in figure 2. These data were obtained by using the information listed in table 1. In the region −40° to +115° C, an analysis of the volume-temperature derivatives, as calculated from the *original* experimental points, shows that the standard deviation is a little less than 3 percent in this interval. The smoothed data in table 1 lead to $d\overline{V}/dT$ versus T curves that are for all practical purposes identical to those obtained from the original experimental points.

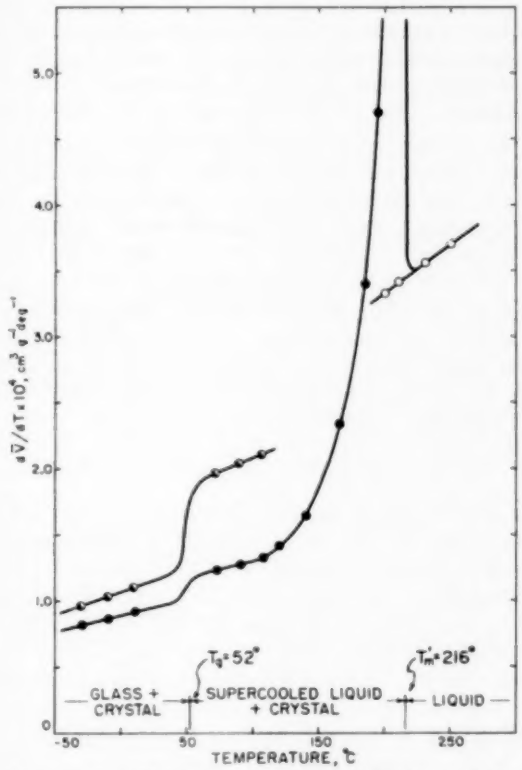

FIGURE 2. *Volume-temperature derivatives of the poly(chlorotrifluoroethylene) specimens as a function of temperature.*

●, 5-day crystallized material; ◑, quenched material; ○, liquid and supercooled liquid material.

It is seen in figure 2 that there is no upswing in the volume-temperature derivative of the crystallized sample indicative of melting out of small crystallites until a temperature of about 120° C is reached. This, together with the fact that the specific volume of both the quenched and crystallized specimens are invariant with time below ~115° C, justifies the assumption to be used later that the degree of crystallinity of the specimens does not change appreciably below 115° C.

A glass transition is clearly apparent in the $d\overline{V}/dT$ data for the quenched sample between 40° and 60° C (fig. 2). A similar but less obvious transition also appears in the crystallized specimen, a fact which conclusively shows that it is not completely crystallized. The glass transition takes place only in the amorphous component of the polymer. Hence the semicrystalline samples consist of glass plus crystal below T_g, and supercooled liquid plus crystal from T_g up to T_m'.

The glass-transition temperature has been determined by plotting the difference between the specific volume of the crystalline and quenched samples as a function of temperature by using the smoothed data in table 1 (fig. 3). This method tends to sub-

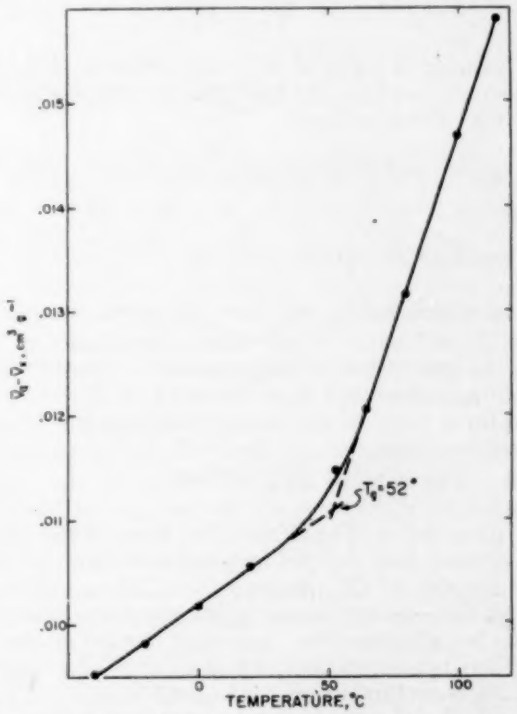

FIGURE 3. *Determination of the glass-transition temperature, T_g, for poly(chlorotrifluoroethylene).*

[4] Considerable care must be exercised to prevent crystallization from affecting the precision of the data in the supercooled region. Brief heat treatment at *ca.* 300° C renders almost all of the heterogeneous nuclei in the polymer inactive, and thus lowers the rate of crystallization in the supercooled region. This permitted precise data to be obtained down to 190° C in the present case. It was found that accurate results could not be obtained at lower temperatures by extrapolating back to zero time.

[5] The authors thank J. M. Cameron of the statistical engineering laboratory of NBS for carrying out this analysis.

[6] Strictly speaking, $d\overline{V}/dT$ is the *specific*-volume-temperature derivative, but this cumbersome term is not used in the text.

tract out the greater part of the curvature inherent in the volume-temperature curves, and therefore yields a plot through which two intersecting straight lines may be drawn with some confidence. The glass-transition temperature determined in this way is 52° C. This is in fair agreement with the value of 45° C determined by Mandelkern and co-workers [8], and a value attributed to Reding [13], and is in good agreement with the value of 50° C mentioned by Boyer [14]. A further discussion of the glass transition is given in section 6.5.

4. Theory

4.1. Preliminary Considerations

The basic assumption is made that the volumes of the crystalline and amorphous material in a semicrystalline polymer are additive. In the units used here, namely, specific volume, this leads to the relation

$$\chi_s \overline{V}_c + (1-\chi_s)\overline{V}_{l,g} = \overline{V}_s, \tag{1}$$

where $\overline{V}_{l,g}$ is the specific volume of the purely amorphous (supercooled liquid or glassy) regions, $\overline{V}_s$ is the specific volume of the semicrystalline sample, and $\overline{V}_c$ the specific volume of the entirely crystalline material. χ_s is the *mass fraction* of the sample, that is crystalline, and will[1] henceforth be called the *degree of crystallinity*.[7] It is seen from eq (1) that

$$\chi_s = \frac{\overline{V}_{l,g} - \overline{V}_s}{\overline{V}_{l,g} - \overline{V}_c}. \tag{2}$$

This formula is valid at all temperatures. By taking the derivative of eq (1) with respect to temperature, we obtain the equations

$$\chi_s(d\overline{V}_c/dT) + (1-\chi_s)(d\overline{V}_l/dT) = (d\overline{V}_s^+/dT) \tag{3}$$

and

$$\chi_s(d\overline{V}_c/dT) + (1-\chi_s)(d\overline{V}_g/dT) = (d\overline{V}_s^-/dT), \tag{4}$$

each of which holds only for any given temperature where $d\chi_s/dT=0$. In the above equations, $d\overline{V}_s^+/dT$ refers to the volume-temperature derivative of the sample as calculated from data *above* T_g, where the amorphous part of the semicrystalline polymer has the volume-temperature derivative of a supercooled liquid. The symbol $d\overline{V}_s^-/dT$ refers to the volume-temperature derivative of the sample as calculated from data *below* T_g, where the amorphous part of the polymer has the volume-temperature derivative characteristic of the glassy state. It is understood that all the volume-temperature derivatives in eq (3) are to be obtained at the same temperature, and a similar statement applies to eq (4). The condition $d\chi_s/dT=0$ certainly holds at and below T_g, and can generally be shown to apply at temperatures sufficiently far above T_g to permit the estimation of $d\overline{V}_s^+/dT$. From eq (3) and (4) we obtain the relations

$$\chi_s = \frac{(d\overline{V}_l/dT) - (d\overline{V}_s^+/dT)}{(d\overline{V}_l/dT) - (d\overline{V}_c/dT)}, \tag{5}$$

and

$$\chi_s = \frac{(d\overline{V}_g/dT) - (d\overline{V}_s^-/dT)}{(d\overline{V}_g/dT) - (d\overline{V}_c/dT)}. \tag{6}$$

For any temperatures where $d\chi_s/dT=0$, eq (2), (5), and (6) must lead to identical values of χ_s for a given sample.

It is instructive at this point to indicate the nature of the difficulties that are encountered in estimating the degree of crystallinity from specific-volume measurements alone if data on only a *single* specimen are used. It is assumed in the following discussion that specific-volume data exist for the semicrystalline range from well below T_g up to T_m', and for the liquid range near and well above T_m'. These circumstances correspond to the experimental situation that prevails for poly(chlorotrifluoroethylene) and certain other polymers that tend to transform rapidly to a semicrystalline state below T_m'.

Equation (2) cannot be used to calculate χ_s directly because $\overline{V}_c$ is not known, and we therefore turn to a consideration of eq (5). Here the quantity $d\overline{V}_s^+/dT$ may be regarded as experimentally known in the region near T_g. In order to compute the degree of crystallinity, it is thus necessary to estimate $d\overline{V}_l/dT$ and $d\overline{V}_c/dT$. The assumption is commonly made that the volume-temperature derivative of the semicrystalline sample below T_g, where the polymer consists of glass plus crystal, may be taken as being representative of the pure crystal. This gives the approximation

$$d\overline{V}_s^-/dT \cong d\overline{V}_c/dT. \tag{7}$$

However, there is no fundamental reason for supposing that eq (7) is really exact (it will emerge later that it is in error by about 10 percent even for the crystallized sample of poly(chlorotrifluroroethylene)). Further, the data in the liquid region can be analyzed by using a least-squares fit to an equation of the form $\overline{V}_l = \alpha + \beta T + \gamma T^2$, and a value of $d\overline{V}_l/dT$ obtained by a long downward extrapolation to the range where $d\overline{V}_c/dT$ and $d\overline{V}_s^+/dT$ have been evaluated. Unfortunately, this procedure will generally lead to a rather uncertain $d\overline{V}_l/dT$ value unless the specific-volume data for the liquid are extraordinarily precise. In the case of poly(chlorotrifluoroethylene), where the standard deviation of the $\overline{V}_l$ equation in the liquid range is only $0.00037 \text{cm}^3\text{g}^{-1}$, the $d\overline{V}_l/dT$ value at T_g as obtained by the extrapolation procedure is 2.27×10^{-4} $\text{cm}^3 g^{-1}\text{deg}^{-1}$, with a standard deviation of 0.80×10^{-4}. This corresponds to a coefficient of variation of 35 percent. It is clear from the foregoing that the use of approximation (7), together with the long extrapolation necessary to estimate $d\overline{V}_l/dT$ at or near T_g, will

[1] The *volume fraction* of crystals is given by the expression $\lambda_s = (\rho_s - \rho_{l,g})/(\rho_c - \rho_{l,g})$, where ρ is the density.

tend to produce large errors in χ_s despite the precision of the input data in the region of direct measurement.

The approximate nature of the procedures required to analyze data on a single specimen also have an adverse effect on the accuracy of $\overline{V}_l$ and $\overline{V}_c$ at T_g. By using a long downward extrapolation of the liquid data, a rough value of $\overline{V}_l$ can be obtained at T_g. For poly-(chlorotrifluoroethylene), $\overline{V}_l$ turns out to be 0.4875 cm^3g^{-1}, with a standard deviation of 0.0070, despite the relatively high precision of the input data in the region of measurement (the standard deviation would have been even greater had the equation $\overline{V}_l=\alpha+\beta T$ been used to represent the liquid data). If this quantity is inserted in eq (2), together with the rough value of χ_s previously obtained, an estimate of $\overline{V}_c$ at T_g can be made. It is clear, however, that crystal properties determined in this way are not especially reliable.

It is seen that the major difficulty with the single-specimen method is the inaccuracy of the values of $\overline{V}_l$ and $d\overline{V}_l/dT$ at T_g obtained by the long "unguided" extrapolation of the liquid data from high temperatures. In order to obtain satisfactory results it would be necessary to know $\overline{V}_l$ at T_g to within about 0.0015 cm^3g^{-1}, and $d\overline{V}_l/dT$ at the same temperature to within about 5 percent. In the present case, this would require data in the experimentally accessible liquid range (190° to 260° C), which had a standard deviation of about 0.00007 cm^3g^{-1}. Data of such high precision would not be easily obtained for any polymer in the liquid state, especially at high temperatures.

In this type of situation, it is considerably more satisfactory to employ the method to be described in section 4.2, which deals with *two* samples, one highly crystalline and the other as amorphous as is practical. This method completely avoids the use of approximation (7), and does not require extrapolation over long temperature ranges. The principal input data are obtained where the measurements are most precise, and the volume-temperature derivatives are obtained at a common temperature. Both $\overline{V}_l$ and $\overline{V}_c$ can be obtained to within about 0.0015 cm^3g^{-1}, and the degree of crystallinity to a standard deviation of about 0.05.

4.2. Calculation of the Degree of Crystallinity Near T_g Using Two specimens

Consider now the case of two samples, one highly crystalline and the other strongly quenched. The degree of crystallinity of these samples is denoted χ_x and χ_q, respectively. Thus we may write

$$\chi_q=\frac{\overline{V}_l-\overline{V}_q}{\overline{V}_l-\overline{V}_c}=\frac{(d\overline{V}_l/dT)-(d\overline{V}_q^+/dT)}{(d\overline{V}_l/dT)-(d\overline{V}_c/dT)}, \tag{8}$$

and

$$\chi_x=\frac{\overline{V}_l-\overline{V}_x}{\overline{V}_l-\overline{V}_c}=\frac{(d\overline{V}_l/dT)-(d\overline{V}_x^+/dT)}{(d\overline{V}_l/dT)-(d\overline{V}_c/dT)}, \tag{9}$$

by analogy with eq (2) and (5). The quantities $\overline{V}_q$, $\overline{V}_x$, $d\overline{V}_q^+/dT$, and $d\overline{V}_x^+/dT$ are known and the quantities χ_q, χ_x, $\overline{V}_l$, $\overline{V}_c$, and $d\overline{V}_l/dT$ are unknown. Equations (8) and (9) contain the important notion that, for a given specimen, the degree of crystallinity computed directly from the specific volumes must be identical to that obtained from the volume-temperature derivatives when $d\chi/dT=0$. Initially the degree of crystallinity will be calculated from data in the vicinity of the glass transition where it is certain that the condition $d\chi/dT=0$ is fulfilled.

The first step in the procedure is to construct an equation for $\overline{V}_l$ that gives an acceptable fit in the liquid region and conforms with the demands imposed by eq (8) and (9). An important assumption at this point is that the correct form of the equation for the liquid and supercooled liquid all the way down to T_g is

$$\overline{V}_l=A+BT+CT^2. \tag{10}$$

By eliminating the ratio $[(d\overline{V}_l/dT)-(d\overline{V}_c/dT)]/(\overline{V}_l-\overline{V}_c)$ from eq (8) and (9), one finds

$$\overline{V}_l[(d\overline{V}_q^+/dT)-(d\overline{V}_x^+/dT)]+(d\overline{V}_l/dT)(\overline{V}_x-\overline{V}_q)$$
$$=\overline{V}_x(d\overline{V}_q^+/dT)-\overline{V}_q(d\overline{V}_x^+/dT). \tag{11}$$

Then substituting $\overline{V}_l=A+BT+CT^2$ and $d\overline{V}_l/dT=B+2CT$ into this equation, the relation

$$A[(d\overline{V}_q^+/dT)-(d\overline{V}_x^+/dT)]+$$
$$B\{(\overline{V}_x-\overline{V}_q)+T[(d\overline{V}_q^+/dT)-(d\overline{V}_x^+/dT)]\}+$$
$$C\{[(d\overline{V}_q^+/dT)-(d\overline{V}_x^+/dT)]T^2+2T(\overline{V}_x-\overline{V}_q)\}$$
$$=\overline{V}_x(d\overline{V}_q^+/dT)-\overline{V}_q(d\overline{V}_x^+/dT) \tag{12}$$

is obtained. The volume-temperature derivatives in eq (12) must, of course, all be obtained at some common temperature. It is convenient, though not necessary, to choose $T=T_g$. Observe that all of the quantities in eq (12), except A, B, and C, are experimentally known from the specific-volume and volume-temperature derivatives as obtained on the two semicrystalline specimens in the vicinity of T_g. At this point, two equations describing the liquid data at two temperatures, T_1 and T_2, in the region of direct measurement are introduced:

$$A+BT_1+CT_1^2=\overline{V}_l^{(T_1)} \tag{13}$$

$$A+BT_2+CT_2^2=\overline{V}_l^{(T_2)}. \tag{14}$$

Since $\overline{V}_l$ is known experimentally at T_1 and T_2, the three simultaneous equations (12 to 14) may now be solved for A, B, and C. This yields an equation for the liquidus down to T_g, which not only fits the observed liquid data extremely well, but also gives $\overline{V}_l$ and $d\overline{V}_l/dT$ values near T_g, which, because of the conditions imposed by eq (8) and (9), are certain to yield the same degree of crystallinity for a given

sample by both the specific-volume and volume-temperature derivative methods. The values of $\overline{V}_l$ and $d\overline{V}_l/dT$ at T_g are, through eq (12), controlled largely by the experimental volume-temperature derivative data on the semicrystalline samples in the general vicinity of T_g, and not by a long extrapolation of the observed liquid data down to T_g. The fundamental nature of the method is most easily perceived by noting that eq (12) is altogether equivalent to having another equation of the form of (13) and (14) where V_l is known at T_g.

The next step involves the calculation of the volume-temperature derivative of the pure crystal. By eliminating the ratio $(d\overline{V}_l/dT - d\overline{V}_c/dT)/(d\overline{V}_g/dT - d\overline{V}_c/dT)$ from the equations

$$\chi_q = \frac{(d\overline{V}_g/dT)-(d\overline{V}_q^-/dT)}{(d\overline{V}_g/dT)-(d\overline{V}_c/dT)} = \frac{(d\overline{V}_l/dT)-(d\overline{V}_q^+/dT)}{(d\overline{V}_l/dT)-(d\overline{V}_c/dT)}, \tag{15}$$

and

$$\chi_x = \frac{(d\overline{V}_g/dT)-(d\overline{V}_x^-/dT)}{(d\overline{V}_g/dT)-(d\overline{V}_c/dT)} = \frac{(d\overline{V}_l/dT)-(d\overline{V}_x^+/dT)}{(d\overline{V}_l/dT)-(d\overline{V}_c/dT)}, \tag{16}$$

which are based on eq (5) and (6), and then eliminating $d\overline{V}_g/dT$, it is found that

$$d\overline{V}_c/dT = \frac{(d\overline{V}_x^+/dT)(d\overline{V}_q^-/dT)-(d\overline{V}_x^-/dT)(d\overline{V}_q^+/dT)}{(d\overline{V}_x^+/dT)+(d\overline{V}_q^-/dT)-(d\overline{V}_x^-/dT)-(d\overline{V}_q^+/dT} \tag{17}$$

The term on the right-hand side of the expression involves only experimentally known quantities. The degree of crystallinity of each sample is then computed by inserting the known values of $d\overline{V}_c/dT$, $d\overline{V}_l/dT$, $d\overline{V}_x^+dT$, and $d\overline{V}_q^+/dT$ into eq (8) and (9). As a final step, $\overline{V}_c$ may be calculated from both eq (8) and (9) because $\overline{V}_l$, $\overline{V}_x$, $\overline{V}_q$, and χ_x and χ_q, are now known. Agreement between the two $\overline{V}_c$ values provides a convenient check of the calculations.

4.3. Calculation of the Degree of Crystallinity as a Function of Temperature

In order to determine the degree of crystallinity as a function of temperature, an equation of the form of (2) will be used. The specific volume of the sample, $\overline{V}_s$, is experimentally known at all temperatures of interest, and $\overline{V}_l$ is also determined as a function of temperature by the procedure outlined in the previous section. Hence, if the temperature dependence of $\overline{V}_c$ is known, χ_s can then be computed as a function of temperature. The remainder of this section is devoted to showing how the temperature variation of $\overline{V}_c$ is determined.

A direct way of obtaining $\overline{V}_c$ as a function of temperature, which also yields other information of interest, is to calculate $\overline{V}_c$ values above and below T_g, combine them with that already calculated at T_g, and solve the three simultaneous equations to obtain the constants in the relation

$$\overline{V}_c = A' + B'T + C'T^2. \tag{18}$$

$\overline{V}_c$ can be calculated for that region above T_g where χ_x is already evaluated from the relation

$$\chi_x = \frac{\overline{V}_l - \overline{V}_x}{\overline{V}_l - \overline{V}_c}, \tag{19}$$

because both $\overline{V}_l$ and $\overline{V}_x$ are known as a function of temperature. (At this stage, χ is known only at temperatures where $d\chi/dT=0$.) $\overline{V}_c$ and $\overline{V}_g$ can readily be obtained at temperatures below T_g by simultaneously solving the equations

$$\chi_x = \frac{\overline{V}_g - \overline{V}_x}{\overline{V}_g - \overline{V}_c}, \tag{20}$$

and

$$\chi_q = \frac{\overline{V}_g - \overline{V}_q}{\overline{V}_g - \overline{V}_c}. \tag{21}$$

It should be noted that $\overline{V}_c$ is actually determined from the data only from the lowest temperature of measurement up to the highest temperature where one is still certain that the degree of crystallinity is not changing with temperature. Thus, to obtain the degree of crystallinity as a function of temperature up to the melting point, an extrapolation of V_c is required. Fortunately, this extrapolation will not ordinarily lead to serious errors, since the constants B' and C' are quite small for a crystal, and can be based on data obtained for a temperature range that is longer than the implied extrapolation. This extrapolation will generally be a much less serious matter than the long "unguided" extrapolation of the liquidus down to T_g discussed in section 4.1; for liquids, the temperature range where data can be obtained will for various reasons generally be considerably shorter than the implied extrapolation, and β and γ will be large owing to the strong dependence of the volume on temperature characteristic of liquids. The method described to obtain $\overline{V}_c$ as a function of temperature applies only if there is no solid-state phase transitition in the crystalline material between T_g and T_m.

5. Application to Poly(chlorotrifluoroethylene)

5.1. Degree of Crystallinity Near T_g

The general procedure described in section 4.2 is used here.

The method of deriving the volume-temperature derivatives at T_g is illustrated in figure 4. The volume-temperature derivatives were first calculated at a number of temperatures by using the smoothed

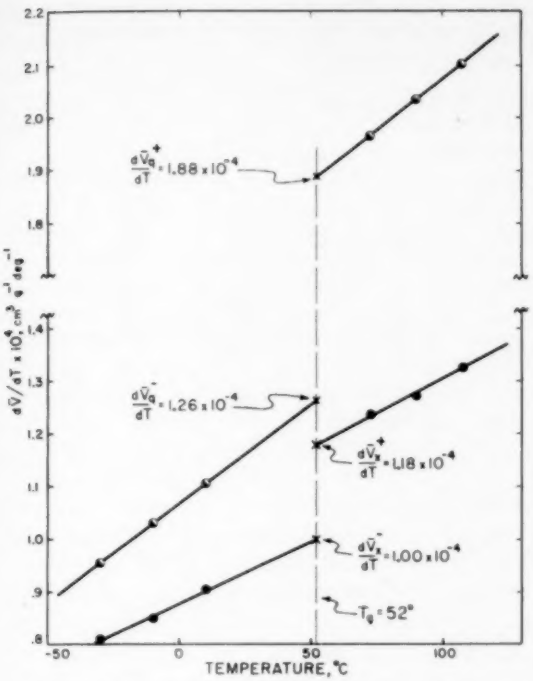

FIGURE 4. *Determination of the volume-temperature derivatives of the 5-day crystallized (●) and quenched (◑) specimens at T_g.*

data in table 1, plotted as a function of temperature, and the desired derivatives obtained at T_g by a short extrapolation. The input data are summarized in table 2. It should be noted that the $\overline{V}_x$ and $\overline{V}_g$ values at T_g listed in table 2 are those which would be obtained if the glass transition occurred abruptly at 52° C, i. e., at the intersection of two curved lines. The $\overline{V}_x$ and $\overline{V}_g$ values listed in table 2 are the correct ones to use in the analysis, but final results differing only slightly from those to be given would emerge if those listed in table 1 were used instead.

The equation for the liquid and supercooled liquid is readily calculated. Inserting the data from table 2 into eq (12), one finds

$$0.700A-74.60B-9{,}651.2C=0.31212. \quad (22)$$

Now, selecting two suitably spaced temperatures in the liquid region, say 210° and 240° C, and taking the appropriate specific volumes from table 1, we find:

$$A+210B+44{,}100C=0.53253 \quad (23)$$

$$A+240B+57{,}600C=0.54310. \quad (24)$$

Solving these simultaneous equations, it is found that

$$\overline{V}_l=0.47337+2.199\times10^{-4}T+2.943\times10^{-7}T^2. \quad (25)$$

This equation fits the original liquid data extremely well, the standard deviation being only 0.00040 cm^3g^{-1}. The calculated value of $\overline{V}_l$ at T_g is 0.4856 cm^3g^{-1}.

TABLE 2. *Input data at T_g=52° C*

Specific volume of quenched sample, $\overline{V}_g$.....	0.4757 cm^3g^{-1}.
Specific volume of crystallized sample (5 day), $\overline{V}_x$.	0.4646 cm^3g^{-1}.
Volume-temperature derivative of quenched sample from data above T_g, $d\overline{V}_g^+/dT$.	1.88×10⁻⁴ $cm^3g^{-1}deg^{-1}$.
Volume-temperature derivative of quenched sample from data below T_g, $d\overline{V}_g^-/dT$.	1.26×10⁻⁴ $cm^3g^{-1}deg^{-1}$.
Volume-temperature derivative of crystallized sample from data above T_g, $d\overline{V}_x^+/dT$.	1.18×10⁻⁴ $cm^3g^{-1}deg^{-1}$.
Volume-temperature derivative of crystallized sample from data below T_g, $d\overline{V}_x^-/dT$.	1.00×10⁻⁴ $cm^3g^{-1}deg^{-1}$.

The volume-temperature derivative obtained from eq (25) is

$$d\overline{V}_l/dT=2.199\times10^{-4}+5.886\times10^{-7}T, \quad (26)$$

from which is found that $d\overline{V}_l/dT=2.505\times10^{-4}$ cm^3g^{-1} at T_g=52° C. Equations extremely close to (25) and (26) would have been obtained had data for temperatures different than 210° and 240° C, say 190° and 260° C, been employed to construct equations analogous to eq (23) and (24). Values of $\overline{V}_l$ computed by using eq (26) are given in table 1 for temperatures between 52° and 180° C.

The next step is to calculate the volume-temperature derivative of the pure crystal at T_g, using eq (17). Inserting the appropriate data from table 2 into this formula, it is found that $d\overline{V}_c/dT=0.894\times10^{-4}$ $cm^3g^{-1}deg^{-1}$ at this temperature. Now that $d\overline{V}_c/dT$ and $d\overline{V}_l/dT$ are determined, the degree of crystallinity of each specimen can be calculated by using eq (8) and (9):

$$\chi_g=(2.505-1.880)\times10^{-4}/(2.505-0.894)\times10^{-4}=0.388 \quad (27)$$

$$\chi_x=(2.505-1.180)\times10^{-4}/(2.505-0.894)\times10^{-4}=0.822\,. \quad (28)$$

Using these values of χ_g and χ_x, $\overline{V}_c$ at T_g can be calculated from both eq (8) and (9). Thus,

$$\chi_g=0.388=(0.4856-0.4757)/(0.4856-\overline{V}_c), \quad (29)$$

and

$$\chi_x=0.822=(0.4856-0.4646)/(0.4856-\overline{V}_c)\,, \quad (30)$$

from which it is found that $\overline{V}_c$=0.46007 cm^3g^{-1} at T_g in each case. A value for $d\overline{V}_g/dT$, the volume-temperature derivative of the pure glass, can be obtained at T_g by the use of eq (15) and (16), together with the results already obtained. A summary of the results of the calculations at T_g is given in table 3.

TABLE 3. *Results of calculations at $T_g = 52°$ C*

Degree of crystallinity of quenched sample, χ_q.	0.388.
Degree of crystallinity of crystallized sample (5 day), χ_x.	0.822.
Volume-temperature derivative of pure crystalline phase, $d\overline{V}_c/dT$.	0.894×10^{-4} cm^{3}g^{-1}deg^{-1}.
Volume-temperature derivative of pure glassy state, $d\overline{V}_g/dT$.	1.492×10^{-4} cm^{3}g^{-1}deg^{-1}.
Volume-temperature derivative of pure supercooled liquid, $d\overline{V}_l/dT$.	2.505×10^{-4} cm^{3}g^{-1}deg^{-1}.
Specific volume of pure supercooled liquid and glassy state, $\overline{V}_l = \overline{V}_g$.	0.48560 cm^{3}g^{-1}.
Specific volume of pure crystalline phase, $\overline{V}_c$.	0.46007 cm^{3}g^{-1}.

5.2. Degree of Crystallinity as a Function of Temperature

The procedure outlined in section 4.3 is followed here. From the previous section, we already have the value $\overline{V}_c = 0.46007$ cm^{3}g^{-1} at 52°C. At 115°C, we use eq (19) with the value $\chi_x = 0.822$ and $\overline{V}_l = 0.50255$, the latter value calculated from eq (25). It is found that $\overline{V}_c = 0.46608$ cm^{3}g^{-1} at 115°C. At −40°C, using $\chi_x = 0.822$ and $\chi_q = 0.388$, together with the values of $\overline{V}_x$ and $\overline{V}_g$ listed in table 1, it is found by simultaneously solving eq (20) and (21) that $\overline{V}_c = 0.45254$ cm^{3}g^{-1} and $\overline{V}_g = 0.47445$ cm^{3}g^{-1}. Thus, we have three simultaneous equations of the form of eq (18) for the pure crystal covering the interval −40° to +115°C, the latter being the highest temperature where it is certain $d\chi/dT = 0$:

$$A' - 40B' + 1600C' = 0.45254 \quad (31)$$

$$A' + 52B' + 2704C' = 0.46007 \quad (32)$$

$$A' + 115B' + 13225C' = 0.46608. \quad (33)$$

It is found from eq (31 to 33) that

$$\overline{V}_c = 0.45563 + 0.8079\times10^{-4}T + 0.874\times10^{-7}T^2. \quad (34)$$

This result may be checked for consistency by calculating $d\overline{V}_c/dT$ at 52° C. The value is 0.899×10^{-4} cm^{3}g^{-1}deg^{-1}, which is in good agreement with the value 0.894×10^{-4} cm^{3}g^{-1}deg^{-1} obtained from eq (17).

The degree of crystallinity of the 5-day crystallized sample is obtained as a function of temperature by inserting values of $\overline{V}_l$ and $\overline{V}_c$ calculated with eq (25) and (34), together with the values of $\overline{V}_x$ listed in table 1, into expression (2) or (20). These operations are conveniently carried out by using the numerical values for $\overline{V}_l$ and $\overline{V}_c$ listed in table 1. Values of the degree of crystallinity calculated for the 5-day crystallized sample from 52° to 216° C are given in table 4 and plotted in figure 5.

The degree of crystallinity of the quenched specimen has been calculated from 52° to 115° C in an analogous way, and the results are indicated in table 4 and figure 5.

TABLE 4. *Degree of crystallinity of poly-(chlorotrifluoroethylene) as a function of temperature*

Temperature	Crystallized sample (5-day), χ_x	Quenched sample, χ_q
°C		
52 (T_g)	0.822	0.388
65	.822	.386
80	.822	.386
100	.822	.387
115	.822	.388
130	.820	.....
150	.809	.....
180	.764	.....
190	.730	.....
200	.657	.....
210	.532	.....
215	.127	.....
216 (T'_m)	.000	.....

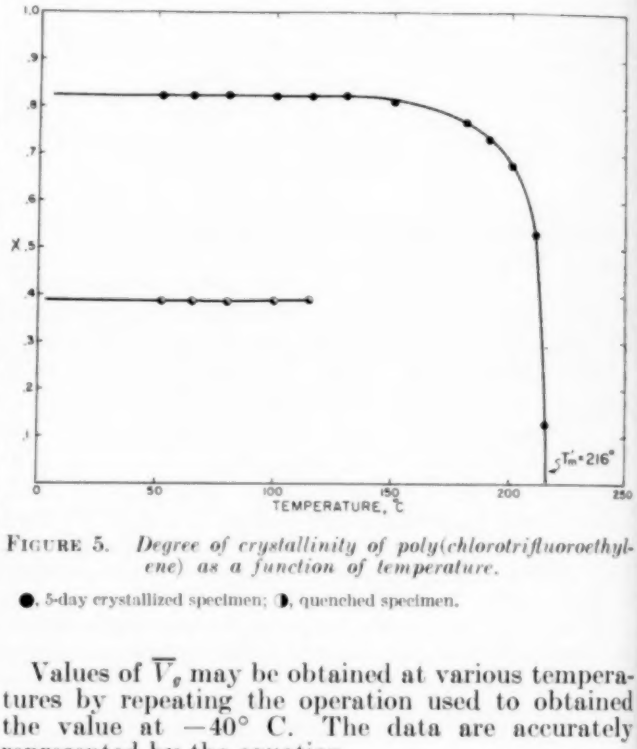

FIGURE 5. *Degree of crystallinity of poly(chlorotrifluoroethylene) as a function of temperature.*

●, 5-day crystallized specimen; ◑, quenched specimen.

Values of $\overline{V}_g$ may be obtained at various temperatures by repeating the operation used to obtained the value at −40° C. The data are accurately represented by the equation

$$\overline{V}_g = 0.47884 + 1.186\times10^{-4}T + 2.20\times10^{-7}T^2. \quad (35)$$

Values of $\overline{V}_g$ obtained at various temperatures are given in table 1.

5.3. Errors

A rigorous analysis of the errors is prohibitively difficult, but under certain assumptions, a reasonable estimate of the standard deviation associated with the essential results can be made. As indicated earlier, the standard deviation of each of the four measured volume-temperature coefficients at T_g is close to 3 percent. Using an equation involving

first derivatives of the form $\chi_s=[(d\overline{V}_l/dT)-(d\overline{V}_s{}^+/dT)]/[(d\overline{V}_l/dT)-(d\overline{V}_c/dT)]$, where the term in $d\overline{V}_c/dT$ is determined by using eq (17), and assuming that the standard deviation of $d\overline{V}_l/dT$ is also 3 percent, it is found that the standard deviation is 0.05 for both χ_x and χ_q. This estimate is provisional on account of the fact that the error assumed for $d\overline{V}_l/dT$ at T_g is somewhat arbitrary, but it is believed that the standard deviations quoted for χ_x and χ_q are fairly close to correct. The view that the standard deviation in χ is small is considerably strengthened by the fact that a straightforward calculation based on *second* derivatives gives χ_x and χ_q values in close accord with those obtained with the first derivative form (see below). Raising the assumed error in $d\overline{V}_l/dT$ to 6 percent, which is certainly an upper limit, increases the standard deviation of χ_x and χ_q to only 0.07.

Taking the error in χ_x and χ_q to be 0.05, it is found that the standard deviation in $\overline{V}_l$ and $\overline{V}_c$ at T_g is about 0.0015 cm^3g^{-1}. Approximately the same value of the error holds for $\overline{V}_g$ and $\overline{V}_c$ from T_g down to $-40°$ C, and for $\overline{V}_l$ and $\overline{V}_c$ up to 115° C. Above 115° C, the deviation in $\overline{V}_l$ begins to fall, eventually becoming about 0.00040 cm^3g^{-1} at 190° C. The standard deviation in $\overline{V}_c$ increases above 115° C, and reaches a value of about 0.0025 cm^3g^{-1} at 200° C. As a consequence, the standard deviation of the degree of crystallinity, as calculated from eq (2), does not exceed a value of approximately 0.05 at any temperature. The deviation in $\overline{V}_l$ at T_g is seen to be much less than the value 0.0070 cm^3g^{-1}, which would have resulted had the usual unguided extrapolation of the liquidus from high temperatures been employed.

It might be thought that the present treatment could be materially improved by including terms of the order of T^3 and higher in eq (10). There is no basic objection to the use of such higher terms. However, the present analysis, using three constants for describing the specific volume of the liquid and supercooled liquid states, is actually good enough to give roughly correct results even with second derivatives. By taking the second derivative of eq (3) with respect to temperature, we obtain an equation for the degree of crystallinity of the form $\chi_q=[(d^2\overline{V}_l/dT^2)-(d^2\overline{V}_s{}^+/dT^2)]/[(d^2\overline{V}_l/dT^2)-(d^2\overline{V}_c/dT^2)]$. Then, using the appropriate formulas in the text to obtain numerical values of $d^2\overline{V}_l/dT^2$ and $d^2\overline{V}_c/dT^2$, and taking the slopes of the volume-temperature coefficients above T_g in figure 4, it is found that the above expression gives $\chi_x=0.82$ and $\chi_q=0.49$. This is a harsh test of the data, and the good agreement of these values with the ones obtained by using the first derivatives lends credence to the accuracy of the latter. This also shows that terms of T^3 and higher order in the liquidus equation are not necessary to carry out the analysis to an acceptable degree of accuracy. Extremely precise data in the true liquid range might warrant the use of a T^3 term in eq (10). All that would be required to evaluate the constant associated with this additional term would be to include another equation of the type of (13) and (14) in the analysis.

6. Discussion

6.1. Degree of Crystallinity and Specific Volume: Comparison With Earlier Results

The degree of crystallinity calculated for the quenched sample, $\chi_q=0.39\pm0.05$, which holds for temperatures below 115° C, compares favorably with the value $\chi_q=0.35$ obtained by the specific-heat method [4]. Owing to the presence of certain approximations inherent in the method of analysis used in the determination based on specific heats, and the approximate nature of that data, it is believed that more reliance may be put in the present result. It is also of interest to note that the specific volume values obtained for the quenched specimen are in good agreement with those published by earlier investigators [8], the difference generally being only about 0.0010 cm^3g^{-1}.

There is good reason for the general agreement found by various investigators concerning the specific volume and degree of crystallinity of quenched samples ~1.5 to 3.0 mm thick, the explanation being found in the details of the kinetics of cristallization [3]. As noted in section 2.3, even 3-mm-thick samples removed from a hot mold and "quenched" in air have a specific volume, and hence a degree of crystallinity, not too far removed from that characteristic of an efficiently quenched specimen of similar dimensions.

Based on the results mentioned above, it would appear that the degree of crystallinity of quenched samples 1.5 mm thick prepared elsewhere, using the technique mentioned in section 2.3, should be close to the same as was found in the present investigation. However, samples differing significantly in molecular weight, or containing a greatly different number of heterogeneous nuclei, may lead to different results. Agreement with the present work should only be expected in the cases where the method employed to measure the degree of crystallinity is capable of sensing the presence of all the crystalline regions, large and small, and measures the mass fraction of the polymer that is crystalline. The degree of crystallinity of a quenched specimen will increase markedly if it is heated much above 115° C for any length of time, so that the degree of crystallinity becomes a function of both time and temperature between ~115° and 216° C. It is therefore recommended that comparisons between the results of various types of measurement of the degree of crystallinity not be made in this temperature interval by using quenched samples.

The degree of crystallinity of the 5-day specimen, $\chi_x=0.82\pm0.05$, cannot be compared directly with the results of earlier work. This follows from the fact that this sample was crystallized considerably longer, and is certainly more highly crystalline, than any used previously. Owing to the reproducibility

and stability of the 5-day specimen, it is recommended that this type of crystalline sample, rather than one crystallized at a specified cooling rate [4, 5], be used in future investigations aimed at a comparison of methods.

A comparison of results that should be free of errors due to sample variation may be made in the case of authors who have determined the degree of crystallinity of two specimens of known specific volume, and therefore are able to compute the specific volume of the pure amorphous and the pure crystalline material. Using degree of crystallinity data on several specimens obtained by the infrared method, Matsuo [5] has calculated that the specific volume of purely crystalline poly(chlorotrifluoroethylene) at 25° C would be 0.4575 ± 0.0015 cm^3g^{-1}. This is in excellent agreement with the value $\overline{V}_c = 0.4577 \pm 0.0015$ cm^3g^{-1} obtained in the present study.[8] However, for the pure glassy state at the same temperature, we find $\overline{V}_g = 0.4820 \pm 0.0015$ cm^3g^{-1}, whereas Matsuo gets the much higher value 0.4901 ± 0.0006 cm^3g^{-1} for the pure "amorphous" component. The latter value cannot be reconciled with the present data.

Support for the validity of the suggested $\overline{V}_g$ value may be found in Matsuo's specific-volume data on thin films when considered together with information concerning the kinetics of crystallization. By subjecting a film 0.03 mm thick to strong quenching, Matsuo [5] was able to produce polymer that had a specific volume of 0.4820 cm^3g^{-1} at 25° C. Now this figure is just that predicted by the present treatment for the specific volume of the pure glassy state at 25° C, whereas Matsuo's infrared measurements indicated that material of this type was about 25 percent crystalline. Therefore, evidence from another source which indicated that a film treated in this way is essentially noncrystalline, would support the present results. Assuming that such a thin film is quenched through the relatively small temperature interval where the crystallization is quite rapid in a time interval on the order of a tenth of a second or less it is clear from kinetic data [3] that the specific volume of the polymer would never be able to get appreciably below $\overline{V}_l$, i. e., it would suffer very little crystallization. Even if one supposed that the degree of crystallinity scale as measured from $\overline{V}_l$ was in error by a factor of 2, the degree of crystallinity of the 0.03-mm quenched-film studies by Matsuo could hardly exceed 5 percent, and it is probably considerably less. It is believed that the above argument indicates that the specific-volume value predicted here for the pure glassy state at 25° C is more nearly correct than the higher figure given by Matsuo.

[8] The unit cell determined from X-ray studies (see [21 and 22]) yields $\overline{V}_c = 0.47$ cm^3g^{-1} at 25° C. However, the estimated error in this figure is in the vicinity of several percent (private communication from H. S. Kaufmann).

6.2. Practical Method of Determining χ Near Room Temperature

It is worth pointing out that the degree of crystallinity of poly(chlorotrifluoroethylene) may readily be measured from a single specific-volume measurement taken near room temperature. For example, using the data in table 1, it is found that at 20° C that

$$\chi_s = (0.4814 - \overline{V}_s)/0.0241. \tag{36}$$

Measurements of the specific volume are easily made to 0.0001 cm^3g^{-1} in this temperature region. Equations applicable at other temperatures may be readily found by using the data in table 1.

6.3. Properties of the Pure Supercooled Liquid, Glassy, and Crystalline Phases

In the course of calculating the degree of crystallinity of the quenched and crystallized samples, we have indicated *passim* the manner in which the specific volume of the purely amorphous and purely crystalline phases of this polymer were obtained at various temperatures. The results are summarized in table 1 (figures in ordinary type) and plotted as dashed lines in figure 1.

The line describing the specific volume of the liquid and supercooled liquid phases as a function of temperature has a definite positive curvature. This is suggested even by the statistical analysis of the points actually observed for the liquid and supercooled region between 260° and 190° C, a straight line of the form $\overline{V}_l = \alpha + \beta T$ not fitting the data nearly as well as the curved line $\overline{V}_l = \alpha + \beta T + \gamma T^2$, and thereby being excluded as a proper fit. The more detailed analysis given in the paper, which essentially fixes $\overline{V}_l$ at T_g, using volume-temperature derivatives measured near T_g, conclusively demonstrates that fitting the liquid and supercooled liquid data with a straight line would have been considerably in error.

The predicted specific volumes of the pure glassy state of this polymer are of interest, especially when compared with those of the pure crystal. Perhaps the most notable point here is that the fractional free volume in the glassy state decreases with lowering temperature. At T_g, the fraction of free volume in the glass, which is calculated as $[\overline{V}_g - \overline{V}_c]/\overline{V}_g$, is 0.053. This quantity falls to 0.046 at −40° C. There is little doubt concerning this result, at least from a qualitative standpoint. The difference between the specific volumes of the quenched and crystallized samples becomes considerably less in the same temperature interval to an extent that greatly exceeds the experimental error (note diminishing value of $\overline{V}_q - \overline{V}_x$ below T_g in figure 3). This, taken together with the fact that χ_x and χ_q, whatever their true values, must certainly be constant below T_g, then leads to the result that the glass must shrink faster than the crystal.

The free volume of the glassy state at T_g defined in the usual way as $\phi_g=[\overline{V}_g(T=T_g)-\overline{V}_g(T=0°K)]$ is found to be 0.023 cm^3g^{-1}, using eq (35). Actually, this value is a little too high owing to the fact that the volume-temperature derivative of the glass tends toward zero at 0°K as depicted in figure 6, and it is estimated that the true value of ϕ_g is nearer 0.022 cm^3g^{-1}. This compares favorably with the value 0.019 to 0.025 cm^3g^{-1} found to be consistent with the viscosity data for many linear polymers.

The relatively large additional rise of specific volume in the pure amorphous phase, which begins near T_g (compare $\overline{V}_l$ and $\overline{V}_g$ curves in figure 1), marks the inception of the supercooled liquid state. Thus, the fractional free volume of the glassy state increases slowly and monotonically up to T_g, where a large excess fractional free volume begins to make its appearance. Factors involved in the relatively small but nevertheless real change of fractional free volume with temperature in the glassy state will be mentioned subsequently.

The relationship between the volume-temperature derivatives of the pure liquid, supercooled liquid, glassy, and crystalline phases over a wide range of temperature is depicted in figure 6, where the quantities mentioned are plotted on an absolute temperature scale.

The dashed line on the left-hand side of the lower curve in figure 6 represents approximately the type of behavior one would expect at low temperatures for the volume-temperature derivative of the pure crystalline phase, $d\overline{V}_c/dT$. This line was sketched in using as a guide a common extension of Grüneisen's theory relating specific heat and the volume-temperature derivative [15, 16, 17], which states that

$$d\overline{V}_c/dT=\overline{V}^0\ [Q_0C_v/(Q_0-KE)^2]. \qquad (37)$$

Here C_v is the specific heat at constant volume, E the energy of the intermolecular vibrations in the system, $\overline{V}$ the volume at 0° K, Q_0 a constant usually expressed in calories per mole, and K a constant that depends on the details of the intermolecular potential.[9] At low temperatures Q_0 is considerably in excess of KE, causing the temperature dependence of $d\overline{V}_c/dT$ to vary directly as C_v. Now according to the theories of Einstein [18] and Debye [19], the specific heat of a crystal is zero at 0° K, rises at first in an increasingly steep manner, and then begins to level off at its "classical" value near a characteristic temperature, θ. Hence, from eq (37) we must expect the volume-temperature derivative of the crystalline phase of the polymer to behave in a qualitatively similar way. It has been assumed in sketching in the dashed line in figure 6 that θ is 200° K, a reasonable value for a molecular crystal. In contrast to the models with 3 degrees of freedom treated by Einstein and Debye, it is likely in the present case that only the two

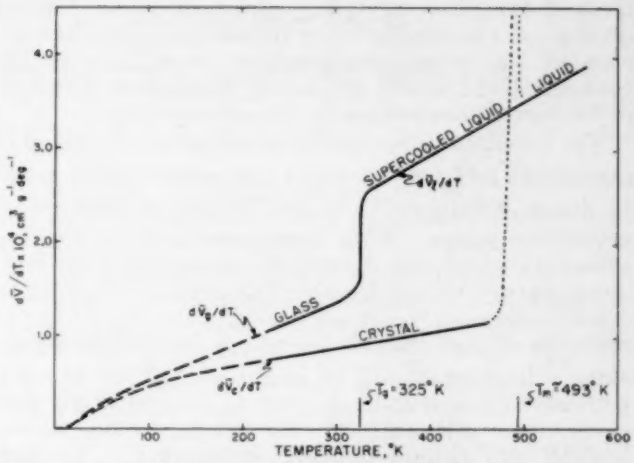

FIGURE 6. *Estimated volume-temperature derivatives of the pure supercooled liquid, glassy, and crystalline states of poly(chlorotrifluoroethylene) as a function of temperature (Kelvin scale)*

------ lines sketched in using eq (37) as a guide; ..... approximate type of melting behavior to be expected for the hypothetical completely crystalline phase.

degrees of freedom transverse to the long molecular axis are connected with the expansion of the polymer crystal, and that more than one θ temperature is involved, but this does not alter the qualitative description given. The gradual increase of $d\overline{V}_c/dT$ evident in the classical region may be partly due to a continued rise of C_v, but it seems likely that the diminishing value of the term $(Q_0-KE)^2$ arising from the increase of E with temperature is also important. To the extent that the latter term is responsible for the moderate increase of $d\overline{V}_c/dT$ in this region, the expansion of the polymer crystal is attributable to the tendency of thermal agitation (as measured by E) to overcome lattice forces (as represented in at least an approximate way by Q_0).[10]

The volume-temperature derivative, $d\overline{V}_g/dT$, of the pure glassy state in the region below 233° K has been sketched in figure 6 with essentially the same concepts in mind. The value $\theta=175°$ K was used. Thus the glassy state has been regarded as having an "average" intermolecular potential, so that it is theoretically permissible to assign θ, Q_0, and K values to it. The construction of the dashed line representing $d\overline{V}_g/dT$ at low temperatures in figure 6 is in accord with the experimental observation [8] that the length-temperature coefficient of quenched poly(chlorotrifluoroethylene) shows a continuous rise at low temperatures, which tends to level off at around 213° K. This suggests a θ temperature of around 150° to 200° K.

Considering the points mentioned above concerning the low-temperature behavior, together with the results obtained in a straightforward way from the experimental data at higher temperatures (solid lines in figure 6), there is no doubt that starting at very low temperatures, the volume-temperature deriva-

[9] The constant Q_0 is known to be related to the melting temperature [16], and it is therefore presumably related to the lattice energy. Q_0 is generally of the order of magnitude of 10^3 calories/mole for metals, and K of the order two.

[10] The authors thank R. K. Kirby for many helpful discussions concerning the volume-temperature behavior of solid bodies.

tives of the pure crystalline and pure glassy states diverge as the temperature increases. The divergence of the volume-temperature derivatives is, of course, related to the previously mentioned increase of fractional free volume in the glassy state.

The question must now be raised as to why $d\overline{V}_g/dT$ exceeds $d\overline{V}_c/dT$. Certainly a part of this effect must be due to differences in Q_0 and $\overline{V}^0$ for the glassy and crystalline states. $\overline{V}^0$ is certain to be larger for the glassy state than the crystalline one owing to the less dense nature of the former; the polymer molecules are disordered in the glassy state and therefore occupy more space than they do in the crystal. This factor alone will cause $d\overline{V}_g/dT$ to exceed $d\overline{V}_c/dT$ by several percent. Also, it is likely that Q_0 is smaller for the more open structure of the glassy state, again leading to a volume-temperature derivative for the glassy state exceeding that of the crystalline. Differences in C_p, arising at least in part from the existence of different θ temperatures for the two states, must also contribute. It is worth pointing out in this connection that the precise specific-heat data of Bekkedahl and Matheson [20] on natural rubber in the completely amorphous (glassy) and partially crystalline conditions reveal that C_p for the glassy phase everywhere (except at 0° K) exceeds that of the crystalline. These data imply that C_p(glass)$>$ C_p(crystal). Their plot of C_p versus T bears a remarkable resemblance to the volume-temperature derivative plots shown in figures 2 and 6.[11]

In view of the foregoing, it is not surprising that approximation (7) fails when subjected to a rigorous test, because there are excellent theoretical reasons for believing that $d\overline{V}_g/dT$ must exceed $d\overline{V}_c/dT$, except at 0° K, where they are both zero. It is clear from the present study that this approximation should be avoided whenever attempting a precision calculation of the degree of crystallinity, or in estimating the properties of pure phases.

Evidence based on dielectric data shows that the crystalline phase is orientationally disordered to some extent down to low temperatures, and that this disorder increases as the temperature is raised [2]. However, there is no indication from either the dielectric or specific-volume measurements that the gradually increasing degree of disorder culminates in a first-order phase transition in the crystalline state anywhere in the range −40° to +216° C. The $\overline{V}_c$ data thus refer to a crystal that possesses a certain degree of imperfection due to molecular motion.

6.4. Melting Process

The semicrystalline 5-day sample exhibits melting over a wide range of temperature. This is evident in figures 1, 2, and 5. The broad nature of the melting phenomenon in this polymer may be attributed to the presence of small crystallites that melt well below the equilibrium melting temperature. The smallest of these begin to melt at about 120° C, whereas the largest and most perfect crystallites in the sample, which are sufficient in number to appreciably affect the volume, melt at the quasi-equilibrium melting temperature, T'_m=216° C. (Somewhat larger crystallites of insufficient number to be detected may persist above T'_m.) As indicated earlier, the latter figure is still below the equilibrium melting temperature, T_m. Even then, it is worth noting that the 5-day specimen melts above the value 210° to 212° C frequently quoted in the literature [1, 4, 21, 22]. The last half of the sample melts in a temperature interval of about 6°C. The fractional free volume in the liquid at $T_m \cong 220°$ C, as calculated by using $(\overline{V}_l - \overline{V}_c)/\overline{V}_l$, is 0.11. This is to be compared with the value 0.053 at T_g=52° C.

6.5. Glass Transition

The glass transition in a semicrystalline polymer has been treated in this paper as if it occurred abruptly at the intersection of two curved lines, one representing the volume-temperature relation of the system glass plus crystal below T_g, and the other the system supercooled liquid plus crystal above T_g. In any such analysis it is necessary to avoid the use of data too close to the nominal glass temperature owing to the fact that the glass transition, which takes place in the amorphous part of the polymer, is not actually abrupt. Proof of the finite breath of the transition is not lacking in the present case. For instance, the specific volume of the quenched sample undergoes a marked premonitory increase beginning 10° to 15° C below T_g. The basically somewhat diffuse character of this transition in completely amorphous bodies was clearly pointed out by Kauzmann in his review paper [23] on the nature of the glassy state. However, there is no basic thermodynamic objection to treating this transition in both completely amorphous and semicrystalline media as if it took place abruptly at a certain temperature corresponding to the intersection of two curved lines.

The method used to obtain T_g, which consisted of plotting $(\overline{V}_g - \overline{V}_x)$ against T and noting the point of intersection, requires comment. This procedure has the advantage of not requiring an explicit knowledge of the form of the two curved lines that make the two intersecting volume-temperature curves of each sample. However, this method would have to be applied with caution if the glass temperature varied with the degree of crystallinity. It is possible to show for poly(chlorotrifluoroethylene) that T_g does not depend markedly on the degree of crystallinity. By fitting the data given in table 1 describing the specific volume above and below T_g for a given semicrystalline specimen to an equation of the form $\overline{V}_g = a + bT + cT^2$, and simultaneously solving the two equations, it was shown that the glass temperatures of the two samples were within 1.2° C of each other. This shows that the glass-transition temperatures of

[11] A plot of C_p versus T should quite generally be expected to strongly resemble a plot of $d\overline{V}/dT$ versus T for corresponding states. The rough specific-heat data for crystallized poly(chlorotrifluoroethylene) [4] bear a marked similarity to the $d\overline{V}_c/dT$ data shown in figure 2. Unfortunately, the comparison cannot be carried further because the specific-heat data are faulty below T_g for the quenched specimen, the glass transition having been overlooked as the result of a calorimeter start-up effect.

the two semicrystalline specimens are identical within experimental error, and justifies the use of the plot of $(\overline{V}_g - \overline{V}_x)$ versus T that was employed to obtain the reported value $T_g = 52°$ C. Data between $-40°$ and $+25°$ C, and $+65°$ and $+115°$ C were used in this analysis, and all curve-fitting was accomplished by using least-squares.

Precisely the same input data lead to T_g values of 50° and 45° C for the samples if an equation of the form $\overline{V}_x = a + bT$ is used with a least-squares fit to represent the specific-volume–temperature relations above and below T_g. The value $T_g = 52°$ C is to be preferred owing to the fact that it is based on an analysis that admits of the curvature inherent in the experimental specific-volume–temperature data. The apparent difference found for the glass-transition temperature of the two specimens using the "straight-line" analysis does not mean that T_g actually varies with x for this homopolymer, but is simply an artificial result arising from the inability of a straight line to accurately represent the data even at temperatures well removed from the glass transition.

WASHINGTON, November 1, 1957.

7. References

[1] F. P. Price, J. Am. Chem. Soc. **74,** 311 (1952).
[2] J. D. Hoffman, A. H. Scott, A. J. Curtis, D. J. Scheiber, and J. I. Lauritzen, Jr., (manuscript in preparation).
[3] J. D. Hoffman and J. J. Weeks (manuscript in preparation).
[4] J. D. Hoffman, J. Am. Chem. Soc. **74,** 1696 (1952).
[5] H. Matsuo, J. Polymer Sci. **25,** 234 (1957).
[6] H. Matsuo, Bul. Chem. Soc. Japan **30,** 593 (1957).
[7] F. P. Price, J. Chem. Phys. **19,** 973 (1951).
[8] L. Mandelkern, G. M. Martin, and F. A. Quinn, Jr., J. Research NBS **58,** 137 (1957) RP2703.
[9] R. B. Sosman, Properties of silica, p. 307 (Chemical Catalogue Co., New York, N. Y., 1927).
[10] W. Souder and P. Hidnert, BS Sci. Pap. **21,** 1 (1926–1927) S524.
[11] L. Mandelkern, Chem. Revs. **56,** 903 (1956).
[12] J. D. Hoffman and J. J. Weeks (manuscript in preparation).
[13] R. F. Boyer, J. Appl. Phy. **25,** 185 (1954).
[14] R. F. Boyer, Changement de Phases, Compt. rend. 2d reunion de chemie physics, p. 384 (1952).
[15] B. Dayal, Proc. Indian Acad. Sci. **20** (1944).
[16] Am. Inst. Physics Handbook, p. 4–63 (McGraw-Hill Book Co., New York, N. Y., 1957).
[17] W. Hume-Rothery, Proc. Phys. Soc. (London) **57,** 209 (1945).
[18] A. Einstein, Ann. physik. **22,** 180 (1907); **34,** 170 (1911).
[19] P. Debye, Ann. physik. **39,** 789 (1912).
[20] N. Bekkedahl and H. Matheson, J. Research NBS **15,** 503 (1935) RP844.
[21] H. S. Kaufman, Tech. Assoc. Pulp Paper Ind. **37,** 140 (1954).
[22] H. S. Kaufman, J. Am. Chem. Soc. **75,** 1447 (1953).
[23] W. Kauzmann, Chem. Revs. **43,** 219 (1948).

Journal of Research of the National Bureau of Standards Vol. 60, No. 5, May 1958 Research Paper 2863

Heat and Ultraviolet Aging of Poly(vinyl chloride)[1]

Charles F. Bersch, Mary R. Harvey, and Bernard G. Achhammer

Four poly(vinyl chloride) polymers prepared with different initiators were exposed to ultraviolet radiant energy and to heat, in a vacuum and in air. The gaseous products evolved were analyzed by mass spectrometry. Changes in chemical structure were followed by infrared spectrophotometry. Benzene was among the products evolved in most cases, and acetone was produced during exposure to heat in air. Catalyst fragments or other incorporated impurities affected initiation at very mild conditions. Susceptibility to degradation increased with increasing oxygen content and unsaturation of the untreated polymer. Pyrolysis studies indicated a two stage degradation: (1) dehydrochlorination, and (2) decomposition of the resultant polyene chain. Color formation was attributed to both oxidation and conjugated unsaturation because exposure in air following exposure in a vacuum, and vice versa, caused bleaching of the degraded polymer.

1. Introduction

The degradation of poly(vinyl chloride) has been studied extensively [1 to 16] [2] because of the commercial importance of this material. The mechanism of decomposition has not been resolved and the initiation step is especially elusive. Druesdow and Gibbs [7] suggested peroxides and catalyst residues as possible sites for initiation of degradation. Fox [4] and his coworkers proposed random splitting out of hydrogen chloride, and Arlman [8, 13] suggested end initiation plus random oxidation. Baum and Wartman [16] reported that the sites for initiation are chain ends at about 150° C and tertiary chlorine atoms above 190° C.

Dehydrochlorination is generally accepted as the propagation step. An allyl-chloride-type reaction is considered as the probable mechanism. However, there are other products from and changes occurring in the polymer. Mack [15] suggested that, in the presence of oxygen, dehydrochlorination and consequent development of conjugated double bonds compete with oxidation of the conjugated system. Both chain scission and crosslinking have been observed [1, 2, 3, 7], often simultaneously.

The identification, measurement of the amount evolved, and rate of evolution of the products on exposure to laboratory weathering or pyrolysis [18 to 22] are among the most frequently used methods for investigating the degradation process. The evolution of hydrogen chloride has been studied in a vacuum, oxygen, air, nitrogen, hydrogen, and hydrogen chloride. Wilson [11] found another product, a condensable gas, which he identified as water. In his work on *sec*-butyl chloride as a prototype of poly(vinyl chloride), Kenyon [1] found carbon dioxide, methane, hydrogen chloride, and masses at 95, 97, 110, and 112 among the gaseous products analyzed by mass spectrometry. Benzene has been identified as a product of pyrolysis [18 to 22].

The complexity of the situation has led to many apparent contradictions. Some investigators have proposed that the loss of hydrogen chloride is autocatalytic [3 to 7], others deny this [13], and still others have found autocatalysis only in certain atmospheres [1, 3, 7, 15]. Color formation and loss of hydrogen chloride are usually considered as related, but Wilson [11] suggested that the color developed on degradation was at least partially due to the action of light on oxygen-containing impurities. Another source of controversy has been whether color in the degraded polymer is bleached in the presence of oxygen [5 to 10].

This paper describes an attempt to clarify some aspects of the degradation process in poly(vinyl chloride). The effects of several different initiators on the stability of poly(vinyl chloride) on exposure to heat and to ultraviolet radiant energy were investigated. Several exposures were conducted in a vacuum to isolate breakdown of the basic polymer from oxidative degradation. Analyses of the gaseous degradation products and the polymer residue were made at various stages in the treatments to follow the chemical structural changes. Color changes were studied in the hope of correlating them with the structural changes or conditions of exposure.

2. Material and Procedures

2.1. Material

Table 1 lists the four poly(vinyl chloride) polymers used in this investigation. The polymers catalyzed with benzoyl peroxide and 2-azo-bis(isobutyronitrile), respectively, were polymerized from vinyl chloride monomer distilled directly from a storage cylinder into glass tubes containing the catalysts. The tubes containing the monomer, frozen under liquid nitrogen, were sealed under vacuum. Polymerization was accomplished by immersion of the tubes in a water bath at 40° C for 3 days. For the gamma-initiated polymer, the vinyl chloride monomer was fractionally distilled under essentially equilib-

TABLE 1.—*Description of poly(vinyl chloride) materials*

γ-PVC	Vinyl chloride bulk-polymerized in a vacuum by exposure to gamma (Co-60) radiation.
bp-PVC	Vinyl chloride bulk-polymerized in a vacuum, with initiation by 0.10-mole percent benzoyl peroxide.
azo-PVC	Vinyl chloride bulk-polymerized in a vacuum, with initiation by 0.02-mole percent 2-azo-bis(isobutyronitrile).
101-PVC	Geon 101, supplied by the B. F. Goodrich Chemical Co.

[1] This paper was presented before the Division of Polymer Chemistry at the 130th meeting of the American Chemical Society in Atlantic City, New Jersey, Sept. 16–21, 1956.

[2] Figures in brackets indicate literature references at the end of this paper.

rium conditions. A 33-in. column packed with glass helices was used. The middle third of the distillate was redistilled into glass tubes, which were sealed as above, and the tubes were then inserted in a 0.3-curie cobalt-60 source. The center of each tube was 1.5 in. from the center of the source. The time of exposure was approximately 270 hr.

The three laboratory-prepared polymers were in the form of solid bars when polymerization was completed. These bars were pulverized with a stainless-steel mortar and pestle under liquid nitrogen. The fractions of these polymers and of the commercial polymer that passed through the U. S. Standard No. 325 Sieve (nominal opening 44μ) were used for these experiments.

The polymers were studied in powder form. Poly(vinyl chloride) films were not used because they retain the polar solvents necessary to dissolve the polymers. This can interfere with both the mechanism of degradation and the interpretation of analytical data. Pressed pellets of the polymer are not satisfactory because they provide a very small surface to volume ratio in addition to being partially degraded as a result of the heat required in the pelleting operation.

A typical sample used for an experiment weighed from 0.15 to 0.30 g. The choice of sample size was a compromise between the desire for a monoparticle layer in the exposure tube and the necessity for sufficient pressure from the gaseous degradation products to make mass spectrometric analysis practical.

2.2. Equipment

The polymer powder samples were exposed, in quartz tubes, to various conditions of heat or ultraviolet radiant energy or both, in a vacuum and in air. The exposure tube, exposure chamber, and general procedure have been described previously [24]. The only alteration was the use of F–1 fluorescent sunlamps in place of RS sunlamps for the ultraviolet radiant energy exposures. Six F–1 lamps were mounted in banks of three in planes 3 in. above and below the polymer samples.

2.3. Exposures and Analytical Procedures

The major experimental work consisted of exposure of the same samples of the four polymers to the following three conditions, in sequence: (1) Ultraviolet radiant energy, in a vacuum, at 45°±2° C for 100 hr; (2) 100°±2° C, in a vacuum, for 100 hr; and (3) 100° ±2° C, in air, for 100 hr. The gaseous degradation products evolved during each stage were analyzed by mass spectrometry. Color determinations were made after each treatment, using the Munsell colors of the Intersociety Color Council–National Bureau of Standards (ISCC–NBS) Method of Designating Colors. Samples of the polymer powder were removed from duplicate tubes after each exposure for infrared analysis. The powder removed for infrared analysis was pelleted with potassium bromide [23], and a sodium chloride prism was used to determine the infrared spectrum in the 2- to 15-μ region.

Several additional experiments and analyses were made. 101–PVC was exposed to 100°C, in air, for 25 hr, in an attempt to induce hydroperoxide formation, prior to a sequence of exposures and analyses, as described above. 101–PVC and azo-PVC were exposed to 100° C, in a vacuum, for 200 hr, with mass spectrometric analyses of the gaseous products after 1, 3, 5, 10, 20, 30, 50, 100, and 200 hr; 101–PVC was used in a similar experiment in which ultraviolet radiant energy was used in place of heat. 101–PVC was exposed to 100° C in a vacuum for 150, 288, and 400 hr; to ultraviolet radiant energy at 50° C in air, for 400 hr; and to ultraviolet radiant energy at 45° C, in a vacuum, for 150, 288, and 400 hr.

Samples of 101–PVC and γ-PVC were pyrolyzed in a small evacuated tube furnace. The gaseous products were passed directly into a mass spectrometer. The temperature of pyrolysis was raised in steps from 87° to 429° C, and the mass spectra were recorded at each step. The equipment, method, and some of the results of this pyrolysis have been described by Bradt [19, 20].

3. Results

3.1. Analysis of Original Polymers

Table 2 shows the results of the oxygen-content determinations on the four polymers. The two methods used are similar, and the results can be compared directly.

Infrared absorption spectra of the untreated polymers are shown in figure 1. The γ-PVC polymer (dotted line) shows a very weak absorption at 6.27μ, which is attributed to stretching vibrations of conjugated C=C structures [30, p. 31]. The double-bond structure was probably formed as a result of some dehydrochlorination of the polymer while exposed to gamma radiation. Mass spectrometric analysis of the gases above the γ-PVC polymer immediately after polymerization showed a small amount of hydrogen chloride. 101–PVC (solid line) has a weak band at 6.05μ assigned to C=C stretching of a nonconjugated nature [30, p. 31]. The presence of double bonds in the untreated 101–PVC may also be due to loss of hydrogen chloride during polymerization [15, 17]. Azo–PVC (dashed and dotted line) shows a weak absorption at 9.83μ, which was not identified, and a generally lower transmittance. There also appears to be a very weak absorption at about 6.27 μ, as in

TABLE 2. *Oxygen content of poly(vinyl chloride) polymers*

Polymer	Oxygen
	wt %
101-PVC	[a] 0.90
γ–PVC	[b] .21
bp–PVC	[b] .65
azo–PVC	[b] .43

[a] By the method of Walton, McCulloch, and Smith, J. Research NBS **40**, 443 (1948) RP1889. Oxygen content reported here refers to <44-μ particles used in this investigation; the oxygen content of the bulk 101–PVC was 0.18 percent as measured by the same method.

[b] By a modification of the Unterzaucher direct microdetermination of oxygen, S. Ishihara, unpublished.

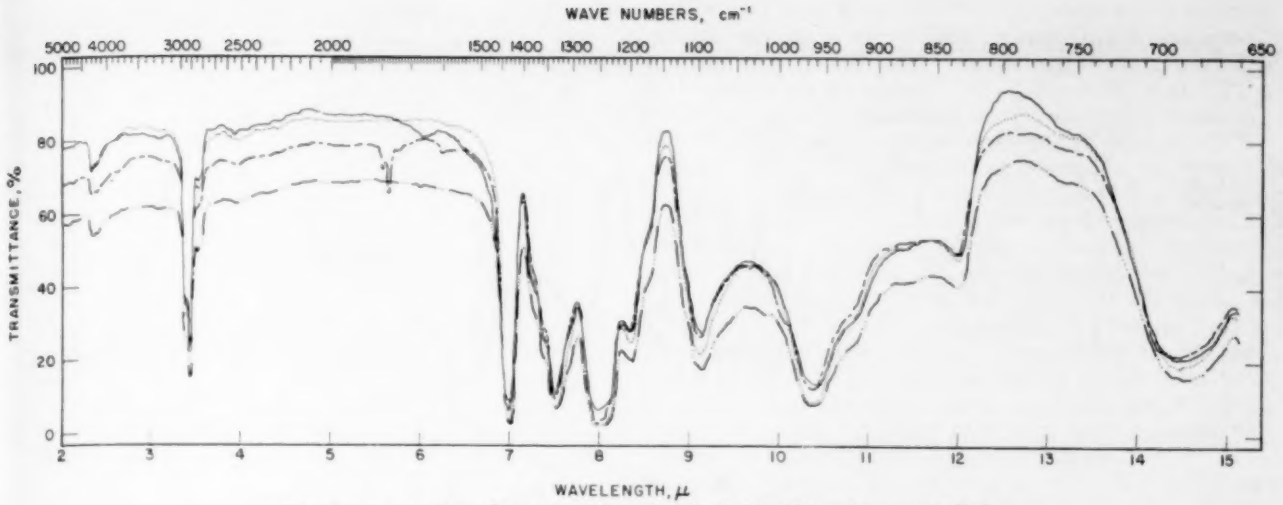

FIGURE 1. *Infrared spectra of the poly(vinyl chloride) polymers studied.*
101-PVC; γ-PVC; bp-PVC; azo-PVC.

γ-PVC. In addition to absorptions at 5.57 and 5.64μ assigned to carbonyl vibrations in the catalyst used [30, p. 111], bp–PVC (dashed line) has a band at 6.22 μ attributed to C=C stretching vibrations. The band at 10.08μ is probably due to unreacted catalyst [30, p. 106].

An absorption around 12μ in the region associated with hydroperoxide absorption by Shreve et al. [25] was present in about equal amounts in all the polymers. No changes were observed in this absorption either as a result of degradative treatment of the polymer or during the attempt to induce hydroperoxide formation. Krimm and Liang [31] assign this band to chain stretching in the polymer.

3.2. Mass Spectrometric Analysis of Degraded Polymers

The gaseous degradation products evolved by the polymers on exposure to ultraviolet radiant energy are shown in table 3. The γ-PVC gave 50 to 80 percent less gaseous products than the other polymers, and showed less discoloration as a result of the exposure. The benzene and large amount of carbon dioxide from the bp-PVC polymer were attributed to breakdown of the catalyst used. Hydrogen was a product of 101–PVC only, and

TABLE 3. *Gaseous products evolved by poly(vinyl chloride) exposed to ultraviolet radiant energy in a vacuum at 45° C for 100 hr*

Product	Amount evolved per gram of sample—		
	101-PVC	bp-PVC	γ-PVC
	Micromoles	*Micromoles*	*Micromoles*
Hydrogen chloride	4.3	4.6	0.9
Water	1.0	1.2	1.2
Carbon dioxide	1.0	13.5	1.1
Carbon monoxide and/or nitrogen	1.1	0.0	0.9
Benzene	0.0	.6	.0
Hydrogen	.6	.0	.0
Final color [a]	10.0 YR 8/4 (pale orange yellow)	5.0 YR 5/5 (light brown)	7.5 YR 9/2 (pale yellowish pink)

[a] According to the Munsell System and the ISCC-NBS Method of Designating Colors.

appeared at each stage of the degradation. The colors developed after the exposure to ultraviolet radiant energy are shown for purposes of comparison. The intensity of the color for any sample correlates with the total amount of products reported for that sample, but not with the amount of hydrogen chloride reported for that sample.

The 101–PVC, exposed at 100° C in air for 25 hr prior to exposure to ultraviolet radiant energy, gave results essentially the same as obtained with 101–PVC without pretreatment. The pretreatment apparently did not induce formation of hydroperoxides in the polymer.

The same samples that were exposed to ultraviolet radiant energy as described above were further exposed to heat in a vacuum. The results obtained with bp-PVC, shown in table 4, are typical of those from the other polymers with two exceptions. The products from γ-PVC were too small to measure in the mass spectrometer, and the benzene evolved by bp-PVC was about three times as much as was evolved by the other polymers.

The mass spectrometer does not measure hydrogen chloride accurately because of adsorption on the walls of the expansion chamber [26]. The presence of water vapor and carbon dioxide in the mass spectrometer background and as products of poly(vinyl chloride) degradation further complicate analysis. Since efforts to evaluate these factors were unsuccessful, the values reported for hydrogen chloride, water, and carbon dioxide must be con-

TABLE 4. *Gaseous products evolved by bp-PVC polymer exposed to 100° C in a vacuum for 100 hr*

Prior treatment: 100-hr exposure to ultraviolet in a vacuum at 45° C

Product	Amount evolved per gram of sample—	
	A	B
	Micromoles	*Micromoles*
Hydrogen chloride	28.1	17.4
Water	1.9	9.1
Carbon dioxide	0.9	1.1
Benzene	.3	0.2

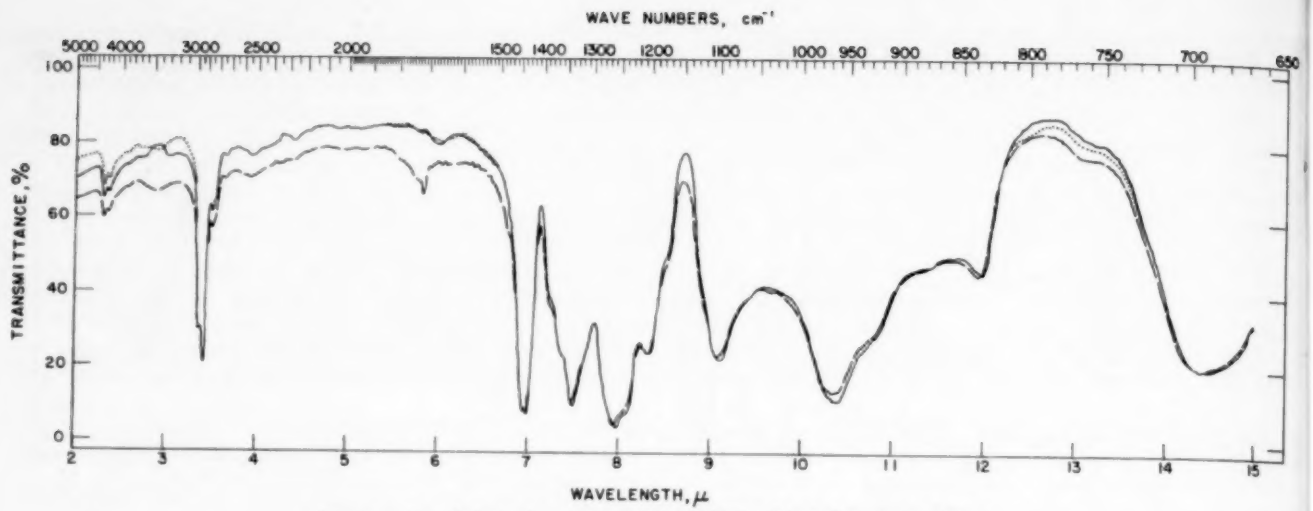

FIGURE 2. *Infrared spectra of 101-PVC subjected to degradation.*

———— Untreated; ..... 100-hr exposure to ultraviolet in a vacuum at 45° C.; ——— ——— ——— 100-hr exposure to ultraviolet in a vacuum at 45° C, plus 100-hr exposure at 100° C, in a vacuum, plus 100-hr exposure at 100° C in air.

sidered as approximations. Comparison of the results of experiments A and B in table 4 gives an indication of the poor reproducibility obtained when measuring hydrogen chloride and water simultaneously in the mass spectrometer. The example given is an extreme case for duplicate measurements.

The polymer samples previously exposed to ultraviolet radiant energy and to heat in a vacuum were finally exposed to heat in air. The water and carbon dioxide frozen from the air by liquid nitrogen when the air was being pumped from the tubes prior to mass spectrometric analysis masked these gases as possible degradation products. No hydrogen chloride was detected. About 0.1 micromole of benzene per gram of sample was found in the products of γ-PVC and bp-PVC, but not in the products of 101–PVC. Hydrogen was again a product of 101–PVC. From 2 to 23 micromoles of acetone per gram of sample were found in the products of all the polymers except γ-PVC, where the results were inconclusive because one sample showed no acetone and the other was accidentally contaminated with acetone.

TABLE 5. *Gaseous products evolved by 101-PVC polymer in 3-hr exposures to ultraviolet radiant energy and to 100° C in a vacuum*

Product	Amount evolved per gram of sample in 3 hr of exposure to—	
	Ultraviolet	Heat
	Micromoles	*Micromoles*
Hydrogen	0.36	0.20
Water	2.38	1.30
Carbon monoxide and/or nitrogen	0.53	0.27
Oxygen	.00	.02
Carbon dioxide	.36	.51
C_7H_{16}	.00	.11
C_7H_{14}	.00	.41
Benzene	Trace	.02
Toluene	Trace	.10
Styrene	0.00	.04
Alkyl benzene	.00	.02

The products evolved by 101–PVC after 3 hr of exposure to ultraviolet radiant energy are shown in table 5. Traces of hydrogen chloride were reported after 50 and 100 hr of exposure, and hydrogen chloride was the major product after 200 hr of exposure. The results after 3 hr of exposure to heat are also listed in table 5. The amount of hydrogen chloride evolved after 200 hr at 100° C was about 13 times as much as was reported for a 200-hr exposure to ultraviolet radiant energy.

Azo-PVC was also exposed to 100° C in a vacuum for 200 hr. Except for considerable amounts of unidentified nitriles [27] found in the first 30 hr, the amounts and types of products were similar to those found with the other polymers.

Uninterrupted exposures of 101–PVC to 100° C in a vacuum and to ultraviolet radiant energy at 45° C in a vacuum for 150, 288, and 400 hr resulted in hydrogen chloride, water, hydrogen, carbon monoxide, and carbon dioxide, plus small amounts of unidentified hydrocarbons. Benzene and toluene were found after exposure to heat but not after exposure to ultraviolet radiant energy.

3.3. Infrared Analysis of Degraded Polymers

The infrared absorption spectra obtained after carrying out the progressive exposure series on 101–PVC are shown in figure 2. Exposure to heat in a vacuum after exposure to ultraviolet produced no substantial change in the spectrum. The changes around 3 μ reflect compensation difficulties in the OH region due to water absorption in some potassium bromide pellets. Exposure to heat in air removed the weak band at 6.05 μ attributed to double bonds, and produced a broad carbonyl absorption band around 5.85 μ. The changes observed are of about the same order as, or larger than, those occurring in the other polymers under the same conditions.

Figure 3 shows the 5- to 7-μ region of the spectra of bp-PVC. The original polymer shows absorptions at 5.57 and 5.64 μ attributed to residual benzoyl

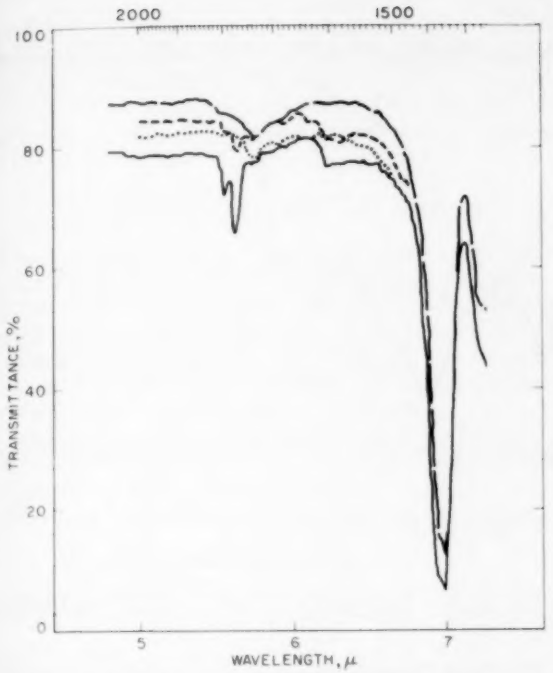

FIGURE 3. *Infrared spectra of bp-PVC subjected to degradation.*

———— Untreated; ------ ------ ------ 100-hr exposure to ultraviolet in a vacuum at 45° C; ---------- 100-hr exposure to ultraviolet in a vacuum at 45° C, plus 100-hr exposure at 100° C in a vacuum; —— —— —— 100-hr exposure to ultraviolet in a vacuum at 45° C, plus 100-hr exposure at 100° C in a vacuum, plus 100-hr exposure at 100° C in air.

peroxide catalyst, and at 6.22 μ attributed to conjugated double bonds. After exposure to ultraviolet radiant energy, the absorptions at 5.77 and 5.64 μ decreased considerably, whereas the absorption at 6.22 μ increased slightly. After subsequent exposure to heat in a vacuum, the absorptions at 5.57, 5.64, and 6.22 μ disappeared, and a carbonyl band appeared at 5.85 μ. Exposure to heat in air caused a rise in transmittance and a stronger and broader carbonyl absorption.

Figure 4 contains the spectra of untreated 101-PVC (solid line) and 101-PVC exposed to ultraviolet radiant energy in air at 50° C for 400 hr (dashed line). A wide absorption band extending from 2.7 to 4 μ with shoulders at about 2.85, 3.03, 3.50, and 3.77 μ is present in the spectrum of the degraded material. The absorption occurring between 3.7 and 4 μ is indicative of the OH stretching vibration of strongly hydrogen-bonded OH groups [30, p. 142]. The absorption around 2.7 to 2.85 μ has been assigned to the OH valence stretching of the unbonded hydroxyl group [30, p. 85], and the absorption in the 2.85- to 3.15-μ range may be caused by the OH vibration of intermolecular and intramolecular hydrogen bonds. The broad, intense carbonyl absorption in the 5.8- to 5.9-μ region is probably caused by the C=O stretch in a variety of structures such as aldehydes, ketones, acids, etc. The shoulder at 6.05 μ may indicate the presence of unconjugated double bonds.

Figure 5 shows the spectra of 101–PVC after exposure to 100° C in a vacuum for 150 and 400 hr. After 150 hr (dotted line), the absorption at 6.05 μ, attributed to unconjugated unsaturation, changed very little. Slight absorptions in the 6.25- and 6.65-μ regions indicate some formation of conjugated double bonds or possibly some aromatics. The absorption at 5.8 μ is attributed to carbonyl formation. The oxygen must have come from the polymer because mass spectrometry gave no evidence of leakage in the exposure tube. Except for an increase in the carbonyl absorption, there was little change after 400 hr of exposure.

3.4. Color Changes

Table 6 shows the color developed by each polymer at each stage in the set of experiments described in section 3.2. The higher the number before the slash mark, the lighter the color; the higher the number after the slash mark, the more intense the hue.

A comparison of the data in the second and third columns shows that oxygen causes bleaching of the color developed in polymers degraded in a vacuum. The γ-PVC developed the least discoloration. Bp-

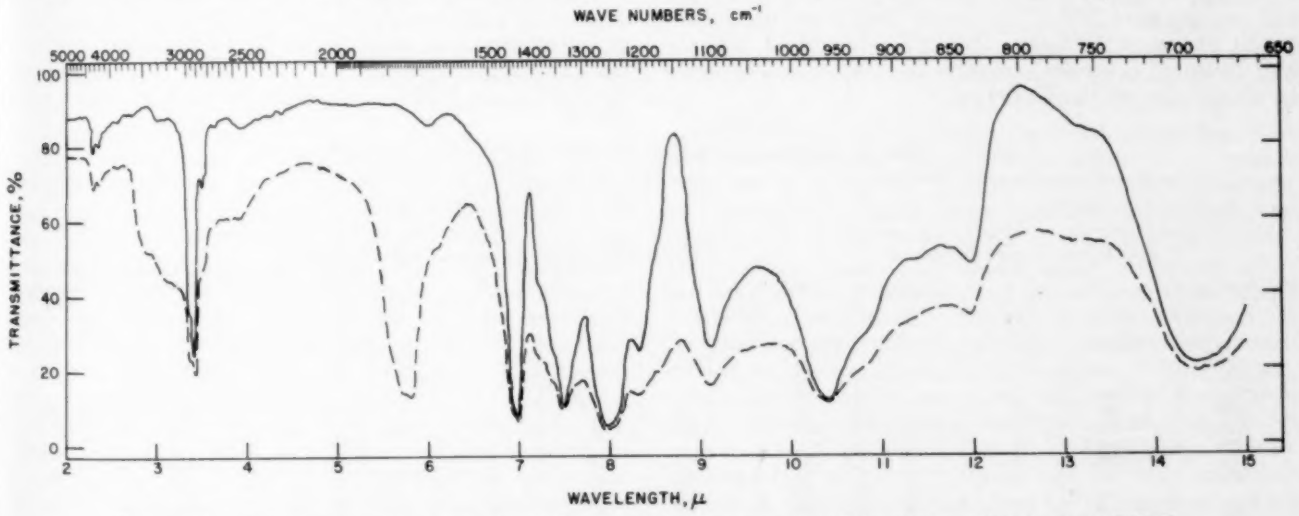

FIGURE 4. *Infrared spectra of 101-PVC before and after exposure to 400 hr of ultraviolet in air at 50° C.*

———— Untreated; —— —— —— treated.

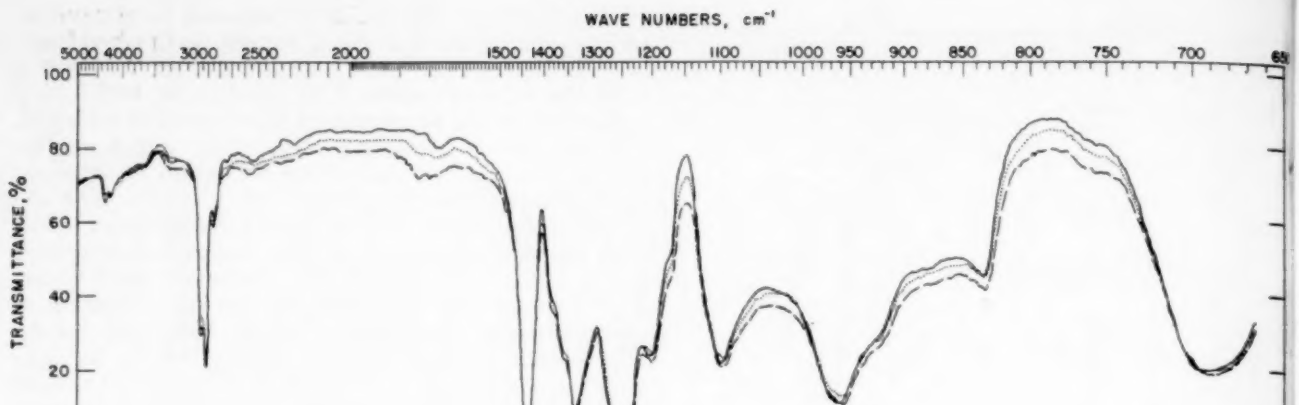

FIGURE 5. *Infrared spectra of 101-PVC subjected to heat degradation.*

———— Untreated; ---------- 150-hr exposure at 100° C in a vacuum; —— —— —— 400-hr exposure at 100° C in a vacuum.

TABLE 6. *Colors developed in degraded poly (vinyl chloride)*

Polymer	Munsell designation and color [a] after exposure to—		
	100 hr of ultraviolet in a vacuum	Plus 100 hr at 100° C in a vacuum	Plus 100 hr at 100°C in air
101-PVC	10.0 YR 8/4 (pale orange yellow)	2.5 R 3.5/4 (grayish red-dark red)	7.5 YR 7/4 (light yellowish brown)
γ-PVC	7.5 YR 9/2 (pale yellowish pink)	10.0 R 7.5/4 (moderate yellowish pink)	7.5 YR 9/2 (pale yellowish pink)
bp-PVC	5.0 YR 5/5 (light brown)	7.5 P 7/4 (pale purple)	10.0 R 8/2 (pale yellowish pink-grayish yellowish pink)
azo-PVC	7.5 YR 8/3.5 (pale orange yellow)	7.5 YR 7/4 (light yellowish brown)	10.0 YR 8/4 (pale orange yellow)

[a] The ISCC (Intersociety Color Council)—NBS Method of Designation Color.

PVC discolored most on exposure to ultraviolet radiant energy and 101-PVC discolored most on subsequent exposure to heat. Bp-PVC bleached slightly and changed color on exposure to heat after exposure to ultraviolet radiant energy.

3.5. Pyrolytic Degradation of 101-PVC and γ-PVC

The relative ratios of the major products evolved during continuous pyrolysis of γ-PVC and 101-PVC at various temperatures as analyzed by mass spectrometry are given in table 7. A small amount of hydrogen chloride was evolved from 101-PVC at 127° C. Benzene was a product of both polymers at about 175° C, along with relatively large amounts of hydrogen chloride. The maximum evolution of hydrogen chloride from 101-PVC occurred at 220° C, whereas for γ-PVC the maximum was at 238° C. The largest evolution of benzene and measurable amounts of mass 91, naphthalene, and anthracene were observed in the 220° to 240° C range. Above 300° C very little hydrogen chloride was evolved and mass 91 became the major product. Mass 91 represents the principal decomposition product of alkyl-aromatic compounds. It was accompanied by a large number of different hydrocarbons of varying degrees of saturation. At 389° C there were products of every mass number from 78 to 600, the limit of the resolving power of the mass spectrometer. Beyond mass 200 the amounts of each product were

TABLE 7. *Gaseous products evolved by 101-PVC and γ-PVC during pyrolysis*

γ-PVC				101-PVC							
Temp	Peak heights, in scale divisions for mass numbers—			Temp	Peak heights, in scale divisions for mass numbers—					Largest mass number	Probable composition
	36	78	91		36	78	91	128	178		
°C				°C							
				127	7	.....	.....	.....	.....	.....	.....
172	24	0.5	.....	179	218	12.5	.....	.....	.....	.....	.....
190	164	27	.....	194	440	48	.....	.....	.....	128	$C_{10}H_8$
214	736	52	.....	220	2,294	244	4	14	3.5	179	$C_{14}H_{11}$
238	2,416	94	1								
251	338	6	1	250	1,015	45	.....	.....	.....	.....	.....
284	18	9	14	280	1,290	43	13	13.5	2.5	179	$C_{14}H_{11}$
				306	126	51	72	40	10.5	192	$C_{15}H_{12}$
331	4	4	26	335	59	37	123	67	26	253	$C_{20}H_{13}$
381	1.8	3.9	26	389	3.5	11.5	89	21	31	596	.....

about equal, and between mass 400 and mass 600 the spectrum resembled a sine wave with maxima at all the even mass numbers.

The γ-PVC sample was smaller than the 101-PVC sample, and this is reflected in the lower values for γ-PVC at each step.

4. Discussion and Conclusions

The stability of poly(vinyl chloride) is a function of: (1) the structure of the polymer, including structural deviations and chemically or physically incorporated impurities; (2) the processing and storage history of the polymer; and (3) the conditions of exposure, including the ambient atmosphere and the wavelength and intensity of the incident energy. Recognition of these factors, combined with the results obtained in this investigation, lead to possible explanations that may account for some of the observations recorded here and in the literature.

4.1. Initiation

Initiation of degradation probably occurs at several different sites, the particular polymer and the conditions of exposure being determining factors. The susceptibility to degradation of the polymers studied increased both with the oxygen contents of the polymers and with the initial unsaturation. The effects of the two were not separated, but both are probably factors of some importance in initiation.

Several investigators [7, 8, 13] have proposed that oxygen contained in a polymer is a factor in degradation, but the actual mechanism by which that oxidation, presumably occurring during polymerization, contributes to the decomposition of the polymer has not been isolated. Although the oxygen contents of the polymers studied here may in part be due to peroxidic structures, none were found; neither were any other oxygenated structures except in the case of bp-PVC where an excess of an oxygen-containing catalyst was apparent both in the infrared spectra and in the gaseous degradation products.

The presence of unsaturation in undegraded poly(vinyl chloride) has been established by others [8, 9, 16]. Baum and Wartman [16] have shown that it occurs at chain ends, probably as a result of disproportionation, and is a major factor in initiation of degradation at 150° C.

The presence of catalyst fragments has also been proposed as providing sites for initiation of degradation [7]. The importance of impurities incorporated chemically or physically was illustrated here by the gaseous products that resulted from the decomposition of catalysts, soap, etc. when 101-PVC and azo-PVC were exposed to heat in a vacuum for short periods of time and when bp-PVC was exposed to ultraviolet radiant energy in a vacuum, even over extended periods of time. In the latter case the decomposition of the catalyst could be followed in the infrared absorption spectra as well as by analysis of the gaseous degradation products. Since the exposure conditions were little more stringent than actual service conditions, and since γ-PVC, which did not contain any catalyst residue, was much more stable than the other polymers, it is possible that incorporated impurities are a major factor in instability under normal service conditions.

Initiation of degradation of γ-PVC was probably due to oxygenated or unsaturated structures in the polymer. If this is so, it might be said that the earlier and greater instability of the other polymers was solely due to the greater amount of oxygenation and unsaturation in these polymers. Both were probably of considerable importance, but the very early occurrence of the decomposition products from incorporated impurities and the fact that the incorporated impurity was largely responsible for the high oxygen content in bp-PVC seem to indicate that impurities play a large role in mild conditions of exposure. The failure of other investigators to find any effect from incorporated impurities may be attributed to the transitory nature of the reaction and to the possibility that at the more stringent conditions usual in degradation studies, other factors such as unsaturation assume greater importance. Thus, at relatively low temperatures some labile groups may become active, and as the temperature is raised other labile groups, possibly more predominant but relatively dormant at the lower temperature, may become so active as to obscure the effects of the less prevalent structures. A somewhat parallel situation occurred when Baum and Wartman found unsaturation of primary importance at 150° C and tertiary chlorine assuming a larger role when degradation was carried out at 190° C or higher.

The type and conditions of exposure, especially the wavelength and intensity of the incident energy, have specific degradative effects dependent on the chemical structure of the polymer. For example, bp-PVC is more susceptible to ultraviolet radiant energy, and the 101-PVC and azo-PVC polymers are more susceptible to heat.

4.2. Propagation

After initiation the degradation of poly(vinyl chloride) proceeds in a complex manner. The most obvious feature is dehydrochlorination, which Arlman [13] has shown to be a free-radical reaction. Pyrolysis indicates that two stages actually occur in the degradation of poly(vinyl chloride), exclusive of oxidation reactions. Dehydrochlorination leaves a polyene backbone that further decomposes into a mixture of aliphatic, aromatic, and alkyl-aromatic materials. The first such product observed was benzene, possibly formed by cyclization of unsaturated chain ends [21]. The early appearance of benzene as a product of degradation under mild conditions seems to confirm the mechanism of cyclization and also is another indication of end initiation and a zipper-type reaction. The failure to produce more than a small amount of benzene is attributed to decreased mobility of the chains as unsaturation proceeds and crosslinking occurs. Ultimately, under pyrolytic conditions, sufficient energy is available for random C—C rupture. This accounts for the multitude of other carbon compounds produced in pyrolysis.

461441—58——5

In degradation under service conditions oxygen may affect both stages of the degradation of poly(vinyl chloride). Oxidation of both saturated and unsaturated portions of the polymer chain may lead to chain scission and to an increased concentration of free radicals, which may accelerate dehydrochlorination. This has been observed frequently [1, 3, 5, 7]. The presence of ultraviolet radiant energy accelerates oxidation reactions.

The production of acetone is probably due to a mechanism similar to that found by George and Walsh [28, 29]. This would result in chain scission. Whether the necessary oxygen to form the acetone came from the ambient atmosphere or from the oxygen contained in the polymers was not determined. The polymers with higher oxygen contents produced more acetone but acetone only appeared after exposure in air.

The mechanism by which dehydrochlorination occurs has generally been accepted to be of an allylic nature [2, 4, 5, 7, 9], that is, a chlorine atom in the beta position to a double bond requires less energy for removal. However, many of the proposed mechanisms were not presented as free-radical chain reactions, though the occurrence of a free-radical reaction has been established [12, 13]. The mechanism proposed by Stromberg et al [21] combines allylic excitation with a free-radical reaction and can be made to fit any or all of the proposed mechanisms of initiation. It also allows for the effects of oxidation in that oxygenated radicals as well as a chlorine radical freed by allylic excitation may initiate a chain reaction. One minor modification suggested is that removal of a hydrogen atom to start a chain reaction need not necessarily occur adjacent to a double bond.

Crosslinking is possible whenever two chains with free radicals are in proximity. A moderately frequent occurrence of this nature is conceivable. Scission probably occurs principally as a result of oxidative degradation except in pyrolysis, where there is usually sufficient energy available to rupture C—C bonds.

4.3. Color

The degradation of poly(vinyl chloride) is accompanied by a discoloration that has been attributed to the polyene system. It was observed by some investigators that exposure of degraded poly(vinyl chloride) to oxygen led to bleaching of the color, whereas others failed to find this occurring. In view of the results obtained in this study, it seems that two sources of chromophores are possible, from conjugated unsaturation and from oxygenated structures. If a polymer is degraded in a vacuum and exposed to air, the color due to unsaturation may be bleached. A carbonyl absorption in the polymer occurs simultaneously. In the case of degradation on exposure to ultraviolet radiant energy with oxygen present, color formation seems to be due either to oxygenation only or to both types of chromophores. Absorptions due to carbonyls and conjugated unsaturation may be found. Further exposure to oxygen does not lead to bleaching. On the other hand, if a polymer containing both chromophores is subjected to heat in a vacuum, bleaching will also occur as well as a change in hue. A shift in the carbonyl absorption occurs at this stage. Probably the oxygenated chromophore is removed slowly, and if the exposure were carried far enough the color would again increase in intensity. Ultraviolet radiant energy is probably necessary to produce oxygenated chromophores.

The authors are indebted to the Mass Spectrometry Section for the mass spectrometric analyses, to the Organic Chemistry Section and to Shigeru Ishihara for the oxygen-content determinations, and to Shigeru Ishihara for assistance in some of the experimental investigations.

5. References

[1] A. S. Kenyon, Symposium on polymer degradation mechanisms, NBS Circ. 525, p. 81 (1953).
[2] M. Imoto and T. Otsu, J. Inst. Polytech., Osaka City Univ. [C] **4,** 269 (1953).
[3] M. Imoto and T. Otsu, J. Inst. Polytech., Osaka City Univ. [C] **4,** 124 (1953); J. Chem. Soc. Japan (Ind. Chem. Sec.) **54,** 771 (1951).
[4] V. W. Fox, J. G. Hendricks, and H. J. Ratti, Ind. Eng. Chem. **41,** 1774 (1949).
[5] A. L. Scarbrough, W. L. Kellner, and P. W. Rizzo, Modern Plastics **29,** 111 (1952); NBS Circ. 525, p. 95 (1953).
[6] C. B. Havens, NBS Circ. 525, p. 107 (1953).
[7] D. Druesdow and C. F. Gibbs, NBS Circ. 525, p. 69 (1953); Modern Plastics **30,** 123 (1953).
[8] E. J. Arlman, J. Polymer Sci. **12,** 547 (1954).
[9] L. H. Wartman, Ind. Eng. Chem. **47,** 1013 (1955).
[10] C. S. Marvel, J. H. Sample, and M. F. Roy, J. Am. Chem. Soc. **61,** 3241 (1939).
[11] J. E. Wilson, J. Am. Chem. Soc. **72,** 2905 (1950).
[12] J. Furukawa and T. Kimara, J. Chem. Soc. Japan (Ind. Chem. Sec.) **55,** 133 (1952).
[13] E. J. Arlman, J. Polymer Sci. **12,** 543 (1954).
[14] H. Batzer and A. Nisch, Makromol. Chem. **16,** 69 (1955).
[15] G. P. Mack, Modern Plastics **31,** 150 (1953).
[16] B. Baum and L. H. Wartman, Paper presented at North Jersey Section, American Chemical Society Meeting in Miniature, Jan. 28, 1957.
[17] S. Wakano and K. Yamamoto, J. Chem. Soc. Japan (Ind. Chem. Sec.) **54,** 513 (1951).
[18] P. D. Zemany, Anal. Chem. **24,** 1709 (1952).
[19] P. Bradt, V. H. Dibeler, and F. L. Mohler, J. Research NBS **50,** 201 (1953) RP2410.
[20] P. Bradt and F. L. Mohler, J. Research NBS **55,** 323 (1955) RP2637.
[21] R. R. Stromberg, S. Straus, and B. G. Achhammer, Paper presented at ACS National Meeting, Atlantic City, N. J., Sept. 20, 1956.
[22] R. R. Stromberg, S. Straus, and B. G. Achhammer, J. Research NBS **60,** 147 (1958) RP2832.
[23] M. R. Harvey, J. E. Stewart, and B. G. Achhammer, J. Research NBS **56,** 225 (1956) RP2670.
[24] B. G. Achhammer, M. J. Reiney, L. A. Wall, and F. W. Reinhart, J. Polymer Sci. **8,** 555 (1952).
[25] O. D. Shreve, M. R. Heether, H. B. Knight, and D. Swern, Anal. Chem. **23,** 282 (1951).
[26] B. G. Achhammer, Anal. Chem. **24,** 1925 (1952).
[27] F. M. Lewis and M. S. Matheson, J. Am. Chem. Soc. **71,** 747 (1949).
[28] P. George and A. D. Walsh, Trans. Faraday Soc. **42,** 94 (1946).
[29] A. D. Walsh, Trans. Faraday Soc. **42,** 269 (1946).
[30] L. J. Bellamy, The Infra-red spectra of complex molecules (John Wiley & Sons, Inc., New York, N. Y. 1954).
[31] S. Krimm and C. Y. Liang, J. Polymer Sci. **22,** 95 (1956).

Washington, December 9, 1957.

Journal of Research of the National Bureau of Standards Vol. 60, No. 5, May 1958 Research Paper 2864

Determination of Water Vapor from the Change in Electrical Resistance of a Hydroscopic Film

Elmer R. Weaver, Ernest E. Hughes, and Albert W. Diniak*

The electrical conductivity of a thin film of such a material as phosphoric acid changes over a wide range with changes in the concentration of water in the atmosphere with which it is in contact. By adjusting the pressures of a sample of gas of known composition and one of unknown composition, they can be made to have the same concentration of water (more accurately the same fugacity) shown by the production of equal resistances of the detecting film. Modifications of the apparatus, procedures, and calculations described in an earlier publication are presented and numerous applications of the method are discussed. The method has the merits of simplicity, speed, and great sensitivity. Only small samples are needed, and few substances interfere.

1. Introduction

1.1. Purpose of Paper

This paper is a revision and extension of an earlier one [1][1] now out of print. Several improvements have been made in methods of building and using the apparatus for measuring water and have been described in various publications and reports [2, 3]. It is the purpose of this paper to give in one place the information that is needed for the effective use of the method; but the earlier paper contains material on some equipment and applications not included here, and should be consulted when special problems are encountered.

1.2. General Method

The measurement of water vapor in gases by observing the resistance of thin films of electrolyte has been employed occasionally at the National Bureau of Standards for a variety of purposes for nearly 40 years. The essentials of the method are extremely simple. A thin film of liquid, which may be such a material as phosphoric or sulfuric acid or a solution containing one or more acids, bases, or salts with a binding material such as gelatin or a high-polymer plastic, is spread over the surface of a solid insulator between metallic electrodes. The electrolyte tends to reach equilibrium with the water vapor in the atmosphere that surrounds it, and to form a solution the electrical resistance of which is a measure of the water vapor in the atmosphere. We need, in addition, some instrument for measuring or comparing electrical resistances and a means of calibrating the film by comparison with a gas of known moisture content. Polarization makes advisable the use of alternating current for the measurement.

The method was devised initially [4] to detect very small concentrations of water vapor in gases entering a catalytic reaction in which water is a poison. The material first tried for the conducting film was a salt, calcium chloride; but it was soon found that the salt became a nonconducting solid at a humidity far higher than that to be detected, and numerous other electrolytes were tried. Among them phosphoric and sulfuric acids were found most useful because they served to detect the smallest concentrations of water vapor. However, films of these materials changed resistance so rapidly that it seemed hardly worthwhile to calibrate them by comparison with known atmospheres, laboriously prepared.

The method therefore fell into disuse except for qualitative work until F. W. Dunmore [5, 6] employed it successfully for much higher humidities in connection with meteorological observations. He used a salt, lithium chloride, as the electrolyte in a plastic film of very high resistivity, but one which held its calibration well. The Dunmore elements or modifications of them are used extensively in both meteorology and industry, and numerous independently developed resistance units of somewhat similar types have appeared [7]. The need during the war for a method of determining rapidly very small quantities of water vapor in aviator's oxygen led to the development of a means of calibrating a sensitive film at the time of its use so quickly and simply that little need remained for a permanent calibration. This at once greatly extended the possible applications of the method.

1.3. Principle Involved in Calibration by the Adjustment of Pressure

As a rough approximation, deviations from which will be discussed later, the resistance of a given film is independent of the gases other than water vapor with which it is in contact and depends only on the amount of water contained in unit volume. If a sample of gas, such as oxgyen or air, of known water content per unit volume, is passed over the film it will assume a certain resistance. If a second sample of gas of unknown water content is then passed over the film, the resistance will usually be different, but it may be restored to its original value by compressing or expanding the second sample until it contains the same quantity of water per unit volume (more exactly until the water vapor has the same fugacity) as the first sample. When this condition is reached, we note the pressure and readily compute what the water content would be in a unit volume at any other

*Present address, Vitro Corp., Penns Grove, N. J.

[1] Figures in brackets indicate the literature references at the end of this paper.

pressure (usually, but not always, 1 atm). If the unknown gas is initially at atmospheric pressure, it may be more convenient to change the pressure of the standard gas until the same resistance is produced by both.

As a simple illustration of the first procedure, let us say that the first sample of gas used as a standard is known to contain 2 mg of water per liter, and that the second sample causes the detecting film to have the same resistance as the first (and that it therefore also contains 2 mg of water per liter) when at a pressure of 100 atm. If the second sample of gas is now expanded to 1 atm, it has about 100 times the volume but the same total quantity of water as before expansion, and the water content is, therefore, 0.02 mg/liter. The second procedure may be illustrated by the following example. A cylinder of air known to contain 8 μg (0.008 mg) of water per liter when expanded to atmospheric pressure was used as the standard gas. The resistance produced by exposing the film to a sample of Freon at atmospheric pressure was matched by adjusting the air to 18 psig (pounds per square inch gage) or a total pressure of 2.2 atm. Then the Freon at atmospheric pressure contained 2.2 times as much water as did the air at atmospheric pressure, or 18 μg/liter.

Frequently it is convenient, in order to make the best use of available gages, to set one gas to an arbitrary pressure of no interest in itself and to match it by adjusting the pressure of the other For brevity, the process of adjusting the pressure of one or both gases to produce the same electrical resistance of the detector will be called comparing the gases. In general four pressures are involved in a comparison:

P_s, the pressure at which the standard gas contains a known concentration of water vapor, S.

P_c, the comparison pressure at which the standard gas is matched with the electrical resistance produced by the unknown gas at pressure P_x.

P_x, defined by the preceding statement.

P_w, the pressure at which we wish to know the concentration of water in the unknown gas.

The water content, C, of the standard gas at the comparison pressure is

$$C=S\frac{P_c}{P_s}. \tag{1}$$

Since it is known that the unknown gas has this same water content at the matching pressure P_x, the water content, W_x, at pressure P_w of the unknown gas is derived from C, just as C was derived from S:

$$W_x=C\frac{P_w}{P_x}=\frac{SP_cP_w}{P_sP_x}. \tag{2}$$

Having determined the value of W_x we can obviously use the newly analyzed gas as the standard to determine W_{x_1}, the water content of still another unknown gas at P_{w_1} after matching it electrically at pressure P_{x_1} against the new standard at P_w, thus:

$$W_{x_1}=W_x\frac{P_{w_1}}{P_{x_1}}=S\frac{P_cP_wP_{w_1}}{P_sP_xP_{x_1}}. \tag{3}$$

There is obviously no limit to the number of steps of this kind that can be taken, but because some error is involved in each comparison, the results soon lose significance.

A gas that contains an approximately known concentration of water, to be used as the first or the only standard, can be obtained easily by saturating compressed air (or other compressed gas that may be available) with water vapor at any convenient pressure. S then represents the concentration of water vapor in equilibrium with liquid water at the temperature of the measurement, and P_s is the pressure in the saturator. S and W may be expressed in any units, not necessarily in micrograms per liter, pounds per thousand cubic feet, or other units of mass per unit of volume; they may also be expressed as partial pressures, relative humidities, or percent by volume. Since only ratios of pressures are involved in the computation of W and S, any unit of pressure may be used, provided it is kept clearly in mind that total pressures are involved, not gage pressures (above atmospheric).

In the application of the method that has been most extensively made—determining the moisture content of compressed gases—it is convenient to use as the standard gas air, oxygen, or nitrogen saturated at about 35-atm pressure and expanded to 1 atm. The water content of the unknown gas is to be determined at 1 atm. Hence, if pressures are expressed in atmospheres, P_c and P_w of eq 2 are both unity, and the equation becomes

$$W_x=\frac{S}{P_sP_x}, \tag{4}$$

in which S is the concentration of water vapor in equilibrium with liquid water.

In the method of use described, the pressure gages are the measuring instruments. We are usually not at all concerned with the actual value of the electrical resistance of the sensitive film, and the electrical instruments are used only to show that two resistances, corresponding to measured pressures, are the same; but in some cases, especially when following changing concentrations of water vapor, it is impracticable to make a separate calibration through the adjustment of pressure for every variation of humidity, and readings of the electrical instruments are recorded and interpreted, usually by interpolation between values determined by pressure readings. The electrical circuit is then truly used as a measuring instrument and not merely as a null-point indicator.

In the foregoing description of principles, it was necessary to qualify many of the statements with the words about, approximate, etc. The corrections to be made to produce more accurate results and the sources of error will be discussed after the construction of the instrument and its operation have been described.

2. Description of Apparatus Employed

2.1. General Arrangement and Procedure

The general method that has been outlined above may be employed with apparatus of great variety. For certain purposes the equipment may be designed for pressures either above or below atmospheric, and many of the parts may be made of glass, metal, or plastic in numerous arrangements. Several of these are described in reference [1] and will be omitted from this paper.

The essential electrodes, the separating insulation on which the conducting film is spread, and their support will be called collectively the detector; and the small tight enclosure in which the detecting surface is exposed to the gases is called the cell. The electrical equipment used for showing equality of resistance of the film under different conditions will be called the indicator. A simple arrangement for testing compressed gases is shown in figure 1. The

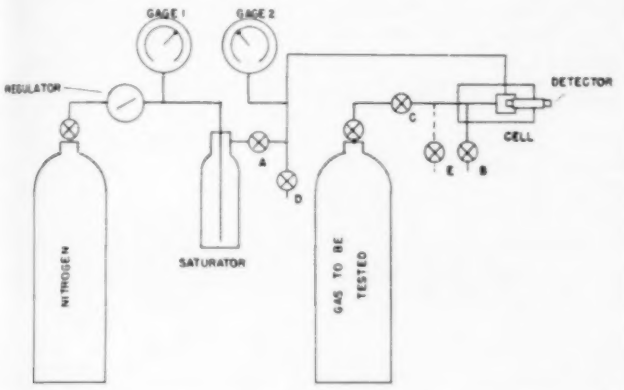

FIGURE 1. *Diagram of mechanical connections for testing compressed gas.*

regulator on the nitrogen cylinder is set to deliver gas to the saturator at a pressure of about 500 psi, as shown by gage 1. Nitrogen is suggested for this use because it will not corrode an ordinary steel cylinder if used as a saturator. Otherwise air or oxygen is just as good. The saturated gas is admitted in a slow stream to the cell through valve A and, after passing over the detector, is discharged through valve B, which is generally left wide open. When the detector has reached equilibrium, the indicating circuit is adjusted so that the galvanometer needle is on scale and the reading is noted. The reading of gage 1 plus 1 atm is P_s of eq 2, and that of gage 2 with the same correction is P_c. In this case both P_c and P_w are 1 atm, and eq 4 is substituted for eq 2 in the calculation of the water content. Valves A and B are then closed, and valve D is opened. The gas to be tested is admitted at a moderate rate of flow through valve C, and valve D is closed until the galvanometer balances at the point previously noted. The reading of gage 2 plus 1 atm is entered in eq 4 as P_x, and the equation is complete.

In the arrangement illustrated, slight leakage of gas through valves A or C, which it is hard to avoid with complete certainty, does not affect the result, because in each case the leaking gas is discharged without reaching the detector. If only one cylinder of gas is to be tested, it may first be attached to the saturator to provide the standard gas and then connected as the gas to be tested. If a high-pressure regulator is not available and gage 1 has a sufficient range, the full pressure of the cylinder may be applied to the saturator, but this ultimately results in the waste of compressed gas and a certain amount of inconvenience or a reduced accuracy in the reading of pressures.

At present, the arrangement diagrammed in figure 2 is used for more accurate work in the labora-

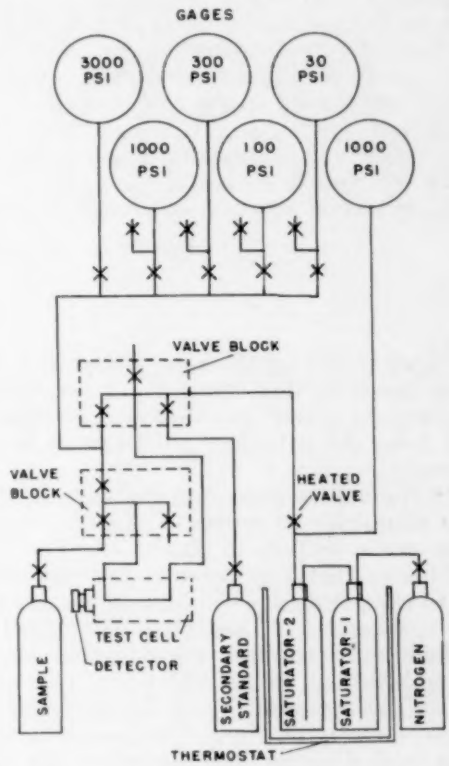

FIGURE 2. *Diagram of mechanical connections for very accurate testing of compressed gases.*

tory. The two-stage saturator reduces the degree of uncertainty that saturation is complete at the indicated temperature, especially if the bottles are immersed in a thermostated oil bath. The bank of pressure gages covering the five ranges shown in the figure permits pressures to be read with accuracy in any part of the range.

The arrangement of a portable model of the instrument is shown in figure 3. The valves are lettered as in figure 1. A spare valve, E, connecting to the system at the same point as valve C, is not needed for the testing of gas for compliance with Army-Navy specifications, but is very convenient

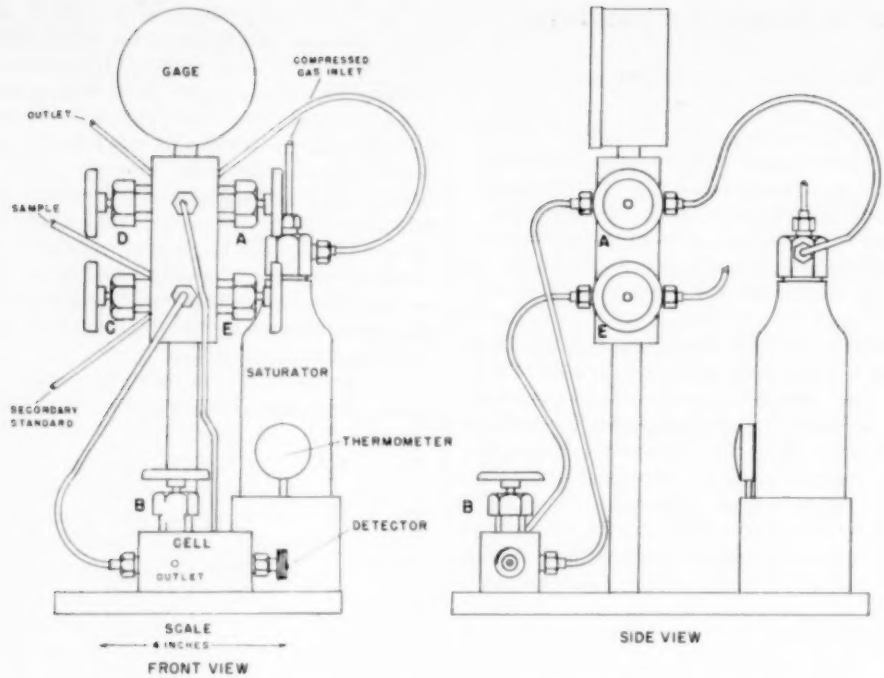

FIGURE 3. *Front and side elevation of portable instrument.*

in other work either for the attachment of a pressure gage more sensitive than "gage 2" or for introducing a "secondary standard" gas that is drier than can be obtained from the saturator with gas at any available pressure.

Four of the valves were mounted in a single valve block for simplicity of support. Further details are shown in cross section in figure 4. The block is made of heavy metal to conduct heat as readily as possible to the points of expansion of the gas through the principal valves. The cell is connected to the valve block only through considerable lengths of small metal tubing to minimize the effects of expansion on the temperature of the detector. Valve B is placed directly on the cell to minimize the pressure drop from detector to outlet when the standard gas is to be used at 1 atm without measurement or corrections. It is quick-opening, and its passages are large for the same reason.

Several instruments of this design were made in 1943 and supplied to stations of the Armed Forces. One of these was used to test 56,000 cylinders without repair except the replacement of the detector; and at least one is still in occasional use. Tests for compliance with the specified limit of 20 μg of water per liter in aviators oxygen were routinely made with one instrument at the rate of 100 per hr. A precision of about ± 0.2 μg/liter, roughtly 2 parts per 10 million by volume is obtainable at the specified limit if care is taken, and only 100 or 200 ml of gas need be expended per test.

Details of construction of the various parts will now be discussed.

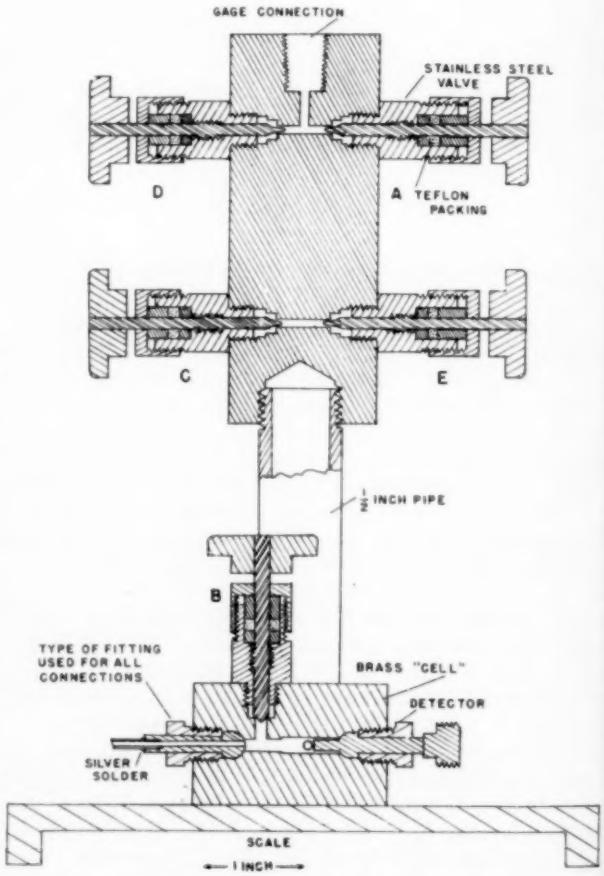

FIGURE 4. *Section of valve block and cell block of portable instrument.*

2.2. Detector

a. Detector Currently Used

In figure 5 is shown the detector preferred by the authors because of its compactness and ease of handling when recoating or transferring from a place of use to a cell for calibration, and also because it can withstand repeated pressures up to 6,000 psi without developing cracks in the glass insulation. Unless otherwise specified, it may be considered to be the detector referred to throughout the remainder of this paper. A central electrode is made by filling a piece of small thin-walled platinum tubing with "French sealing-in glass" and gold-soldering a platinum wire to one end. The outside diameter of the tube should not exceed 1 mm, and its wall thickness is preferably kept below one-tenth of the diameter. The outer electrode is a platinum tube about 3 mm in outside diameter with a similarly low ratio of wall thickness to diameter. Platinum is wet readily by the molten glass used, and clear beads of it should be allowed to flow into the tubes by capillarity rather than forced into place. Otherwise a film of air may be trapped between glass and metal. Nickel is preferred for the detector body because it has a sufficiently high melting point and can be gold-soldered to platinum more readily than can stainless steel.

Heating must be controlled rather carefully to a temperature between that at which the glass flows freely and that at which it begins to decompose with the formation of bubbles. Cooling should be done slowly in a glass-blower's lehr. If the glass cracks or separates from the metal during construction or use it is very difficult to repair because air is likely to be trapped during resealing.

The materials and precautions described are needed to make a detector that will withstand high and rapidly changing compressive stresses. Glass and metal do not have exactly the same modulus under compression and separate quickly if a flaw develops. If pressures during use do not exceed a few hundred pounds per square inch, a durable detector is rather easily made; but rapid changes from 100 to 400 atm (the highest pressure at which detectors have been regularly used) cause early failure unless the detectors are extremely well made.

The platinum wire from the inner end of the center electrode leads through the nickel shaft to a specially designed terminal for connection to an Amphenol cable. The wire is shielded from contact with the shaft by a small plastic tube, is threaded through a Teflon disk that fits into a recess in the terminal head, and is soldered to a small brass insert in the Teflon. A loosely fitting ⅜-in. sleevenut, 24 threads per in., placed on the shaft before the head is screwed into place serves to attach the detector to the cell.

After assembling, the end of the detector is ground to expose the electrodes in a surface that need not be polished but should be without irregularities visible to the unaided eye. The dull finish left by grinding with abrasive grains 20 μ in diameter seems to be about right.

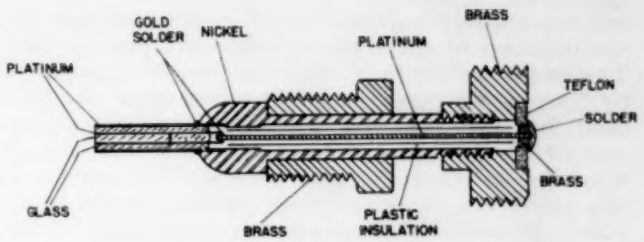

FIGURE 5. *Detail of detector.*

2.3. Electrical Indicator

Two indicating circuits are shown in figures 6 and 7. They differ in two respects. In the first, and less expensive circuit, the primary bridge is composed of the detector and three resistances each of 1 meg; and the output of the twin triode is used in a second bridge of which the slidewire R_4 constitutes two arms. In the more elaborate circuit, two of the 1-meg resistors of the primary bridge have been replaced by 400-mh inductances with apparent but slight improvements in performance. The slidewire R_4 of figure 6 has been replaced by a fixed resistance and a resistance box. The two modifications of the cir-

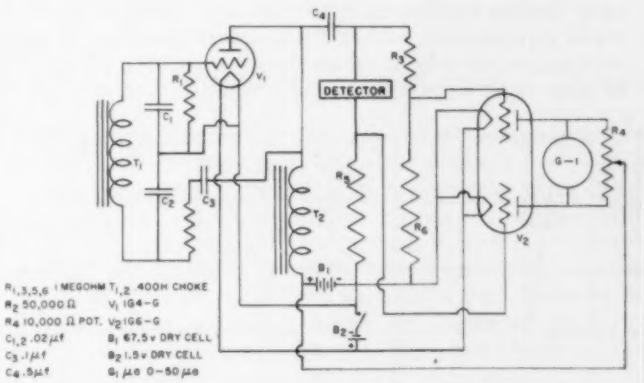

FIGURE 6. *Diagram of indicating circuit used when gages are employed as primary measuring instruments.*

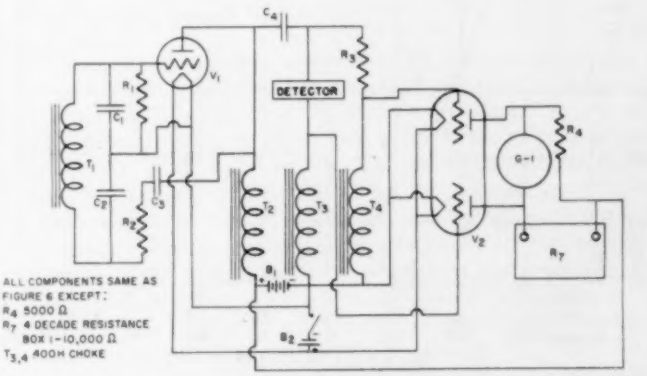

FIGURE 7. *Diagram of measuring circuit used when measurements depend on electrical calibration.*

cuit are entirely independent of each other, and any combination of the different elements can be used. Two or three circuits in which batteries were replaced by 60-cycle alternating-current power have also been used, but they lack the portability of the battery-operated indicator and have otherwise been somewhat less satisfactory. For continuous operation at one place, the batteries could without doubt be replaced by suitable direct-current power supplies derived from the alternating power line.

In both the circuits illustrated, the twin-electrode vacuum tube supplies pulsating direct current to two branches of a circuit. The "galvanometer" (usually a microammeter) connects these two branches and, with the resistors in each branch, operates like the galvanometer and two branches of an ordinary Wheatstone bridge.

In the use of the indicating circuit of figure 6, the contact on resistance R_4 is simply adjusted until the galvanometer reading is brought to a convenient point of the scale, which need not be zero, and this reading is noted and reproduced in subsequent "comparisons." In this use of the indicator, the electrical instruments are simply used to show a common null point, and the actual measurements are made with the pressure gages.

The second circuit permits the electrical resistance of the detector to be measured with moderate accuracy and is employed when for any reason the electrical equipment, rather than a combination of pressure gages, is to be used as the measuring instrument. It was used in studies of the equilibrium resistance of films, the rate of attainment of equilibrium, etc., and is frequently useful for interpolating between indications of the standard, particularly when rapid changes of humidity are being followed.

The characteristics of the electrical indicator as a whole are shown for the circuit of figure 7 by the calibration curves of figure 8. The galvanometer used had a resistance of 123 ohms and a range of 15 μa. The variable resistance, R_7, was a plug-box of 10,000 ohms in steps of 0.1 ohm. The three curves in the figure, with their corresponding scales, show resistances of the detector and corresponding values of the variable resistance, R_7, required to bring the galvanometer to balance. The calibration was made by replacing the detector with successive measured fixed resistances. The entire range of possible resistances from short circuit to open circuit is covered. The higher resistances are plotted on a reciprocal scale.

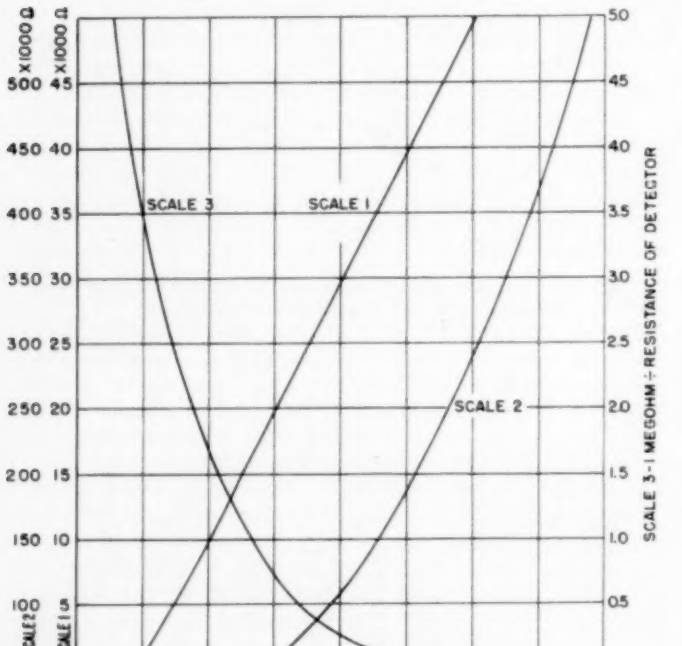
X1000 Ω
X1000 Ω
SCALE 3
SCALE 1
SCALE 2
SCALE 3-1 MEGOHM = RESISTANCE OF DETECTOR
SCALE 2
SCALE 1
7 SCALE 1 8 9 10 11 12 13 14 15X100 Ω
0 SCALE 2 5 10 15 20 25 30 35 40X100 Ω
20 SCALE 3 30 40 50 60 70 80 90 100X100 Ω
BALANCING RESISTANCE

FIGURE 8. *Calibration of measuring circuit in terms of resistance of detector.*

2.4. Saturator

The saturator shown diagramatically in figure 9 is the type generally used. Saturators with more elaborate packing have not worked as well. The sand used in filling the saturator does not have to meet accurately the specifications given in the figure. Gravel of larger size will do as well. When the water level was kept as low as shown, no trouble has been encountered with spray from cylinders filled in this way, even when the rate of flow of gas was much greater than needed.

A single saturator leaves much to be desired. The sand has a high heat capacity, and with cooling from evaporation at the bottom and changing temperature

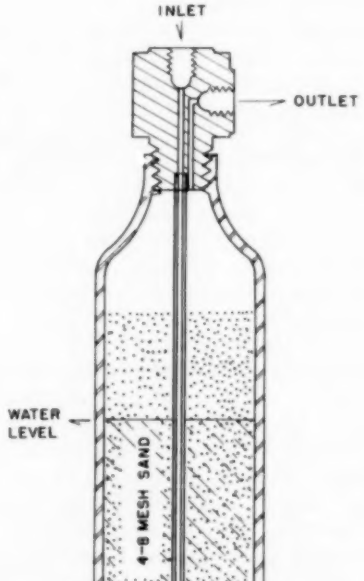

FIGURE 9. *Saturator.*

in the surroundings, the actual temperature of saturation is uncertain. For highly accurate results, a double saturator and trap, shown schematically in figure 10, immersed in a bath of oil or other convenient liquid is to be preferred.

In the series of cylinders shown in figure 10, the first cylinder has enough capacity to retain all the water in all three cylinders and its function is to guard against flooding other parts of the apparatus if mistakes are made in the manipulation of valves when gas at very high pressure is being tested. The second cylinder is the principal saturator. The third cylinder serves both as an additional spray catcher and as a final saturator when continuous evaporation in the middle cylinder results in appreciable cooling. The bath may be thermostated for precise work, but it is ordinarily necessary only to read a thermometer immersed in the bath liquid. In the most exacting work, also, it may be desirable to warm the outlet valve to prevent cooling and condensation by expansion at that point, but this is ordinarily unnecessary because of the heat capacity of the valve and the small volume of gas expanded through it. The valve must not be colder than the saturator, of course.

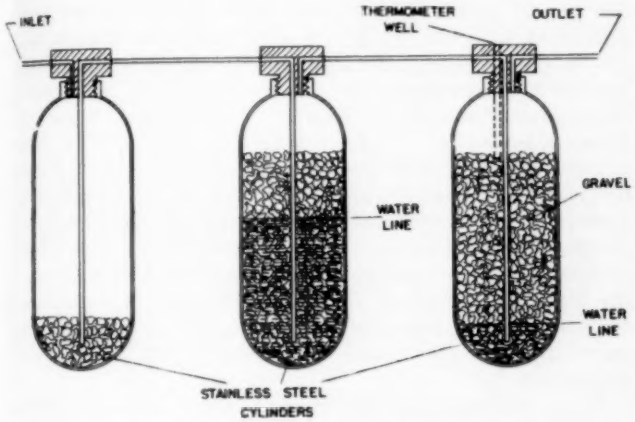

FIGURE 10. *Double saturator and trap.*

2.5. Valves, Connections, Gages, Regulators

Accurately made needle valves of the simple construction shown in figure 11 have been mostly used. Valves of other types that have been tried have been no more satisfactory at the best. Because they may at times get wet, and they must not corrode, ordinary steel should not be used for either valve stem or valve body. Good results have been obtained with stainless steel needle valves with bodies of brass or a softer stainless steel that will not score in contact with the needle.

The packing of the valves is very important. Teflon, a polymer of tetrafluoroethylene, is a suitable packing material. It is not wet by water, offers little friction on the valve stem, is easily machined or molded to an exact fit, has enough elasticity to remain tight when compressed, and can be heated to well above the boiling point of water without damage when the apparatus is being dried out.

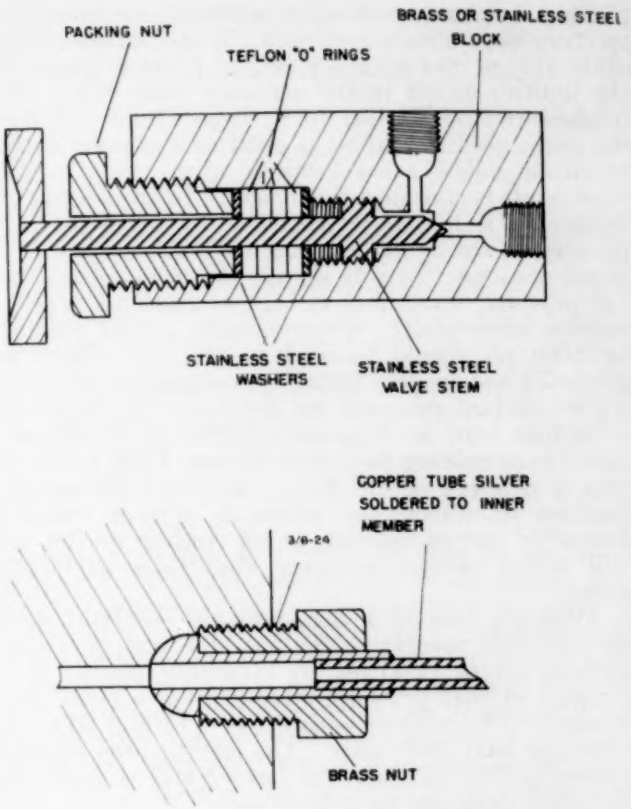

FIGURE 11. *Needle valve and connector.*

The apparatus should be easy to take apart completely for drying, and easy to reassemble. The connecting fittings shown also in figure 11 have been particularly satisfactory; they are simple, rugged, and easy to make tight. Only metal-to-metal joints should be considered. Threads, tapered or otherwise, cannot be made tight without a vast amount of trouble; fiber washers and other forms of packing are as bad or worse, chiefly because they retain water.

If threaded couplings only are available one piece can be "tinned" thinly with solder. When connected, the mating piece cuts a new thread in the solder and is tight until the joint is broken, but it is difficult to take apart and will not remain tight after many separations.

In making up the assembly of valves and connections, every precaution must be taken to eliminate places where water can be stored by such things as hygroscopic salts, rubber, or rust (which is a good adsorbent and acts much like a little silica gel). Soldering flux is particularly bad, and capillary spaces such as screw threads can be troublesome. It is good practice before final assembly of the equipment to wash the parts with a solvent for grease and then to boil them for several hours with several changes of water to remove hygroscopic salts. Finally, the parts are dried in an oven.

Gages of the Bourdon type have been used exclusively for work involving pressures above atmos-

pheric. In some work below atmospheric pressure, mercury manometers were used. If care is taken with other things, the accuracy of the pressure gages is the limiting factor in the accuracy with which the method can be applied to most problems. Hence the gages used should be as good as it is practicable to obtain unless a lower degree of accuracy in the final result is considered sufficient. In the testing of oxygen, it is frequently desirable to apply the full pressure of the cylinder to the cell. Even when this is not the case, there is always the chance that the full pressure, sometimes as high as 2,640 psi, will be applied accidentally. Consequently, a gage reading to 3,000 psi should be used on the cell. There is generally less trouble from obscure sources of water if the standard gas is not too dry, hence the saturator is seldom kept at a pressure higher than 500 psi, and a gage reading to 500 or at most 1,000 psi is all that is required at this point. If only high concentrations of water, say above 1 percent relative humidity, are of interest, gages reading to 200 psi will afford greater accuracy than those of higher range.

Although lack of a high-pressure regulator does not preclude saturating the gas at a high pressure, such as 500 or 1,000 psi, by attaching directly to a cylinder at that pressure, a regulator is a great convenience. Regulators with upper limits of 500 and 1,000 psi have been used. The latter works slightly better at 500 psi than the former and is probably the more desirable for general use.

3. Conducting Films

3.1. Composition of the Film

The film recommended for use in most work is a mixture of phosphoric and sulfuric acids. A drop or two of concentrated sulfuric acid added to a small lump of phosphorus pentoxide or to several drops of concentrated phosphoric acid will serve to produce detecting films for weeks of use. The proportions of the acids are not important. Phosphoric acid alone is to be preferred except for rather dry gases. It behaves irregularly at humidities of less than about 8μg/liter, probably because of the formation of metaphosphoric acid or other solid phase. This erratic behavior has never been observed in the presence of an appreciable fraction of sulfuric acid, but the phosphoric acid coating disappears less rapidly than sulfuric acid, probably because it is less volatile.

No film of either or both acids remains stable very long. Resistance always increases either because the acids evaporate or because they react with their supporting materials or with neutralizing gases in the atmosphere. Usually they do not change appreciably during a half hour, and a single comparison with a standard can be used that long if temperature is constant; but, unless the detector has to be so located that it is not accessible for comparison, it is easier to make a calibrating comparison with each reading than to control or keep track of temperature changes, and the regular checking of each reading leads to more certain results. A film usually retains its sensitivity well enough for use, when regularly compared with the standard, for a half day.

At least a part of the acid that is lost from the detecting film dissolves in the supporting glass. After a few days the glass becomes conducting; it comes to equilibrium with the atmosphere very slowly; and the result is that readings, which should become nearly constant in a few seconds after a change of humidity, change promptly to a nearly constant value and then drift endlessly at a slow rate. To avoid this difficulty it is necessary to remove the contaminated surface of the glass. This can be done by rubbing the detector surface several times across a drop of glycerine and fine abrasive on a hard surface (a microscope slide is suitable). If this is done daily only a few seconds of grinding will suffice to keep the detector in good condition. To minimize reaction between acid and glass, it is worthwhile to rinse the detecting surface with water and wipe dry when the detector is not to be used even for an hour.

A large number of experiments have been made by the authors and others with films containing hygroscopic salts in various media. These have had several objects, (1) to obtain films that always have the same resistance at the same temperature and humidity and can be given a permanent calibration, (2) to obtain films the calibration of which will not be altered by exposure to a saturated or nearly saturated atmosphere, and (3) to measure water in atmospheres that would react with acids. The first fairly successful detectors containing salts were those prepared by Dunmore [5, 6] which have been commercially produced and extensively used in meteorological and industrial work since about 1940. Their properties have been gradually improved or modified for various purposes [7]. One of the more recent ones, especially adapted to the conditions of measurement in the upper atmosphere, is that of Wexler and associates [8].

The Dunmore elements and most of the others require long and careful "conditioning" before they are calibrated and used; and they must be protected from long exposures to very wet or very dry gases. For some purposes solutions of salts in glycerine or glycerine and gelatin can be used satisfactorily, without prior aging, on the detector ordinarily used with phosphoric and sulfuric acids [1, pp. 186–9].

3.2. Application of the Film

Films of sulfuric and phosphoric acid of ample sensitivity are thin enough and viscous enough to require no binder unless they are exposed for more than a few seconds to humidities very near to saturation. The detector is coated simply by touching a stick, such as a toothpick, to the acid and then to the detecting surface, and wiping off the excess acid with a bit of cotton. Less than a minute is usually required. One soon learns about how much to rub off. Wiping with a moderate pressure on three successive clean portions of the cotton is one rule of thumb. Another is to wipe until the finely ground glass surface appears dull but not quite dry. If

greater accuracy is desired, the adjustable resistances of the indicator can be set to approximately the desired reading in room air and the coating wiped off with one light touch of the cotton after another until the swing of the galvanometer needle shows that the resistance has become higher than corresponds to electrical balance.

Fortunately, the thickness of the film is not at all critical. One film may have several times the resistance of another, but their difference be hardly noticeable in use. In some ranges of humidity, it is quite possible to use interchangeably films having a ratio of resistances of 50:1. In general, a thicker film permits greater sensitivity, and a thinner one reaches equilibrium more rapidly. The rule is, therefore, to use as thin a film as will have the desired sensitivity.

3.3. Sensitivity

The actual resistance of a single phosphoric acid film, film A, over almost the whole range of humidities was measured with the circuit of figure 7. The observed data are given in table 1 and represented by curve 1 of figure 12. The concentration of water in micrograms per liter is plotted on a logarithmic scale with respect to the balancing resistance (resistance R_7 of fig. 7) on a linear scale. The approximate resistance of the film itself is plotted on a logarithmic scale with respect to the same ordinate in curve 2, the data for which were taken from curve 1 and the calibration of figure 8. Film A was such as would ordinarily be used in the lower part of the range accessible to phosphoric acid. For humidities in the higher range, a thinner film is preferable because it reaches equilibrium with the atmosphere more quickly and does not begin to flow at so low a humidity. A typical application of phosphoric acid for this purpose, film B, is represented by curve 3, drawn on the same scale as curve 1. One film has about 20 times the resistance of the other, but both are readily usable over most of the range of humidities. In figure 13, the balancing resistances are plotted with respect to relative humidity. The two films were used at different temperatures of 83.6° and 81° F, hence, the ratios of weights per unit volume and of relative humidities are not the same. The resistance of film B reached a minimum before a relative humidity of 100 percent was reached, and

TABLE 1. *Resistance of a film of phosphoric acid (A) at various concentrations of water vapor*

Balancing resistance	Resistance of detector	Concentration of water				
		μg per liter [a]	Relative humidity at 83.6° F	Partial pressure	Approximate dew point	
Ohms	*Ohms*		*Percent*	*mm Hg*	*° C*	*° F*
5,730	2,870×10³	11.3	0.039	0.011	−74	−101
5,664	2,700	22.0	.076	.021	−53	−63
5,541	2,390	35.2	.12	.034	−49	−56
5,540	2,050	56.4	.19	.055	−45	−47
5,167	1,600	86.9	.30	.084	−41	−42
4,913	1,280	138	.48	.13	−38	−36
4,700	1,040	171	.59	.17	−35	−31
4,320	720	263	.91	.26	−30	−22
3,836	528	411	1.4	.40	−26.7	−16.2
3,420	394	563	1.9	.55	−23.5	−10.3
3,195	337	655	2.3	.64	−22	−7.6
3,174	332	655	2.3	.64	−22	−7.6
2,955	280	790	2.7	.77	−20	−4
2,830	253	879	3	.85	−19	−2.2
2,304	154	1,520	5.2	1.48	−13.1	+9.4
1,980	106	2,170	7.5	2.11	−9.1	15.6
1,825	88	2,600	9	2.53	−7	19.4
1,420	50	4,510	15.6	4.38	−0.5	31.1
1,177	37	7,220	24.9	7.01	+6	42.8
973	17	13,200	45.5	12.8	15	59
886	8	20,800	71.7	20.2	22.3	72.2
790	0	(b)	-----	-----	-----	-----
7,814	∞	(c)	-----	-----	-----	-----

[a] To obtain parts per million by volume, multiply micrograms per liter by 0.804. To obtain parts per million of air by weight, multiply by 0.62.
[b] Short circuit. [c] Open circuit.

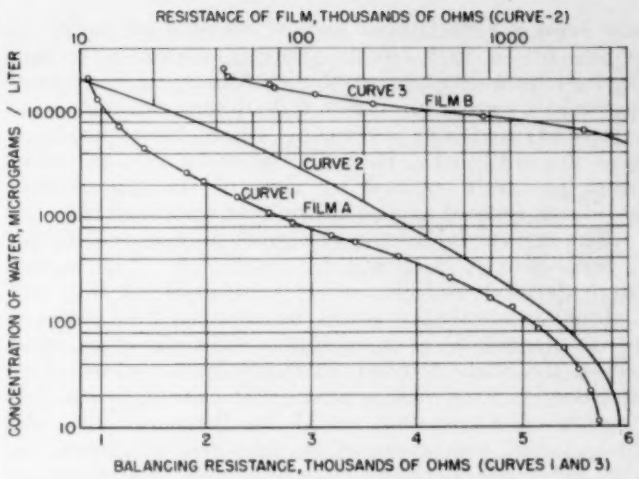

FIGURE 12. *Calibration of two conducting films in terms of concentration of water.*

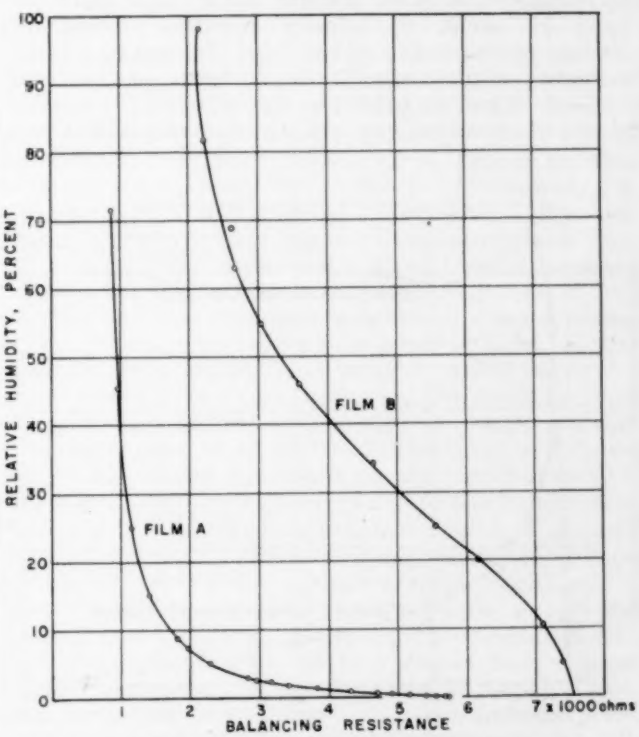

FIGURE 13. *Calibration of two conducting films in terms of relative humidity.*

the hook on the upper end of curve 3 of figure 12 represents a real effect. During exposure to the highest humidity observed with film A, its resistance passed through a minimum (which was the resistance recorded) and was increasing when the experiment was discontinued. In both cases the effects noted were probably caused by flow of the too mobile solutions formed as saturation was approached.

The sensitivity of the electrical indicator of figure 7 with film A is shown by figure 14. The curves were derived as follows. It was assumed that the balancing resistance could be read to 0.05 percent of its magnitude at any point. This corresponds to about 0.8 scale division of the galvanometer. The sensitivity, by which is meant the change in concentration of water that could be observed with the instrument, was assumed to have the same ratio to the difference between two observed humidities as the 0.05 percent of the mean balancing resistance had to the difference between balancing resistances, and this sensitivity was plotted with respect to the average of the two observed humidities. It is apparent at once that the sensitivity approaches about 0.3 μg/ liter or 0.1 percent of the water present, whichever is greater.

Figure 14 indicates instrumental sensitivity only. It must not be supposed that an absolute accuracy as great as this is usually or ever obtainable. The effects of all other sources of uncertainty remain to be accounted for. Actually, electrical sensitivities, in the lower range of humidities at least, can be considerably increased by using thicker films or by substituting an electronic null-point indicator for the galvanometer, but at present there is usually no object in doing so, chiefly because sufficiently accurate adjustment and readings of pressure cannot be made. Higher sensitivities in terms of the ratio of water vapor to total gas (or of weight per unit volume of expanded gas) are readily obtainable when the gas to be measured is under high pressure, and they are occasionally useful.

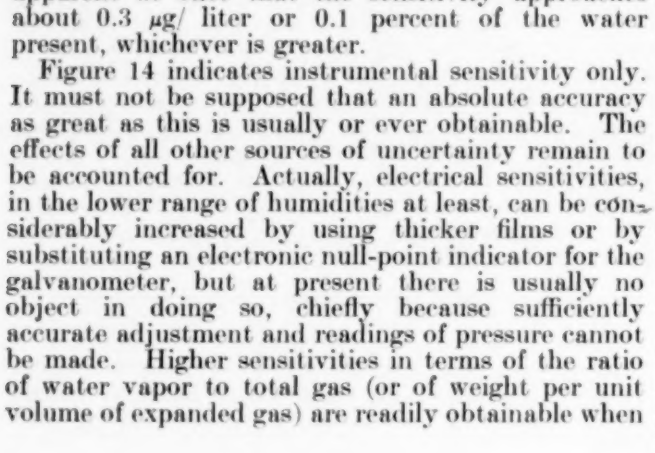

FIGURE 14. *Sensitivity of typical phosphoric acid film.*

3.4. Speed of Response

The greatest improvement made in technique since the publication of [1] was the result of experiments reported in that paper on the rate at which equilibrium is attained between the detector and the atmosphere to which it is exposed. Those experiments indicated that the acid dissolved in the glass insulator, producing a thin, slightly conducting, and slowly changing layer beneath the fast-acting surface coating. When the contaminated glass has been removed by surface grinding and an acid film of ordinary thickness has been applied, 90 percent of the change of resistance resulting from a change of atmosphere occurs within a second or two. A more precise determination of lag is difficult to make because it is not easy either to specify the thickness of film used or to provide an instantaneous change of atmosphere.

The grinding (or honing) of the detector surface was previously described. When it has been properly done, there is almost no drifting of the electrical reading when the detecting surface is in an atmosphere of constant humidity. When the detector is exposed to the air of an occupied room, the needle of the indicator waves like a flag in a breeze because it is following the different humidities always encountered in the fluctuating air currents in such a room.

4. Procedures, Corrections, and Sources of Error

4.1. Operation of the Instrument

a. Procedure in Testing Compressed Gas

The method of operating the instrument when testing aviators' oxygen has already been given briefly but is so simple that it will be repeated here for convenience in the more detailed discussion of points of interest. Referring to figure 1, gas from the nitrogen (or compressed air) cylinder is maintained in the saturator at a pressure of about 500 psi by means of the regulator. The cylinder of gas to be tested is connected to valve C. Valve B is opened widely and valve A is opened a little to permit a slight flow of gas from the saturator through the cell. The indicating circuit is adjusted, usually by changing resistance R_4 of figure 6 to produce any convenient scale reading of the galvanometer, and as soon as this reading is sufficiently constant, it is noted. This reading will be referred to as the balance-point. Valves A and B are closed in that order and valve D opened widely. Valve C is then opened to permit a moderately brisk flow of the gas to be tested through the cell. As soon as this gas reaches the cell, the galvanometer needle goes off scale on the dry side, corresponding to a high resistance of the detector. Valve D is now closed gradually, and the pressure is built up in the cell until the galvanometer needle swings back to the balance point.

If the balance point is passed, it can be approached from the other side by carefully opening valve D. When a satisfactory check of the balance point has been reached, the pressure in the cell, P_x, is read. If there is any doubt that the pressure reading is sufficiently accurate, valve C or D is changed and another adjustment of the galvanometer to balance is made. When the observer is satisfied as to the balancing pressure, the thermometer is read and the concentration of water vapor is computed.

b. Control of Standard Gas

Details of the measurement will now be discussed. A saturator pressure, P_s, of 500 psi is selected for this particular purpose, because at ordinary room temperature, oxygen that meets Army-Navy specification for aviator's oxygen will have a substantially equal balancing pressure, P_x. If there is the same probable error in reading the two gages, the probable error of the comparison and the correction for deviation from the ideal gas laws are both minimized by making the two pressures equal.

One source of error is some uncertainty regarding the water content of the gas from a single saturator, and this is affected by the condition of the apparatus and the rates of flow employed. To begin with, the regulator rarely controls perfectly the pressure in the saturator. When flow is stopped, the pressure builds up a little; when flow is resumed the pressure falls, and this change tends to produce an increase in the water content of the gas as flow is increased. On the other hand, the evaporation of water within the cylinder tends to cool the gas and cause the water content to decrease during the test. If the rate of flow is too high, there may not be time for complete saturation. Observable effects of the two last mentioned causes are eliminated by using the double saturator previously described. Expansion at the valve causes a sharp drop in temperature of the gas with a tendency to precipitate the water as liquid. Fortunately most of the cooling takes place after the gas passes the narrowest passage in the valve, and any mist that is formed reevaporates, but sometimes water droplets formed on the surface of the metal are large enough when detached to cause a readable irregularity in the galvanometer reading. This effect can be completely eliminated by separating the outlet valve somewhat from the saturator and heating it a little with a small resistance coil. In a portable instrument, the valve is usually placed in a mass of metal large enough to prevent, by conduction, any important error from this source.

Usually in routine testing the outlet valve from the cell is left wide open for the standard gas, which is then assumed to be at atmospheric pressure in the detector cell. Of course it is not, or it would not flow. Consequently, the detector is exposed to a little higher concentration of water than would otherwise be the case. An auxiliary valve for limiting flow may be placed in series with valve A and given a permanent setting, or the operator may make sure by trial that the flow is slight enough so that stopping it entirely makes no prompt and significant difference in the galvanometer reading. (A slow change in the galvanometer reading beginning after a little delay usually indicates diffusion into the cell from the outside.) The gas cooled by expansion may not reach room temperature by the time it arrives at the detector. This affects the reading in two ways; the lower temperature tends to condense more water in the film and thus cause a decrease of resistance, but a film containing a given quantity of water has a high temperature coefficient in the opposite direction. The first effect is likely to predominate, but for the duration and rate of flow usually employed a significant error does not occur because of differences of temperature of the detector when the "comparison" and "test" gases are interchanged. At high rates of flow, the temperature effect may become significant particularly when carbon dioxide or a refrigerant is being tested.

The discussion thus far would indicate that accuracy is promoted by making the flow of gas from the saturator very slow. We should add that at a very high rate of flow there is danger that liquid water will be carried over from the saturator mechanically, and that there is even the possibility that a sudden blast of gas over the detector will displace the film (this not infrequently happens with the gas to be tested if valves are manipulated carelessly).

Another factor of importance enters, however. The dry side of the instrument is rarely completely dry. Even though the parts of the apparatus are made, dried, and assembled with care, they seem to have the property of sorbing water from moist gas and giving it up later to a drier atmosphere in sufficient quantity to be readily detected. Gages are the worst parts of the apparatus in this respect; valve packings probably next, although the trouble from packings was largely eliminated by the use of Teflon. This exchange of moisture with surfaces and pockets within the apparatus generally affects the resistance of the detector when there is no flow of gas. A very small flow is affected to some extent, a large flow is not affected appreciably. For this reason we do not want gas from the saturator to flow too slowly; there is also a saving of time in reaching equilibrium if the rate is increased. A rate of 250 ml/min from the saturator is probably usually about right. It is not necessary to measure it, however; the observer soon learns to control it satisfactorily by other means. In a quiet room the gas escaping from the saturator at 500 psig should be barely audible to a normal ear, or silent but on the verge of audibility. The stream issuing from the small outlet of valve B should not be perceptible to the hand unless the outlet is blocked momentarily with a thumb. The little spurt of gas when the pressure is relieved should be noticeable. Momentarily blocking the flow should also cause the galvanometer to respond decisively and at once. If the apparatus is thoroughly dry, the galvanometer reading should be the same for any rate of flow of gas sufficient to prevent diffusion upstream from the outlet valve and not great enough to build up appreciable pressure in the cell. To save time, it is better to adjust near the second limit than the first.

c. Troubleshooting

The condition of the apparatus can usually be judged by the quick and simple tests that follow. With valve B partially closed, set the rate of flow (with valve A) at what is considered a little more than is desirable, to produce a slight pressure in the cell, then close the valve half way. A prompt but slight deflection toward the dry side (higher resistance) is the normal reaction if the system is dry, because the pressure in the cell diminishes. An immediate and permanent deflection toward the wet side indicates that water is entering the gas stream steadily as it evaporates from a packing, screw thread, or other source near the main channel of gas flow. A strong momentary deflection followed by the return to a steady reading, which is equal to or on the dry side of the reading obtained before the change of flow, indicates a nearly isolated pocket in which wet gas can accumulate and from which it is released only by a change of pressure. This pocket is usually the gage. If no deflection occurs when the rate of flow is changed it may be because the rate was initially too low to produce appreciable pressure in the cell, because the detector or indicator is insensitive, or because there is so much water in the cell or its connections that the gas is nearly saturated regardless of rate of flow.

The conditions may be further explored by checking and releasing the flow with a thumb at the outlet of valve B. Usually the galvanometer deflects sharply to the wet side when flow is stopped, and returns to the original reading when it is released. Sometimes a sequence of deflections will follow the release in such a way as to disclose a source of water, but this is less likely than with the less violent changes of flow produced by valve A.

If stopping and starting the flow at the outlet does not produce normal deflections of the galvanometer, the detector should be taken out of the cell and its response to the ever-changing humidity of room air noted, particularly the effect of bringing the detecting film near the operator's hand. If the indicator responds normally to this by promptly indicating a much lowered resistance, and particularly if the resistance of the detector in the cell was low, the apparatus is probably flooded. If exposing the detector to the atmosphere near the skin does not cause a sharp decrease of resistance, the system is inherently insensitive. If touching the electrodes with the finger does not produce a quick off-scale deflection, the trouble is in the electrical indicator and may be caused by a run-down battery, a broken connection, shunting by a low resistance, or the like. If the response to touching the electrodes is normal the trouble is in the film, which must be renewed.

The troubleshooting procedure is not as cumbersome as its description suggests. It should not require more than 2 or 3 min including the renewal of the sensitive film, if that is needed. Correcting faults in the electrical system and drying out the apparatus, when this is necessary, take longer.

If liquid water in quantity has gotten into the dry side of the apparatus, it is all but impossible to remove it completely except by disassembling the apparatus and baking the individual parts. If the moisture has come only from exposure to gases of fairly high humidity, it can usually be removed sufficiently by attaching a cylinder of dry gas and alternately building up and discharging a pressure of several atmospheres in the system. The cycle can be repeated every 2 or 3 sec. If 500 or 1,000 cycles are not effective, more thorough means of drying should be resorted to. This treatment is usually needed and usually successful after the apparatus has been out of use for a considerable period of time.

In addition to conditions previously mentioned, readings may be affected by changing battery voltage and the effect of changes of temperature and humidity on the measuring circuit, including the resistance of the insulation of leads and detector. Changes of capacitance resulting from movements of parts of the apparatus may also produce effects. When comparisons are completed promptly all these effects are practically equal on the readings for standard gas and sample and cancel out. Because they may change, it is advisable to complete comparisons promptly and with as little disturbance of the equipment as possible.

When tests are being made only to determine whether gas does or does not meet a specification, one takes account of the temperature and the setting of the regulator and computes the pressure at which gas that just meets the specification would balance. Thereafter until test conditions are changed, it is necessary only to run the pressure of the gas to be tested up to the predetermined value and note whether the galvanometer reading is to the right or left of that made with the standard gas. A setting with the standard gas is made with each cylinder, but this is easily done by an observer while someone else changes the test cylinder. It has been found practicable for one observer, with a sufficient crew of laborers to shift cylinders, to make tests by this method at the rate of 800 cylinders per 8-hr day. If it is to be determined how much water is present, not merely whether it is above or below a certain limit, more time is required. A test does not often require more than 2 min exclusive of the time required to move and connect the cylinder.

d. Use of Compressed Gas and Standard

Actually it is not practicable to measure the water content of most of the aviators' oxygen now made by direct comparison with gas from a saturator, even if the saturation pressure is 1,000 psi instead of the recommended 500 psi. If, for example, gas saturated at 1,000 psi and 25° C (77° F) and expanded to 1 atm matches gas at the usual charging pressure for storage cylinders, 2,000 psi, the water content of the stored gas is 4 μg liter (after expansion to 1 atm).

If the saturation pressure is 500 psi, the minimum measurable water content of the stored gas is 7 μ g/per liter. Most of the aviator's oxygen tested at the Bureau, after the oxygen manufacturers began trying to comply with the specified maximum of 20 μg has contained less than 4 μg/liter. To determine the water content actually present in such dry compressed gas, or to measure conveniently the water

content below 0.2 or 0.3 mg/liter of gas not initially under pressure, it is best to use a cylinder of fairly dry compressed gas as a secondary standard. Even for gases within range of direct comparison with the saturator, the cylinder is a convenience because less care is required than in the control of the saturator, and the composition of the standard gas is less dependent on temperature.

The gas to be used as the secondary standard must be compared frequently with gas from the saturator, for the water content of gas discharged from a cylinder invariably increases as the pressure falls, because the gas in the cylinder is always in near equilibrium with water adsorbed on the walls. This equilibrium is somewhat affected by temperature, but changes in the gas are slow.

A cylinder of gas to be used as a secondary standard in testing other cylinders can usually be selected from the lot. Otherwise it can be conveniently prepared in a laboratory in which compressed air and a vacuum pump are available by thoroughly drying an evacuated cylinder, admitting as much air from the room as is desired, and filling with compressed air, dried with a good desiccant after compression. As an example, assume that a water content of about 25 μg/liter is desired in the secondary standard, that compressed air is available at 1,800 psi, and that the laboratory air is 50 percent saturated at 25° C. The room air contains about 11,500 μg of water per liter. At 1,800 psi, the cylinder will contain about 125 volumes (at 1 atm) of air. Hence, we want about $(25\times125)/11{,}500=0.27$ atm$=210$ mm Hg of room air in the cylinder. As a secondary standard this gas can be used, while still at the initial pressure, to measure gas at 1 atm containing from about 25 to about 3,000 μg/liter, or gas compressed at 1,800 psi at about 0.2 μg/liter after expansion. It will measure the quantity corresponding to saturation with liquid water in the cylinder of any gas above about 4 atm. As the gas in the standard cylinder is used up, the usable range becomes narrower. The upper limit decreases because only lower comparison pressures (P_c of eq (2)) are available; the lower limit increases because some water evaporates from the cylinder walls.

The actual use of standard gas from cylinders differs from the use of a saturator in only one important respect. It is more often advantageous to use the secondary standard at other than a pressure of 1 atm; unless advantage is taken of the fact that the barometric pressure is known more accurately than any small pressure can be measured on the gage attached to the instrument, accuracy is favored by making the pressures of standard and unknown gas as high as practicable. There is less reason than with the saturator to avoid excessive flows, and the observer may wish to gain speed by increasing somewhat the flow used. On the other hand, he may wish to conserve the supply because of the trouble of renewing it.

c. Operations Other Than Testing Compressed Gases

In most of the numerous possible applications of the method other than testing compressed gases, the gas to be tested is at atmospheric pressure. Instead of varying the pressure of the unknown gas to obtain a balance corresponding to an observation already made of the standard gas, the first galvanometer setting is made with the unknown gas, and the pressure of the standard, whether from saturator or calibrated cylinder, is varied to obtain a balance. The details of the procedure are so like those already given that they probably require no further description. Because we lack the ability to change the pressure of the unknown sample, the range of concentrations that can be measured with a single standard is narrower than in testing compressed gas, and we may need two secondary standards in addition to the saturator, whereas we rarely need more than one in work with compressed gases.

One source of error should be emphasized in connection with miscellaneous uses of the instrument. No rubber whatever can be used in any connection through which a gas to be tested flows. Exposing the gas to contact with any rubber surface is almost equivalent to exposing it to contact with an equal free surface of water.

While not to be compared with rubber as a trouble maker, oil dissolves enough water from the vapor phase to cause sluggish readings. The metal tubing used in the apparatus should be cleaned by blowing a stream of hydrogen or city gas through it while a burner is passed from inlet to outlet slowly enough to heat the section above the burner to redness. This leaves the inner surface of the metal free of both oil and oxide.

4.2. Deviation from the Ideal Gas Laws and Computation of Results

a. Air, Oxygen, and Nitrogen

The equations given in the introduction would serve to compute correctly the results of experiments provided all the gases involved, including water vapor, behaved as ideal gases. This statement is meant to include as a part of the behavior of ideal gases the commonly assumed rule that the mass of water vapor per unit volume in equilibrium with liquid water is independent of the presence of other gases. The rule is not strictly true, and the deviation from it is to be attributed to forces between the molecules of water vapor and other gases, which are the same forces that cause the deviations from Boyle's and Dalton's laws. Hence, it is correct as well as convenient to include the rule of constant vapor pressure among those defining relations for ideal gases. Actual gases have what has been described as a solvent effect on water vapor that tends to retain the water molecules in the gas phase.

The deviations from ideality can probably be described most clearly in terms of "fugacity," the tendency of a substance to "escape" from one phase into another. If this tendency is the same in two phases there can be no net transfer between them, that is, they must be in equilibrium so far as their water is concerned. When a steady reading is obtained with a detector exposed to one sample of

gas, it is known that the fugacity of the water vapor in the gas phase and that of dissolved water in the detecting film are equal. If the same reading is obtained when the film is exposed to another sample of gas, the fact indicates that the water has the same fugacity in the two gases.

Actually, then, it is fugacities that are compared by the instrument. In an "ideal" system containing definite relative masses of water and gas, fugacity would be proportional to pressure, and equations 1 to 4, which were introduced as only approximations in the first part of this paper, would be exact. In the actual system a relation between fugacity and pressure must be established by experiment.

This relation may be written by using the formula in which $F=AP(1+KP+K'P^2+\ \ldots)$ in which F is fugacity, A is a constant involving the units in which F is expressed, and which need not be stated because A eventually cancels out, and constants K,K', . . ., are to be determined by observation. The determination has been made for air in the following different ways: (1) by absorbing and weighing the water from measured volumes of air that had been saturated with water at different pressures, (2) by comparing the gravimetric determination of water with the electrical observations of the same sample and adjusting the constants in the equation to bring the two measurements into agreement, and (3) by comparing electrical measurements made with "comparison" gas saturated at different pressures and again adjusting the constants to give the same readings. The first of these three procedures involves no measurement with the electrical instrument, and the third involves nothing else. By substituting air and nitrogen for oxygen in the saturator and making the usual electrical measurements on the same gas, it was found that the difference in the constants for these three gases were outside the limit of accuracy of the measurements. This has been repeated several times with different samples of these gases and with the same result. Experiments in which the second and third methods were used were reported in [1]. They were limited to the pressure range 0 to 2,000 psi, and indicated that over this range K' and coefficients of powers of P higher than 3 could be neglected. For $K'=0$ and the pressure range covered, method 2 applied to the average of a set of gravimetric determinations led to a value $K=-1.5\times10^{-4}$; the third method led to $K=-1.7\times10^{-4}$. The opinion was there expressed that 1.7×10^{-4} would be found to be the more accurate value. Later determinations by the first method, by Howerton [9] and by Diniak and Hughes [10] verified the value $K=-1.7\times10^{-4}$ as the best value to be used for pressures below 2,000 psi when K' is neglected.

A more extensive study by Diniak and Hughes [10] at pressures up to 6,000 psi and room temperature (25° C) led to the simultaneous values $K=-1.9\times10^{-4}$ and $K'=1.4\times10^{-8}$. These values, when used to predict the water content of gases saturated with water vapor and at pressures from 0 to 3,000 psi, yield results that are in excellent agreement with the observations of Webster [11] and others. Putting these values in eq (2), we obtain

$$W_x=S\,\frac{P_cP_w(1-1.9\times10^{-4}P_c+1.4\times10^{-8}P_c^2)}{P_sP_x(1-1.9\times10^{-4}P_s+1.4\times10^{-8}P_s^2)\,(1-1.9\times10^{-4}P_x+1.4\times10^{-8}P_x^2)}. \qquad (5)$$

The values of K and K' change with changing temperature and have not been determined with high accuracy except at "room temperature." Their variation between 20° and 30° C are probably outside the accuracy of measurement. Some data for higher and lower temperatures are to be presented and discussed in [10].

b. Computer and Its Use for Compressed Gas

The solution of eq (5) involves ascertaining the value of S, the saturation pressure of water at the temperature of test, and reducing four pressures from gage readings to the absolute scale before the operations of addition and multiplication indicated by the equation can be performed. The time involved in doing this by longhand is greatly in excess of that needed to make the tests themselves. A computer in the form of a circular slide rule for quickly and simply performing the necessary computations was described in [1]. This has been redesigned [12] to take account of the new values for deviations from ideality and to cover wider ranges of pressure (0 to 6,000 psi) and temperaure (−100° to +120° F).

The new computer is shown in figure 14. It consists of a base disk and two rotating disks with protruding tabs, both of which contain windows of transparent plastic through which scales on lower disks can be read. On the base disk an outer logarithmic (ordinary slide rule) scale divides the circumference of the circle into three decades. It is marked "Water vapor-milligram per liter at 70° F." Near the center is a scale marked "Temp. ° F." It is formed by laying off logarithmically the vapor pressures of water from −30° to +120° F, and marking each pressure with the temperature at which it occurs.

The middle disk has only one major scale, marked "(P_c) comparison pressure." On it, absolute pressures are laid off logarithmically, but each point is marked with the corresponding gage pressure (difference between absolute and barometric pressures) when the barometric pressure is 14.7 psi. At one end of the comparison-pressure scale is a short scale marked "alt. correction" that will be referred to as the "altitude scale" when corrections are discussed.

The upper disk has two principal scales, marked "Test gage pressure (P_x)", and a scale marked "(P_s) saturation pressure." There is also an auxiliary

scale marked "Frost point below −30° F." It is used as an extension of the temperature scale (Scale *T*) on the base plate.

The computer can be used in a great many ways, most of which will be readily understood by comparison with the ordinary slide rule. Multiplications and divisions are made by adding and subtracting angles just as they are made by adding and subtracting lengths on a linear slide rule. Frequently-used conversion factors can be introduced by markings on the appropriate scales as the value of π is commonly marked on the linear slide rule. The widths of the tabs have been shosen to permit direct readings of water concentration in units other than milligrams per liter. There is room to the left of the altitude scale for marking additional conversion factors in the range 1.2 to 100. An example is shown in figure 15, in which the middle disk has two markings,

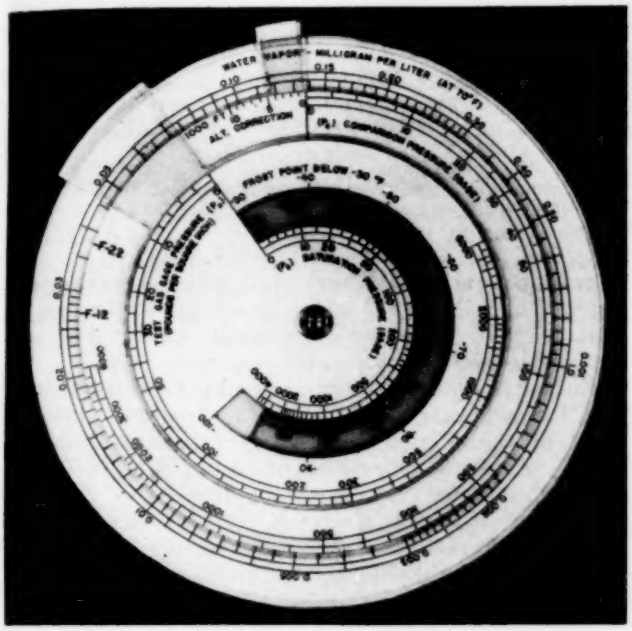

FIGURE 15. *Computor.*

F–12 and F–22, that read directly in parts of water per million parts by weight in the two commercial refrigerants Freon 12 and Freon 22, respectively.

The quantity of water in a gas is designated at various times and for several reasons by a variety of systems and units. It is often necessary or convenient to convert from one system to another. The computer is designed to facilitate, particularly, interconversions among the following:

1. Weight of water per unit volume of gas at a standard temperature: (a) Milligrams per liter at 70° F (almost identical with ounces per thousand cubic feet). (b) Pounds per 10,000 cubic feet.
2. Parts by weight of water per thousand parts of gas.
3. Vapor pressure of water.
4. Dewpoint (frost point below 32° F).
5. Relative humidity.
6. Percentage by volume of vapor in gas.

In the use of the instrument, for testing the dryness of a compressed gas, by comparison with gas from a saturator at high pressure, the pressure in the saturator in pounds per square inch gage is set opposite its temperature; the index of the "comparison pressure scale" is set on the "test gas pressure" scale and the water content of the gas being tested (after expansion to 1 atm at 70° F without change of composition) is read opposite the comparison pressure.

After this setting has been made, the tabs of either disk can be used as the glass slide is used on a linear slide rule to mark a position for further computation.

The angular widths of the tabs have been chosen so that when the right-hand edge of the wider one reads milligrams per liter on the logarithmic scale, the left edge reads pounds of water per 10,000 cubic feet of gas; when the right edge of the narrow tab reads milligrams per liter, the left edge reads pounds of water per thousand pounds of air. The vapor pressure of water in millimeters of mercury is numerically equal to 1.017 times the number of milligrams per liter at 70° F, a factor that can be read on the computer but can usually be neglected. Subject to this error, the outer scale reads directly in vapor pressure units. When the zero of the comparison-pressure scale indicates milligrams per liter at 70° F, the 5,000 mark of the same scale (elongated to aid the memory) indicates percentage of water vapor by volume.

If the water content is less than 1 mg/liter, the dewpoint is read directly on the temperature scale under milligrams per liter on the outer scale. If the water content is more than 1 mg/liter (at about 0° F), the numbers on the outer scale must be multiplied by 1,000 to correspond to the dewpoint (frost point below 32° F) on the adjacent temperature scale. If the right edge of the wide tab, on the upper disk, is brought to the water content in milligrams per liter on the outer scale, the frost point is read on the scale marked "Frost point below −30° F" at the lowest point (−30° F) on the temperature scale. The decimal point must be watched carefully in this operation; it is not taken care of automatically.

The relative amount of water in gases under two conditions is ascertained by finding an angle between the points representing concentrations under each condition. This angle can be set readily as that between the edges of the two protruding tabs. Then, if the middle disk is rotated, the small disk is carried along without disturbing the angle until one tab is above 1.0 of the outer scale on the base disk. The other tab then reads directly the ratio of concentration of water in the two cases. If one of the two conditions represents saturation, the ratio found is "relative humidity" as the term is ordinarily used.

For the sake of simplicity, pressures used in both eq (4) and (5) are expressed as absolute pressures. However, the pressures marked on the computer are gage pressures when the barometric pressure is 1 normal atm, 14.7 psia. If the barometric pressure differs from 1 normal atm the result obtained with the computer is somewhat in error. The correct result may be obtained by converting gage readings

to absolute pressures by adding the barometric pressure and introducing into eq (7), or more easily by changing each gage reading to what it would have been had the barometer read 14.7, and using the computer.

Variations of the barometer at a given point can usually be neglected for ordinary work, but the differences between points at sea level and altitudes of several thousand feet are too great to be disregarded. For convenience in the routine testing of compressed gases by the usual procedure, the total correction for the difference between normal pressure at a given altitude and normal pressure at sea level has been marked on the computer as an extension of the comparison pressure scale and labeled "Alt. correction." The correction was computed for the case in which a sample containing 20 μg of water per liter is compared with a gas saturated at 500 psig and expanded to the average barometric pressure at that altitude. It is applied at the end of the usual computation by reading the scale opposite the altitude in question instead of opposite the zero of the comparison pressure scale. The corrected result represents the water content of the sample at 70° F and 1 normal atm and is not exact except for the conditions of test specified. It may or may not be useful under different conditions of test; this can usually be determined by solving a typical set of real or assumed data with the computer and comparing with the result of a direct substitution in eq (7). If the difference is considered negligible, the correction scale can be used routinely for testing under approximately the conditions assumed.

5. Applications of the Method

5.1. Compressed Gases

The application of the method to the measurement of water in such "permanent" gases as air and oxygen has probably been described in enough detail. It should be added that the composition of the gas in a cylinder usually changes during its discharge because water is adsorbed in the oxide (or rust) coating of the cylinder wall, and tends to evaporate to maintain equilibrium with the gas phase as vapor is discharged with the gas. A typical behavior of an ordinary steel cylinder of gas is shown in figure 16. The cylinder was new, had been dried "thoroughly" by its manufacturer and filled with oxygen by direct evaporation from the liquid. A series of experiments with different cylinders dried by the same procedure and filled at the same time with gas containing about 10 μg/liter showed that there was no significant change in composition after charging to full pressure in the case of an aluminum and a stainless steel cylinder and only negligible though measurable increases during discharge; an ordinary cylinder previously in service for "dry" gases showed about the same trend as figure 16. An oxygen cylinder long used in welding service, deeply rusted and visibly wet, was heated and purged until it was

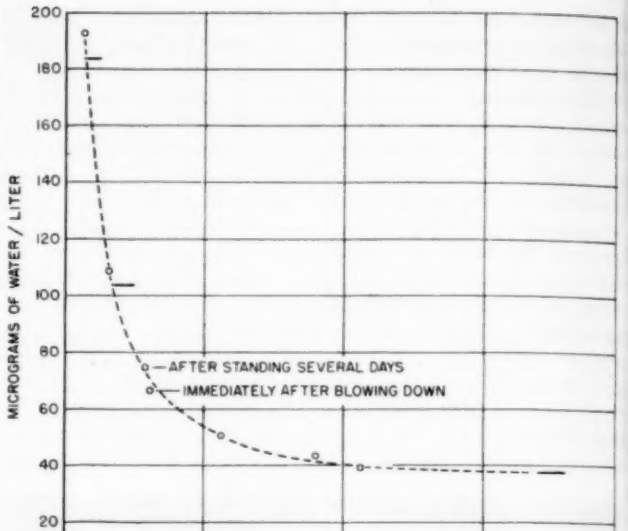

FIGURE 16. *Water vapor in gas from a cylinder of compressed oxygen determined gravimetrically and electrically.*

—, Gravimetric test; ○, electrical test.

apparently thoroughly dry; but after charging with a dry gas, it delivered gas with a high water content that increased almost accurately in inverse proportion to cylinder pressure.

Each gas shows individual deviations from ideality and for accurate work at high pressures this fact must be taken into account by substituting appropriate values for the constants in eq (5). Hydrogen and helium are very close to ideal gases and zero values for constants K and K' can probably be used without significant error. Nitrogen, oxygen, and argon are practically indistinguishable, and eq (5) applies to all three without change. An early approximate determination indicated that at pressures at which the term containing P^2 can be ignored the value of K for methane should be 2.4×10^{-4} making the correction factor by which methane pressures are multiplied (1–0.00024 P). This is to be compared with the best value for air, when the term in P^2 is omitted, of (1–0.00017P).

Two of the Freons were studied in some detail by comparing results of the electric and gravimetric methods. It was concluded that at 25° C, the value of K should be -1.0×10^{-6} for dichlorodifluoromethane (Freon 12) and 1.2×10^{-5} for chlorodifluoromethane (Freon 22), while the value of K' for both remained the same as for air ($K'=1.4\times10^{-8}$).

5.2. Liquefied Gases

"Gases" such as carbon dioxide, propane, butane, sulfur dioxide, methyl chloride, and the Freons, are usually almost entirely in the liquid phase at the time of sampling and we are interested in the com-

position of the liquid; but we must make our measments in the gas phase. There are two solutions to the difficulty. A "partition coefficient" of the water between gas and liquid phases can be determined by experiment or taken from the literature; but this coefficient changes with temperature and to some extent with pressure and is probably hardly worth ascertaining except for rapid approximate tests.

A better method is to permit a slight flow of the liquid through a capillary channel into a heater where it is vaporized completely and continuously. If, as in a refrigerating machine, there is a driving mechanism, it may be possible to return the gas tested to the system without loss. Apparatus and procedures are described by Diniak, Hughes, and Fujii [3] and by Brisken [14] for following changes in a closed system of this kind. The analyses represented by figure 29 in reference [1] were obtained with simpler equipment that discharged the vapor sampled to the air.

Usually the comparison gas used in testing any gas will be air or its equivalent for this purpose, hence in the use of eq (5) only the term $(1-KP_x+K'P_x^2)$ is affected by the nature of the gas analyzed. If, in this case, the computer is used in determining W_x, the result should be multiplied by the quotient of the correction factor for air at pressure P_x divided by that for the gas tested at the same pressure. Thus, if the gas tested is methane, if its water content is represented by W_m, and if W_a is the water content shown by the use of the computer,

$$\frac{W_a}{W_m}=\frac{(1-.19\times10^{-4}+1.4\times10^{-8}P^2)}{(1-2.3\times10^{-4}P_x)}.$$

From the data of Wiebe and Gaddy [13] at 25° C, and in the lower part of the reported pressure range, the correction for the fugacity of water vapor in carbon dioxide was computed [1] to be $(1-6.05\times10^{-4}P+1.2\times10^{-7}P^2)$, which agreed very well with observations made on a cylinder of carbon dioxide. The data from which this factor was taken show a reversal of direction at the pressure of liquefaction of the carbon dioxide-rich phase, and the correction no longer applies. Hence the water content of carbon dioxide is to be determined at as low a value of P_x as practicable. Making the division indicated by the ratio W_a/W_m, a determination of water in carbon dioxide made with air as the comparison gas and calculated on the computer should be multiplied by the factor $(1+4.15\times10^{-4}P+1.5\times10^{-7}P^2)$.

The maximum pressures in the gas phase of the more easily liquefied substances such as propane, butane, and the Freons, minimize the importance of a correction for pressure.

In sampling materials such as the refrigerants, even from the gas phase, any appreciable expansion of the gas in the sampling line before the detector is reached results in cooling that may affect the result unless the gas is brought to detector temperature through a heat exchanger. Long metal connections and slow rates of flow minimize trouble from this source.

5.3. Liquids

The method is convenient and very rapid for making comparisons of the water contents of many liquids. Its usefulness depends on the fact that if air is brought to equilibrium with the liquid, by bubbling or otherwise, the fugacity of water vapor will be equal in the two phases and can be matched with that of gas from a saturator or other known source.

A convenient method of bringing the detecting film to equilibrium, through the gas phase, with the liquid to be tested is to attach the detector to the upper end of a tube, that is dipped into the liquid to nearly its full length. Figure 17 shows a convenient form of apparatus. A glass tube A with a flared top snaps into a stainless steel fitting with hooklike fingers, an action similar to that of a snap garment-fastener on an enlarged scale. Ordinary test tubes of small size have been found satisfactory for the glass tubes. For small samples, a capillary tube with flared end could be used. They may receive a little spherical grinding to make a substantially tight fit with B. The detector D, shown here in cross section, is attached to B by nut E. The glass tube has an opening at the bottom, F, and at one side, G. The springs C hold the tube firmly against the detector block. The connection between tube and detector block is tight enough to prevent appreciable leakage under a few millimeters of water pressure, and the tube can be plunged into the liquid without excessive care and without touching the detector tip although it is only a few millimeters from the liquid surface. Since the liquid flows into the tube from well below

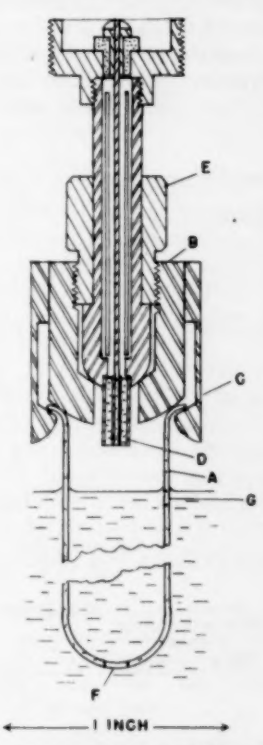

FIGURE 17. *Arrangement used in testing water vapor in equilibrium with a liquid.*

the surface, a reading is obtained that is not much affected by the composition of the liquid immediately at the surface, which sometimes differs materially from that of the bulk of the sample.

The method is extremely sensitive for water in liquids, like the hydrocarbons, that dissolve very little water, less so for ethers, ketones, etc., and least sensitive for such things as the alcohols and nitric and sulfuric acids. Unfortunately, the quantitative significance of the fugacity in terms of water content is different for each liquid; but once worked out on an empirical basis, it should permit a determination almost as quick and in many cases (such as that of the hydrocarbons) much more accurate than is possible with a hydrometer. It is also more specific for water and less subject to the effect of impurities, particularly the homologs of the principal constituent of the liquid, than is density or refractive index.

It should be possible to use the fact that the fugacities of the same quantity of water are very different in different substances to determine the composition of their binary mixtures by adding a known amount of water to their mixtures. This subject is discussed briefly in [2].

5.4. Solids

Interchanges between solids and gases are readily followed in detail. A simple example is the determination of the drying capacity of solid desiccants by passing a measured stream of air of predetermined humidity through them and measuring the water in the outflowing air at intervals. Figure 18 shows the results of tests of three desiccants by this method. The tests were made with saturated air at room temperature, which was fairly constant at an average of 73.8° F. Desiccant and saturator

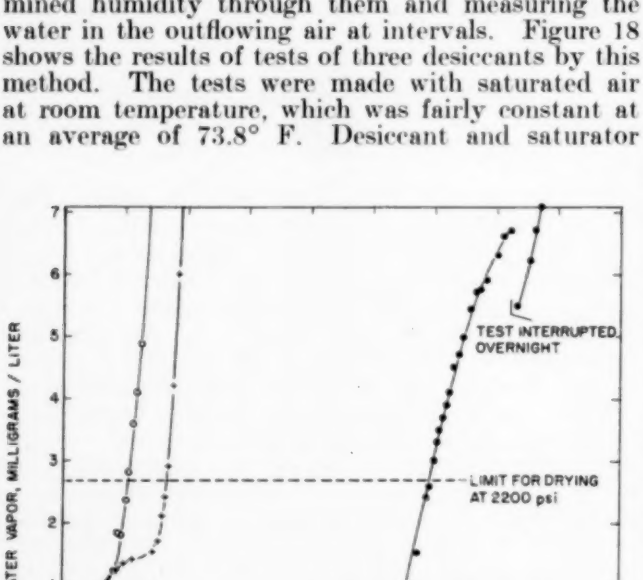

FIGURE 18. *Drying capacity of three desiccants.*
○, Desiccant No. 1; +, desiccant No. 2; ●, silica gel dried at 275° C.

were initially at the same temperature, but there was some (unmeasured) increase in the temperature of the desiccant, contained in a length of half-inch iron pipe, and probably a small reduction in temperature of the second of two saturators, steel cylinders filled with wet sand used in series. The water content of the saturated air was about 30 mg per liter (about 1.8 lb of water per 100 lb of dry air) and the "space velocity" through the desiccant was about 12.5 (12.5 volumes of air passed per minute through unit volume of the desiccant). Thus the "breakpoint" for silica gel at 500 min represents the drying of 6,250 cu ft of air per cubic foot of desiccant-filled dryer volume.

The silica gel in this case was a freshly "reactivated" (dried) lot of old material of the grade supplied to the government for "mothballing" military equipment. It may be of interest that the other two desiccants were of two different types delivered in hermetically sealed containers by different contractors for use in drying aviators oxygen at high pressure. The composition of these desiccants is not stated here because their inferior performance is believed to represent faulty preparation rather than inherent unsuitability of the classes of materials to which they belong.

The "limits" shown on the figure indicate the dryness required in compressed gases at 600 and 2,200 psi if the specification of 0.02 mg/liter in the expanded gas is to be met. The rather impressive possibilities of high-pressure drying are shown by the fact that the silica gel would have dried 606,000 times its volume of air saturated with water at 2,200 psi and 70° F before any of it would have contained more than 0.02 mg/liter after expansion to atmospheric pressure. The contamination of the desiccant near the outlet of its tube by contact with moist air during activation and preliminary handling is shown by the high initial portion of the drying curve. Had this contamination been avoided, oxygen equal to approximately one-half million times the volume of the desiccant would have been dried to contain only ten parts of water per million by weight.

The removable water content of a desiccant, a soil, or similar material can be determined readily with more or less accuracy by any of several procedures. The simplest is to integrate the water content found in a sample of air passed over the solid under whatever conditions are desired. An apparatus successfully used in determining the dryness of silica gel is illustrated and the procedure is described in [1]. If the water is not evolved at a convenient rate for satisfactory measurement in the flowing stream, the water may be frozen out with solid carbon dioxide or liquid air and determined as a whole after vaporizing and diluting by whatever procedure is desired.

5.5. Application to Solids of the Test for Water in Liquids

Water held by capillarity or adsorption on powdered solids such as paper or sand can be determined very rapidly by shaking a sample with a

suitable liquid and determining the water in the resulting solution by the use of the dipping tube previously described for liquids. The liquid used as a solvent for water must be calibrated in advance by adding known small amounts of water to some of it. It should be chosen so that it is never saturated by the water in the sample (alcohol, acetone, sulfuric acid, and other "completely miscible" liquids never are) and is still reasonably sensitive. For small samples of very dry materials, ether or a hydrocarbon can be used. The method is believed applicable to many materials that are hard to dry such as candies, fats and greases, soaps, and emulsions of various types; but in applications of each kind the effects of the material other than water on the fugacity of water in the solvent would have to be considered.

5.6. Determination of Substances That Can Be Converted to Water

The method is often applicable to the determination of substances such as oxygen or oxygen compounds easily reducible by hydrogen, or to hydrogen or known organic compounds, the hydrogen of which can be burned to water. Circumstances particularly favorable to its use exist in the case of argon, which is required for some purposes in extreme purity. Gas at cylinder pressure is first tested for water vapor in the normal manner. Then the gas, still at as high pressure as facilities will permit, is mixed with hydrogen, passed through a small combustion furnace containing platinized asbestos or equivalent catalyst, and again tested for water. Oxygen is computed from the difference between water in the original sample and that found after combustion with hydrogen; or both gases may be dried before entering the furnace by freezing out with liquid air, in which case the water found after combustion represents oxygen in the sample without correction. A sample may then be taken through the furnace after mixing with oxygen instead of hydrogen; the water produced is then a measure of hydrogen or hydrogen compounds in the gas and is to be interpreted in terms of the reducing gas most likely to be present, usually a residue from the process of removing oxygen. If natural gas was used to burn out oxygen, the water should probably be calculated as methane. If these analyses are conducted at or near the usual charging pressures of commercial cylinders, 100 atm or more, the method is sensitive enough to determine parts of water per ten million; the volume of sample and of reagent gases required are negligible; and the method is rapid when once the needed equipment has been assembled.

5.7. Permeability of Membranes

The permeability of membranes to water can be readily measured. The membrane is clamped between the halves of a "cell" with shallow chambers on each side. One side may be completely filled with water, putting the liquid in contact with the membrane; but usually the permeability to water vapor in a saturated atmosphere is desired and the cell is set with the membrane horizontal and the surface of the water in the lower chamber near to but not in contact with it.

The transfer of water through the membrane may be measured in either of two ways. For membranes of high permeability such as rubber, the best method is to measure the water vapor in the inlet and outlet of a constantly flowing stream. Membranes of low permeability are best tested by observing the build-up of moisture in a closed cell. A suitable apparatus is shown in [1].

The principal difficulty in the use of the second method is that of knowing or controlling the initial condition of the membrane. When permeability determinations are made in a flowing stream the test can be continued until a steady state is reached and the initial condition becomes unimportant. For comparative purposes, however, the static method is quicker and may be accurate enough in spite of the initial uncertainty. It may be conveniently conducted as follows:

With water in the lower chamber, the chamber above the membrane is swept out with a rapid stream of dry air for a preselected time to produce an approximately steady water gradient, in the membrane, from saturation at one surface to substantial dryness at the other. Flow is then stopped and the time required to build up the moisture content of the "dry" chamber to a predetermined reading is noted. With a "dry" chamber 1 in. deep at a temperature of 25° C, it requires about 40 sec to reach a relative humidity of 25 percent in the case of a cellulose acetate film 0.03 mm thick. With a Saran film 0.05 mm thick about 1 hr was required to reach a relative humidity of 10 percent. Other tests are reported in [1].

Either of the methods described is easily modified to determine permeability to hydrogen or oxygen. In the static method both a water vapor detector and a heated wire are located in one chamber. The apparatus is thoroughly dried before the test, then one chamber is swept out with dry hydrogen and the other with dry oxygen or air. Unless permeability is very great, the hot wire burns the permeating gas with practical completeness, replacing it with water. If the detector and catalytic burner are on the hydrogen side the build-up of water shows the permeability of the membrane to oxygen; if on the oxygen side, permeability to hydrogen is measured. Instead of hydrogen, permeability to an organic gas or vapor can be determined by substituting it for hydrogen.

Substantially, the procedure here recommended for permeability has several times been used for detecting leaks in apparatus with satisfactory results.

6. References

[1] E. R. Weaver and R. Riley, Measurement of water in gases by electrical conduction in a film of hygroscopic material and the use of pressure changes in calibration, J. Research NBS **40**, 169 (1948) RP1865; Anal. Chem. **23**, 216 (1948).

[2] E. R. Weaver, Electrical measurement of water vapor with a hygroscopic film, Anal. Chem. **23**, 1076 (1951).

[3] A. W. Diniak, E. E. Hughes, and Minoru Fufii, Determination of water content in Freon–12 circulating in a refrigerating system, Refrig. Eng. **62**, No. 2, 56 (Feb. 1954).

[4] E. R. Weaver and P. G. Ledig, Detection of water vapor in closed pipes, Tech. Pap. BS **17**, 637 (1923) T242; Ind. Eng. Chem. **15**, 931 (1923).

[5] F. W. Dunmore, An electrical hygrometer and its application to Radio Meteorology, J. Research NBS **20**, 723 (1938) RP1102.

[6] F. W. Dunmore, An improved electric hygrometer, J. Research NBS **23**, 701 (1939) RP1265.

[7] Arnold Wexler, Electric hygrometers, NBS Circ. **586** (1957).

[8] A. Wexler, S. B. Garfinkel, F. E. Jones, S. Hasegawa and A. Krinsky, A fast responding electric hygrometer, J. Research NBS **55**, 71 (1955) RP2606.

[9] E. K. Howerton (private communication).

[10] E. E. Hughes and A. W. Diniak (in preparation).

[11] T. J. Webster, J. Soc. Chem. Ind. (London) **69**, 343 (1950).

[12] A. W. Diniak and E. R. Weaver, A new computer for calculating the water content of gases, J. Research NBS **56**, 269 (1956) RP2674.

[13] R. Wiebe and V. L. Gaddy, vapor phase composition of carbon dioxide-water mixtures, J. Am. Chem. Soc. **63**, 475 (1941).

[14] W. R. Brisken, moisture migration in Hermetic refrigerating Systems, Refrig. Eng. **63**, 42 (July 7, 1955).

WASHINGTON, October 25, 1957.

Improved Bridge Method for the Measurement of Core Losses in Ferromagnetic Materials at High Flux Densities

William P. Harris and Irvin L. Cooter

Accurate core-loss measurements at high flux densities can be made by bridge methods if the power dissipated in the primary circuit at harmonic frequencies is measured and subtracted from the apparent power dissipated in the ferromagnetic material at fundamental frequency. The determination of this harmonic power term is inconvenient, and must be done with greater accuracy than that required in the final result. An amplifier having negative output resistance was devised and is used in a manner that automatically allows accurate compensation for the harmonic power dissipation.

1. Introduction

In two previous papers by the present authors [1, 2][1], it was shown that accurate results can be obtained by using the a-c bridge to measure core losses in ferromagnetic materials at high flux densities only by determining and applying a "harmonic power" correction. The method described involved the measurement of several harmonic-frequency components, I_h, of the exciting current and the computation of the correction term as the summation of all the $I_h^2 R_p$ terms of sufficient magnitude to affect the result, where R_p is the total resistance of the circuit carrying the exciting current. Since terms as high as the 13th harmonic were not uncommon, the method was complicated and rather slow, and required very accurate measurements with a sharply tuned voltmeter.

The present paper describes a method of measurement employing a power source having current feedback used in such a way as to make the circuit self-compensating with respect to "harmonic power". The result is that accurate measurements can now be made much more conveniently than by the previous method.

2. Theory and Principles

The Maxwell-Wien bridge, used with an Epstein test frame, is one of several circuits used for the measurement of core losses in specimens of ferromagnetic material. This circuit is depicted in figure 1, and the equivalent-circuit diagram is shown in figure 2. The inductance, L_d, and the resistance, R_d, are both caused by the presence of the ferromagnetic material in the test frame, and are nonlinear because of the nature of the hysteresis cycle of the material. This nonlinearity gives rise to harmonic-frequency components in current I, even with source E_s supplying a distortionless sine wave voltage. It is the power dissipated at these harmonic frequencies in the resistive elements of the circuit ($\Sigma I_h^2 R_p$) that causes the difficulties encountered when this circuit is used to measure core losses at high flux densities.

Previously, core losses were computed from the product $I^2 R_d$, where I is the rms value of the current,

[1] Figures in brackets indicate the literature references at the end of this paper

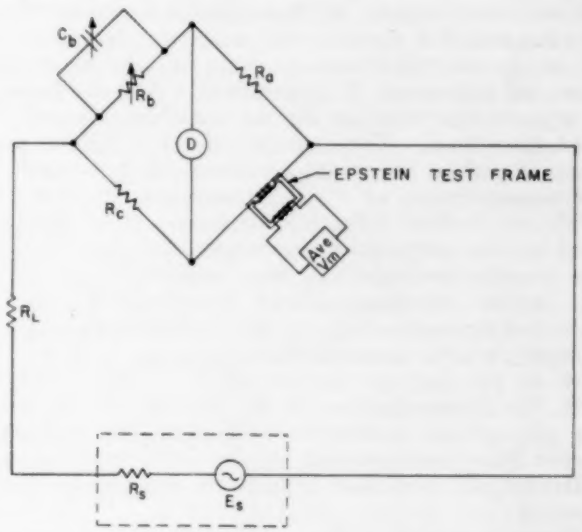

FIGURE 1. *Maxwell-Wien bridge circuit for measuring core losses, using Epstein test frame.*

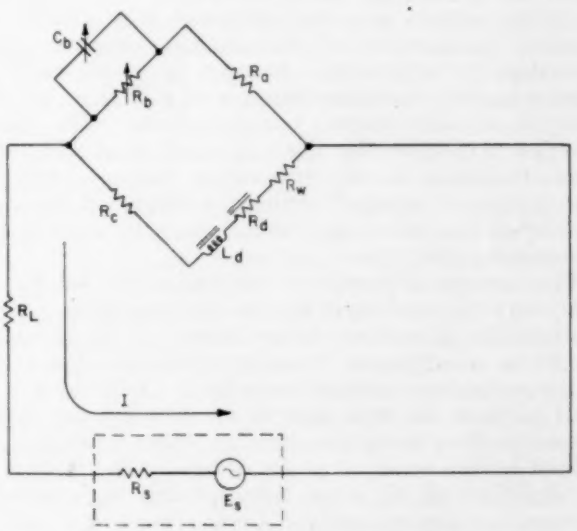

FIGURE 2. *Equivalent-circuit diagram of the circuit shown in figure 1.*

and R_d is the resistance associated with the ferromagnetic material in the test frame. R_d was usually determined at fundamental frequency from the bridge balance equations and the values of R_a, R_b, and R_c at balance, indicated by the tuned detector, D. The authors have shown [1,2] that the term I^2R_d includes not only the power dissipated in the iron but also all the power dissipated at harmonic frequencies in all the linear resistive elements of the circuit. The true core loss is then given by

$$P_c = I_1^2 R_d - \Sigma\, I_h^2 R_p,$$

where I_1 is the fundamental frequency component of the exciting current. The correction term $\Sigma I_h^2 R_p$ is negligible at low flux densities, but increases very rapidly at flux densities above 12 or 13 kilogausses in ordinary silicon-iron core materials, becoming several times as large as the true core losses as saturation is approached. A great burden of accuracy is thus put on the determination of the correction term. For example, if the $\Sigma I_h^2 R_p$ is four times P_c, then to attain accuracy of 2 percent in the measurement of P_c, it is necessary to measure $\Sigma I_h^2 R_p$ to better than 0.5 percent. The method used in the original investigation and described in the reports thereon [1,2] was sufficiently accurate, but rather complicated and inconvenient. It involved the measurement of each significant harmonic current, which included harmonics as high as the 13th at the highest flux densities measured, along with the determination of R_p, taking into account the changes of resistance with changing temperature. The measurement of R_p is further complicated by the fact that it includes the source resistance, R_s.

It was desired to devise a more convenient method of making core-loss measurements with an accuracy of 1 or 2 percent. This end would be achieved if the correction term $\Sigma I_h^2 R_p$ could be reduced to zero. This could be done if the harmonic currents I_h, could be eliminated, or if the ohmic resistance R_p could be reduced to zero. Although it is possible to suppress harmonics in the exciting current, this procedure is undesirable because it produces harmonics in the secondary voltage of sufficient amplitude to seriously distort the waveform. The usual practice is to strive for the conditions that will yield least distortion in the secondary voltage, and in fact measurements are ordinarily corrected to indicate what the core losses would be with a perfectly sinusoidal voltage wave.

The second alternative, the reduction of R_p to zero, was the one used in this investigation. It is the practice to reduce the resistance of the primary circuit to a minimum in order to reduce distortion in the secondary voltage waveform. But there is a limit to how far this can be carried by the usual means, such as using heavier wire, short leads, lower-valued bridge arms, etc. In order for the bridge to be useful at all, R_c must have a value high enough to measure conveniently. In the present work, 1 ohm was found to be the lowest practical value for R_c. The test-frame winding has appreciable resistance, ranging from 0.2 ohm to several ohms for practical sizes. Leads, power source, switches, etc, unavoidably add their contributions, bringing the least practicable values of primary resistance to more than 2 ohms in most cases. The elimination of the resistance that remains after the measures mentioned have been employed is the heart of the problem.

In order to reduce the total resistance, R_p, to zero, we have merely to add this same absolute value of negative resistance. Fortunately, this is no longer a fanciful wish. For about 25 years, electronic circuits having negative resistance properties, chiefly feedback amplifiers, have been known [3, 4, 5, 6, 7, 8, 9]. More recently the use of feedback to control the internal impedance of amplifier and other circuits has grown so widespread and so much has been published on the subject, that it is impossible to refer to all applicable publications. Those few cited should serve as a suitable point of departure for those wishing to pursue this subject.

For the present work, a high quality, 200-w amplifier was used. This amplifier had the usual feedback loops for achieving stable, distortion-free operation over a wide range of frequency. In addition, a special loop of current feedback was employed to alter the output impedance, making it possible to achieve reasonable values of negative impedance with controllable, stable operation. The essential elements of this feedback method, and the means employed to adjust it to give exactly the correct magnitude of negative resistance to counteract the positive resistance of the circuit, are described in the next section of this paper.

An alternative method of approach to the harmonic-dissipation problem is to consider the circuit as containing a series of harmonic generators, each receiving energy from the main source via the fundamental-frequency current, and delivering it to the circuit at harmonic frequency via harmonic-frequency currents. If this view is taken, the present arrangement is then a means of removing the harmonic generators from the bridge arm containing the ferromagnetic-cored test frame, putting them instead in the main power source. This view is supported by measurements of voltages at the harmonic frequencies appearing across the various elements of the circuit, with and without compensation, as described in the next section.

3. Experimental Procedure

3.1. Simultaneous Measurements

The inclusion of a wattmeter in the circuit, as described in the previous investigation [1, 2], provides a reference measurement made under identical conditions. This feature was found valuable, and was used in the present work. Figure 3 shows the wattmeter, W, with its potential coil connected to the secondary of the test frame, and its current coil in series with the bridge. It was found desirable to connect the current coil outside the bridge rather than in the arm containing the test frame, as was

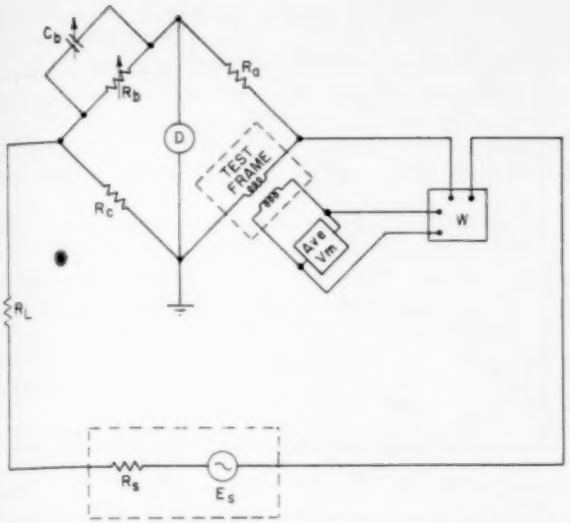

FIGURE 3. *Method of connecting wattmeter, W, for making simultaneous measurements.*

done in the preceding investigation. Small changes in the resistance of the current coil caused less difficulty when not included within the bridge arms. The bridge arm, R_a, was disconnected while reading the wattmeter in order to eliminate the small current in the parallel path [2] through R_a, R_b, and C_b. All measurements were made in simultaneous pairs, and the agreement of the two methods was used as the criterion of the new method.

3.2. Equipment

Essential to the success of the method is the special power source used. This source must have the property of presenting an apparent internal impedance that is negative, and of precisely controllable magnitude. For precise measurements the output voltage of the source must be very stable in magnitude, because the impedance of the test frame with ferromagnetic core is a function of the current in the primary winding. Thus, at high flux densities, a small variation in source voltage causes a relatively large change in the bridge balance parameters.

To achieve the desired characteristics, a high-quality power amplifier with a special feedback circuit was purchased. The basic features of the feedback circuit are shown in figure 4. The voltage developed across a resistor in series with the primary circuit is fed back to an early stage of the amplifier, through an isolating transformer, and with means for variation by minute increments. The series resistor, R_1, can be small, 0.1 to 1 ohm, and should have low residual inductive or capacitive reactance. R_2 is a ten-turn precision potential divider, providing precise control. Variation of the position of the tap

[2] It was found that with R_a not less than 30,000 ohms, the wattmeter reading was increased not more than 1 percent by connecting the current coil outside the bridge arm. Disconnecting R_a caused the reading to be exactly the same as with the current coil in the bridge arm.

The ratio of resistances of the two current branches is seen to be at least 30,000 to 3 (at highest flux densities), and it might be expected that the power difference would be much less than the measured 1 percent. However, the phase angles of the two currents are different, with the power factor of the large-current branch often about 0.05, whereas that of the small-current branch is much larger. Therefore, the very small current in the latter branch contributes disproportionately to the wattmeter indication.

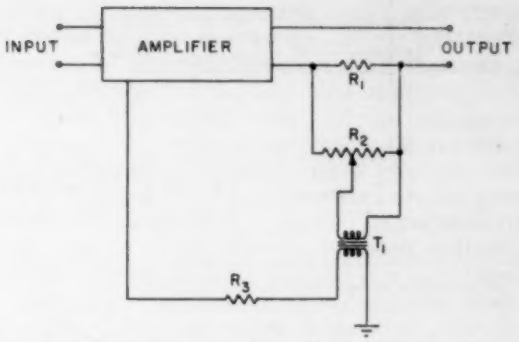

FIGURE 4. *Basic elements of feedback loop used to control output impedance of power source.*

has the effect of varying the apparent source impedance, and therefore this control will hereafter be called the impedance control, abbreviated to "Z control". The transformer, T_1, is needed for isolation, and should be capable of handling a range of frequencies wide enough to include the fundamental and all significant harmonics with a minimum of phase shift or attenuation. In practice, a small amount of phase shift in the fed-back voltage may be corrected by a simple R-C correction network.

The signal input to the amplifier was from a low-distortion oscillator. A frequency of 70 cps was chosen for these tests, in order to eliminate the question of pickup and interference from the power-line frequency.

The test frame was a 25-cm Epstein frame, with primary and secondary of 700 turns each. For this investigation the frame was used without an air-flux-compensating mutual inductor. The values of flux density, B, are therefore slightly too high, but this does not affect the validity of the comparison, because both the wattmeter and bridge methods were used simultaneously.

The bridge-balancing components, R_b and C_b, were high-quality decade boxes, with accurately known values and negligible residual reactances. R_a was a precision resistor of carefully determined value. R_c was a precision resistor of 250-w rating. Lower-powered resistors might be used, provided they would carry current up to 2 amp without changing resistance.

In order to determine the core loss, it is necessary to measure the value of the fundamental-frequency current in the test frame. This can be determined from the fundamental-frequency voltage drop across R_c. The accuracy necessary in this measurement can be readily obtained with the polar potentiometer method [10], which was used for these measurements. The method requires a reference voltage of the same frequency as the unknown, variable in phase and amplitude, with means for accurate determination of the amplitude. Figure 5 depicts the circuit used for this purpose. A signal from the source driving the main amplifier is fed to a phase shifter, capable of shifting the phase by any amount required, with fine control. The phase shifter introduces distortion, which is removed by the filter. The transformer, T_2, is shown to emphasize the need for complete

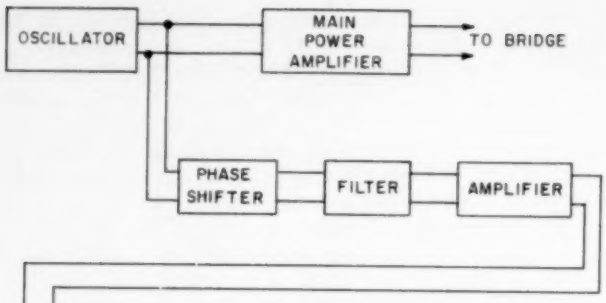

FIGURE 5. *Polar potentiometer used to measure the voltage drop across R_c.*

isolation. A feedback connection to the output side of the output transformer is often found on power amplifiers, and this could render the apparatus unusable unless isolation is employed. Isolation is especially important for measurement of the voltage drop across a resistor, if both ends of the resistor are operating at nonground potentials.

The accuracy of the method is determined largely by the next two elements, the reference voltmeter, V, and precision ratio transformer, PRT. The variable-phase reference voltage is applied to the primary of the PRT, and measured by the reference voltmeter, V. The PRT used has five decade switches, by which the output voltage may be varied in steps as small as 1×10^{-5} times the input voltage. The voltmeter, V, was adjusted to have a zero scale correction at the reference input voltage, and care was taken to maintain the input at this level throughout the measurements. All measured voltages were then determined in terms of a ratio, read from the PRT, times the reference voltage. The accuracy of the measurement of the fundamental-frequency current is estimated to be within ±0.2 percent.

In use, the phase shifter and the PRT are adjusted so that the detector, D, tuned to the fundamental frequency, reads a null. Under these conditions, the output from the PRT matches the fundamental component of the unknown in phase and amplitude.

It is obvious that the apparent loss measured by the bridge is profoundly affected by the setting of the Z control. One of the major problems of this investigation was to devise a means of setting the Z control at the proper point.

It is relatively easy to find the proper setting to compensate for those elements of the circuit whose terminals are accessible. This is evident from a consideration of figure 6, which shows the basic elements of such a circuit as that with which we are concerned. If a tuned detector, such as a wave analyzer, is connected to points 1 and 2, and tuned to the third harmonic of the fundamental frequency,

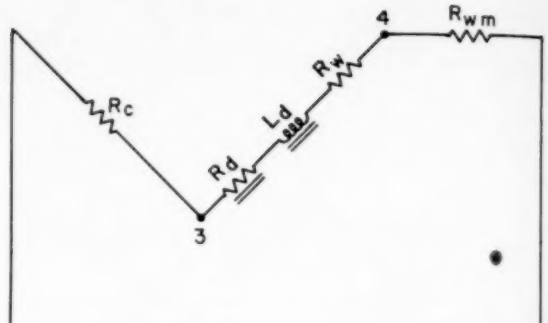

FIGURE 6. *The primary circuit, showing how compensation for part of the circuit resistance may be achieved by varying the negative source resistance, R_s'.*

a setting of the Z control can be found that will yield a minimum deflection of the detector. This is done with the amplifier supplying a current large enough to produce considerable harmonic components. At this setting, the source resistance, R_s, has been compensated by making R_s' equal in magnitude and opposite in sign to R_s. If now the detector is moved to points 2 and 3, and again the Z control is adjusted to produce a minimum deflection, the resistor, R_c, is also compensated, and $R_s'=-(R_s+R_c)$. By connecting to points 3 and 4, we can compensate for R_s, R_c, and R_{wm}. But here this method ends, for the resistance of the primary winding of the test frame, R_w, which remains to be compensated, is not separately available to us; it is associated with L_d and R_d between the terminals of the test frame.

This problem was solved by making a resistor, R_w'', exactly equal in resistance [3] to R_w, and insert-

[3] R_w is the ohmic or d-c resistance of the test frame primary winding. Therefore, R_w'' is a "pure" resistance, i. e., with negligible inductive or capacitive reactance. The d-c and a-c resistance of R_w and R_w'' are equal.

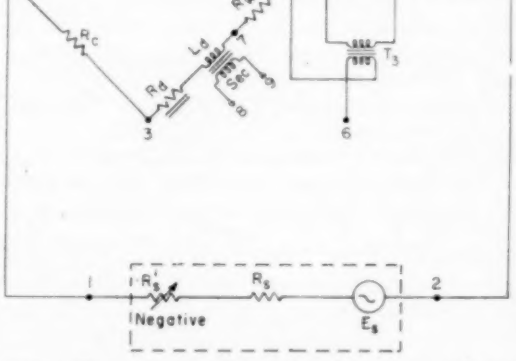

FIGURE 7. *Circuit with R_w'' added, by means of which complete compensation may be achieved.*

ing it in the circuit as shown in figure 7. If the detector were connected to points 3 and 5, and the Z control adjusted for minimum deflection, compensation would be effected for R_s, R_c, R_{wm}, and R_w''. If we could connect the detector to point 3 and the phantom point 7, we could achieve complete compensation for all the ohmic resistance of the circuit.

The transformer, T_3, provides the means for a virtual connection to the phantom point 7. The ratio of this transformer is precisely unity, and its phase shift negligible. The secondary can be connected in such a way that the voltage induced in it opposes the IR drop in R_w. Since the voltage on the primary of T_3 is the IR drop in R_w'', which was made to equal R_w, the induced voltage just equals the IR drop in R_w, and by connecting to 3 and 6, we get the same effect as if we were able to connect to 3 and 7. All that remains is to adjust the Z control for a minimum deflection.

The method of setting the Z control, using the third harmonic produced by the iron, leaves something to be desired. The main power amplifier inevitably produces some harmonic distortion in its own circuit, and this is indistinguishable from that produced by the iron, so that the final setting of the Z control is affected by an unwanted factor. The method yields usable results if the amplifier distortion is kept low enough, but this is a difficult task at the power levels required for testing.

An alternative method of setting the Z control was devised, which avoids the difficulty pointed out above. All that is required is a voltage, to be introduced into the circuit at some point external to the main amplifier without changing the ohmic resistance of the circuit. This can be achieved in practice by applying a voltage to the secondary winding of the test frame, with the specimen in the frame acting as the core of a transformer, and inducing a voltage in the primary winding of the frame. The detector, connected as before, is tuned to the frequency of the injected voltage, and the Z control set by this means.

It was found that the setting of the Z control was slightly dependent upon the amplitude of the injected voltage. Best results were obtained by adjusting this amplitude to yield about the same rms current in the primary circuit with only the injected voltage, operating through the feedback circuit (i. e., no input to the main amplifier input terminals) as the rms current existing under testing conditions. That is, for a test point requiring exciting current of 1 amp rms, the Z control was set with the injected voltage adjusted to give 1 amp rms in the primary circuit. The difference in Z control settings made with various injected voltages was small, however, and could be neglected if errors approaching 3 to 5 percent were allowed.

An obvious advantage of this latter method is that the frequency of the injected voltage may be chosen at will. By choosing several frequencies covering the range of the predominant harmonics of the frequency used for the tests, it was determined that the setting of the Z control was practically the same for all frequencies in this range (50 to 700 cps). If this were not so, it would indicate that the equipment was not suitable for use in this manner, for the predominant harmonics must all be compensated simultaneously in order to get accurate results. In practice, a frequency of 200 to 350 cps was used.

It is necessary to consider the effect on the primary circuit resistance of the transferred impedance of the auxiliary circuit supplying the injected voltage. If this transferred impedance altered the net resistance of the primary circuit, then the Z control would be set wrongly. But no errors arise here, because as the Z control approaches the correct setting, the net resistance of the primary circuit approaches zero, and the resistive component of the transferred impedance paralleling this zero resistance does not alter the total. This was verified experimentally. Various taps of the transformer in the auxiliary injection circuit were tried, and various loads connected across the frame between points 8 and 9 of figure 7. In all cases, the setting of the Z control was unaffected. That this setting also yielded correct core-loss measurements is further proof that no significant error arose from this source.

When the distortion introduced by the main power amplifier was less than about 0.1 percent, the injected-voltage method of setting the Z control agreed with the method using the iron-produced harmonics as described previously. Both methods were used to obtain the data reported herein.

To obtain the power loss in the iron, the value of R_d, which is the apparent increase in the resistance of the frame, is required. Unavoidably, however, the ohmic resistance of the primary winding of the test frame, R_w, is included in the measured arm of the bridge. Two methods are available to separate these two components of resistance. R_w can be determined independently and subtracted from the value obtained from the bridge measurement. Alternatively, the ohmic resistance can be compensated by an auxiliary component in parallel with the balancing arm of the bridge, as devised by Dieterly and Ward [11]. The two methods give identical results, and both were used successfully during the course of this investigation.

The complete circuit is shown in figure 8. Selector switches are shown in proper position for balancing the bridge.

3.3. Specimens

Each specimen weighed approximately 500 g and consisted of strips 3 cm wide and 28 cm or 30.5 cm long. Five grades of nonoriented silicon sheets and one grade of oriented-grain material were used for these tests.

3.4. Measurements

With harmonic power losses fully compensated by means of the feedback circuit, the power loss in the iron is simply

$$P_d = I_1^2 R_d.$$

Thus, there are but two quantities to measure, I_1 and R_d.

FIGURE 8. *Complete circuit for making core-loss measurements with self-compensating bridge method.*

Before these measurements can be made, however, the Z control must be set accurately. Therefore, the procedure described in the next paragraph was followed.

The resistor, R''_w, (see fig. 8) was adjusted [4] to match R_w. R'_w, if used, was set to compensate [5] for R_w. The specimen was then inserted in the frame, and a signal applied to the secondary winding of the frame (Sw 2 in position a, Sw 3 in position b), with no input to the main amplifier. The detector, tuned to the injected-signal frequency, was connected to points 3 and 6 of figure 8 (Sw 1 in position c). The Z control was adjusted to yield a minimum deflection of the detector. The detector was then switched to the main bridge (Sw 1 in position b), and the secondary of the test frame connected to the wattmeter and voltmeters (Sw 2 in position b). A voltage was applied through the main amplifier, and the main bridge balanced by means of R_b and C_b. The polar potentiometer was then used (Sw 3 in position a, Sw 1 in position a) to measure the voltage at fundamental frequency appearing across R_c. The rms voltmeter connected to the secondary of the test frame was read, in order to be able to determine the form factor of the voltage waveform. A reading from the average-indicating voltmeter, used to determine the form factor and flux density, and a reading from the reference wattmeter (with R_a disconnected) completed the measurements.

[4] It was found that the highest current used in this investigation, 2 amp, caused the windings to rise 10° C, causing a change in resistance too large to neglect. Therefore, a chart was prepared to indicate the setting of a fine control on R''_w, corresponding to the temperature of R_w, read from a thermometer held in close contact to R_w. A better method might be to incorporate another winding on the test frame to be used as a resistance thermometer in a very-low-current d-c bridge circuit.

A similar chart was prepared to determine the setting of R'_w as a function of temperature.

[5] Dieterly and Ward [11] showed that if R'_w (fig. 8) is made equal to R_aR_c/R_w, then $R_4=R_aR_c/R_b$. This procedure obviates the necessity of subtracting R_w from each resistance measurement made, for if R'_w is not used, then $R_4=(R_aR_c/R_b)-R_w$.

4. Results

The results of a series of measurements are given in table 1. Each determination of core loss by the compensated-bridge method is accompanied by the reference value from the wattmeter method. The last column gives the difference between the two methods. It will be noted that the greatest difference is 2.5 percent, and that only 6 of the 46 pairs differ by as much as 1.0 percent.

These same results are given in graphic form in figure 9, where it is evident that excellent agreement is obtained.

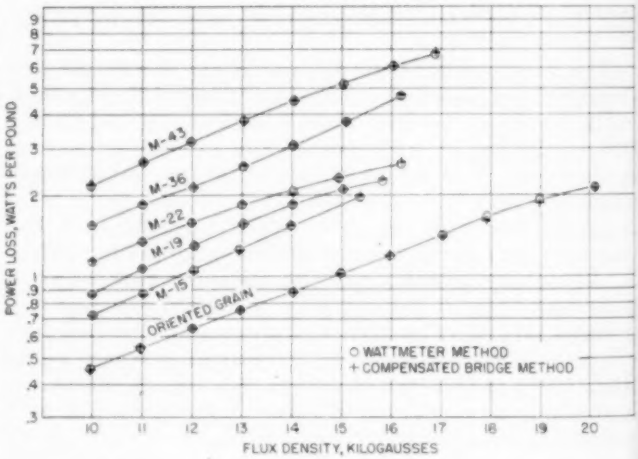

FIGURE 9. *Comparison of power-loss measurements made with compensated bridge and wattmeter, at 70 cps.*

No corrections were made for instrument loss or form factor errors, which are identical for the two methods.

Figure 10 shows the magnitude of the contribution of the compensation method. For comparison, a series of measurements was made with the circuit unchanged, except that no feedback for compensation was used. The uncorrected, or apparent, core loss, $I_1^2 R_d$, is shown as the upper curve, diverging more and more (as flux density is increased) from the true core loss, shown as the lower curve. As pointed out in a previous paper [2], the uncorrected bridge gives results that may be as much as several hundred percent too high.

The power-loss data are not corrected for losses in the measuring instruments (the wattmeter potential coil and the flux voltmeter), or for the errors caused by the departure of the flux waveform from a true sinusoid. These corrections are identical for the two methods, and thus do not affect the validity of the comparison.

TABLE 1. *Comparison of power loss measured by compensated bridge and wattmeter, at 70 cps*

[No corrections were made for instrument loss or form factor errors. These are identical for the two methods, and do not affect the validity of the comparison]

Specimen	Gage	Effective weight	B	Power loss		Δ
				Bridge	Wattmeter	
		lb	*Kilogausses*	*w/lb*	*w/lb*	*%*
Oriented grain	29	0.849	9.98	0.449	0.452	−0.7
			10.98	.540	.538	+.4
			12.00	.642	.641	+.2
			12.99	.749	.749	.0
			14.01	.875	.874	+.1
			15.00	1.018	1.020	−.2
			15.98	1.203	1.197	+.5
			17.02	1.425	1.435	−.7
			17.96	1.643	1.685	−2.5
			18.99	1.888	1.925	−1.9
			20.12	2.128	2.140	−0.6
Nonoriented:						
M-15	29	0.903	10.01	0.714	0.715	−0.1
			11.00	.861	.868	−.8
			12.02	1.042	1.049	−.7
			12.95	1.258	1.271	−1.0
			13.99	1.543	1.539	+0.3
			15.38	1.988	1.973	+.8
M-19	29	0.744	10.00	0.866	0.869	−0.3
			11.00	1.060	1.060	.0
			12.02	1.293	1.294	−.1
			13.00	1.553	1.560	−.4
			14.01	1.835	1.848	−.7
			15.02	2.094	2.096	−.1
			15.83	2.299	2.257	+1.9
M-22	26	0.836	10.00	1.127	1.124	+0.3
			11.00	1.337	1.340	−.2
			12.00	1.578	1.581	−.2
			13.00	1.856	1.849	+.4
			14.03	2.024	2.067	−2.1
			14.95	2.332	2.330	+0.1
			16.21	2.653	2.622	+1.2
M-36	26	0.877	10.00	1.544	1.544	0.0
			11.01	1.854	1.847	+.4
			12.01	2.147	2.148	.0
			13.02	2.572	2.558	+.5
			14.03	3.051	3.055	−.1
			15.10	3.731	3.75	−.5
			16.19	4.720	4.70	+.4
M-43	24	0.895	9.98	2.179	2.171	+0.4
			11.02	2.674	2.658	+.6
			11.99	3.183	3.181	+.1
			13.03	3.774	3.775	.0
			14.04	4.442	4.455	−.3
			15.03	5.194	5.194	.0
			16.04	6.049	6.065	−.3
			16.88	6.747	6.69	+.9

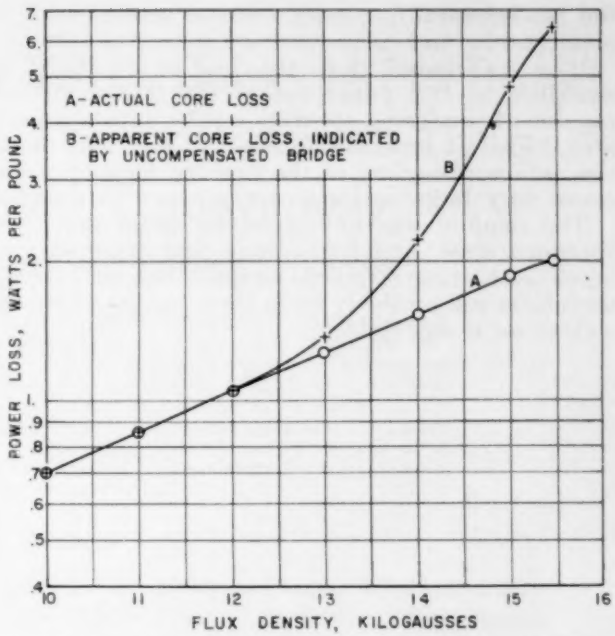

FIGURE 10. *Apparent power loss as measured by uncompensated bridge compared to actual core loss, at 70 cps.*

5. Summary and Conclusions

In order to obtain accurate measurements of core loss by the bridge method, the harmonic power dissipated in the resistive elements of the entire circuit must be taken into account. If each harmonic component must be measured and computed separately, the procedure becomes inconvenient and time consuming. A compensation method, using an electronic power amplifier with "current" feedback, has been devised and found to be sufficiently accurate.

The principal difficulty encountered was the finding of a method of adjusting the feedback to just the correct amount to effect complete compensation, but not under- or overcompensation. This problem was solved, and the method was successfully developed to yield results that differ from those obtained from the wattmeter by not more than 2.5 percent in the worst cases, with most measurements agreeing to 1 percent or better.

It is estimated that the determination of the fundamental-frequency current is accurate to ± 0.2 percent. The variation of the output voltage of the power source was the limiting factor in the precision of balance of the bridge. The nonlinearity of the test frame with ferromagnetic core causes the balance parameters to be strongly dependent on the impressed voltage. At highest flux densities, the precision of balance is estimated to be about 0.5 percent for the equipment used.

The accuracy limitations are seen to be associated with the equipment employed and not inherent in the method. Therefore, further refinement of the power source, including the current feedback circuit for the Z control, and of the method of measuring

the fundamental-frequency current would result in more precise and more accurate measurements.

It is concluded that the use of feedback as described in this paper makes the bridge method capable of producing accurate results with a reasonable degree of convenience, even at high flux densities, where distortion in the exciting current would cause very large errors if not taken into account.

The method was developed by using materials, specimen sizes, and frequencies that were easy to check with the wattmeter method, but its greatest usefulness will probably be in those ranges where the wattmeter is unsuitable.

WASHINGTON, November 29, 1957.

6. References

[1] I. L. Cooter and W. P. Harris, The use of an a-c bridge to measure core loss at high inductions, Trans. Am. Inst. Elec. Engrs. **75,** Part 1, 252 (1956).

[2] I. L. Cooter and W. P. Harris, Investigation of an alternating-current bridge for the measurement of core losses in ferromagnetic materials at high flux densities, J. Research NBS **57,** 103 (1956) RP2699.

[3] H. F. Mayer, Control of the effective internal impedance of amplifiers by means of feedback, Proc. (Inst. Radio Engrs.) **27,** 213 (1939).

[4] H. Bartels, Graphische Berechnung linearer und nichtlinearer Rückkopplungen, Elek. Nach. Tech. **11,** 319 (1934).

[5] T. Sturm, Verfahren zur Klirrverminderung (Linearisierung), Funktechnische Monatshefte, p. 77 (1937).

[6] E. L. Ginzton, Balanced feed-back amplifiers, Proc. (Inst. Radio Engrs.) **26,** 1367 (1938).

[7] E. L. Ginzton, Stabilized negative impedances. Electronics **18.** In three parts: Part 1, p. 140 (1945); Part 2, p. 138 (1945); Part 3, p. 140 (1945).

[8] H. W. Bode, Network analysis and feedback amplifier design (D. Van Nostrand, New York, N. Y., 1945).

[9] J. G. Thomason, Linear feedback analysis (McGraw-Hill Publishing Co., Inc., New York, N. Y., 1955).

[10] F. K. Harris, Electrical measurements (Wiley, New York, N. Y., 1952).

[11] D. C. Dieterly and C. E. Ward, A wide-range a-c bridge test for magnetic materials, Am. Soc. Testing Materials Bul. **182** (1952).

Journal of Research of the National Bureau of Standards Vol. 60, No. 5, May 1958 Research Paper 2866

Stress-Strain Relationships in Yarns Subjected to Rapid Impact Loading: 5. Wave Propagation in Long Textile Yarns Impacted Transversely

Jack C. Smith, Frank L. McCrackin, and Herbert F. Schiefer

The behavior of an infinitely long flexible filament after transverse impact is treated theoretically. The filament is assumed to have a tension-strain curve that is always concave downward, and to have no short-time creep or stress-relaxation effects. Under most conditions the impact initiates a variable strain that propagates down the filament between an "elastic wave" front and a "plastic wave" front. A transverse wave, shaped like an inverted V, then travels in the constant-strain region behind the plastic-wave front. Under special conditions the transverse-wave front may propagate faster than the plastic-wave front, but the shape of the transverse wave remains the same. The theory for both cases is worked out in detail, and some illustrative examples are given.

1. Introduction

The behavior of textile yarns held in clamps 40 to 60 cm apart and impacted transversely was demonstrated and discussed in the fourth paper of this series [1, 2, 3, 4].[1] The present paper deals with the theory of transverse-wave propagation in yarns of infinite length where there are no clamps to reflect the waves. The theory developed here will be used in future discussions of transverse impact.

When a yarn is struck transversely, a strain wave is propagated along the yarn outward in each direction from the point of impact. In the region between each of these wave fronts, material of the yarn is set into motion longitudinally toward the point of impact. This material is taken up by a tent-shaped wave of transverse motion that propagates outward from the impact point. This behavior is demonstrated in figure 1, in which several configurations of a yarn after transverse impact are shown. The position of the longitudinal-strain wave in each of the configurations is shown by the arrows. The backward flow of yarn material is indicated by the white tick marks.

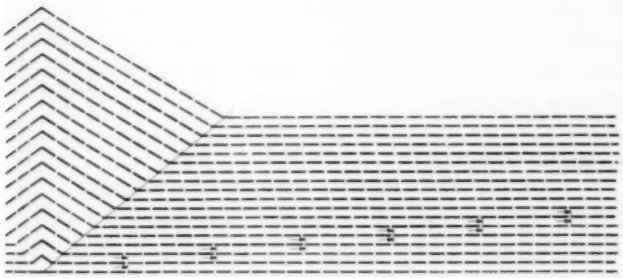

FIGURE 1. *Configurations of a yarn after transverse impact.*

These configurations, 40×10^{-6} sec apart, were calculated for a yarn having a linear (Hooke's law) tension-strain curve. Longitudinal-strain wave velocity was 2,500 m/sec. The positions of the longitudinal-wave front in successive configurations, are designated by the arrows. Impact occurred at the vertex of the transverse wave shown at the left, at impact velocity of 180 m/sec. The leading edge of the transverse wave propagates with velocity 350 m/sec with respect to the unstrained yarn material. Inward flow of yarn material at velocity 50 m/sec is shown by the white tick marks. There is no horizontal component of flow in the region of the transverse wave.

The configurations shown in figure 1 were calculated for a yarn composed of a Hookean material, using relations developed in this paper. The longitudinal strain-wave velocity was 2,500 m/sec. Transverse-impact velocity was 180 m/sec. Under these conditions a 2-percent strain is produced in the wake of the longitudinal-wave front, and yarn material in the region between longitudinal- and transverse-wave fronts flows inward at a velocity of 50 m/sec. In the wake of the transverse-wave front, which propagates at a velocity of 350 m/sec, the yarn material flows transversely at the impact velocity as shown. The time interval between each configuration is 40×10^{-6} sec.

Transverse waves of the type just described have been discussed by Taylor and his associates [5]. Cole, Dougherty, and Huth [6] have treated the problem of transverse-wave propagation in prestressed wires. Craggs [7] and McCrackin [8] have also discussed the problem for

[1] Figures in brackets indicate the literature references at the end of this paper.

plastic-elastic strings, showing the effect of wave reflections and interactions. The problem of oblique impact of an elastic cable has been discussed recently by Ringleb [9]. The treatment presented here extends the work of these authors and makes use of concepts introduced by von Karman [10] and Taylor [11] in their treatments of longitudinal impact.

2. Theory of Longitudinal Impact

Longitudinal-strain waves resulting from a constant-velocity tensile impact do not necessarily have sharp wave fronts. According to von Karman, the strain increases gradually in the region between two wave fronts, an "elastic wave" front [2] propagating at velocity

$$C_e = C(0) = \sqrt{\frac{1}{M}\left(\frac{dT}{d\epsilon}\right)_{\epsilon=0}} \tag{1}$$

and a "plastic wave" front [2] propagating more slowly at velocity

$$C_p = C(\epsilon_p) = \sqrt{\frac{1}{M}\left(\frac{dT}{d\epsilon}\right)_{\epsilon=\epsilon_p}}. \tag{2}$$

In eq (1) and (2), M is the mass per unit length of the unstrained filament material, and $dT/d\epsilon$ is the slope of the tension-strain curve, evaluated at zero strain in eq (1) and at strain ϵ_p in eq (2). In the wake of the plastic-wave front the strain in the filament has the constant value ϵ_p. The value of ϵ_p depends upon the speed at which the filament is impacted longitudinally.

The filament material in the wake of the plastic-wave front flows in the impact direction at a velocity uniform along the filament given by

$$W = \int_0^{\epsilon_p} \sqrt{\frac{1}{M}\left(\frac{dT}{d\epsilon}\right)} d\epsilon = \int_0^{\epsilon_p} C(\epsilon) d\epsilon. \tag{3}$$

For a filament impacted longitudinally at one end, W is the same as the impact velocity.

In deriving the above equations, von Karman assumed a tension-strain curve that was always concave downward. Tension-strain curves for textile yarns often have a concave upward portion which, however, is less pronounced in curves obtained at rapid testing rates. In addition, textile yarns exhibit creep and stress-relaxation phenomena. Such phenomena were not considered by von Karman. Despite this, von Karman's treatment represents a notable advance over theories based on Hookean tension-strain behavior.

3. Theory of Transverse Impact

In the laboratory or observer's coordinate system, let x' and y' denote the horizontal and vertical coordinates, respectively. Let a filament lying along the x' axis be impacted with velocity V in the y' direction at the point where $x'=0$. The motion of the filament is to be described in terms of Lagrangian coordinates. That is, distances along the unstrained length of the filament are given in an x coordinate system, which before impact coincides with the x' coordinates. The displacement of any point x of the filament at any time t relative to its original position is given by $\xi(x,t)$ for horizontal displacements and $\eta(x,t)$ for vertical displacements. The location in the laboratory coordinate system of a point x on the filament is thus given by

$$x' = x + \xi(x,t), \tag{4a}$$

$$y' = \eta(x,t). \tag{4b}$$

[2] The terms "elastic" and "plastic" are used as convenient designations for the wave fronts bounding the region of variable strain. They are not intended to characterize the complex recovery behavior of the material. For example, the theory holds for materials having nonlinear tension-strain curves, but which recover almost completely from large deformations. For these materials, the strain associated with the plastic wave is almost entirely elastic.

Consider an element of the filament of unstrained length Δx. After impact, this element is strained, and its new length, measured in the laboratory coordinate system, becomes $\Delta x\sqrt{[1+(\partial\xi/\partial x)]^2+(\partial\eta/\partial x)^2}$. The increase in length per unit length, or strain ϵ, is thus

$$\epsilon=\sqrt{\left(1+\frac{\partial\xi}{\partial x}\right)^2+\left(\frac{\partial\eta}{\partial x}\right)^2}-1. \tag{5}$$

The angle θ that the element makes with the horizontal is given by

$$\sin\theta=\frac{1}{1+\epsilon}\frac{\partial\eta}{\partial x}, \tag{6a}$$

$$\cos\theta=\frac{1}{1+\epsilon}\left(1+\frac{\partial\xi}{\partial x}\right). \tag{6b}$$

The differential equations that govern the motion of the small element are

$$M\frac{\partial^2\eta}{\partial t^2}=\frac{\partial}{\partial x}(T\sin\theta), \tag{7a}$$

$$M\frac{\partial^2\xi}{\partial t^2}=\frac{\partial}{\partial x}(T\cos\theta), \tag{7b}$$

where M is the mass per unit length of the unstrained filament, and T is the tension. By making use of (6a) and (6b), these equations become

$$\frac{\partial^2\eta}{\partial t^2}=\frac{\partial}{\partial x}\left[\frac{T}{M(1+\epsilon)}\frac{\partial\eta}{\partial x}\right], \tag{8a}$$

$$\frac{\partial^2\xi}{\partial t^2}=\frac{\partial}{\partial x}\left[\frac{T}{M(1+\epsilon)}\left(1+\frac{\partial\xi}{\partial x}\right)\right]. \tag{8b}$$

Assume, as von Karman did, that the tension T is a function $T(\epsilon)$ of the strain only, given by the tension-strain curve. For solutions in which the strain, and consequently the tension, are constant along the filament, eq (8a) and (8b) reduce to

$$\frac{\partial^2\eta}{\partial t^2}=\frac{T}{M(1+\epsilon)}\frac{\partial^2\eta}{\partial x^2}, \tag{9a}$$

$$\frac{\partial^2\xi}{\partial t^2}=\frac{T}{M(1+\epsilon)}\frac{\partial^2\xi}{\partial x^2}, \tag{9b}$$

ξ and η must also satisfy eq (5).

For other solutions in which $\eta=0$ (no transverse wave), eq (8a), (8b), and (5) reduce to

$$\eta=0, \tag{10a}$$

$$\frac{\partial^2\xi}{\partial t^2}=\frac{1}{M}\frac{\partial T}{\partial x}, \tag{10b}$$

$$\epsilon=\frac{\partial\xi}{\partial x}. \tag{10c}$$

This is the case considered by von Karman, and to which his solution, eq (1), (2), and (3), is applicable.

A combination of solutions for the preceding special cases gives the solution to the problem in which a long filament initially at rest along an axis in the x' direction is impacted transversely at $x=0$ with velocity V. The boundary conditions that must be satisfied for the $x>0$ half of the filament are $\xi=0$ and $\eta=Vt$ at $x=0$, and $\xi=\eta=0$ at $x=\infty$.

4. A Simple Solution Usually Applicable

Immediately after impact a train of longitudinal-strain waves propagates outward along the filament. The leading wavelet in the train, or elastic wave, propagates at velocity C_e given by eq (1). At points in advance of the elastic wave the filament is unstrained. The elastic wave is succeeded by a series of other more slowly propagating wavelets, each wavelet adding an increment to the strain in the filament. In the wake of each wavelet, material of the filament flows inward toward the point of impact at a velocity that increases as each wavelet passes. The velocity of each wavelet is proportional to the square root of the slope of the tension-strain curve, hence in order that the wavelets do not overtake each other, the slope of the tension-strain curve must decrease as ϵ increases (be concave downward). The final wavelet in the train, or plastic wave, propagates with velocity C_p given by eq (2). The strain in the wake of the plastic-wave front has the constant value ϵ_p. Filament material in the wake of the plastic-wave front flows inward at the constant velocity W given by eq (3).

For the simple solution discussed here, transverse-wave motion of the filament occurs only in the wake of the plastic-wave front. The transverse wave thus propagates with velocity U, which is less than C_p. For the region in advance of the point Ut on the filament, where only longitudinal-strain waves occur, von Karman's solution [10] is applicable. This solution, satisfying the differential eq (10) and the boundary conditions $\xi=-Wt$ at $x=Ut$ and $\xi=0$ at $x=\infty$, may be written as follows:

For the region $C_e t<x<\infty$,

$$\xi=\eta=\epsilon=0. \tag{11}$$

For the region $C_p t\leq x\leq C_e t$,

$$\eta=0. \tag{12a}$$

To find the amount of motion in the ξ direction, consider a wavelet, which increases the strain in the filament by an increment $d\epsilon$. This wavelet propagates at velocity $C(\epsilon)$ and arrives at point x at time $t=x/C(\epsilon)$. The inward velocity of material flow is increased by an amount $-C(\epsilon)d\epsilon$ during time $t-x/C(\epsilon)$. The distance ξ that point x moves inward is the integrated product of the velocity and time after arrival for each wavelet passing through the point x, or

$$\xi=-\int_0^{\epsilon} C(\alpha)\left[t-\frac{x}{C(\alpha)}\right]d\alpha=-W(\epsilon)t+\epsilon x, \tag{12b}$$

where

$$C(\alpha)=\sqrt{\frac{1}{M}\left(\frac{dT}{d\alpha}\right)}, \tag{12c}$$

$$W(\epsilon)=\int_0^{\epsilon} C(\alpha(d\alpha), \tag{12d}$$

and α is a variable designating strains along the filament in advance of the point where the strain is ϵ.

During the time interval between the arrivals of the elastic and plastic waves at point x, the strain is found as a function of x and t by solving the following equation for ϵ:

$$C(\epsilon)=x/t. \tag{12e}$$

For the region $Ut\leq x\leq C_p t$,

$$\eta=0, \tag{13a}$$

$$\xi=-\int_0^{\epsilon_p} C(\alpha)\left[t-\frac{x}{C(\alpha)}\right]d\alpha=-Wt+\epsilon_p x, \tag{13b}$$

$$\epsilon=\epsilon_p=\text{a constant}. \tag{13c}$$

In order to describe the motion in the transverse-wave region ($0\leq x\leq Ut$) it is necessary to find solutions of eq (9a), (9b), and (5), which satisfy the appropriate boundary conditions. The most general solution of (9a) has the form $\eta=f+g+At+Bx+K$, where f and g are nonlinear functions of the variables $t-x/\sqrt{T/M(1+\epsilon)}$ and $t+x/\sqrt{T/M(1+\epsilon)}$, respectively. Applying the boundary condition that $\eta=Vt$ at $x=0$ gives $Vt=f(0,t)+g(0,t)+At+K$. In order that

this relation be satisfied, it is necessary that $K=0$ and $g(0,t)=-f(0,t)$. Therefore, f and g must be the same function except for sign, and

$$\eta=f(t-x/\sqrt{T/M(1+\epsilon)})-f(t+x/\sqrt{T/M(1+\epsilon)})+Vt+Bx.$$

The condition that $\eta=0$ at $x=Ut$ can only be satisfied if $f\equiv 0$ and $B=-V/U$. Thus $\eta=V(t-x/U)$. For this value of η and for a constant value of ϵ, the most general solution of eq (5) becomes $\xi=x[\sqrt{(1+\epsilon)^2-(V/U^2-1}]+h(t)+K$. The condition $\xi=0$ at $x=0$ requires that $h(t)+K=0$. The solution for ξ just obtained is also a solution of eq (9b); thus: For the region $0\leq x\leq Ut$,

$$\eta=V(t-x/U), \tag{14a}$$

$$\xi=x[\sqrt{(1+\epsilon_2)^2-(V/U)^2}-1], \tag{14b}$$

$$\epsilon=\epsilon_2=\text{a constant}. \tag{14c}$$

The behavior of the negative half of the filament is the same as that just described except for the direction of wave propagation.

The configuration of the positive half of the filament at time t after impact is shown in figure 2 by the line passing through the points A, B, P, Q. Filament material in the transverse-wave region $0\leq x\leq Ut$, moves in the y' direction because $\partial\xi/\partial t=0$ in this region. Thus points A, B, P moving with velocity V, arrive at positions A^*, B^*, P^* at the time $t+dt$. The transverse-wave front moves with velocity U relative to points on the unstrained filament. The horizontal component of the velocity relative to the x', y' coordinate system therefore is $U(1+\epsilon_2)\cos\theta$, and the wave front at point P advances a distance $Udt(1+\epsilon_2)\cos\theta$ to point Q^* in a time dt. Filament material in advance of the transverse-wave front is moving inward with velocity W, so that in time dt point Q moves a distance $-Wdt$ to its new position Q^*.

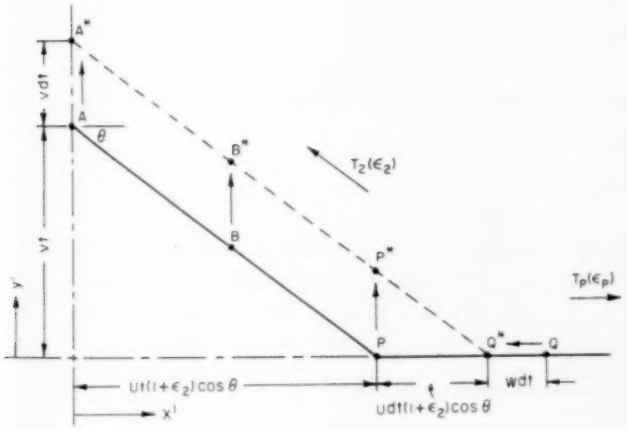

FIGURE 2. *Configuration of positive half of filament t seconds after impact.*

Filament originally lay along the x' axis and was struck with velocity V in the y' direction. After t seconds the positive half of the filament has the configuration $ABPQ$, after $t+dt$ seconds the configuration $A^*B^*P^*Q^*$. The filament is assumed to have strain ϵ_2 and tension T_2 in the transverse-wave region $ABP-A^*B^*Q^*$, and strain ϵ_p and tension T_p in the region in advance of the transverse wave. (It is proved in the text that in most cases $\epsilon_2=\epsilon_p$, $T_2=T_p$.) Filament material in the transverse wave moves vertically with velocity V; material in advance of the transverse wave moves inward horizontally with velocity W. The transverse-wave front moves with velocity U relative to points on the unstrained filament but the horizontal component of its velocity relative to the x', y' coordinate system is $U(1+\epsilon_2)\cos\theta$. The point Q on the filament moves inward to position Q^*, the location of the transverse-wave front at time $t+dt$.

The angle θ that the transverse wave makes with the horizontal is constant along the filament because $\partial\xi/\partial x$ and $\partial\eta/\partial x$ are constant in the region $0\leq x\leq Ut$. The transverse wave is therefore a straight line. θ is given by either of the relations

$$\sin\theta=-\frac{1}{1+\epsilon_2}\frac{V}{U}, \tag{15a}$$

$$\cos\theta=\frac{1}{1+\epsilon_2}\sqrt{1+\epsilon_2)^2-\left(\frac{V}{U}\right)^2} \tag{15b}$$

found by substituting the solutions (14) into the relations (6).

At the point $x=Ut$ where solutions (13) and (14) join, ξ and η must be continuous. Continuity of η is satisfied because $\eta=0$ for both solutions. Continuity of ξ requires that

$$U[\sqrt{(1+\epsilon_2)^2-(V/U)^2}-1]=\epsilon_p U-W. \tag{16}$$

Horizontal and vertical components of the force must also be continuous. Equating the horizontal components gives

$$T_p-MUW=T_2\cos\theta=\frac{T_2}{1+\epsilon_2}\sqrt{(1+\epsilon_2)^2-(V/U)^2}. \tag{17}$$

MU is the element of mass over which the transverse-wave front passes in unit time, so MUW is a force equal to the change of longitudinal momentum per unit time.
Equating the vertical components gives

$$MUV=-T_2\sin\theta=\frac{T_2}{1+\epsilon_2}\frac{V}{U}. \tag{18}$$

The velocity of propagation of the transverse wave U is found from eq (18) to be

$$U=\sqrt{\frac{T_2}{M(1+\epsilon_2)}}. \tag{19}$$

By appropriate manipulation of eq (16), (17), and (18) it is possible to obtain the relation

$$\frac{T_p}{1+\epsilon_p}=\frac{T_2}{1+\epsilon_2}. \tag{20}$$

The meaning of this relationship is illustrated in figure 3, where a typical tension-strain curve is

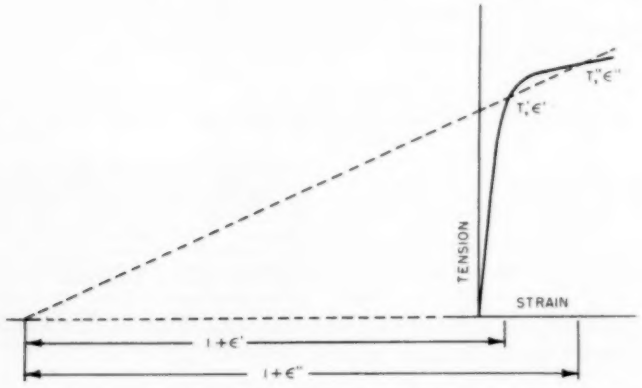

FIGURE 3. *Tension-strain curve whose slope decreases to a value less than $T/(1+\epsilon)$.*

plotted. The long line extending from the point -1 on the strain axis up to and through any point ϵ, T on the tension-strain curve has the slope $T/(1+\epsilon)$. The only values of T and ϵ satisfying eq (20) must be given by intersections of this line with the tension-strain curve. In most cases of practical interest only one intersection exists, and the relation (20) can then be satisfied by

$$\epsilon_p=\epsilon_2, \tag{21a}$$

$$T_p(\epsilon_p)=T_2(\epsilon_2). \tag{21b}$$

Suppose, however, that the tension-strain curve bends over as shown in figure 3 until its slope for large values of ϵ diminishes to or becomes less than $T/(1+\epsilon)$. A second intersection

is possible and two sets of ϵ, T values would be obtained satisfying (20). If a material having such a tension-strain curve were impacted transversely at low speeds, small values of ϵ and T in the wake of the plastic-wave front would be obtained. The slope of the tension-strain curve for these low values of ϵ is greater than $T/(1+\epsilon)$, so the plastic-wave front would travel faster than $\sqrt{T_p/M(1+\epsilon_p)}$, the velocity U of the transverse-wave front. At a higher impact velocity a strain ϵ_1 is obtained at which the slope of the tension-strain curve is just equal to $T_1/(1+\epsilon_1)$. In this special case the plastic-wave front and the transverse-wave front are at the same position and move together at the same velocity. If the material is impacted at a higher velocity than this, the solution just given no longer applies. Thus a criterion for the applicability of the simple solution is

$$\frac{dT}{d\epsilon} \geq \frac{T}{1+\epsilon}. \tag{22}$$

That is, the solution applies if the slope of the tension-strain curve for the material is not less than $T/(1+\epsilon)$ for all strains less than the maximum strain ϵ_p, obtained as a result of the impact. Within this restriction the relations (21) can be used to obtain the results given in the following section. A more general solution, which includes the simple solution as a special case, is given later in the text.

5. Recapitulation of the Simple Solution

If the tension-strain curve for the filament material obtained at rapid strain rates is always concave downward, if the material does not exhibit large stress relaxation or creep effects during a small time interval, and if the conditions of the impact are such that relation (22) applies, the behavior of a flexible filament after transverse impact is described as follows:

Immediately after transverse impact, longitudinal-strain wavelets propagate outward along the filament. The outermost wavelet, called the elastic wave by von Karman, propagates at velocity

$$C_e = \sqrt{\frac{1}{M}\left(\frac{dT}{d\epsilon}\right)_{\epsilon=0}}. \tag{1}$$

The innermost, called the plastic wave by von Karman, propagates at velocity

$$C_p = \sqrt{\frac{1}{M}\left(\frac{dT}{d\epsilon}\right)_{\epsilon=\epsilon_p}}. \tag{2}$$

In the region between the elastic- and the plastic-wave fronts the strain increases to ϵ_p, the maximum value obtained as a result of the impact. The strain remains constant at this value in the wake of the plastic-wave front.

As the strain wavelets pass a given point on the filament, material of the filament flows inward toward the impact point at a velocity that increases to the value

$$W = \int_0^{\epsilon_p} \sqrt{\frac{1}{M}\frac{dT}{d\alpha}}\, d\alpha, \tag{3}$$

the flow velocity for material in the wake of the plastic-wave front.

The material in the wake of the plastic-wave front forms itself into a transverse wave, shaped like a tent with the impact point at the vertex. The base of the tent spreads outward with velocity

$$U = \sqrt{\frac{T_p}{M(1+\epsilon_p)}}. \tag{23}$$

It should be noted that the velocity U is with respect to a Lagrangian coordinate system; i. e., a system fixed to the filament, moving and extending with it. Inasmuch as filament mate-

rail in the wake of the plastic-wave front is in a strained state and moving, the velocity of the transverse-wave front along the filament as seen by an observer in the laboratory would be $(1+\epsilon_p)U-W$. Similarly, the plastic-wave-front velocity in laboratory coordinates would be $(1+\epsilon_p)C_p-W$. The elastic-wave front propagates in an unstrained motionless medium and so would have the same velocity in both coordinate systems.

Material in the transverse-wave tent does not move in the horizontal direction but only in the direction of the transverse impact. The velocity V of this motion can be expressed in terms of ϵ_p, U, and W by rearranging (16) to obtain

$$V=\sqrt{(1+\epsilon_p)^2U^2-[(1+\epsilon_p)U-W]^2}. \tag{24}$$

If the tension-strain curve for the material is known, it is possible to calculate tables of values for U, V, and W as functions of ϵ_p. Then, for instance, if the impact velocity is known, it is possible to find the resulting strain ϵ_p and thus find the corresponding values of U and W.

6. General Solution

When the impact velocity is very great, the transverse-wave front in some cases propagates more rapidly than the plastic-wave front. A solution is then required which provides for a variable strain in the transverse-wave region.

Consider a tension-strain curve that is always concave downward and whose slope eventually becomes less than $T_1/(1+\epsilon_1)$, where ϵ_1, T_1 is the point on the curve such that $dT/d\epsilon=T/(1+\epsilon)$. Such a curve is shown in figure 4. In the region where $\epsilon_1<\epsilon<\epsilon_p$, let this curve be approximated by a number of straight-line segments drawn between the points ϵ_1,T_1; ϵ_2,T_2; . . . ϵ_p,T_p. Point ϵ_p,T_p represents the maximum strain and tension which are attained in the material as the result of an impact.

For this approximate tension-strain curve, consider a solution such as that depicted in figure 5, in which the transverse wave is composed of a number of straight-line segments. The wave front of the leading segment travels at speed U_1 and the strain in the segment is ϵ_1. Wave fronts of succeeding segments travel at decreasing velocities U_2, U_3, . . . U_p, and the successively increasing strains in these segments are ϵ_2, ϵ_3, . . . ϵ_p. In the region in advance of the transverse wave von Karman's solution applies. Thus:

For the region $C_e t<x<\infty$,

$$\eta=\xi=\epsilon=0. \tag{25}$$

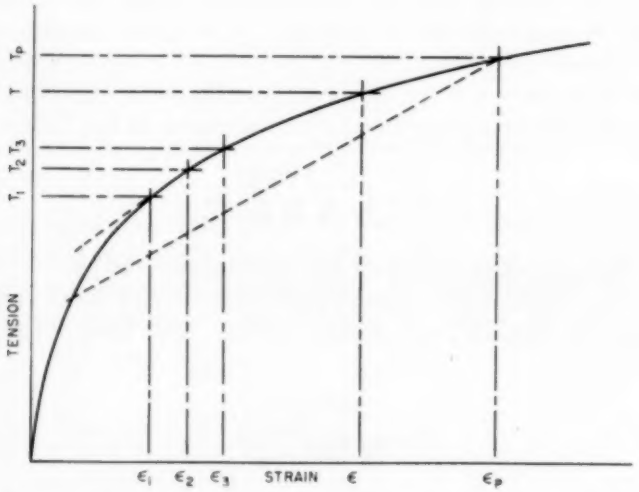

FIGURE 4. *Tension-strain curve assumed in derivation of the general solution.*

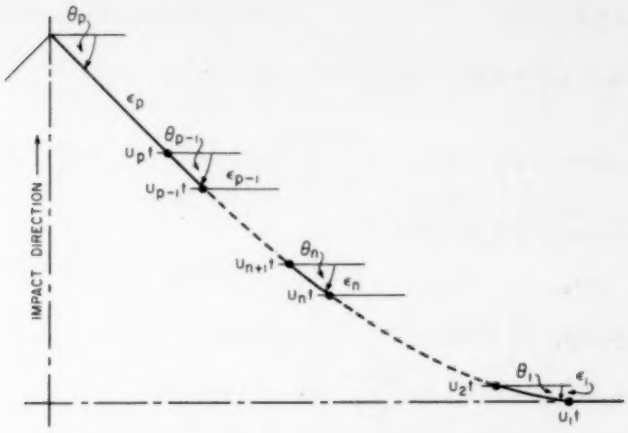

FIGURE 5. *Shape of transverse wave assumed in derivation of the general solution.*

For the region $U_1 t \leq x \leq C_e t$,

$$\eta_0 = 0, \tag{26a}$$

$$\xi_0 = -W(\epsilon)t + \epsilon x. \tag{26b}$$

In the region of the transverse wave the vertical displacement η_n in the nth segment will have a general solution of the form $\eta_n = f_n(t - x/\sqrt{T/M(1+\epsilon_n)}) + g_n(t + x/\sqrt{T/M(1+\epsilon_n)}) + v_n(t - x/U_n) + A_n t + K_n$. The boundary conditions to be satisfied are $\eta_p = Vt$ at $x=0$, $\eta_n = \eta_{n-1}$ at $x = U_n t$ and $\eta_1 = 0$ at $x = U_1 t$. These boundary conditions require that the $K_n = 0$ and that $f_n \equiv g_n \equiv 0$, and provide relations for evaluating the constants v_n and A_n. η_n thus can be expressed in the form $\eta_n = v_n(t - x/U_n) + A_n t$, which when substituted into (5), gives as a general solution for ξ_n, $\xi_n = x[\sqrt{(1+\epsilon_n)^2 - (v_n/U_n)^2} - 1] + h_n(t) + K_n$. ξ_n is a solution of (9b) only when $h(t)$ is a linear function of t. Thus ξ_n can conveniently be expressed as $\xi_n = -w_n(t - x/U_n) + B_n t + K_n$, where $w_n/U_n = \sqrt{(1+\epsilon_n)^2 - (v_n/U_n)^2} - 1$. The boundary conditions to be satisfied are $\xi_p = 0$ at $x=0$, $\xi_n = \xi_{n-1}$ at $x = U_n t$, and $\xi_1 = -W_1 t + \epsilon_1 U_1 t$ at $x = U_1 t$. These conditions require that the $K_n = 0$, and provide relations for evaluating the constants w_n and B_n.

The solution for the transverse-wave region thus can be written;
For the interval $U_2 t \leq x \leq U_1 t$,

$$\eta_1 = v_1(t - x/U_1), \tag{27a}$$

$$\xi_1 = -w_n(t - x/U_1) - W_1 t + \epsilon_1 U_1 t, \tag{27b}$$

$$w_1/U_1 = \sqrt{(1+\epsilon_1)^2 - (v_1/U_1)^2} - 1, \tag{27c}$$

$$\epsilon = \epsilon_1 \tag{27d}$$

$$U_1 = \sqrt{\frac{1}{M}\frac{T_1}{1+\epsilon_1}} = \sqrt{\frac{1}{M}\left(\frac{dT}{d\epsilon}\right)_{\epsilon=\epsilon_1}} \tag{27e}$$

$$W_1 = \int_0^{\epsilon_1} \sqrt{\frac{1}{M}\frac{dT}{d\alpha}}\, d\alpha. \tag{27f}$$

For the interval $U_3 t \leq x \leq U_2 t$,

$$\eta_2 = v_2(t - x/U_2) - t\,[v_1(1 - U_2/U_1)], \tag{28a}$$

$$\xi_2 = -w_2\,(t - x/U_2) - t\,[w_1\,(1 - U_2/U_1) + W_1 - \epsilon_1 U_1], \tag{28b}$$

$$w_2/U_2 = \sqrt{(1+\epsilon_2)^2 - (v_2/U_2)^2} - 1, \tag{28c}$$

$$\epsilon = \epsilon_2. \tag{28d}$$

For any interval $U_{n+1}t \leq x \leq U_n t$,

$$\eta_n = v_n(t - x/U_n) + t \sum_{k=1}^{k=n-1} v_k(1 - U_{k+1}/U_k), \tag{29a}$$

$$\xi_n = -w_n(t - x/U_n) - t\left[\sum_{k=1}^{k=n-1} w_k(1 - U_{k+1}/U_k) + W_1 - \epsilon_1 U_1\right], \tag{29b}$$

$$w_n/U_n = \sqrt{(1+\epsilon_n)^2 - (v_n/U_n)^2} - 1, \tag{29c}$$

$$\epsilon = \epsilon_n. \tag{29d}$$

For the interval $0 \leq x \leq U_p t$,

$$\eta_p = v_p(t - x/U_p) + t \sum_{k=1}^{k=p-1} v_k(1 - U_{k+1}/U_k), \tag{30a}$$

$$\xi_p = -w_p(t - x/U_p) - t\left[\sum_{k=1}^{k=p-1} w_k(1 - U_{k+1}/U_k) + W_1 - \epsilon_1 U_1\right], \tag{30b}$$

$$w_p/U_p = \sqrt{(1+\epsilon_p)^2 - (v_p/U_p)^2} - 1, \tag{30c}$$

$$\epsilon = \epsilon_p. \tag{30d}$$

A point some distance down the filament thus is motionless until the elastic-wave front reaches it. Subsequently the strain at that point increases, and the point moves inward horizontally at increasing velocity until the tip of the transverse wave reaches it. The strain is then ϵ_1 and the inward velocity W_1. As the first segment of the transverse wave passes through the point the trajectory of the point turns upward in a direction inclined to the vertical. As subsequent elements of higher strain pass through the point the trajectory becomes less inclined, until at strain ϵ_p the direction of travel is vertical, parallel to the impact direction.

The motion of filament material remains vertical in the region $0 \leq x \leq U_p t$. There is no horizontal motion of material in this region because of the boundary-condition requirement at $x=0$ that $\xi_p = 0$. In the region of the strained segments $\epsilon_1 \leq \epsilon \leq \epsilon_p$, some flow of material takes place along the horizontal direction. It is this flow that causes the trajectory of a filament point to be inclined from the vertical. The vertical and horizontal components of velocity of a filament point in this region are given by the coefficients of t in eq (29a) and (29b).

Although for generality each of the strained segments ϵ_n shown in figure 5 has been assumed to have a different angle θ_n of inclination to the horizontal, it will be proved that the angles θ_n are all equal and that the configuration of the transverse wave is a straight line.

The displacements ξ_n, η_n, and the horizontal and vertical components of the tension are required to be continuous at each of the points $x = U_1 t, \ldots U_n t, \ldots U_p t$. At the point $x = U_1 t$, ξ_1 and η_1 are continuous by definition, and continuity of the horizontal and vertical tension components leads to eq (27d) and (27e). At $x = U_n t$ and at $x = U_p t$, ξ_n and η_n are continuous by definition. Equating horizontal tension components gives

$$\frac{T_n}{1+\epsilon_n}\sqrt{(1+\epsilon_n)^2 - \left(\frac{v_n}{U_n}\right)^2} - MU_n\left[w_n + \sum_{k=1}^{k=n-1} w_k\left(1 - \frac{U_{k+1}}{U_k}\right) + w_1 - \epsilon_1 U_1\right]$$

$$= \frac{T_{n-1}}{1+\epsilon_{n-1}}\sqrt{(1+\epsilon_{n-1})^2 - \left(\frac{v_{n-1}}{U_{n-1}}\right)^2} - MU_n\left[w_{n-1} + \sum_{k=1}^{k=n-2} w_k\left(1 - \frac{U_{k+1}}{U_k}\right) + w_1 - \epsilon_1 U_1\right],$$

or with the help of eq (29c)

$$\left[\frac{T_n}{1+\epsilon_n} - MU_n^2\right]\sqrt{(1+\epsilon_n)^2 - \left(\frac{v_n}{U_n}\right)^2} = \left[\frac{T_{n-1}}{1+\epsilon_{n-1}} - MU_n^2\right]\sqrt{(1+\epsilon_{n-1})^2 - \left(\frac{v_{n-1}}{U_{n-1}}\right)^2}. \tag{31}$$

Equating vertical tension components gives

$$\frac{T_n}{1+\epsilon_n}\frac{v_n}{U_n}-MU_n\left[v_n+\sum_{k=1}^{k=n-1}v_k\left(1-\frac{U_{k+1}}{U_k}\right)\right]=\frac{T_{n-1}}{1+\epsilon_{n-1}}\frac{v_{n-1}}{U_{n-1}}-MU_n\left[v_{n-1}+\sum_{k=1}^{k=n-1}v_k\left(1-\frac{U_{k-1}}{U_k}\right)\right]$$

or

$$\left[\frac{T_n}{1+\epsilon_n}-MU_n^2\right]\frac{v_n}{U_n}=\left[\frac{T_{n-1}}{1+\epsilon_{n-1}}-MU_n^2\right]\frac{v_{n-1}}{U_{n-1}}. \tag{32}$$

Manipulation of eq (31) and (32) gives the relation

$$\left[\frac{T_n}{1+\epsilon_n}-MU_n^2\right](1+\epsilon_n)=\left[\frac{T_{n-1}}{1+\epsilon_{n-1}}-MU_n^2\right](1+\epsilon_{n-1}), \tag{33}$$

which reduces to

$$U_n=\sqrt{\frac{1}{M}\frac{(T_n-T_{n-1})}{(\epsilon_n-\epsilon_{n-1})}}. \tag{34}$$

Equation (34) also holds when $n=p$. Dividing (32) by (33) gives a simple relationhip

$$\frac{v_n}{(1+\epsilon_n)U_n}=\frac{v_{n-1}}{(1+\epsilon_{n-1})U_{n-1}}. \tag{35}$$

This relationship also holds when $n=p$. Using (6a), eq (35) becomes

$$\frac{v_n}{(1+\epsilon_n)U_n}=\frac{v_p}{(1+\epsilon_p)U_p}=-\sin\theta_p. \tag{36}$$

Applying (36) to (30c), (29b), and (29c), and using (6b), gives the relation

$$\frac{1}{1+\epsilon_n}\left(1+\frac{w_n}{U_n}\right)=\frac{1}{1+\epsilon_p}\left(1+\frac{w_p}{U_p}\right)=\frac{1}{1+\epsilon_p}\sqrt{(1+\epsilon_p)^2-\left(\frac{v_p}{U_p}\right)^2}=\cos\theta_n. \tag{37}$$

At $x=0$ the boundary conditions $\eta_p=Vt$ and $\xi_p=0$ must be satisfied. The first of these conditions gives

$$V=v_p+\sum_{k=1}^{k=p-1}\frac{v_k}{U_k}(U_k-U_{k-1})=v_p+\frac{v_p}{(1+\epsilon_p)U_p}\sum_{k=1}^{k=p-1}(1+\epsilon_k)(U_k-U_{k+1})$$

$$=\frac{v_p}{(1+\epsilon_p)U_p}\left[\sum_{k=1}^{k=p-1}U_{k+1}(\epsilon_{k+1}-\epsilon_k)+(1+\epsilon_1)U_1.\right]. \tag{38}$$

By the use of (38), eq (36) can be expressed as

$$\frac{v_n}{(1+\epsilon_n)U_n}=\frac{V}{\Sigma+(1+\epsilon_1)U_1}=-\sin\theta_n, \tag{39}$$

where Σ is an abbreviation for

$$\Sigma=\sum_{k=1}^{k=p-1}U_{k+1}(\epsilon_{k+1}-\epsilon_k), \tag{40}$$

Similarly, eq (37) becomes

$$\frac{1}{1+\epsilon_n}\left(1+\frac{w_n}{U_n}\right)=\sqrt{1-\left[\frac{V}{\Sigma+(1+\epsilon_1)U_1}\right]^2}=\cos\theta_n. \tag{41}$$

Equation (39) is equivalent to a statement that each $\sin\theta_n$ has the same value given by

$$\sin\theta_n=-\frac{V}{\Sigma+(1+\epsilon_1)U_1}=\sin\theta. \tag{42}$$

Similarly, eq (41) states that each $\cos\theta_n$ has the same value given by

$$\cos\theta_n=\sqrt{1-\left[\frac{V}{\Sigma+(1+\epsilon_1)U_1}\right]^2}=\cos\theta. \tag{43}$$

The configuration of the transverse wave, therefore, is a straight line.

The boundary condition $\xi_p=0$ requires that

$$w_p+\sum_{k=1}^{k=p-1} w_k\left(1-\frac{U_{k+1}}{U_k}\right)+W_1-\epsilon_1U_1=0. \tag{44}$$

It can be shown that

$$\begin{aligned} w_p+\sum_{k=1}^{k=p-1} w_k\left(1-\frac{U_{k+1}}{U_k}\right)&=\frac{1}{1+\epsilon_p}\left(1+\frac{W_p}{U_p}\right)\left[\sum_{k=1}^{k=p-1} U_{k+1}(\epsilon_{k+1}-\epsilon_k)+(1+\epsilon_1)U_1\right]-U_1\\ &=[\Sigma+(1+\epsilon_1)U_1]\cos\theta-U_1\\ &=\sqrt{[\Sigma+(1+\epsilon_1)U_1]^2-V^2}-U_1, \end{aligned} \tag{45}$$

so that eq (44) can be put into the form

$$V=\sqrt{[\Sigma+(1+\epsilon_1)U_1]^2-[(1+\epsilon_1)U_1-W_1]^2}. \tag{46}$$

Equations (46) and (42) can be combined to obtain two different expressions for $\sin\theta$ and $\cos\theta$

$$\sin\theta=-\sqrt{1-\left[\frac{(1+\epsilon_1)U_1-W_1}{\Sigma+(1+\epsilon_1)U_1}\right]^2}, \tag{47}$$

$$\cos\theta=\frac{(1+\epsilon_1)U_1-W_1}{\Sigma+(1+\epsilon_1)U_1}. \tag{48}$$

Equations (31) through (48) can now be used to modify the solutions given earlier. Thus (30a) and (30b) become

$$\begin{aligned} \eta_p&=\left\{v_p+\sum_{k=1}^{k=p-1} v_k\left(1-\frac{U_{k+1}}{U_k}\right)\right\}t-\frac{v_p}{U_p}x\\ &=V\left\{t-\frac{(1+\epsilon_p)x}{\Sigma+(1+\epsilon_1)U_1}\right\}. \end{aligned} \tag{49a}$$

$$\begin{aligned} \xi_p&=-\left\{w_p+\sum_{k=1}^{k=p-1} w_k\left(1-\frac{U_{k+1}}{U_k}\right)+W_1-\epsilon_1U_1\right\}t+\frac{w_p}{U_p}x\\ &=\{(1+\epsilon_p)\cos\theta-1\}x=-\left\{1-(1+\epsilon_p)\left[\frac{(1+\epsilon_1)U_1-W_1}{\Sigma+(1+\epsilon_1)U_1}\right]\right\}x. \end{aligned} \tag{49b}$$

and (29a) and (29b) become

$$\begin{aligned} \eta_n&=t\left\{v_n+\sum_{k=1}^{k=n-1} v_k\left(1-\frac{U_{k+1}}{U_k}\right)\right\}-\frac{v_n}{U_n}x\\ &=t\left\{\frac{v_n}{(1+\epsilon_n)U_n}\left[\sum_{k=1}^{k=n-1} U_k(\epsilon_{k+1}-\epsilon_k)+(1+\epsilon_1)U_1\right]\right\}-\frac{(1+\epsilon_n)V}{\Sigma+(1+\epsilon_1)U_1}x\\ &=V\left\{\left[\frac{\sum_{k=1}^{k=n-1} U_k(\epsilon_{k+1}-\epsilon_k)+(1+\epsilon_1)U_1}{\Sigma+(1+\epsilon_1)U_1}\right]t-\left[\frac{1+\epsilon_n}{\Sigma+(1+\epsilon_1)U_1}\right]x\right\}. \end{aligned} \tag{50a}$$

$$\xi_n=-\left\{w_n+\sum_{k=1}^{k=n-1}w_k\left(1-\frac{U_{k+1}}{U_k}\right)+W_1-\epsilon_1U_1\right\}t+\frac{w_n}{U_n}x$$

$$=-\left\{\left[\sum_{k=1}^{k=n-1}U_{k+1}(\epsilon_{k+1}-\epsilon_k)+(1+\epsilon_1)U_1\right]\cos\theta-[(1+\epsilon_1)U_1-W_1]\right\}t-\{1-(1+\epsilon_n)\cos\theta\}x$$

$$=+\left[(1+\epsilon_1)U_1-W_1\right]\left\{1-\frac{\sum_{k=1}^{k=n-1}U_{k+1}(\epsilon_{k+1}-\epsilon_k)+(1+\epsilon_1)U_1}{\Sigma+(1+\epsilon_1)U_1}\right\}t$$

$$-\left\{1-(1+\epsilon_n)\left[\frac{(1+\epsilon_1)U_1-W_1}{\Sigma+(1+\epsilon_1)U_1}\right]\right\}x \qquad (50b)$$

The equations just given are for the case in which the tension-strain curve is approximated in the region $\epsilon_1\leq\epsilon\leq\epsilon_p$ by a finite number of straight-line segments. The solution sought is the limit solution when the number of straight-line segments approaches infinity and the length of each segment approaches zero. This limit solution is given in the following section.

7. Tabulation and Interpretation of the General Solution

For the interval $0\leq x\leq U_pt$,

$$\eta=V\left\{t-\frac{(1+\epsilon_p)x}{S+(1+\epsilon_1)U_1}\right\}, \qquad (51a)$$

$$\xi=-\left\{1-(1+\epsilon_p)\left[\frac{(1+\epsilon_1)U_1-W_1}{S+(1+\epsilon_1)U_1}\right]\right\}x \qquad (51b)$$

$$\epsilon=\epsilon_p. \qquad (51c)$$

For the interval $U_pt\leq x\leq U_1t$,

$$\eta=V\left\{\left[\frac{S(\epsilon)+(1+\epsilon_1)U_1}{S+(1+\epsilon_1)U_1}\right]t-\left[\frac{1+\epsilon}{S+(1+\epsilon_1)U_1}\right]x\right\}, \qquad (52a)$$

$$\xi=[(1+\epsilon_1)U_1-W_1]\left\{1-\frac{S(\epsilon)+(1+\epsilon_1)U_1}{S+(1+\epsilon_1)U_1}\right\}t-\left\{1-(1+\epsilon)\left[\frac{(1+\epsilon_1)U_1-W_1}{S+(1+\epsilon_1)U_1}\right]\right\}x. \qquad (52b)$$

For the region $U_1t\leq x<\infty$ the solution is given by eq (25) and (26). The symbols used in the above equations have been defined previously, except for

$$S=\int_{\epsilon_1}^{\epsilon_p}\sqrt{\frac{1}{M}\frac{dT}{d\alpha}}d\alpha=W-W_1 \qquad (53)$$

and

$$S(\epsilon)=\int_{\epsilon_1}^{\epsilon}\sqrt{\frac{1}{M}\frac{dT}{d\alpha}}d\alpha=W(\epsilon)-W_1. \qquad (54)$$

The general solution given in this section differs from the simple solution given previously in that the strain in the transverse wave need not be constant. At low impact speeds the equations of the general solution reduce to those of the simple solution. The transverse wave then propagates in a region of constant strain in the wake of the plastic-wave front. However, for a sufficiently high impact velocity and a tension-strain curve of the right shape, the case in which the transverse-wave front and the plastic-wave front coincide occurs. The velocity of propagation of these two wave fronts is U_1 and the maximum strain in the filament is ϵ_1. If the tension-strain curve is known, the values of U_1 and ϵ_1 for this special case can be found from eq (27e).

At higher transverse impact-velocities the plastic-wave front propagates more slowly than the transverse-wave front. A region of variable straining therefore occurs in the transverse wave, and the general solution must be used. The shape of the transverse wave remains a straight line, but the propagation velocity no longer increases with increasing impact velocity. It remains constant at the value U_1. The velocity of propagation of the maximum strained portion of the transverse wave U_p is the same as the plastic-wave velocity C_p and is computed from eq (2). In order to find the value of the maximum strain, or constant strain ϵ_p in the wake of the plastic-wave front, the relation

$$V=\sqrt{[S+(1+\epsilon_1)U_1]^2-[(1+\epsilon_1)U_1-W_1]^2} \tag{55}$$

can be used. The value of S depends upon ϵ_p, so that if the tension-strain curve is known, the value of ϵ_p needed to give a required V can be found by a process of trial and error.

At the transverse-wave front, material of the filament is flowing inward horizontally with velocity W_1. At the point in the transverse wave where the strain attains its maximum value ϵ_p, material is flowing inward along the filament direction with velocity W. The quantity S represents the increase in velocity over W_1 due to the strain increase in the transverse-wave region.

The motion of filament points in the wake of the plastic-wave front is most easily visualized as follows; Suppose there is a second filament, inextensible and fixed to the impacted filament at a point a great distance in advance of the elastic-wave front. Let the end of this filament coincide with the impact point. After impact let the filament be constrained to move alongside the impacted filament but without extending so that its end no longer coincides with the impact point, but recedes from it. To an observer at this filament end the impacted filament would appear to have motion with velocity W.

Although flow of filament material in the wake of the plastic wave occurs, there is no horizontal component of the flow velocity. A horizontal component of the flow does occur in the region where the strain varies: i. e., where $\epsilon_1 \leq \epsilon \leq \epsilon_p$. The magnitude of this velocity component is much smaller than W_1, the horizontal flow velocity in advance of the transverse wave, and decreases to zero where ϵ equals ϵ_p.

At low impact speeds, where the simple theory applies, the angle that the transverse wave makes with the horizontal can be found from the equation

$$\cos\theta=\frac{(1+\epsilon_p)U-W}{(1+\epsilon_p)U}. \tag{56}$$

As the impact velocity is increased, $\cos\theta$ decreases to the value

$$\cos\theta_1=\frac{(1+\epsilon_1)U_1-W_1}{(1+\epsilon_1)U_1}.$$

(θ is a negative angle and attains a greater negative value as the impact velocity is increased.) At higher impact speeds, where only the general theory applies, θ can be found from the relation

$$\cos\theta=\frac{(1+\epsilon_1)U_1-W_1}{S+(1+\epsilon_1)U_1}. \tag{57}$$

The values of ϵ_1, U_1, and W_1 are constants, but S increases as the impact velocity is increased. Cos θ continues to decrease, and the value of θ becomes greater negatively. Thus, although the progagation velocity of the transverse wave is constant for all impact speeds above a certain value, the slope of the transverse wave continues to change.

Figure 6, a, shows the configuration of the filament after a transverse impact of sufficiently slow speed that the simple theory applies. Figure 6, b, shows the configuration after a higher speed impact where only the general theory applies. As pointed out previously, the formula for U expresses the transverse wave velocity relative to a Lagrangian coordinate system.

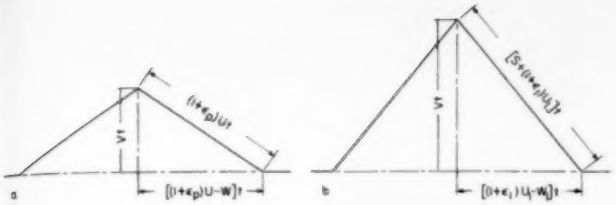

FIGURE 6. *Configuration of filament t seconds after transverse impact.*

a. Simple theory; b. General theory.

In laboratory coordinates the distance that the transverse wave travels along the filament in unit time is $(1+\epsilon_p)U$ for the simple theory, and $S+(1+\epsilon_1)U_1$ for the general theory. The corresponding distances that the wave front travels in the horizontal direction are $(1+\epsilon_p)U-W$ and $(1+\epsilon_1)U_1-W_1$, respectively. These distances are labeled in figure 6, a and b. Thus it is seen how some of the relationships derived above could have been obtained very simply from a knowledge of geometry and an intuitive understanding of the problem.

8. Examples of the Theory

In order to illustrate the theory, the behavior of a filament after transverse impact is computed for two different hypothetical materials. The first material obeys Hooke's law. Its tension-strain curve is given by

$$\frac{T}{M}=C^2\epsilon. \tag{58}$$

As this tension-strain curve is a straight line of constant slope, the simple theory applies. The elastic- and plastic-wave fronts both propagate with velocity C. U, V, and W are given by

$$U=C\sqrt{\frac{\epsilon_p}{1+\epsilon_p}}, \tag{59}$$

$$V=C\sqrt{\epsilon_p(1+\epsilon_p)-\left[\sqrt{\epsilon_p(1+\epsilon_p)}-\epsilon_p\right]^2}, \tag{60}$$

$$W=C\epsilon_p. \tag{61}$$

Curves of U/C, V/C, and W/C as functions of ϵ_p for the Hookean material are plotted in figure 7. The solution of a transverse-impact problem may be found from these curves by reading off the values or ϵ_p, U/C, and W/C corresponding to a particular V/C. The value of C is determined from the Young's modulus and density of the unstrained material.

In order to illustrate a case in which the general theory applies, computations were made for a material whose tension-strain curve is given by [3]

$$\frac{T}{M}=14\tanh 20\epsilon. \tag{62}$$

For this curve, plotted in figure 8, the units of T/M are arbitrary, and the strain ϵ is expressed as a fraction of unity. The slope of the curve, initially 280 arbitrary units per unit strain, continually decreases and approaches a value of zero for very large strains. The slope $d(T/M)/d\epsilon$ and the quantity $T/M(1+\epsilon)$ become equal to 12.308 at a strain of 0.11221. When ϵ is 0.20, the highest strain for which computations were made, the slope is 0.37547. In the region $0\leq x\leq 0.11221$ the simple theory applies. In the region $0.11221\leq\epsilon<\infty$ the general theory applies.

The elastic-wave velocity is $C_e=\sqrt{280}=16.733$ arbitrary velocity units. The plastic-wave velocity is given by

$$C_p=\sqrt{\frac{d}{d\epsilon}\left(\frac{T}{M}\right)_{\epsilon=\epsilon_p}}=\sqrt{280\ \mathrm{sech}^2\ 20\epsilon_p}=C_e\ \mathrm{sech}\ 20\epsilon_p. \tag{63}$$

[3] The functional relationship (62) was chosen because tables were available that simplified the calculations. The numbers 14 and 20 have no significance, and were chosen only for convenience in plotting the curve. Other relationships involving more familiar functions could have been used, such as, $T/M=a+b\epsilon-\sqrt{a^2+b^2\epsilon^2}$, where a and b are arbitrary constants.

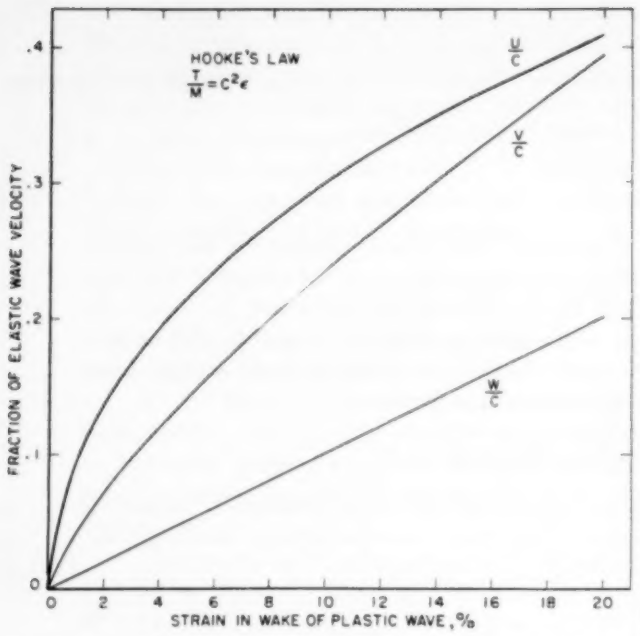

FIGURE 7. *Curves of U/C, V/C, and W/C as functions of ϵ_p for a filament having a linear tension-strain curve.*

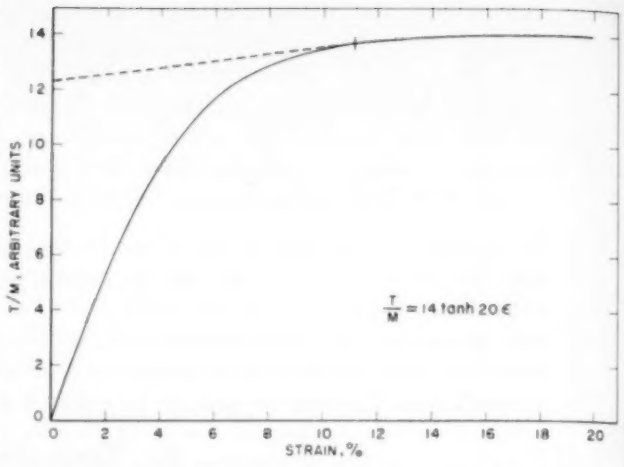

FIGURE 8. *Plot of tension-strain curve given by $(T/M)=14\tanh 20\epsilon$.*

Point of tangency with dotted line indicates strain and tension at which the slope of the curve equals $T/M(1+\epsilon)$.

In the region $0\leq\epsilon_p\leq 0.11221$ the transverse-wave velocity is given by

$$U=\sqrt{\frac{T}{M(1+\epsilon_p)}}=C_e\sqrt{\frac{0.05\tanh 20\epsilon_p}{1+\epsilon_p}}. \tag{64}$$

When ϵ_p is equal to or greater than 0.11221, the transverse-wave velocity is constant at the value $U_1=0.20967C_e$.

Filament material in the wake of the plastic-wave front flows inward at a velocity given by

$$W=\int_0^{\epsilon_p}\sqrt{\frac{1}{M}\frac{dT}{d\alpha}}d\alpha=0.05C_e\tan^{-1}(\sinh 20\epsilon_p). \tag{65}$$

Figure 9 gives the curves of U/C_e, V/C_e, and W/C_e as functions of ϵ_p for this material. The dotted lines give portions of the corresponding curves for the Hookean material.

Other behavior features of a material having the nonlinear tension-strain curve of eq (62) are given in figures 10, 11, 12, and 13. Figure 10 shows the strain distribution along the filament after transverse impact at various speeds up to $0.177C_e$. The dimensionless parameter x/C_et is used as the abscissa. A particular value of this parameter, 0.6 for instance, can be interpreted as a distance down the fiber 0.6 as far as the elastic wave has propagated. The dotted line gives the strain at the transverse-wave front as a function of the location of the transverse-wave front. Thus the strain in the filament after a transverse impact at velocity of $0.151C_e$ increases as shown up to a strain of 8 percent between the elastic- and plastic-wave fronts, and then remains constant. The plastic-wave front propagates at a velocity of $C_p=0.388C_e$, and the transverse-wave front at a velocity of $U=0.207C_e$ for this case.

Figure 11 shows the horizontal component of the inward-flow velocity for different points along the filament. The location of a point on the filament is designated by the same distance parameter used in figure 10. Consider, for instance, the case in which the filament is impacted at velocity $0.173C_e$. The strain in the wake of the plastic-wave front is 16 percent. The flow velocity at various points along the filament between the elastic-wave front and the transverse-wave front at $x/C_et=0.210$ increases to the value $0.0680C_e$ as shown. As the filament is horizontal in this region all of the flow is horizontal and directed inward. In the wake of the transverse-wave front the filament has changed its direction. The horizontal component

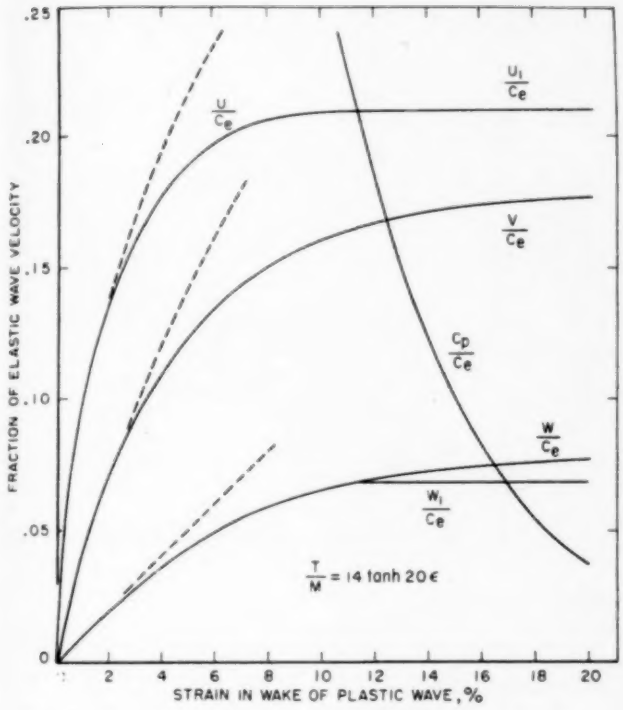

FIGURE 9. *Curves of U/C_e, V/C_e, and W/C_e as functions of ϵ_p for a filament with tension-strain curve given by $(T/M)=14 \tanh 20\epsilon$.*

Dotted lines show portions of similar curves for filament having linear stress-strain curve.

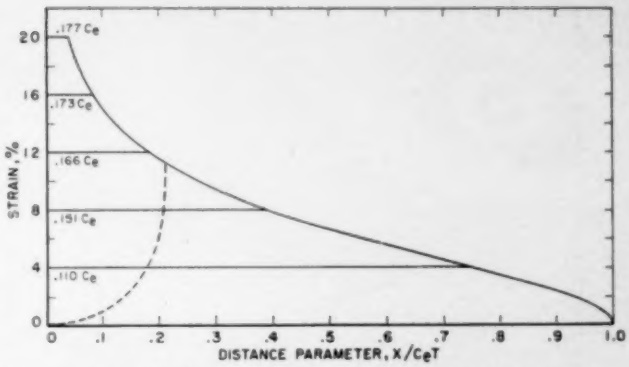

FIGURE 10. *Strain distribution along filament having tension-strain curve given by $(T/M)=14 \tanh 20\epsilon$, after transverse impact.*

If the filament is impacted, for example, with velocity $0.151C_e$, the strain increases to a value of 8 percent in the region between the elastic- and plastic-wave fronts, and then remains constant. The plastic-wave front in this case propagates at a velocity of $C_p=0.388C_e$, its position along the filament in distance parameter units is thus 0.388. The position of the dotted line gives the position of the transverse-wave front, which in this case propagates at velocity $U=0.207C_e$.

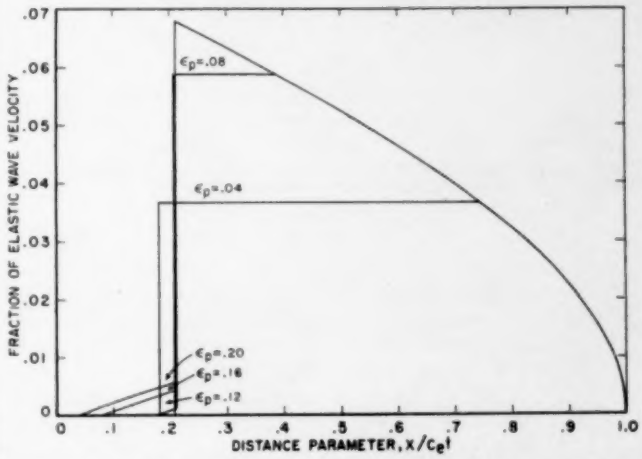

FIGURE 11. *Horizontal component of flow velocity at various points along the length of filament having tension-strain curve given by $(T/M)=14 \tanh 20\epsilon$, after transverse impact.*

A filament impacted at velocity $V=0.173C_e$, for example, has a strain in the wake of the plastic-wave front of 16 percent. The inward-flow velocity at various points along the filament between the elastic-wave front and the transverse-wave front at $x/C_et=0.210$ increases to the value $0.0680C_e$. In the wake of the transverse-wave front the filament has changed direction, and the horizontal component of flow velocity, therefore, decreases abruptly to the value $0.0045C_e$, and then decreases gradually to zero at $x/C_et=0.081$, the location of the plastic-wave front.

of the flow velocity, therefore, decreases abruptly to the value $0.0045C_e$. It then decreases gradually to zero at $x/C_et=0.081$, the location of the plastic-wave front. Between the plastic-wave front and the impact point the horizontal component of the flow velocity is zero.

Figure 12 shows how the angle θ of the transverse wave varies with the strain ϵ_p in the wake of the plastic-wave front. The solid line gives calculated values of cos θ and θ for the material with the nonlinear tension-strain curve. The dotted line gives the values calculated for the Hookean material. The angle θ increases negatively very rapidly for small values of ϵ_p. Thus even at low values of ϵ_p and correspondingly low impact velocities, a well-defined tent-shaped wave may be expected. (For instance, if $C_e=2{,}400$ m/sec and $V=0.026C_e=62.5$ m/sec, $\epsilon_p=0.5$ percent and $\theta=-21.75°$.) At higher values of ϵ_p the configuration of the transverse wave does not change much. This is illustrated in figure 13, where several configurations after impact are plotted for the filament having the nonlinear stress-strain curve. The locations of the plastic-wave front on several of these configurations where ϵ_p exceeds 0.11221 are given by the black dots.

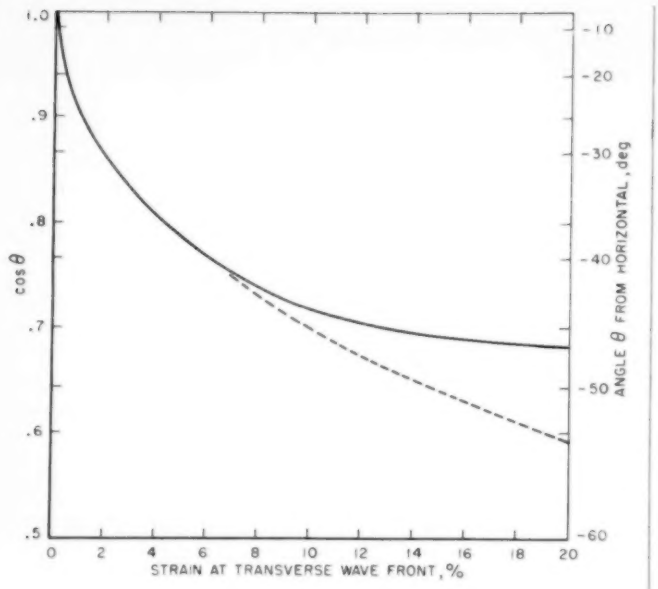

FIGURE 12. *Angle θ which transverse wave makes with horizontal plotted as a function of the strain (ϵ_p or ϵ_1) at the transverse-wave front.*

Solid line: Filament having tension-strain curve given by $(T/M)=14 \tanh 20\epsilon$.
Dotted line: Filament having linear tension-strain curve.

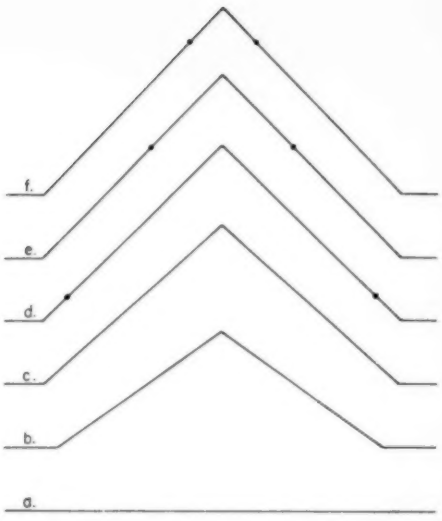

FIGURE 13. *Configurations after transverse impact for filament having tension-strain curve given by $(T/M)=14 \tanh 20\epsilon$.*

a. Before impact.
b. $\epsilon_p=0.04$, $V=0.110\ C_s$, $\theta=-36.4°$.
c. $\epsilon_p=.08$, $V=.151\ C_s$, $\theta=-42.5°$.
d. $\epsilon_p=.12$, $V=.166\ C_s$, $\theta=-45.3°$.
e. $\epsilon_p=.16$, $V=.173\ C_s$, $\theta=-46.4°$.
f. $\epsilon_p=.20$, $V=.177\ C_s$, $\theta=-46.9°$.

Black dots in last three configurations show positions of plastic-wave fronts.

9. References

[1] W. K. Stone, H. F. Schiefer, and G. Fox, Stress-strain relationships in yarns subjected to rapid impact loading: 1. Equipment, testing procedure, and typical results, J. Research NBS **54,** 269 (1955) RP2589; Textile Research J. **25,** 520 (1955).

[2] F. L. McCrackin, H. F. Schiefer, J. C. Smith, and W. K. Stone, Stress-strain relationships in yarns subjected to rapid impact loading: 2. Breaking velocities, strain energies, and theory neglecting wave propagation, J. Research NBS **54,** 277 (1955) RP2590; Textile Research J. **25,** 529 (1955).

[3] J. C. Smith, F. L. McCrackin, and H. F. Schiefer, Stress-strain relationships in yarns subjected to rapid impact loading: 3. Effect of wave propagation, J. Research NBS **55,** 19 (1955) RP2601; Textile Research J. **25,** 701 (1955).

[4] J. C. Smith, F. L. McCrackin, H. F. Schiefer, W. K. Stone, and K. M. Towne, Stress-strain relationships in yarns subjected to rapid impact loading: 4. Transverse impact tests, J. Research NBS **57,** 83 (1956) RP2695; Textile Research J. **26,** 821 (1956).

[5] G. I. Taylor, unpublished (1942).

[6] J. D. Cole, C. B. Dougherty, and J. H. Huth, Constant strain waves in strings, J. Appl. Mechanics, **20,** 519 (1953).

[7] J. W. Craggs, Wave motion in plastic-elastic strings, J. Mech. and Phys. of Solids **2,** 286 (1954).

[8] F. L. McCrackin, Impact tests of textile filaments, Doctor's dissertation, Lehigh University, Bethlehem, Pa. (1957).

[9] F. O. Ringleb, Motion and stress of an elastic cable due to impact, J. Appl. Mechanics **24,** 417 (1957).

[10] T. von Karman and P. Duwez, The propagation of plastic deformation in solids, J. Appl. Phys. **21,** 987 (1950).

[11] G. I. Taylor, The plastic wave in a wire extended by an impact load, British Official Report R. C. 329 (1942).

WASHINGTON, September 19, 1957.

THE NATIONAL BUREAU OF STANDARDS

The scope of activities of the National Bureau of Standards at its headquarters in Washington, D. C., and its major laboratories in Boulder, Colorado, is suggested in the following listing of the divisions and sections engaged in technical work. In general, each section carries out specialized research, development, and engineering in the field indicated by its title. A brief description of the activities, and of the resultant publications, appears on the inside of the front cover.

WASHINGTON, D. C.

Electricity and Electronics. Resistance and Reactance. Electron Devices. Electrical Instruments. Magnetic Measurements. Dielectrics. Engineering Electronics. Electronic Instrumentation. Electrochemistry.

Optics and Metrology. Photometry and Colorimetry. Optical Instruments. Photographic Technology. Length. Engineering Metrology.

Heat. Temperature. Physics. Thermodynamics. Cryogenic Physics. Rheology. Engine Fuels. Free Radicals Research.

Atomic and Radiation Physics. Spectroscopy. Radiometry. Mass Spectrometry. Solid State Physics. Electron Physics. Atomic Physics. Neutron Physics. Nuclear Physics. Radioactivity. X-ray and Betatron. Nucleonic Instrumentation. Radiological Equipment.

Chemistry. Organic Coatings. Surface Chemistry. Organic Chemistry. Analytical Chemistry. Inorganic Chemistry. Electrodeposition. Molecular Structure and Properties of Gases. Physical Chemistry. Thermochemistry. Spectrochemistry. Pure Substances.

Mechanics. Sound. Mechanical Instruments. Fluid Mechanics. Engineering Mechanics. Mass and Scale. Capacity, Density, and Fluid Meters. Combustion Controls.

Organic and Fibrous Materials. Rubber. Textiles. Paper. Leather. Testing and Specifications. Polymer Structure. Plastics. Dental Research.

Metallurgy. Thermal Metallurgy. Chemical Metallurgy. Mechanical Metallurgy. Corrosion. Metal Physics.

Mineral Products. Engineering Ceramics. Glass. Refractories. Enameled Metals. Concreting Materials. Constitution and Microstructure.

Building Technology. Structural Engineering. Fire Protection. Air Conditioning, Heating, and Refrigeration. Floor, Roof, and Wall Coverings. Codes and Safety Standards. Heat Transfer.

Applied Mathematics. Numerical Analysis. Computation. Statistical Engineering. Mechanical Physics.

Data Processing Systems. SEAC Engineering Group. Components and Techniques. Digital Circuitry. Digital Systems. Analog Systems. Application Engineering.

• Office of Basic Instrumentation. • Office of Weights and Measures.

BOULDER, COLORADO

Cryogenic Engineering. Cryogenic Equipment. Cryogenic Processes. Properties of Materials. Gas Liquefaction.

Radio Propagation Physics. Upper Atmosphere Research. Ionospheric Research. Regular Propagation Services. Sun-Earth Relationships. VHF Research.

Radio Propagation Engineering. Data Reduction Instrumentation. Modulation Systems. Navigation Systems. Radio Noise. Tropospheric Measurements. Tropospheric Analysis. Radio Systems Application Engineering. Radio Meteorology.

Radio Standards. High Frequency Electrical Standards. Radio Broadcast Service. High Frequency Impedance Standards. Electronic Calibration Center. Microwave Physics. Microwave Circuit Standards.

Recent Publications of the National Bureau of Standards

Periodicals

Journal of Research of the National Bureau of Standards, Volume 60, No. 3, March 1957 (RP2833 to RP2843 incl.). 60 cents. Annual subscription $4.00, $1.25 additional for foreign mailing.

Technical News Bulletin, Volume 42, No. 3, March 1958. 10 cents. Annual subscription $1.00, 35 cents additional for foreign mailing.

Basic Radio Propagation Predictions for June 1958. Three months in advance. CRPL-D 163. Issued March 1958. 10 cents. Annual subscription $1.00, 25 cents additional for foreign mailing.

Miscellaneous Publications

M223. Annual Report 1957—National Bureau of Standards. 45 cents.*

Circulars

C585. The measurement of thickness. 30 cents.*

Available from the Superintendent of Documents, U. S. Government Printing Office, Washington 25, D. C. The above NBS periodicals are available on a 1-, 2-, or 3-year subscription basis, although no reduction in rates can be made.

*Foreign postage, one-fourth additional.

UNITED STATES
GOVERNMENT PRINTING OFFICE
DIVISION OF PUBLIC DOCUMENTS
WASHINGTON 25, D. C.

OFFICIAL BUSINESS

PENALTY FOR PRIVATE USE TO AVOID
PAYMENT OF POSTAGE, $300
(GPO)

UNIVERSITY OF MICHIGAN
GENERAL LIBRARY
DOCUMENTS DIVISION
1276 ANN ARBOR MICH

Journal of Research of the National Bureau of St[illegible] May 195[illegible]

Contents

		Page
Forces on cylinders and plates in an oscillating fluid. Garbis H. Keulegan and Lloyd H. Carpenter.	RP2857	423
Reaction of portland cement with carbon dioxide. Charles M. Hunt, Vernon Dantzler, Lewis A. Tomes, and Raymond L. Blaine.	RP2858	441
Average energy of sulfur-35 beta decay. Howard H. Seliger, Wilfrid B. Mann, and Lucy M. Cavallo.	RP2859	447
Effect of structure on the thermal decomposition of polymers. Leo A. Wall and Roland E. Florin.	RP2860	451
Comparison of theoretical and empirical relations between the shear modulus and torsional resonance frequencies for bars of rectangular cross section. Sam Spinner and Rudolph C. Valore, Jr.	RP2861	459
Specific volume and degree of crystallinity of semicrystalline poly-(chlorotrifluoroethylene), and estimated specific volumes of the pure amorphous and crystalline phases. John D. Hoffman and James J. Weeks.	RP2862	465
Heat and ultraviolet aging of poly(vinyl chloride). Charles F. Bersch, Mary R. Harvey, and Bernard G. Achammer.	RP2863	481
Determination of water vapor from the change in electrical resistance of a hygroscopic film. Elmer R. Weaver, Ernest E. Hughes, and Albert W. Diniak.	RP2864	489
Improved bridge method for the measurement of core losses in ferromagnetic materials at high flux densities. William P. Harris and Irvin L. Cooter.	RP2865	509
Stress-strain relationships in yarns subjected to rapid impact loading: 5. Wave propagation in long textile yarns impacted transversely. Jack C. Smith, Frank L. McCrackin, and Herbert F. Schiefer.	RP2866	517

[A list of recent NBS publications is given on page 3 of the cover.]

For sale by the Superintendent of Documents, U. S. Government Printing Office, Washington 25, D. C. Price 60 cents (single copy)
Subscription price: $4.00 a year; $1.25 additional for foreign mailing.

UNITED STATES GOVERNMENT PRINTING OFFICE, WASHINGTON : 1958